

Copyright

by

Katharine Lee Harrison

2012

**The Dissertation Committee for Katharine Lee Harrison Certifies that this is the
approved version of the following dissertation:**

**Microwave-Assisted Synthesis and Characterization of Inorganic
Materials for Energy Applications**

Committee:

Arumugam Manthiram, Supervisor

John B. Goodenough

Allen J. Bard

Paulo J. Ferreira

Desiderio Kovar

**Microwave-Assisted Synthesis and Characterization of Inorganic
Materials for Energy Applications**

by

Katharine Lee Harrison, B.S.; M.S.E.

Dissertation

Presented to the Faculty of the Graduate School of
The University of Texas at Austin
in Partial Fulfillment
of the Requirements
for the Degree of

Doctor of Philosophy

**The University of Texas at Austin
August, 2012**

Dedication

To my loving, patient, and supportive husband.

Acknowledgements

I would like to thank the National Science Foundation for supporting my graduate studies through the Graduate Research Fellowship Program and the University of Texas at Austin College of Engineering for granting me a Graduate Engineering Doctoral Scholarship. This work was funded by Office of Vehicle Technologies of the U.S. Department of Energy under Contract No. DE-AC02-05CH11231 and the Department of Energy Basic Energy Sciences grant number DE-SC0005397. The Quantas 650 FEG scanning electron microscope, Kratos Axis Ultra X-ray-photoelectron spectroscopy instrument (grant number 0618242), and the Hitachi S-5500 scanning electron microscope/scanning transmission electron microscope (grant number 0821312) used in this work were funded by the National Science Foundation.

I would like to thank my advisor Dr. Arumugam Manthiram for his invaluable guidance and support throughout this process. He has been an excellent advisor who is both passionate about research and is truly concerned with the success of his students. I consider myself very fortunate to be graduating from his group. I would also like to thank my other committee members Dr. Allen Bard, Dr. John B. Goodenough, Dr. Paulo Ferreira, Dr. Desidero Kovar, and Dr. Jeremy P. Meyers for their helpful comments and assistance.

Additionally, I would like to thank all of my group members for their understanding, assistance, input, and encouragement, without which this dissertation would not have been possible. Specifically, I would like to acknowledge Dr. A. Vadivel Murugan for teaching me how to perform microwave synthesis and Danielle Applestone for her help with XPS data collection and pouch cell fabrication. Danielle in particular was constantly very helpful and supportive, and I have always greatly appreciated her

contributions to the lab as well as her scientific counsel. Additionally, I would like to thank James Knight for help with our collaboration on microwave synthesis of TiO_2 powder and for organizing supplies and keeping the lab running smoothly. I have also enjoyed collaborating with Daniel Varnado in Dr. Christopher Bielawski's group, who has helped me with the chemical lithiation described in Chapter 6 of this dissertation. Although none of our collaborations have thus far been fruitful, I would like to thank Arturo Gutierrez and Hyunwoo Cho, who I have had the opportunity to work closely with. I have learned much from our many discussions and have always appreciated their support.

I have also had the pleasure to work very closely with B. Reeja Jayan to complete the work described in Chapter 7 of this dissertation. I am very grateful that I had the opportunity to collaborate with her, and it would not have been possible for me to complete that project alone. I would like to thank her and Chih-Liang Wang for preparing and etching ITO-coated slides as well as helping with GIXRD and cross sectional SEM data collection. Kai Yang and Dr. Ali E. Yilmaz in the Electrical and Computer Engineering department have also been very helpful in aiding understanding of the film growth process discussed in Chapter 7 through simulations of the microwave experiments. Their contributions to this project are greatly appreciated.

Through the Basic Energy Sciences grant, I have also had the opportunity to work with several scientists at Oak Ridge National Laboratory (ORNL), Argonne National Laboratory (ANL), and Illinois Institute of Technology (IIT). The neutron diffraction data presented in Chapter 3 were collected by Craig Bridges and Clarina de la Cruz at the High Flux Isotope Reactor (HFIR) at ORNL. Research at HFIR was sponsored by the Scientific User Facilities Division, Office of Basic Energy Sciences, U.S. Department of Energy. I was able to visit ORNL and take part in the neutron diffraction data collection,

which was a very valuable experience. I would specifically like to extend many heartfelt thanks to Craig Bridges, who has spent a great deal of time advising me and answering my relentless questions regarding Rietveld refinement and structural analysis. His insightful comments and suggestions have been greatly appreciated. The tunneling electron microscopy/electron energy loss spectroscopy data presented in Chapter 3 were also collected at ORNL by Juan Carlos Idrobo with support from Oak Ridge National Laboratory's Shared Research Equipment (ShaRE) User Facility, which is sponsored by the Office of Basic Energy Sciences, U.S. Department of Energy. The Raman data presented in Chapter 3 was collected by Victor A. Maroni at ANL. Use of Raman instrumentation at the ANL Center for Nanoscale Materials was supported by the USDOE, Office of Science, Office of Basic Energy Sciences. X-ray absorption spectroscopy measurements were taken at the MRCAT (Sector 10, Advanced Photon Source) bending magnet beam line at Argonne National Laboratory by Mariappan Parans Paranthaman (ORNL), John Katsoudas (IIT), and Carlo U. Segre (IIT). MRCAT operations are supported by the Department of Energy and the MRCAT member institutions. XANES data analysis was performed by Carlo U. Segre.

I also am very grateful to Neil Boesl and Reynhardt Kloppe at Anton Paar who have provided much technical support and answered hundreds of questions regarding microwave synthesis. Michael Ronalter at the University of Texas at Austin glass shop has also contributed greatly to this work by designing and fabricating custom glass baskets used in Chapter 7 of this dissertation.

Above all, I would like to thank my husband who has been infinitely patient with my long hours in the lab and who has always encouraged me in everything that I have done. This dissertation would not have been possible without his unwavering support. I

would also like to thank my family for always being there for me through the frustration that accompanies earning a Ph.D, and I am very grateful for their support.

Microwave-Assisted Synthesis and Characterization of Inorganic Materials for Energy Applications

Katharine Lee Harrison, Ph.D.

The University of Texas at Austin, 2012

Supervisor: Arumugam Manthiram

Lithium-ion batteries play a crucial role in portable electronics, but require further innovation for electric vehicle and grid storage applications. To meet this demand, significant emphasis has been placed on developing safe, inexpensive, high energy density cathode materials.

LiFePO_4 is a candidate cathode material for electric vehicle and grid storage applications. Vanadium-doped LiFePO_4 cathodes of the form $\text{LiFe}_{1-3x/2}\text{V}_{x/2}\text{PO}_4$ ($0 \leq x \leq 0.25$) were synthesized here by a facile, low-temperature microwave-assisted solvothermal (MW-ST) method. Such an approach offers manufacturing-energy and cost savings compared to conventional synthesis. Additionally, although $\text{LiFe}_{1-3x/2}\text{V}_{x/2}\text{PO}_4$ has been synthesized previously by conventional methods, it is shown here that the MW-ST method allows much higher doping levels than can be achieved at conventional temperatures, indicating that metastable phases can be isolated through the low-temperature microwave-assisted synthesis.

LiFePO_4 suffers from poor ionic conductivity, but this limitation can be minimized by microwave-assisted synthesis through a tuning of the particle size, allowing for decreased Li^+ diffusion paths. LiVOPO_4 is another polyanion material with higher energy density than LiFePO_4 , but similar ionic conductivity limitations. It has not

been previously synthesized by MW-ST. Thus, a MW-ST method was developed here to prepare LiVOPO_4 . By varying reaction conditions, three polymorphic modifications of LiVOPO_4 were accessed and the electrochemical performance was optimized. LiVOPO_4 can be further discharged to Li_2VOPO_4 , which has been suggested in the literature, but the structural transformation that accompanies this process has not been detailed. To this end, the delithiation process was studied by *ex situ* XRD measurements to better understand how the second lithium is accommodated.

Finally, MW-ST has also been exploited to grow thin films of anatase TiO_2 phase on indium tin oxide (ITO)-coated glass substrates. The microwave field is selectively absorbed by the conductive ITO layer on the glass substrates, leading to ohmic heating. The resulting heated ITO layer acts as a favorable site for nucleation and growth. TiO_2 thin films have widespread applications in the energy and electronics sectors. Such selective microwave-assisted ohmic heating of solid materials within a growth solution represents a promising new avenue for microwave synthesis, which has been minimally explored in the literature.

Table of Contents

List of Tables	xv
List of Figures	xvii
List of Schematics	xxviii
Chapter 1: Introduction.....	1
1.1 Motivation.....	1
1.2 Lithium-ion Batteries.....	1
Operating principle	2
Lithium-ion battery performance.....	3
History of lithium-ion batteries.....	6
1.3 Cathode materials for lithium-ion batteries	7
Layered structured cathodes	8
Spinel structured cathodes	8
Polyanion-containing cathodes	9
1.4 Thin Film Batteries	13
1.5 Microwave Theory.....	14
1.6 Objectives	17
Chapter 2: Experimental Procedures	20
2.1 Materials characterization.....	20
Inductively coupled plasma (ICP)	20
Thermogravimetric Analysis (TGA).....	20
Powder X-ray diffraction (XRD) and glancing incidence X-ray diffraction (GIXRD)	20
Neutron diffraction (PND).....	21
X-ray absorption near-edge spectroscopy (XANES).....	21
X-ray photoelectron spectroscopy (XPS)	22
Fourier transform infrared analysis (FTIR) and Raman spectroscopy	22
Scanning electron (SEM) and scanning transmission electron (STEM) microscopy.....	23

2.2 Electrochemical characterization	24
Electrode preparation	24
Coin cell fabrication.....	24
Electrochemical measurements.....	25
Chapter 3: Microwave-assisted Solvothermal Synthesis and Characterization of $\text{LiFe}_{1-3x/2}\text{V}_x\text{PO}_4$ Cathodes	27
3.1 Introduction.....	27
3.2 Experimental	28
Microwave-assisted solvothermal synthesis	28
Conventional synthesis	31
3.3 Results and discussion	32
Structural and chemical characterization	32
Determination of transition-metal oxidation states.....	39
Determination of transition-metal occupancies	47
Spectroscopic characterization.....	54
Electrochemical characterization	58
3.4 Conclusions.....	68
Chapter 4: Phase Stability of $\text{LiFe}_{1-3x/2}\text{V}_x\text{PO}_4$ Cathodes.....	69
4.1 Introduction.....	69
4.2 Experimental	69
Microwave Synthesis	69
Conventional synthesis	70
4.3 Results and discussion	72
Structural characterization	72
STEM and EDS analysis.....	80
Spectroscopic characterization.....	83
Electrochemical characterization	86
4.4 Conclusion	92

Chapter 5:	Microwave-assisted Solvothermal Synthesis and Characterization of Various Polymorphs of LiVOPO_4 Cathodes	93
5.1	Introduction.....	93
5.2	Experimental	93
5.3	Results and discussion	95
	Synthesis of LiVOPO_4 polymorphs	95
	Effects of the solvent	101
	Optimization of particle size	109
	Cycling performance.....	116
5.4	Conclusions.....	120
Chapter 6:	Chemical and Electrochemical Lithiation of LiVOPO_4 Cathodes.....	121
6.1	Introduction.....	121
6.2	Experimental	122
	Synthesis of LiVOPO_4	122
	Chemical Lithiation	123
6.3	Results and discussion	124
	Chemical lithiation.....	124
	Electrochemical lithiation	131
6.4	Conclusions.....	143
Chapter 7:	Microwave-assisted Solvothermal Synthesis of TiO_2 Thin Films.....	145
7.1	Introduction.....	145
7.2	Experimental	148
7.3	Results and discussion	150
	Synthesis condition optimization and film growth mechanism	150
	Selective heating of the ITO layer	157
	Attempts to grow films by conventional solvothermal method.....	163
	Film growth in other microwaves	168
	MW-ST synthesis comparison in SiC and glass vessels.....	170
	Cyclic voltammetry of thin films	173
	Summary of results from collaborators.....	178

7.4 Conclusions.....	179
Chapter 8: Summary	180
Appendices.....	184
A. Synthesis of bulk TiO ₂ powder for lithium-ion batteries.....	184
B. Scale up of microwave-assisted solvothermal graphene synthesis	187
C. Reduction of metal oxides by microwave-assisted solvothermal process	191
References.....	195
Vita	203

List of Tables

Table 3.1.	<i>Lattice parameters obtained by Rietveld refinement for samples prepared according to $\text{LiFe}_{1-x}(\text{VO})_x\text{PO}_4$ with $0 \leq x \leq 0.25$.....</i>	<i>35</i>
Table 3.2.	<i>Elemental ratios obtained from ICP analysis of samples prepared according to $\text{LiFe}_{1-x}(\text{VO})_x\text{PO}_4$ with $0 \leq x \leq 0.25$.</i>	<i>36</i>
Table 3.3.	<i>ICP data for V-doped samples prepared according to $\text{LiFe}_{1-x}(\text{VO})_x\text{PO}_4$, $\text{LiFe}_{1-2x}\text{V}_x\text{PO}_4$, and $\text{LiFe}_{1-3x/2}\text{V}_{x/2}\text{PO}_4$.....</i>	<i>38</i>
Table 3.4.	<i>Vanadium oxidation state analysis from XANES least squares fit (± 0.03).</i>	<i>44</i>
Table 3.5.	<i>Rietveld refinement occupancy results of XRD data for undoped and V-doped LiFePO_4 (with fit parameter χ^2 shown).</i>	<i>48</i>
Table 3.6.	<i>Rietveld refinement results of the neutron diffraction data for samples prepared according to $\text{LiFe}_{1-x}(\text{VO})_x\text{PO}_4$.....</i>	<i>51</i>
Table 3.7.	<i>Second CV cycle charge and discharge peak voltages at a 0.05 mV/s rate for samples prepared according to $\text{LiFe}_{1-x}(\text{VO})_x\text{PO}_4$ with $0 \leq x \leq 0.25$.....</i>	<i>62</i>
Table 4.1.	<i>Summary of as-prepared and post-heated samples of undoped and V-doped LiFePO_4.....</i>	<i>71</i>
Table 4.2.	<i>Summary of the lattice parameters of the as-prepared and post-heated undoped and V-doped LiFePO_4 (obtained by Rietveld refinement of XRD data with fit parameter χ^2 shown).</i>	<i>75</i>
Table 4.3.	<i>Fractional occupancy and phase fraction results for as-prepared and post-heated samples of undoped and V-doped LiFePO_4 from Rietveld refinement.</i>	<i>78</i>

Table 5.1.	<i>Dominant products from MW-ST synthesis in water or mixed water and ethanol solvent with various ratios of Li:V:P. All reactions were run to a maximum pressure of 40 bar for a total reaction time of 50 minutes with a V concentration of 0.067 M.</i>	<i>97</i>
Table 5.2.	<i>Lattice parameters for LiVOPO₄ determined by Rietveld refinement.</i>	<i>98</i>
Table 5.3.	<i>Examples of transition to α polymorph with increased pressure (which equates to increased temperature). All tests were run to a maximum of either 40 or 50 bar with a V concentration of 0.067 M.</i>	<i>100</i>
Table 5.4.	<i>Elemental analysis of samples prepared at 230 °C in 3:1 water:ethanol with varying amounts of CTAB solution substituted for water. All samples were synthesized with a V concentration of 0.067 M.</i>	<i>116</i>
Table 6.1.	<i>Elemental analysis of pristine and chemically lithiated LiVOPO₄. *</i>	<i>125</i>
Table 7.1.	<i>Summary of results for conventional solvothermal synthesis tests. ITO-coated glass slides were placed in acid digestion vessels containing 5 mL sol-gel and 20 mL TEG for times ranging from 2-72 h at 150 and 180 °C.....</i>	<i>164</i>

List of Figures

Figure 1.1.	<i>Basic operating principle of a lithium-ion battery.</i>	<i>2</i>
Figure 1.2.	<i>Energy diagram of the energies of cathode and anode materials relative to the electrolyte window.</i>	<i>5</i>
Figure 1.3.	<i>Energies of $\text{Co}^{3+/2+}:3d$ and $\text{Co}^{4+/3+}:3d$ redox couples relative to the nonmetal $\text{O}^{2-}:2p$ and $\text{S}^{2-}:3p$ bands.</i>	<i>7</i>
Figure 1.4.	<i>Energy diagram depicting the position of the $\text{Fe}^{2+/3+}$ redox couples in various materials (not to scale).</i>	<i>10</i>
Figure 3.1.	<i>XRD patterns for LiFePO_4 and V-doped LiFePO_4 samples with a comparison over a smaller 2θ range.</i>	<i>34</i>
Figure 3.2.	<i>XRD of 15 % V-doped LiFePO_4 with varying Fe/P ratio in the precursor solution.</i>	<i>38</i>
Figure 3.3.	<i>XPS (a) V 2p and (b) C 1s core lines for sample prepared according to $\text{LiFe}_{0.85}(\text{VO})_{0.15}\text{PO}_4$.</i>	<i>40</i>
Figure 3.4.	<i>V edge XANES data of V-doped LiFePO_4 samples and $\text{Li}_3\text{V}_2(\text{PO}_4)_3$ and LiVOPO_4 standards. With the exception of $\text{LiFe}_{0.775}\text{V}_{0.15}\square_{0.075}\text{PO}_4$, the formulas for the V-doped LiFePO_4 samples reflect the intended sample compositions and the precursor ratios that were used for synthesis, rather than the actual compositions.</i>	<i>42</i>
Figure 3.5.	<i>XANES of V-doped LiFePO_4 samples and standards with inset close up of V pre-edge region. With the exception of $\text{LiFe}_{0.775}\text{V}_{0.15}\square_{0.075}\text{PO}_4$, the formulas for the V-doped LiFePO_4 samples represent the intended sample compositions and the precursor ratios that were used for synthesis, rather than the actual compositions.</i>	<i>43</i>

Figure 3.6. Representative XANES absorption spectrum least squares fit for sample prepared according to $\text{LiFe}_{0.85}(\text{VO})_{0.15}\text{PO}_4$. The $\text{Li}_3\text{V}_2(\text{PO}_4)_3$ and LiVOPO_4 curves are scaled by their relative contributions to the fit. 44

Figure 3.7. Fe edge XANES data of V-doped LiFePO_4 samples as well as FePO_4 , conventional LiFePO_4 , and MW-ST LiFePO_4 standards. With the exception of $\text{LiFe}_{0.775}\text{V}_{0.15}\square_{0.075}\text{PO}_4$, the formulas for the V-doped LiFePO_4 samples represent the intended sample compositions and the precursor ratios that were used for synthesis, rather than the actual compositions.45

Figure 3.8. XANES of V-doped LiFePO_4 samples and standards with the inset showing the Fe pre-edge region. With the exception of $\text{LiFe}_{0.775}\text{V}_{0.15}\square_{0.075}\text{PO}_4$, the formulas for the V-doped LiFePO_4 samples represent the intended sample compositions and the precursor ratios that were used for synthesis, rather than the actual compositions. ...46

Figure 3.9. Representative XRD Rietveld refinement fit for 15 % V-doped sample.49

Figure 3.10. Representative neutron diffraction refinement fit for sample synthesized according to $\text{LiFe}_{0.85}(\text{VO})_{0.15}\text{PO}_4$ with Li at (0,0,0).52

Figure 3.11. STEM Z-contrast images depicting interstitial defects ((a) and (b)) and bright field image (c) of a nanorod for 15 % V-doped LiFePO_453

Figure 3.12. EELS data taken on a 15 % V-doped LiFePO_4 nanorod.54

Figure 3.13. FTIR spectra for LiFePO_4 and V-doped LiFePO_4 compared to standards. Also shown is an amorphous product formed when performing MW-ST synthesis with Li, V, and P precursors in the absence of Fe.55

Figure 3.14. Raman spectroscopy of LiFePO_4 , 15 % V-doped LiFePO_4 prepared according to $\text{LiFe}_{0.775}\text{V}_{0.15}\square_{0.075}\text{PO}_4$, and LiVOPO_4 .	57
Figure 3.15. SEM micrographs of LiFePO_4 (left) and 15 % V-doped LiFePO_4 prepared according to $\text{LiFe}_{0.85}(\text{VO})_{0.15}\text{PO}_4$ (right).	59
Figure 3.16. Second CV cycle at a rate of 0.1 mV/s in the range of 2.0 to 4.3 V for LiFePO_4 and V-doped LiFePO_4 prepared according to $\text{LiFe}_{1-x}(\text{VO})_x\text{PO}_4$ with $0 \leq x \leq 0.25$ compared to vanadium phosphate standards (note changes of scale for the vanadium phosphate standards).	61
Figure 3.17. Second CV cycle at a 0.1 mV/s rate in the range between 1.8 and 4.8 V for LiFePO_4 and $\text{LiFe}_{0.775}\text{V}_{0.15}\square_{0.075}\text{PO}_4$ synthesized under the same MW-ST conditions. The data are compared to vanadium phosphate standards (note the changes of scale for the vanadium phosphate standards).	63
Figure 3.18. First charge-discharge curves between 2 and 4.3 V for LiFePO_4 and V-doped LiFePO_4 prepared according to $\text{LiFe}_{1-x}(\text{VO})_x\text{PO}_4$ with $0 \leq x \leq 0.25$ compared to vanadium phosphate standards (note change of scale for LiVOPO_4).	64
Figure 3.19. Open-circuit voltage curve for 25 % V-doped LiFePO_4 sample prepared according to $\text{LiFe}_{0.75}(\text{VO})_{0.25}\text{PO}_4$.	66
Figure 3.20. Cycle performance data at a C/10 rate for LiFePO_4 and V-doped LiFePO_4 samples prepared according to $\text{LiFe}_{1-x}(\text{VO})_x\text{PO}_4$ with $0 \leq x \leq 0.25$.	67
Figure 4.1. XRD patterns of as-prepared and post-heated samples of undoped and V-doped LiFePO_4 with an internal Si standard.	73

Figure 4.2. Representative XRD Rietveld refinement fit of V-doped LiFePO_4 , $\text{Li}_3\text{V}_2(\text{PO}_4)_3$, and Si phases.	77
Figure 4.3. Maximum V content demonstrated versus temperature. Heated MW-ST V-doped LiFePO_4 samples are compared to conventionally prepared V-doped LiFePO_4 samples from this study (red triangles) and from other literature (black symbols). The legends indicate the heating environment and heating time. The values used here are ' $V_{\text{occupancy}}$ from % LVP' from Table 4.3 where applicable. The MW-ST data point is the $V_{\text{occupancy}}$ value found for the Fe site in the '25 %' V-doped sample.	80
Figure 4.4. STEM images and corresponding elemental dot maps of (a) MW-LFVP-unheated and (b) MW-LFVP- H_2 -725-6h. Note that (b) was obtained for a sample previously heated at 700 °C rather than 725 °C, but this is not anticipated to change the result.	82
Figure 4.5. STEM images and corresponding elemental dot maps of (a) CONV-LFVP- H_2 -525-6h and (b) CONV-LFVP- H_2 -725-6h. Note that images were obtained for samples previously heated at 500 °C and 700 °C rather than 525 °C and 725 °C, but this is not anticipated to change the results.	83
Figure 4.6. FTIR absorbance spectra for as-prepared and post-heated samples of undoped and V-doped LiFePO_4 , conventionally prepared V-doped LiFePO_4 , and reference compounds.	85
Figure 4.7. First charge-discharge curves at a C/10 rate for MW-ST LiFePO_4 , heated and unheated MW-ST V-doped LiFePO_4 samples, conventionally prepared V-doped LiFePO_4 samples, as well as $\text{Li}_3\text{V}_2(\text{PO}_4)_3$ and LiVOPO_4 for a comparison.	87

Figure 4.8. Charge-discharge data at a C/10 rate in the voltage range from 2.0 – 4.3 V, which is the typical range for LiFePO_4	88
Figure 4.9. Second cycle CV data at a 0.1 mV/s rate for MW-ST LiFePO_4 , heated and unheated MW-ST V-doped LiFePO_4 samples, conventionally prepared V-doped LiFePO_4 samples, as well as $\text{Li}_3\text{V}_2(\text{PO}_4)_3$ and LiVOPO_4 for comparison.....	90
Figure 4.10. Second cycle CV data at a 0.1 mV/s rate in the voltage range of 2.0 - 4.3 V, which is a more typical range for LiFePO_4 than the range of 1.5 - 4.8 V.	91
Figure 5.1. XRD patterns for the three polymorphs of LiVOPO_4 compared to the database patterns [58, 68, 75]. All three syntheses were run for a total reaction time of 50 minutes (~ 25 min hold time) with a concentration of 0.067 M in V. Slight impurities for $\beta\text{-LiVOPO}_4$ are indicated with red arrows.	99
Figure 5.2. FTIR absorbance spectrum for $\alpha\text{-LiVOPO}_4$ synthesized at 230 °C with a V concentration of 0.067 M and a total reaction time of 50 min.	101
Figure 5.3. XRD of $\alpha\text{-LiVOPO}_4$ synthesized with a V concentration of 0.067 M for a 50 min total reaction time and Li:V:P = 5:1:5 in various solvent mixtures.....	102
Figure 5.4. XRD of $\alpha\text{-LiVOPO}_4$ synthesized at 230 °C with a V concentration of 0.067 M for a 50 min total reaction time (~25 min hold time) and Li:V:P = 5:1:5 in various solvent mixtures.	103
Figure 5.5. SEM images of $\alpha\text{-LiVOPO}_4$ synthesized at 230 °C with a V concentration of 0.067 M for a 50 min total reaction time (~ 25 min hold time) in various solvents.	105

Figure 5.6. First charge-discharge curves at 3.0 - 4.5 V with a C/20 rate for α -LiVOPO ₄ synthesized. All solutions contained a V concentration of 0.067 M for a 50 min total reaction time in different solvents. All samples were prepared at 230 °C except for the sample prepared in water, which was held at 240 °C.....	106
Figure 5.7. First charge-discharge curves at 2.0 - 4.5 V with a C/20 rate for α -LiVOPO ₄ synthesized. All solutions contained a V concentration of 0.067 M for a 50 min total reaction time in different solvents. All samples were prepared at 230 °C except for the sample prepared in water, which was held at 240 °C.....	108
Figure 5.8. SEM of α -LiVOPO ₄ synthesized in 3:1 water:ethanol. All samples were prepared at 230 °C with varied concentration and reaction time. .	110
Figure 5.9. First charge-discharge curves at 3.0 - 4.5 V with a C/20 rate for α -LiVOPO ₄ synthesized in 3:1 water:ethanol at 230 °C with varied reaction time and concentration.	111
Figure 5.10. First charge-discharge curves at 2.0 - 4.5 V at C/20 rate for α -LiVOPO ₄ synthesized in 3:1 water:ethanol at 230 °C with varied reaction time and concentration.	112
Figure 5.11. SEM of α -LiVOPO ₄ synthesized in 3:1 water:ethanol at 230 °C. The reactions were run with a V concentration of 0.067 M with varied reaction time and amounts of CTAB solution substituted for water.	114
Figure 5.12. First charge-discharge curves at 3.0 - 4.5 ad 2.0 - 4.5 V at C/20 rate for α -LiVOPO ₄ synthesized in 3:1 water:ethanol at 230 °C. The reactions were run with a V concentration of 0.067 M with varied amounts of CTAB solution substituted for water.....	115

Figure 5.13. Cycle performance of samples synthesized in mixtures of water and various solvents with a V concentration of 0.067 M and a temperature of 230 °C (except for the sample synthesized in water at 240 °C) for a reaction time of 50 min.	117
Figure 5.14. Cycle performance of samples synthesized in mixtures of water and ethanol with a temperature of 230 °C for varied reaction time, concentration, and CTAB and PEDOT additives.	118
Figure 5.15. First charge-discharge curves of the PEDOT:PSS-coated sample compared to the sample before coating (prepared in 3:1 water:ethanol with a reaction time of 10 min) with voltage windows of 2 – 4.5 and 3 – 4.5 V.	119
Figure 6.1. Pictures of LiVOPO_4 products before and after chemical lithiation. The color change was immediate upon addition of <i>n</i> -butyllithium.	124
Figure 6.2. FTIR spectra of $\alpha\text{-LiVOPO}_4$ and $\beta\text{-LiVOPO}_4$ before and after chemical lithiation.	126
Figure 6.3. XRD patterns of $\alpha\text{-LiVOPO}_4$ and $\beta\text{-LiVOPO}_4$ before and after chemical lithiation compared to database patterns.	129
Figure 6.4. XRD patterns in a small range of angles for (a) pristine $\alpha\text{-LiVOPO}_4$, (b) chemically lithiated $\alpha\text{-Li}_{1.5}\text{VOPO}_4$, (c) chemically lithiated $\alpha\text{-Li}_2\text{VOPO}_4$, (d) pristine $\beta\text{-LiVOPO}_4$, (e) chemically lithiated $\beta\text{-Li}_{1.5}\text{VOPO}_4$, and (f) chemically lithiated $\beta\text{-Li}_2\text{VOPO}_4$	130
Figure 6.5. Discharge curves for $\alpha\text{-LiVOPO}_4$ and $\beta\text{-LiVOPO}_4$ with states of discharge used for ex situ XRD indicated (note changes in scale).	131
Figure 6.6. Ex situ XRD patterns of $\alpha\text{-LiVOPO}_4$ at various states of discharge.	135

Figure 6.7. <i>Ex situ XRD patterns of α-LiVOPO₄ at various states of discharge, detailing the low-angle region.</i>	136
Figure 6.8. <i>Comparison between chemically lithiated and electrochemically lithiated α-LiVOPO₄ samples.</i>	138
Figure 6.9. <i>Ex situ XRD patterns of β-LiVOPO₄ at various states of discharge.</i>	139
Figure 6.10. <i>Ex situ XRD Patterns of β-LiVOPO₄ at various states of discharge, detailing the low-angle region.</i>	140
Figure 6.11. <i>Comparison of the chemically and electrochemically lithiated β-LiVOPO₄ samples.</i>	142
Figure 6.12. <i>Ex situ XRD patterns of LiVOPO₄ after the pristine material is charged to 4.5 V and after the fully discharged material is charged to 4.5 V.</i>	143
Figure 7.1. <i>GIXRD patterns for films grown with a 60 min hold time at 140 °C. Films are grown with varying amounts of TEG and ethanol as additives, but all growth solutions contained 5 mL of Ti sol-gel.</i>	150
Figure 7.2. <i>GIXRD patterns of films grown with a 60 minute hold time at various temperatures with 5 mL sol-gel, 15 mL ethanol, and 5 mL TEG *except for the film at 180 °C, which was grown in 5 mL sol-gel and 20 mL ethanol.</i>	152
Figure 7.3. <i>GIXRD patterns of patterned films grown with a 60 minute hold at various temperatures. Films are grown with 5 mL sol-gel and 20 mL TEG.</i>	153
Figure 7.4. <i>GIXRD patterns of films grown at 150 °C for various hold times. Films are grown with 5 mL sol-gel and 20 mL TEG.</i>	154
Figure 7.5. <i>GIXRD patterns of patterned films grown at 150 °C for various hold times. Films are grown with 5 mL sol-gel and 20 mL TEG.</i>	154

Figure 7.6. GIXRD of films grown on ITO-coated glass slides at 150 °C with a 60 minute hold time in solutions consisting of 20 mL TEG and 5 mL sol-gel.	155
Figure 7.7. TiO ₂ film grown at 150 °C for 60 min reaction inside microwave reactor with 10 W/m power ramp rate. A large area SEM view is shown in (b), and a magnified region is shown in (a). A cross sectional image reveals a thickness of approximately 800 nm in (c).	156
Figure 7.8. Various ITO patterns before the microwave reactions, TiO ₂ films grown on ITO after microwave reactions, and computational predictions showing the time-averaged absorbed power density in the ITO layer (units of dB).	159
Figure 7.9. Simulations of the time-averaged absorbed power density in the ITO layer (units of dB) compared to experiments detailing the effects of ITO pattern size and ITO sheet resistance. Note that the sheet resistance of the ITO for the left and middle columns is 10 Ω/□ for simulations and experiments. The resistivity of the ITO on the right is 1000 Ω/□ for the simulations and 450 ohm/sq for the experiments.	161
Figure 7.10. Conventional solvothermal reactions were performed in the vessel shown in (a) on ITO-coated glass slides (c). After the reaction at 180 °C for 72 h, the glass holder and slide were covered with off-white precipitate (b and d). This was easily washed to produce the slide shown in (e).	165
Figure 7.11. GIXRD of the ITO-coated glass slide (pictured in Figure 7.10) after the 180 °C reaction held for 72 h compared to a microwave-synthesized film.	166

- Figure 7.12.** EDS results of the ITO-coated glass slides (a) after solvothermal reaction at 180 °C for 72 h and (b) after microwave solvothermal deposition at 150 °C for 60 min with a 10 W/min power ramp rate. Both growth solutions contained 5 mL sol-gel and 20 mL TEG.167
- Figure 7.13.** Pictures and GIXRD of TiO₂ films grown in three different microwaves. The film grown in the Monowave is a different size because smaller vessels used cannot accommodate larger slides.169
- Figure 7.14.** Comparison of the thermal profiles in glass and SiC vessels. The ramp time, temperature, and hold time were nearly identical in both vessels. There is slightly more temperature variation during the hold time in the SiC vessel, because it is more difficult to control the temperature. This is because thermal convection is a slow heat transfer process relative to direct dielectric heating of the solvent and ohmic heating of the ITO layer.172
- Figure 7.15.** Comparison of ITO slides before and after microwave reactions in glass and SiC vessels for a reaction ramped to 160 °C in approximately 3 min and held for 60 minutes. Only reactions in the glass vessel led to film formation. The color of the ITO layer (square patterned in center of slides) is different than previously shown slides, because the slides were from a different batch with a slightly higher resistance. It should be noted that different temperatures and different ramp times did not change these results.173

Figure 7.16. CV of (a) a very crystalline microwave-grown TiO_2 film on ITO-coated glass, (b) a more weakly crystalline TiO_2 film, (c) an amorphous TiO_2 film, and (d) TiO_2 film on ITO-coated glass grown by conventional spin coating of Ti sol-gel and subsequent furnace heating at 450 °C. Note changes in current density scale.	175
Figure 7.17. Films grown on Al-coated glass and ITO-coated plastic compared to films grown on ITO-coated glass.	177
Figure A.1. XRD of TiO_2 powder.	185
Figure A.2. SEM image of TiO_2 powder.	185
Figure A.3. First charge-discharge curves (top) and cycle performance (bottom) of TiO_2	186
Figure A.4. XRD of graphene prepared in the Masterwave.	189
Figure A.5. First charge-discharge curves of graphene prepared in the Synthos (left) and Masterwave (right) microwaves.	189
Figure A.6. XRD patterns of various oxides before and after microwave reaction.	193
Figure A.7. XRD patterns for various oxides before and after microwave reaction.	194

List of Schematics

<i>Schematic 3.1.</i>	<i>Illustration of the microwave-solvothermal synthesis of V-doped LiFePO_4 prepared according to $\text{LiFe}_{1-x}(\text{VO})_x\text{PO}_4$.....</i>	<i>30</i>
<i>Schematic 5.1.</i>	<i>Schematic summarizing the typical synthesis conditions for α-LiVOPO_4</i>	<i>95</i>
<i>Schematic 7.1.</i>	<i>Comparison of the MW-ST synthesis to conventional thin film deposition (top) with a summary of synthesis method and resulting TiO_2 thin films (bottom). The blue square shown on the glass slide is ITO that was patterned onto the slide by chemical etching.</i>	<i>149</i>

Chapter 1: Introduction

1.1 MOTIVATION

As energy usage increases across the globe, energy storage becomes a more and more critical hurdle to overcome. Development of electrified transportation is essential for cleaner, more efficient vehicles and for curbing national security concerns that are associated with importing oil. Energy storage is also needed for practical utilization of electricity generation from intermittent renewables such as solar and wind, and batteries are a candidate for large-scale storage. Finally, growth in the portable electronics market has led to demand for lighter devices with longer battery lives. Improvements in cost, safety, and performance of batteries are needed for widespread adoption of electric vehicles, grid storage, and to keep up with developments in portable electronics.

1.2 LITHIUM-ION BATTERIES

Batteries can be divided into two categories: primary and secondary batteries. Primary batteries can be used a single time and then are discarded, whereas secondary batteries are rechargeable. Only secondary batteries are practical for electric vehicles, electric grid storage, and the plethora of portable electronics the modern society depends on every day. Secondary batteries can be divided into several different chemistries. The most commonly used chemistries are lead-acid, nickel-cadmium, nickel metal hydride, and lithium-ion batteries. Of all the secondary battery chemistries currently commercialized, lithium-ion batteries offer the highest gravimetric and volumetric energy densities. Despite this, the realizable energy and power densities are still limited by materials challenges. Thus, the discovery and optimization of new materials for lithium-ion batteries has been the subject of intense research. Improvements in cost, performance (cycle life, power density, and energy density), and safety are all needed for lithium-ion

batteries to expand from current portable electronics markets to widespread adoption in electrified transportation and electric grid storage applications.

Operating principle

Lithium-ion batteries involve transporting Li^+ ions back and forth between the electrodes during operation by inserting or extracting Li^+ ions into and out of the electrode materials (lithium insertion or intercalation materials). Between the electrodes lies an electrolyte, a medium that is a Li^+ -ion conductor, but an electrical insulator. During charge (energy input), Li^+ ions move from the cathode through the electrolyte into the anode, while electrons move through the external circuit from the cathode to the anode (from positive to negative charge). In essence, an oxidation reaction occurs at the cathode, and a reduction occurs at the anode during charge. During discharge (energy output), the Li^+ ions move from the anode through the electrolyte into the cathode while electrons move through the external circuit from the anode to the cathode (from negative to positive charge). This is depicted below in Figure 1.1.

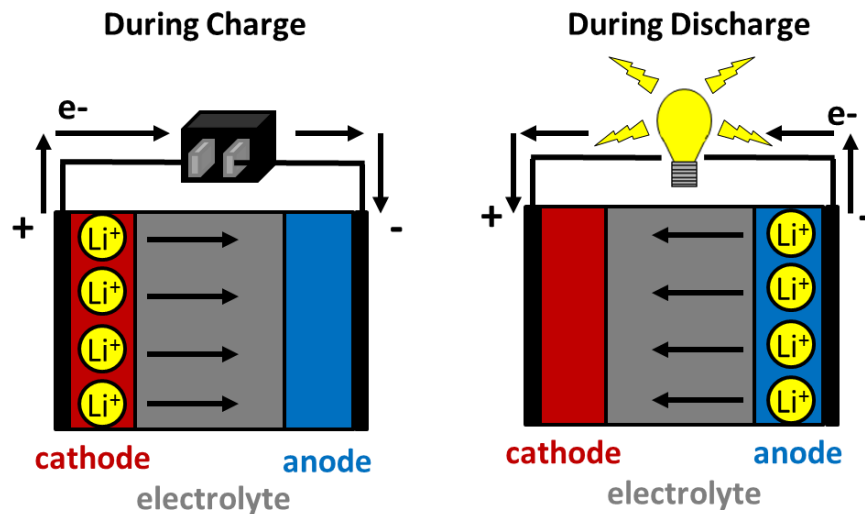


Figure 1.1. Basic operating principle of a lithium-ion battery.

Lithium-ion battery performance

The theoretical gravimetric energy density, ϵ_g , of an electrode material is determined by multiplying the potential at open circuit (with no current flowing), V_{oc} , and the theoretical gravimetric capacity, Q_g [1, 2].

$$\epsilon_g = V_{oc} * Q_g$$

To calculate the gravimetric capacity of an electrode material, Faraday's constant ($F = 26.8 \text{ Ah/mol}$), the charge per mol of electrons, is used. The gravimetric capacity is given below where W is the formula weight of the material and n is the number of moles of electrons transferred per formula unit of the electrode material. The number of Li^+ ions that can be inserted or liberated per formula unit is equal to n .

$$Q_g = \frac{F * n}{W}$$

The open-circuit voltage is a function of the difference in the lithium chemical potential between the cathode, $\mu_{\text{Li},cathode}$, and the anode, $\mu_{\text{Li},anode}$.

$$V_{oc} = \frac{\mu_{\text{Li},cathode} - \mu_{\text{Li},anode}}{F}$$

The chemical potential of Li^+ depends on the transition metal couples that are active in the electrode materials as well as the structure of the electrode materials. The batteries fabricated in this dissertation are constructed as half-cells, where the electrode material being studied is tested versus Li metal. Because of this, V_{oc} is always the potential of the electrode material relative to Li metal.

The theoretical energy densities of battery materials are not generally realized in practice [1, 2]. The practical operating gravimetric energy density, $\epsilon_{g,op}$, is given by the product of the practical operating voltage, V_{op} , and practical operating capacity, $Q_{g,op}$.

$$\epsilon_{g,op} = V_{op} * Q_{g,op}$$

V_{op} is always lower than V_{oc} because of polarization losses in the cell. Ohmic polarization or IR drop, is a function of the operating current, I , and the internal resistance, R_i , in the cell arising from resistance in moving electrons through the electrode material and Li^+ ions through the electrolyte. Activation polarization, η_a , results from kinetic limitations in the reaction occurring at the electrode-electrolyte interface. Finally, concentration polarization, η_c , arises due to limitations in mass transport, which leads to imbalance of reactant and product concentrations in the bulk and at the electrode surfaces. For purposes of calculating the practical operating energy density, V_{op} is usually measured and is equal to the potential difference between the cathode and anode, or relative to Li metal for the half-cells in this study:

$$V_{op} = V_{oc} - I * R_i - \eta_a - \eta_c = V_{cathode} - V_{Li}$$

$Q_{g,op}$ is also generally lower than the theoretical capacity for many reasons such as kinetic limitations, structural limitations, and chemical instability. Thus, the specific capacity is determined by multiplying the current flowing during operation by the operating time and dividing by the weight of active electrode material, w_{active} .

$$Q_{g,op} = \frac{I * t}{w_{active}}$$

The performances of electrode materials are highly dependent on the current, which is related to the kinetic limitations during charge/discharge. The rate of charge/discharge of a battery is characterized by the C-rate, which has units of [1/h]; for example, a C/10 rate indicates that it takes 10 hours to charge or discharge the electrode

material in a half cell. Similarly, a C-rate of 10C, means it takes 1/10th of an hour (6 minutes) to charge or discharge the electrode material.

Lithium-ion batteries have the potential to achieve high energy density due to the non-aqueous electrolytes used [1, 2]. Water-based electrolytes limit the cell voltage because there is a window of less than 2 V where water is stable and will not be oxidized or reduced during battery operation. The organic electrolytes used in lithium-ion batteries have a much larger electrolyte potential window. This is demonstrated in Figure 1.2. The highest occupied molecular orbital (HOMO) and the lowest unoccupied molecular orbital (LUMO) of the electrolyte are separated by an energy gap, E_g . The lithium chemical potential of the cathode, $\mu_{Li,cathode}$, and the anode, $\mu_{Li,anode}$, must fall ideally between the HOMO and LUMO to prevent the electrolyte from undergoing oxidation and reduction rather than the transition metal couples in the electrode materials. To achieve thermodynamic stability, the cell voltage must satisfy the following criterion:

$$eV_{oc} = \mu_{cathode} - \mu_{anode} \leq E_g$$

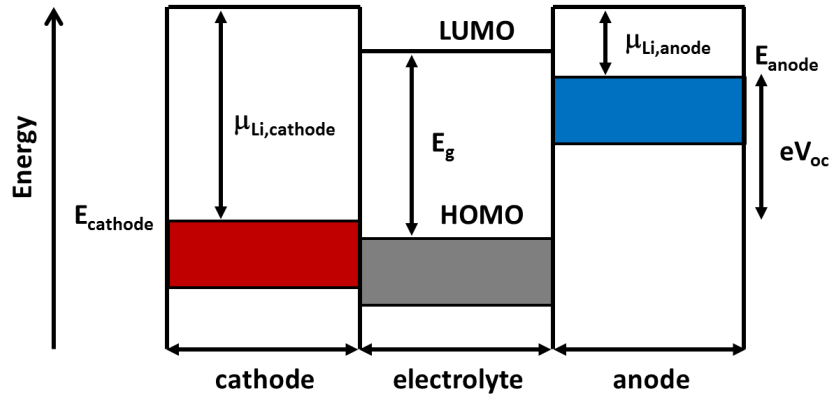


Figure 1.2. Energy diagram of the energies of cathode and anode materials relative to the electrolyte window.

History of lithium-ion batteries

The idea for the rechargeable lithium-ion batteries was developed in the 1970s, and the first concept was based on TiS_2 as the cathode, metallic lithium as the anode, and LiPF_6 dissolved in propylene carbonate as the electrolyte [1, 2, 3]. TiS_2 has a layered structure with spaces in the Van der Waals gap between the sulfide layers into which lithium ions can intercalate during discharge. The battery can be repeatedly charged and discharged because the structure remains stable while lithium ions intercalate into or out of the electrode material with the simultaneous oxidation or reduction of titanium ions. This battery design has safety problems because during charge when the lithium metal moves back onto the Li metal electrode, it plates unevenly and leads to dendrite growth across the cell, resulting in short circuits and potentially catastrophic safety problems.

The other problem with cathodes based on sulfides is the low cell voltage (< 2.5 V versus Li metal). The use of non-aqueous electrolytes in lithium-ion batteries allows for much higher voltages to be stable compared to other battery chemistries, but high voltages cannot be achieved with sulfides. Although the cell potential is not limited by the organic electrolyte, there are constraints on electrode potential from the S^{2-} . In order to insert and remove Li^+ from an electrode material reversibly, the energy of the transition metal couple has to be above the top of the nonmetal (S^{2-}) outer p band; otherwise, electrons will be removed from the nonmetal instead of the transition metal. The small difference in energy between the sulfide 3p band and Li/Li^+ prevents access to high oxidation states of transition metal ions since the higher-valent metal-d bands overlap with the S^{2-} :3p band. This means that electrons can be removed from S^{2-} :3p band rather than from the transition metal band when Li^+ ions are removed, resulting in the formation of species such as S_2^{2-} . Therefore, it is difficult to stabilize higher oxidation states in sulfides and realize higher voltages.

Recognizing the challenge associated with obtaining high cell voltages with sulfide-based cathode materials, the Goodenough group pursued oxides rather than sulfides in the 1980s because the $O^{2-}:2p$ band is lower in energy than the $S^{2-}:3p$ band [1, 2, 4]. Because of this, higher oxidation states of transition metals can be stabilized in oxides than in sulfides without creating holes in the nonmetal band. This concept is illustrated in Figure 1.3 for the $Co^{2+/3+}$ transition metal couple. Understanding this concept led to the discovery of $LiCoO_2$ and $LiNiO_2$ in the 1980s with potentials of ~ 4 V versus Li/Li^+ . This cathode, paired with graphitic carbon as the anode and an organic electrolyte, was the basis of the first commercialized Li-ion battery.

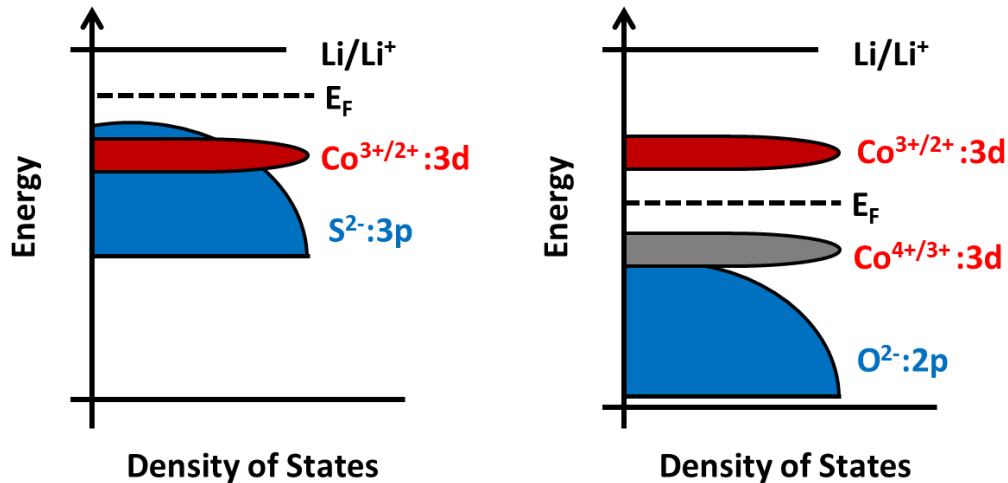


Figure 1.3. Energies of $Co^{3+/2+}:3d$ and $Co^{4+/3+}:3d$ redox couples relative to the nonmetal $O^{2-}:2p$ and $S^{2-}:3p$ bands.

1.3 CATHODE MATERIALS FOR LITHIUM-ION BATTERIES

The electrode materials and electrolyte composition greatly affect battery performance. Because of this, much research effort has been focused on developing new materials for lithium-ion battery electrodes and new electrolyte compositions. Many

cathode materials have been developed in the past few decades, but there are three broad classes of materials that are being actively pursued: layered oxides, spinel oxides, and polyanion materials. The work in this dissertation focuses on cathode materials, so that will be the focus of this introduction, but it is worth noting that there is also a large body of active research devoted to anode materials and electrolytes.

Layered structured cathodes

Although the theoretical capacity of LiCoO_2 is 274 mAh/g, only $\sim 50\%$ of the capacity can be realized in actual operation [1, 2, 4, 5]. The capacity limitation occurs because this material operates on the $\text{Co}^{3+/4+}$ couple which partially overlaps with the O^{2-} :2p energy band (Figure 1.3). Thus, when the material is fully delithiated, holes form in the O^{2-} :2p band and oxygen evolves from the structure. This leads to irreversible capacity loss, structural instability, and safety problems. Because of the limited capacity and safety problems associated with LiCoO_2 and due to the toxicity and high cost of Co, replacement of Co with many other 3d transition metals in the same rock salt layered structure were investigated, but these materials all suffer from problems that prevent their commercialization. However, partial substitution of some Ni and/or Mn for Co leads to improved performance/safety and these solid solution materials are now used in commercial cells [1, 2, 5, 6].

Spinel structured cathodes

Although development of Co-based layered oxides as cathode materials for lithium-ion batteries was an enabling achievement that led to commercialization of lithium-ion batteries, these electrodes are not ideal because of cost, toxicity, stability, and safety concerns. Thus, spinel LiMn_2O_4 has been explored as an alternative to layered oxides since this material is safer, cheaper, and environmentally benign [1, 2, 7]. Also,

due to the strong Mn-Mn interaction across the edge-shared MnO_6 octahedra, the material exhibits good electrical conductivity, while the interconnected interstitial lithium sites allow for 3D Li^+ ion conduction, so spinel structured materials can be charged and discharged rapidly. However, the practical capacity is limited with this material (~ 120 mAh/g at ~ 4 V), and the spinel material tends to exhibit capacity fade upon cycling due to various factors including structural instability and Mn dissolution into the electrolyte [8, 9]. Cationic substitution and surface coatings are often employed to mitigate capacity fade [10-14]. Doping can sometimes lead to a 5 V plateau which increases the energy density, so there is a growing body of research on $\text{LiMn}_{1.5}\text{Ni}_{0.5}\text{O}_4$ and related compounds.

Polyanion-containing cathodes

Although oxide cathodes can operate based on oxidation and reduction of high-oxidation-state transition-metal redox couples like $\text{Co}^{3+/4+}$ and $\text{Mn}^{3+/4+}$, it is more difficult to access the $\text{Fe}^{3+/4+}$ redox couple, and the $\text{Fe}^{2+/3+}$ redox couple offers too low of a potential versus Li/Li^+ to be useful in oxides due to its high redox energy. Iron is a very attractive transition metal for lithium-ion batteries because it is environmentally benign, abundant, and inexpensive. In the 1980s, Manthiram and Goodenough proposed the use of polyanion compounds with XO_4 as the anion rather than oxygen, where $\text{X} = \text{S}, \text{Mo},$ and W [15, 16]. While the $\text{Fe}^{2+/3+}$ couple offers a potential of less than 2.5 V versus Li/Li^+ in oxides, the potential is raised to 3.0 - 3.6 V in polyanion host materials. The locations of the $\text{Fe}^{2+/3+}$ couple in various materials are shown in Figure 1.4. This increase in the potential (lowering of the redox energy) of the $\text{Fe}^{2+/3+}$ couple versus Li/Li^+ occurs due to the inductive effect. Since $\text{Fe}_2(\text{SO}_4)_3$ and $\text{Fe}_2(\text{MoO}_4)_3$ compounds are isostructural, the difference in potential of the $\text{Fe}^{2+/3+}$ redox couple can be attributed to differences in the X-O bond strength. As the X-O bond covalency increases (S-O bond is more covalent

than Mo-O bond), the Fe-O bond covalency decreases, resulting in a lowering of $\text{Fe}^{2+/3+}$ redox energy and a larger potential difference between the $\text{Fe}^{2+/3+}$ and Li/Li^+ couples. The covalently bonded polyanion groups in these materials also lead to higher thermal stability, which is an important safety attribute for the large battery packs needed for electric vehicles or grid storage applications.

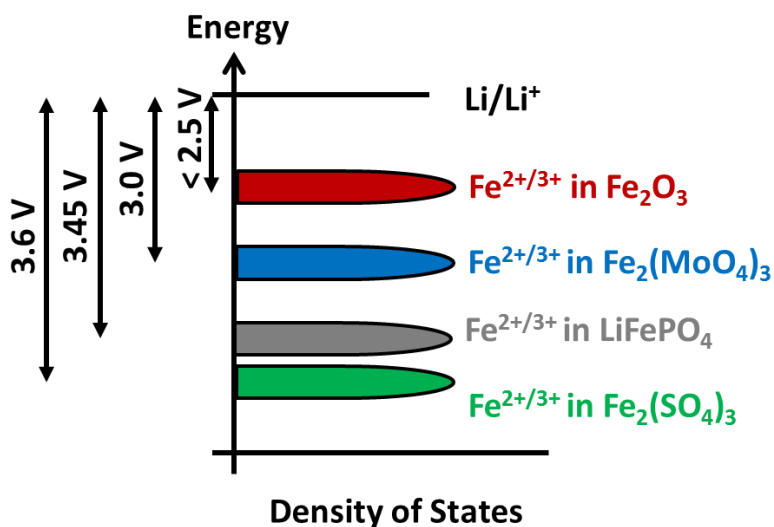


Figure 1.4. Energy diagram depicting the position of the $\text{Fe}^{2+/3+}$ redox couples in various materials (not to scale).

Several polyanion-based cathode materials have been developed since this initial work, but of particular interest is the discovery of olivine structured LiFePO_4 by Padhi *et al.* [17]. Since it was discovered in 1997, LiFePO_4 has been widely studied in the literature and has also been commercialized [18-20]. LiFePO_4 has a high theoretical capacity of 170 mAh/g with a discharge plateau at 3.45 V versus Li/Li^+ and Fe-based electrode materials are appealing because Fe is cheap, abundant, and environmentally benign. However, this material suffers from poor electronic conductivity. A phase change also occurs in LiFePO_4 with little solid solution between the LiFePO_4 and

FePO₄ end-members, limiting the charge carriers which are forced to migrate through small-polaron hopping [21-23]. In addition to poor electronic conductivity, the material also suffers from poor ionic conductivity. The lithium ions can only move through one dimensional channels, unlike the layered oxides and spinel oxides where lithium diffusion is two and three dimensional, respectively. Because of the conductivity limitations, high capacity can only be realized after coating LiFePO₄ with carbon or other conductive materials and by reducing the effective diffusion length through synthesizing small particle sizes [24-33]. Nanoscale particles have also been shown to change the solid-solution range of the two end-member phases and the mechanism for the phase transition; the miscibility gap shrinks with decreasing particle size and increasing non-stoichiometry [34-36].

Attempts to improve the electronic conductivity through aliovalent cation doping were first made in 2002 [37]. Although large increases in electrical conductivity were attributed to doping, this explanation was soon contested, and other explanations have been proposed to account for the increase in electrical conductivity [38, 39]. Computational studies have suggested that aliovalent doping is not energetically favorable on either cation site, and doping LiFePO₄ with aliovalent cations has also been deemed unlikely based on energetic arguments due to strong ionicity and the unbreakable PO₄³⁻ bonding which prevents charge balance by oxygen vacancy formation [23, 40]. In opposition to these studies, evidence of aliovalent doping in LiFePO₄ has since been observed, and many of these studies have measured higher electronic conductivity in doped samples [41-51]. Even without gains in electrical conductivity, aliovalent doping could be useful because doping has been shown to increase the solid-solution range of FePO₄ and LiFePO₄, which could also

have rate implications for charge and discharge [21, 22, 42].

In addition to olivine-structured cathodes, there are many other proposed polyanion materials. LiVOPO_4 is another candidate cathode material with a theoretical capacity of 159 mAh/g, which is only slightly lower than that of LiFePO_4 . However, its higher operating voltage of up to 4.0 V allows for higher overall energy density than LiFePO_4 . There is much literature dedicated to delithiated VOPO_4 , which forms seven polymorphs, but could only be used with lithiated anode materials [52-59]. LiVOPO_4 forms in three different polymorphic phases including triclinic (α), orthorhombic (β), and tetragonal (α_1) [58, 60-75].

There has been significant emphasis in the literature on synthesizing LiVOPO_4 by many different methods because the various methods lead to widely varying electrochemical performance. The triclinic phase has been synthesized by solution-based reaction followed by solid-state heating [60, 61, 67, 74], chemical lithiation of VOPO_4 [66], glass ceramic processing [69], hydrothermal [70], and solvothermal methods [72]. The orthorhombic phase has been synthesized by solution-based reaction followed by solid-state heating [60, 62], carbothermal reduction of VOPO_4 [63], chemical lithiation [64], hydrothermal [68], glass ceramic processing [69], sol-gel [71], and microwave-assisted solid-state heating methods [73]. The tetragonal phase has been synthesized by chemical lithiation [58] as well as hydrothermal synthesis followed by conventional heating [65]. The processing conditions are critical since favorable morphology and small particle size can improve electrochemical performance in materials like LiVOPO_4 with poor electronic and ionic conductivities [63, 68, 74]. Previous reports have demonstrated the importance of small particle size for obtaining good electrochemical performance in LiVOPO_4 even at very slow rates [61, 62]. Similar to LiFePO_4 , a couple of studies have

also shown that the electrochemical performance of LiVOPO_4 can be improved by conductive coating of the particles [62, 71] .

1.4 THIN FILM BATTERIES

Conventional lithium-ion batteries are not ideal for all applications. Some applications require very small-scale batteries that can be made flexible and liquid electrolyte free. Thin film batteries have been developed for these applications and are primarily used for powering a variety of electronics including CMOS, smart cards, RFID cards, implantable medical devices, and wireless sensors [76, 77]. They are advantageous because they are small and can be designed to conform to a wide variety of shapes without electrolyte leakage due to the use of the solid lithium phosphorous oxynitride (LIPON) electrolyte. This electrolyte also allows a larger, stable electrolyte window than the Li-ion batteries with typical liquid electrolytes. Thin film batteries typically have less wasted packaging weight and volume than Li-ion batteries and contain no additives (carbon and binder) in the electrode materials. The thin-film battery electrodes and the electrolyte are generally deposited directly on the current collector or substrate by various methods including chemical vapor deposition, spray pyrolysis, pulsed laser deposition, vacuum evaporation, and sputtering [76-79]. The lack of conductive carbon and binder in the electrode materials and the reduced Li-ion conductivity of the solid electrolyte necessitate very thin electrode and electrolyte layers to achieve reasonable power density.

Thin film batteries generally are composed of lithium-ion battery intercalation materials for the cathode and LIPON as the electrolyte, but they differ in the anode construction [76]. Lithium metal thin-film batteries use lithium metal as the anode, which has the advantage of high energy density but is problematic since lithium metal sputtering is difficult and dangerous due to the reactivity of lithium metal in air [80]. Also, lithium

metal anodes cause difficulty as lithium metal melts at 180 °C, which is lower than the temperature required for solder reflow (250 °C). Solder reflow is the process used for attaching thin film batteries to circuit boards and is a primary application of this technology [76, 80]. The problem of high solder reflow temperature can be avoided by constructing a lithium-free thin film battery in which there is no anode in the pristine battery. Instead, lithium metal plates out *in situ* during the first charge cycle [76, 80, 81]. However, cycling performance of these batteries is limited due to the small amount of lithium in the cell. Finally, lithium-ion thin film batteries use lithium-ion intercalation materials as the anode in addition to the cathode.

1.5 MICROWAVE THEORY

Many of the materials discussed in this dissertation were synthesized by microwave-assisted methods, so it is relevant to introduce the basic fundamentals of microwave heating. Microwave synthesis techniques are used primarily because of their ability to dramatically reduce processing time, improve yields, or improve properties through control of particle size, morphology, purity, and crystallinity [82-84]. Conventional solvothermal heating is slow because it depends on thermal conduction/convection of heat from the outside of a reaction vessel to the solution. It is also inefficient because an entire oven must be heated to heat the vessels and, in turn, the solution.

Microwave heating is fundamentally different because the heating mechanism involves raising the temperature of the solution directly and uniformly through volumetric dielectric and ohmic heating [82-84]. The microwave oven can be designed such that most of the microwave energy can be absorbed directly by the solution, making microwave heating a fast and efficient process that heats the solution from the inside out.

This inside-out heating is achieved by direct interaction of the molecules in the reaction solution being coupled with the microwave field. The dipoles of a polar solvent align in the direction of the electric field and oscillate in resonance with the field (dipolar polarization effect), causing molecular friction and dielectric heating. The efficiency of this heating is directly related to the polarity of the solvent, because a polar solvent is required for the dipoles to be able to realign themselves effectively with the electric field. Similarly, the charged ions dissolved in solution also contribute to heating by oscillating with the electric field (ionic conduction or ohmic heating) and colliding with the surrounding molecules and ions. The ability of a material to absorb microwaves and dissipate the energy as heat is described using complex permittivity $\tilde{\epsilon}$ of the form:

$$\tilde{\epsilon} = \epsilon' - j\left(\epsilon'' + \frac{\sigma}{\omega}\right)$$

where ϵ' is the permittivity, ϵ'' represents the dielectric loss, σ is the electrical conductivity, and ω is the angular frequency of the microwave field. This quantity is temperature and frequency dependent, and the higher the permittivity, the more efficiently microwaves can be converted to heat. The dielectric loss, ϵ'' , is a measure of how well microwave energy can be converted to heat by dielectric heating, and the dielectric constant, ϵ' , is a measure of the polarizability of molecules in the microwave. The term σ/ω represents the contribution to heating from ohmic losses.

Microwave ohmic and dielectric heating are fundamentally different from conventional conductive, convective, and radiative heating. Microwave-assisted heating can lead to unique conditions such as extremely rapid thermal ramp rates and heating from the ‘inside-out’ rather than the ‘outside-in’ (inverted heat transfer). These characteristics are difficult to be replicated by conventional heating and sometimes can lead to unexpected products [82-84]. For example, preparing isotopically labeled drugs

with short half-lives and certain catalysis reactions can only be achieved by microwave synthesis. To explain these reaction products, it is sometimes argued that ‘specific microwave effects’ exist that are defined as being thermal in nature but lead to results that cannot be replicated by conventional heating methods. Some also postulate the existence of ‘non-thermal microwave effects,’ which are argued to be unrelated to thermal effects such as rapid heating rates. Such effects are poorly understood and are controversial.

An example of a thermal effect called ‘overheating’ involves the observation that many solvents boil at a higher temperature when heated by microwave irradiation rather than by conventional convective/conductive heating [82-84]. This difference can be fairly significant for some solvents. For example, the boiling point of methanol is elevated by 19 °C when heated by microwave irradiation. This occurs because, during conventional heating of a solution, the vessel walls are generally at a higher temperature so imperfections in the vessel walls can lead to nucleation sites where boiling can occur. When heating a solution in a vessel by microwave irradiation, the vessel walls are usually at the lowest temperature, because the vessels are usually designed to be poor microwave absorbers. Thus, boiling begins in the bulk of the solution rather than at the walls. For this reason, some argue that the true boiling point of a solution should be measured during microwave heating.

Another thermal effect that is sometimes postulated is the possibility of ‘selective heating’ [82-84]. Some materials absorb microwaves readily and some do not. For a solvent, this depends on the polarity. There are several examples in the literature where mixing two solvents leads to products during microwave synthesis that do not form during conventional heating. This is sometimes attributed to the fact that one solvent

absorbs microwaves more readily than the other, which could lead to differences in the temperatures of the two solvents and local hot spots in solution. It is difficult to prove in cases like this that the different product formed by microwave heating is really due to the selective heating of the solvents rather than some other effect such as rapid thermal ramping or some other variable that is not directly comparable to conventional heating.

In addition to these and other thermal effects, controversial “non-thermal microwave effects are suggested when the products of microwave reactions cannot be explained based on thermal effects alone [82-84]. Microwaves are not high-energy enough to break bonds and are non-ionizing, but some argue that there could be thermodynamic effects (enthalpic or entropic effects). These arguments generally revolve around lowering the Gibbs free energy of reaction through storage of microwave energy in molecular vibration or by alignment of the molecules in the correct orientation to react. However, since it is often difficult to reproduce the conditions present during microwave heating by other methods, it is difficult to determine definitively why products vary between microwave and conventional synthesis.

1.6 OBJECTIVES

For large-scale battery applications such as electric vehicles and electric grid storage, safety concerns due to overheating become a more critical obstacle. Because of such safety concerns, polyanion materials such as LiFePO_4 are of particular interest. However, due to rate limitations, previous research has explored the possibility that doping may improve performance. The ability to dope LiFePO_4 with supervalent cations has been a subject of great controversy, which has not been adequately resolved. My first objective was to determine whether supervalent-vanadium doping was possible in

LiFePO₄ by a facile, low temperature, microwave-assisted solvothermal synthesis method, and whether that doping could improve electrochemical performance.

After successfully doping LiFePO₄ with at least 20 % vanadium by a low-temperature microwave-assisted method, my second objective was to determine why I was able to achieve such high doping levels when the literature suggests that only about 10 % vanadium can be accommodated into the olivine lattice. This question was addressed by heating the V-doped samples at conventional temperatures and comparing the results to conventionally synthesized V-doped LiFePO₄.

Microwave-assisted synthesis of LiFePO₄ was previously shown by the Manthiram group to result in single-crystal nanorods with excellent electrochemical performance that could be attributed to the tunable particle size and morphology. A polyanion material with similar ionic and electronic limitations, LiVOPO₄, has never been synthesized by microwave-assisted methods, so my third objective was to develop a low-temperature microwave-assisted method to synthesize the various polymorphs of LiVOPO₄ in an attempt to tune the electrochemical properties through morphology control.

It has recently been demonstrated that a second Li⁺ ion can be inserted into LiVOPO₄, but this insertion process has not been extensively studied. My fourth objective was to perform chemical and electrochemical lithiation experiments to gain a better understanding of the structural change that occurs when the second lithium is inserted into LiVOPO₄.

Finally, it is well established that microwave-assisted dielectric and ohmic heating can decrease reaction time, decrease energy use and manufacturing cost, improve product yield, and improve material properties through morphology and purity control. However,

it is not always well accepted when scientists argue unexpected results to be the consequence of thermal effects such as ‘selective’ heating. My fifth and final objective was to determine if the unique properties of microwave-assisted ohmic heating could also be exploited to ‘selectively’ heat a strongly microwave-absorbing solid material for the purpose of catalyzing thin film growth directly and selectively on a substrate. Specifically, I was interested in the nucleation of TiO_2 thin films grown on indium tin oxide (ITO)-coated glass and determining whether selective interaction of the ITO with the microwave field was responsible for such film growth.

This dissertation seeks to address the above five objectives.

Chapter 2: Experimental Procedures

The objectives outlined in the previous Chapter involve extensive materials synthesis and characterization. Details regarding materials synthesis are discussed in each Chapter for clarity. A brief description of the equipment and techniques employed for materials characterization are provided here.

2.1 MATERIALS CHARACTERIZATION

Inductively coupled plasma (ICP)

Elemental analysis was performed with a Varian 715-ES ICP optical emission spectrometer to determine ratios of elements in materials. Four standards were prepared for each element by diluting concentrated commercial ICP standards. Errors between calibration standard data points and the calibration curve were always less than 2 – 3 % for the data presented here.

Thermogravimetric Analysis (TGA)

Precursors in this work were characterized with a Perkin Elmer TGA 7 to determine water content. Approximately 5 – 10 mg of precursor was typically analyzed.

Powder X-ray diffraction (XRD) and glancing incidence X-ray diffraction (GIXRD)

XRD was performed on Philips and Rigaku Ultima IV X-ray diffractometers with filtered Cu K α radiation to obtain structural information regarding the materials synthesized here. Lattice parameters, phase fractions, and elemental occupancies were obtained from Rietveld refinement [85] of the XRD patterns in Fullprof/WinPLOTR [86, 87]. To obtain diffraction patterns of the thin films synthesized in Chapter 7, GIXRD experiments were performed using a Rigaku Ultima IV diffractometer operating in

parallel beam (PB) mode using CuK α radiation ($\lambda = 1.54 \text{ \AA}$) with a glancing angle of 0.5° .

Neutron diffraction (PND)

Because neutrons are sensitive to lithium, but X-rays are not, PND data were collected at 300 K on the HB2A beamline at the High Flux Isotope Reactor (HFIR) located at Oak Ridge National Laboratory for more detailed structural analysis. The use of isotopically enriched lithium (^7Li) removes uncertainties in the correct bound coherent neutron scattering length (-2.22 fm for ^7Li) that can exist in the use of natural lithium. For natural lithium, it is known that the content of ^6Li may slightly vary between different lithium sources. Also, the lower absorption correction of ^7Li than natural lithium should create less of a concern for the collection of high quality data, and for the Rietveld refinement (though for these materials the absorption has only a small effect on the thermal parameters, and essentially no effect within error on the other parameters). The samples were contained in 8 mm vanadium cans. Powder neutron diffraction data were analyzed for unit cell constants, phase fractions, and structural information by using Rietveld refinement [85] with GSAS/EXPGUI [88, 89] and Fullprof/WinPLOTR [86, 87].

X-ray absorption near-edge spectroscopy (XANES)

To examine oxidation states of the materials presented here, X-ray absorption data were taken at the Fe and V K-edges in transmission at the MRCAT (Sector 10, Advanced Photon Source) bending magnet beam line at Argonne National Laboratory. Samples were prepared by grinding between 5 mg and 20 mg (depending on V and Fe composition) of finely powdered specimen with boron nitride and Polyvinylpyrrolidone (PVP). The mixtures were then pressed into 7 mm diameter pellets of less than 1 mm

overall thickness. For LiFePO_4 samples, a 50/50 mix of boron nitride (25 mg) and PVP (25 mg) were used for aiding easy sample release from the press and to bind a better pellet (with 5 mg of sample). The X-ray energy was selected by a water cooled Si (111) monochromator with a 50 % detuned second crystal for the elimination of harmonics. Data were taken in transmission mode with a metal reference foil downstream of the sample. The 20 cm long ion chambers contained flowing gas mixtures tuned to obtain 10 % absorption in I_o and 80 % absorption in I_t and I_{ref} .

XANES data were processed with Athena software package [90, 91] by first aligning the reference spectra for all data sets, then adjusting the normalization parameters so as to have all spectra match before the edge and approximately 150 eV above the edge. Least squares fitting was performed within Athena, constraining all fractions to add up to 1 and requiring any energy shift to be identical for all standards.

X-ray photoelectron spectroscopy (XPS)

For oxidation state and elemental analysis, X-ray photoelectron spectra were acquired with a Kratos AXIS Ultra DLD instrument (monochromatic Al $K\alpha$ radiation). The pass energy was set to 20 eV, and automatic charge neutralization was used for all samples. Carbon spectra were collected for each sample, and the peaks were shifted such that the largest carbon peak was centered at 284.5 eV. Sputtering was done at a beam energy of 4 keV for 50 s leading to an estimated 3 nm of material removal. Peak fitting was performed using CasaXPS software with Shirley type background removal and 30 % Gaussian – 70 % Lorentzian curves.

Fourier transform infrared analysis (FTIR) and Raman spectroscopy

FTIR and Raman spectra were collected to obtain vibrational structure information. Pellets for FTIR analysis in a PerkinElmer BX FTIR were prepared by

grinding and pressing samples with dried KBr powder. The Raman measurements were made at Argonne National Laboratory using a Renishaw inVia Raman Microscope equipped with a set of four lasers that provide excitation wavelengths at 785, 633, 514, 442, and 325 nm. The samples (in powder form) were loaded into a threaded Teflon holder equipped with a rubber o-ring seal to prevent contact of the sample with ambient atmosphere. In this embodiment, the powder was pressed between a stainless backing disc and a BaF₂ window (10 mm in diameter and 2 mm thick). Raman spectra were recorded through the BaF₂ window using a 50× focusing/collection optic with a numerical aperture of 0.5. The excitation laser was brought to a focus at the sample/BaF₂ interface and the beam was spread to a circular area approximately 10 μm in diameter. The effective laser power density used in these measurements did not exceed 1 mW/μm².

Scanning electron (SEM) and scanning transmission electron (STEM) microscopy

To examine the morphology of materials, SEM images were obtained with JEOL JSM-5610, LEO 1530, and FEI Quanta 650 SEMs. The energy dispersive spectroscopy (EDS) discussed in Chapter 7 was collected with the JEOL JSM-5610 instrument to obtain elemental ratios. STEM micrographs were obtained in a Nion aberration-corrected UltraSTEM 100 [92] at Oak Ridge National Laboratory, which is equipped with a Gatan Enfina spectrometer. This instrument was used to examine crystallinity and defects in the materials discussed in Chapter 3. Electron energy loss spectroscopy (EELS) data, which provides oxidation state information, were also collected on the UltraSTEM 100. A Hitachi S5500 SEM/STEM microscope with EDS capability was used for the work in Chapter 4 for morphological imaging and elemental mapping.

2.2 ELECTROCHEMICAL CHARACTERIZATION

Electrode preparation

Electrodes were prepared by grinding active material with conductive carbon and teflonated acetylene black (TAB) in a mortar and pestle. TAB consists of polytetrafluoroethylene (PTFE) and acetylene black. Electrodes discussed in Chapters 3 and 4 were fabricated with 75 wt. % active material, 12.5 wt. % carbon, and 12.5 wt. % TAB. Electrodes in Chapters 5 and 6 were fabricated with 70 wt. % active material, 15 wt. % carbon, and 15 wt. % TAB. The resulting composites were rolled into thin sheets and cut into 0.64 cm² (Chapters 3-5) and 1.27 cm² (Chapter 6) area circles using a punch. They were then pressed to Al mesh to be used as a current collector. The electrodes consisted of 4 – 7 mg of active material for samples discussed in Chapters 3 – 5 and approximately 7 – 10 mg of active material for samples discussed in Chapter 6. The electrodes were dried overnight in a vacuum oven at 115 °C before constructing cells.

Electrodes of TiO₂ powder and graphene (Appendices 1 and 2) were prepared by stirring 70 wt. % active material with 15 wt. % polyvinylidene fluoride (PVDF) dissolved in N-methyl-2-pyrrolidone (NMP) as a binder and 15 wt. % carbon overnight. The resulting slurries were ground with a mortar and pestle and cast onto Cu foil. The films were dried in an air oven at 70 °C for 3 h and then transferred to a vacuum oven at 115 °C and dried overnight. The films were punched into 1.27 cm² area circles with approximately 2 – 3 g of active material.

Coin cell fabrication

For Chapters 3 – 5, CR2032 coin cells were assembled in an argon filled glove box using a metallic lithium anode, Celgard polypropylene separators, and 1 M LiPF₆

in 1:1 diethyl carbonate / ethylene carbonate as the electrolyte.

Coin cells constructed with the microwave-synthesized TiO_2 thin films on indium tin oxide (ITO)-coated glass (discussed in Chapter 7) were assembled by scraping an edge of the TiO_2 film off of the ITO and wrapping Cu foil around the glass substrate to provide contact between the ITO layer and the cell cap. The cells were constructed versus lithium metal as described above. The thin films were approximately 0.5 cm^2 in area and the Cu foil was approximately 1 cm^2 .

For Chapter 6, pouch cells were also constructed using aluminized barrier liner (Bemis Shield Pack) as the pouch material with the electrodes pressed to Al mesh current collectors and the Li metal pressed to Cu metal current collectors. The electrodes were separated by one layer each of polypropylene (cathode side) and blown microfiber separators (anode side). The cells were filled with 1:1 ethylene carbonate:diethyl carbonate as the electrolyte with LiPF_6 salt and were impulse sealed in an Ar filled glove box. To obtain good electrical contact, the cells were pressed in vises consisting of two plastic plates with foam separators.

Electrochemical measurements

The coin cells and pouch cells were cycled at various rates on Arbin battery cyclers for charge-discharge tests and on a Radiometer Analytical Voltalab PGZ402 potentiostat for cyclic voltammetry (CV) tests. All charge-discharge and CV tests were performed in coin or pouch cells versus Li/Li^+ .

For the *ex situ* XRD measurements described in Chapter 6, the cells were discharged at a C/100 rate to various states of discharge and charge. The cells were transferred to an Ar filled glove box and cut open to retrieve the electrodes. The electrodes were then sealed between tape and Kapton film (Chemplex number 442)

and were secured to a glass slide for XRD measurements with a Rigaku Ultima (IV) X-ray diffractometer.

Chapter 3: Microwave-assisted Solvothermal Synthesis and Characterization of $\text{LiFe}_{1-3x/2}\text{V}_{x/2}\text{PO}_4$ Cathodes

3.1 INTRODUCTION

The Manthiram group has recently demonstrated that LiFePO_4 can be synthesized at low temperatures ($< 300^\circ\text{C}$) by a microwave-assisted solvothermal (MW-ST) method [30-33]. This process results in single crystalline, uniform size LiFePO_4 nanorods with the lithium diffusion direction along the short axis of the rods, which leads to high rate capability due to the short path length that the Li^+ ions must travel through the rods. The previous MW-ST studies also employed various *in situ* and *ex situ* coating strategies to improve the electrochemical performance.

It is now well accepted that small particle sizes and conductive coatings can be used to improve the electrochemical performance of LiFePO_4 . Conversely, claims of performance improvements resulting from doping of LiFePO_4 with aliovalent cations remain controversial [23, 38-40, 93, 94]. Regardless, many reports indicate that aliovalent cation doping is possible, and some of these studies find significant improvements in electrochemical performance which are often attributed to doping, particularly for vanadium doping [37, 41-51]. Even without gains in electrical conductivity, aliovalent doping could be useful because doping has been shown to increase the solid-solution range between FePO_4 and LiFePO_4 , which could still have rate implications for charge and discharge [21, 22, 42].

Substituting small amounts of V into LiFePO_4 is particularly interesting, because it has been shown to improve electrochemical performance, and many studies also report improved electrical conductivity [43-51]. A recent computational study suggests that doping LiFePO_4 with V reduces the band gap and also decreases the activation energy for Li^+ -ion diffusion in both LiFePO_4 and FePO_4 [95]. There is still

some disagreement among studies regarding the exact V oxidation state, the maximum level of V doping without forming an impurity, and the directions of lattice parameter shifts. Although there was initial disagreement regarding whether V substituted on the anion or cation site, there is now general agreement that V substitutes for Fe [44, 45]. To contribute understanding to the questions of whether it is possible to dope LiFePO₄ and how the electrochemical performance is affected, the MW-ST method, which has been previously used to synthesize LiFePO₄, was adapted here to dope LiFePO₄ with up to at least 20 % V. The doping levels demonstrated here are much higher than those previously reported by other synthesis methods. Vanadium is found to occupy the Fe site in the olivine lattice, as is evidenced by X-ray and neutron diffraction results, which indicate lattice parameter shifts and iron deficiency. The doped samples also show a sloping charge-discharge curve, indicating suppression of the two-phase charge-discharge behavior characteristic of LiFePO₄.

3.2 EXPERIMENTAL

Microwave-assisted solvothermal synthesis

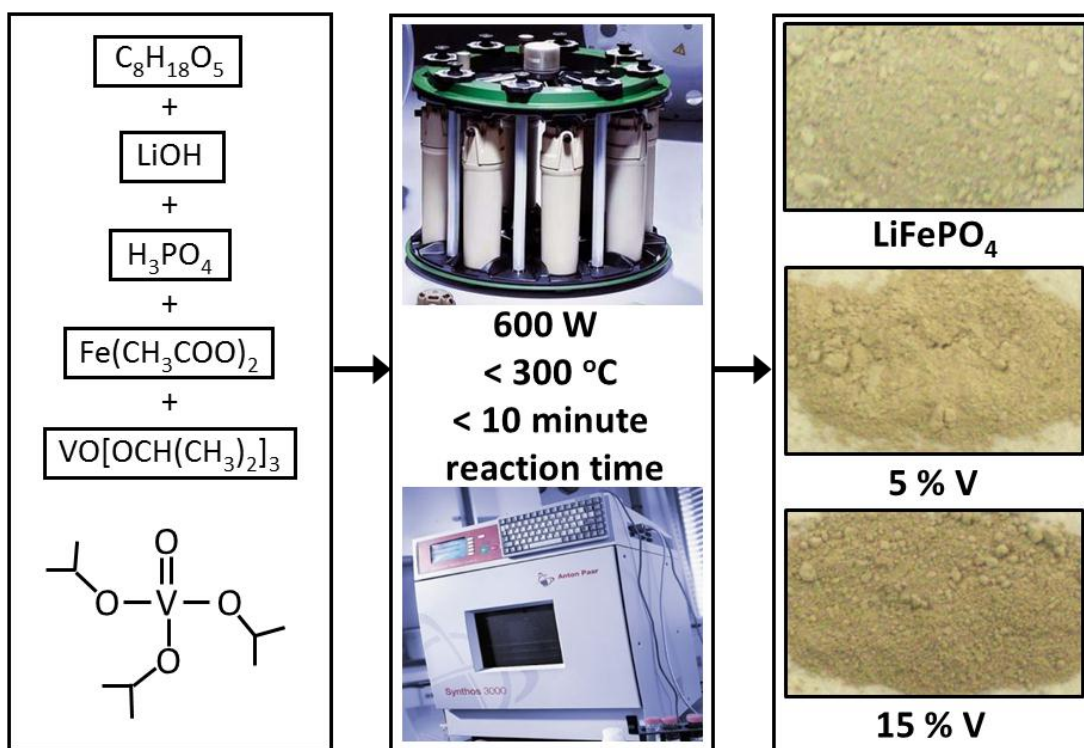
V-doped LiFePO₄ samples were synthesized by a rapid MW-ST method. Stoichiometric ratios of lithium hydroxide (Fisher), iron acetate (STREM), phosphoric acid (Fisher), and vanadium tri-isopropoxide oxide (VO(OC₃H₇)₃, Alfa Aesar) precursors were dissolved in tetraethylene glycol (Alfa Aesar). The precursor solutions were prepared stoichiometrically according to the following formulas: LiFe_{1-x}(VO)_xPO₄ with $0 \leq x \leq 0.25$, LiFe_{1-2x}V_x□_xPO₄ with $0 \leq x \leq 0.15$, and LiFe_{1-3x/2}V_x□_{x/2}PO₄ with $0 \leq x \leq 0.15$). These formulas take into account different expectations for the V oxidation state and coordination environment, as will be discussed later in more detail. The resulting brown solutions were transferred to high pressure 80 mL quartz vessels, which were then

sealed to allow autogeneous pressure generation during the reaction. These vessels were secured on a rotor that was placed on a turntable in a microwave reaction system (Anton Paar Synthos 3000). The turntable was spun during synthesis to ensure uniform microwave heating, and magnetic stir bars were placed in each vessel to obtain uniform reactant mixing. The power was programmed to a constant level of 600 W. It took 20 – 30 min to ramp the temperature up to 260 °C, at which point the products formed. For the samples prepared according to $\text{LiFe}_{1-x}(\text{VO})_x\text{PO}_4$, a constant power of 600 W was applied for 5-10 additional min after reaching 260 °C, during which time the temperature remained between 260 and 280 °C. For samples prepared according to $\text{LiFe}_{1-2x}\text{V}_x\text{PO}_4$ and $\text{LiFe}_{1-3x/2}\text{V}_{x/2}\text{PO}_4$, the temperature was ramped to 300 °C and held for 30 minutes in an attempt to improve crystallinity and give adequate time for any impurities that may be present to crystallize.

The temperatures of the vessels were monitored by infrared temperature sensors. Because the particle size is dependent on the concentration of the precursors, the concentrations of lithium and phosphate ions were kept constant at 0.17 M for the products prepared according to $\text{LiFe}_{1-x}(\text{VO})_x\text{PO}_4$. The concentration was decreased slightly to 0.14 M for the samples prepared according to $\text{LiFe}_{1-3x/2}\text{V}_{x/2}\text{PO}_4$ to better control the pressure, which increased readily due to the low boiling point of the vanadium precursor. After synthesis, the microwave system went into convective cooling mode, and when the temperature was below 50 °C, the vessels were removed. A schematic of the synthesis process is depicted in Schematic 3.1.

The magnetic stir bars in the vessels had varying amounts of a dark brown powder impurity stuck to them after initial synthesis attempts were made to prepare $\text{LiFe}_{1-x}(\text{VO})_x\text{PO}_4$ samples. This impurity was removed by stirring the solution repeatedly with a

magnetic rod until the rod came out of the solution clean. The amount of magnetic impurity increased with increasing vanadium content. The magnetic impurity was collected, dried, and analyzed by XRD; it was identified as Fe_3O_4 (magnetite).



Schematic 3.1. Illustration of the microwave-solvothermal synthesis of V-doped LiFePO_4 prepared according to $\text{LiFe}_{1-x}(\text{VO})_x\text{PO}_4$.

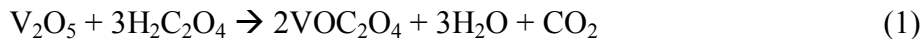
The Fe_3O_4 impurity was present despite careful analysis to ensure that the precursors were added to the solution in the intended ratios. TGA and ICP analysis were utilized to determine the water content of the iron acetate and lithium hydroxide precursors. The TGA and ICP results agreed with each other within 2 %. The phosphoric acid precursor concentration was confirmed by ICP and acid-base titration, which agreed within 2 %. Finally, the vanadium tri-isopropoxide oxide concentration was also

confirmed by ICP. Adjusting amounts of precursors based on the ICP and TGA measurements ensured that the intended concentrations were being added to the reactant solutions.

After removing the Fe_3O_4 impurity from samples prepared according to $\text{LiFe}_{1-x}(\text{VO})_x\text{PO}_4$, the precipitates were washed with acetone and centrifuged several times until the decanted solution was clear. Then the products were dried overnight at $150\text{ }^\circ\text{C}$ in a vacuum oven. The LiFePO_4 powder was light gray in color and the samples containing vanadium were grayish-brown with an increasing pink tint with increasing vanadium. Mixing precursors with a Li:V:P ratio of 1:1:1 in the absence of Fe resulted in an amorphous reddish-brown colored product.

Conventional synthesis

For comparison, two vanadium phosphate samples were synthesized. LiVOPO_4 was prepared by a sol-gel method [71]. V_2O_5 (Alfa Aesar) and oxalic acid (Fisher) were dissolved in water (1:3 ratio) and stirred at $70\text{ }^\circ\text{C}$ until the solution turned blue. Lithium nitrate (Acros Organics) and ammonium dihydrogen phosphate (Acros Organics) were then added, and the resulting solution was stirred for 4 h. The solution was then dried in an air oven at $100\text{ }^\circ\text{C}$ until a green powder was formed. The powder was heated in air at $300\text{ }^\circ\text{C}$ for 4 h and then at $500\text{ }^\circ\text{C}$ for 4 h. The relevant reactions are given below.



$\text{Li}_3\text{V}_2(\text{PO}_4)_3$ was prepared by drying the vanadyl oxalate prepared by reaction (1) above. This product was ball milled with ammonium dihydrogen phosphate and lithium hydroxide monohydrate (stoichiometric ratios) in a plastic bottle with zirconia balls on a rolling ball mill for 5 days to form $\text{Li}_3\text{V}_2(\text{PO}_4)_3$. The resulting powder was

fired at 350 °C for 3 h in a flowing 5 % H₂ – 95 % Ar environment and then the temperature was raised to 725 °C for 6 h.

Finally, LiFePO₄ was prepared by a conventional process according to the procedure for Li₃V₂(PO₄)₃, except iron oxalate rather than vanadyl oxalate was ball milled with ammonium dihydrogen phosphate and lithium hydroxide monohydrate in stoichiometric ratios.

3.3 RESULTS AND DISCUSSION

Structural and chemical characterization

Initial reports in the literature discussing incorporation of V into LiFePO₄ showed disagreement regarding the site that vanadium occupies in the structure, *i.e.*, whether V resides in the Fe (cation) or P (anion) site [43, 44, 46, 48, 96]. To investigate this discrepancy, preliminary MW-ST synthesis attempts were made such that the precursor solutions were stoichiometric according to LiFeP_{1-x}V_xPO₄, but these experiments led to large amounts of Fe₃O₄ impurity in the product. Therefore, it seemed likely that V occupies the Fe site instead of the P site. This conclusion is also expected based on the stability of the redox couples present since substituting V⁵⁺ for P⁵⁺ would likely lead to reduction of V⁵⁺ by the Fe²⁺ such that $V^{5+} + 2Fe^{2+} \rightarrow V^{3+} + 2Fe^{3+}$. This has been demonstrated for the ‘LiFeVO₄’ system, which cannot be synthesized because V^{4+/5+} is reduced by Fe²⁺ [97]. The Fe₃O₄ in these initial products was removed magnetically and the resulting products were analyzed by XRD to be phase-pure olivine-structured materials. The oxidation state of vanadium was unknown at that time, but lattice parameter changes suggested that vanadium had been incorporated into the olivine lattice. In this preliminary stage, (VO)²⁺ seemed to be the plausible species that would substitute for Fe²⁺ because it involves substitution of a cation with the same oxidation state as Fe.

Also, preliminary FTIR results indicated the possible presence of a V=O bond in accordance with the vanadyl precursor used (as will be later discussed). Aliovalent doping with V^{3+} or V^{4+} was not initially considered because of the skepticism in the literature at the time that $LiFePO_4$ could be doped with aliovalent cations.

Because $(VO)^{2+}$ was deemed to be the logical species that was substituting for Fe, synthesis attempts were then made to prepare olivine cathodes of the form $LiFe_{1-x}(VO)_xPO_4$ with $0 \leq x \leq 0.25$. Curiously, Fe_3O_4 impurity still formed after this synthesis, albeit in much smaller amounts than occurred when attempting to substitute V for P. The Fe_3O_4 was again removed magnetically. XRD patterns for these samples are shown in Figure 3.1 for $0 \leq x \leq 0.25$. Impurity peaks for Fe_3O_4 are not detectable, demonstrating that the impurity has been adequately removed by stirring with a magnet, as discussed previously. The $LiFe_{1-x}(VO)_xPO_4$ patterns resemble the MW-ST $LiFePO_4$ pattern very closely. Figure 3.1 also shows the patterns over a smaller range of 2θ to demonstrate the clear peak shifts to higher angles with increasing V-doping. Since the $(VO)^{2+}$ ion is larger than Fe^{2+} , one would expect an opposite trend, *i.e.*, one would anticipate the unit cell volume to steadily increase with increasing $(VO)^{2+}$ substitution. This contradictory behavior, and the fact that Fe_3O_4 forms when preparing the material according to $LiFe_{1-x}(VO)_xPO_4$, indicates that $LiFe_{1-x}(VO)_xPO_4$ may not be the correct formula.

Although Fe_3O_4 did not form as an impurity for pristine $LiFePO_4$, adding excess Fe precursor during synthesis of $LiFePO_4$ did lead to Fe_3O_4 formation, confirming that Fe_3O_4 is the species likely to form in the presence of excess Fe. This was analyzed by synthesizing $LiFePO_4$ with 5 %, 10 %, and 15 % excess iron acetate. ICP analysis (not shown here) confirmed that the excess iron does not wash out of solution for these

samples and remains in ratios proportional to the amount of extra iron precursor taken in the reaction mixture. XRD confirms that the excess iron is in the form of Fe_3O_4 .

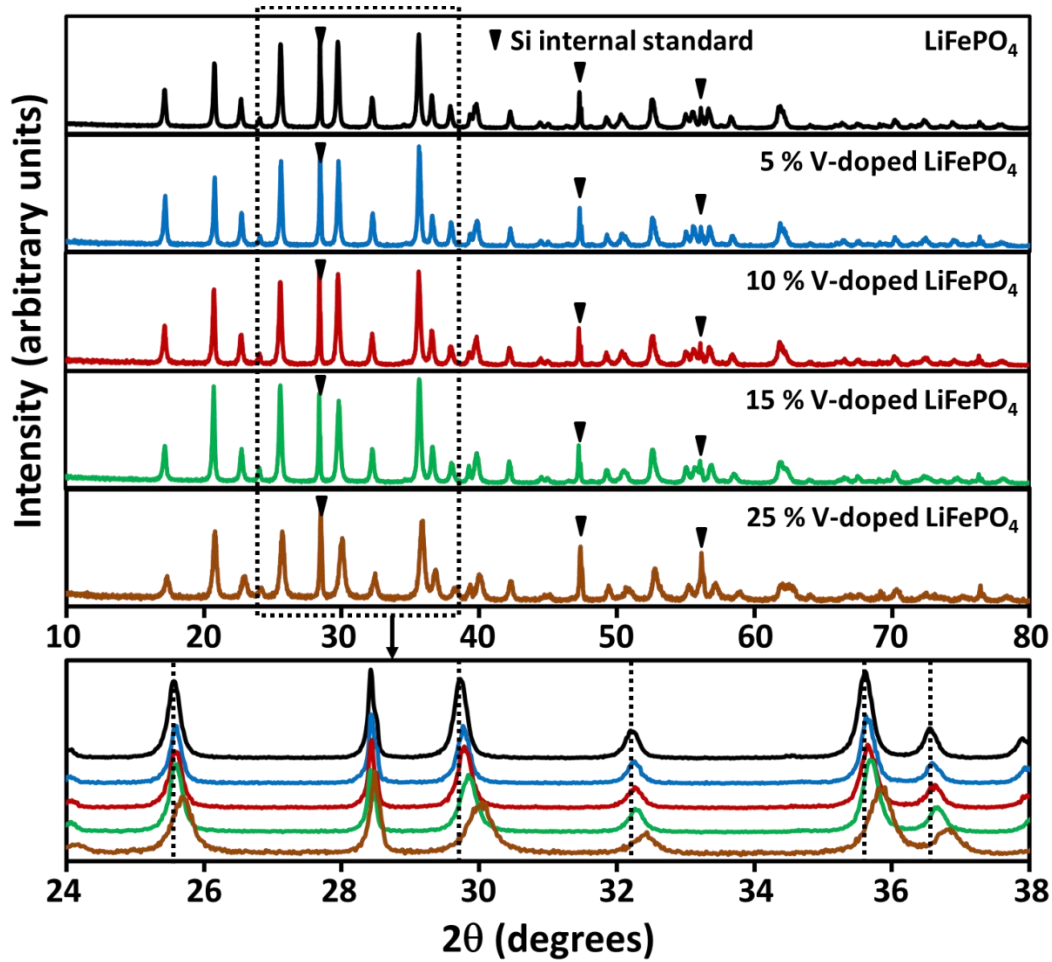


Figure 3.1. XRD patterns for LiFePO_4 and V-doped LiFePO_4 samples with a comparison over a smaller 2θ range.

Table 3.1 gives lattice parameters for the samples and quantifies the systematic decrease in unit cell volume with increasing V content. Also worth mentioning is that a sample with no V but with 15 % deficient Fe was synthesized ($\text{LiFe}_{0.85}\text{PO}_4$), and the

lattice parameters were the same as the LiFePO_4 sample. This confirms that the lattice parameter changes are due to vanadium incorporation rather than simply from non-stoichiometric precursor solutions. To obtain accurate values, a Si internal standard was used in this study and Rietveld refinement was employed.¹

Table 3.1. *Lattice parameters obtained by Rietveld refinement for samples prepared according to $\text{LiFe}_{1-x}(\text{VO})_x\text{PO}_4$ with $0 \leq x \leq 0.25$.*

Sample	a (Å)	b (Å)	c (Å)	V (Å ³)
LiFePO₄	10.32093(20)	6.00127(12)	4.69262(9)	290.655(10)
‘LiFe_{0.85}PO₄’	10.32392(14)	5.99971(8)	4.69249(6)	290.655(7)
5 % V	10.31193(21)	5.99441(12)	4.69345(9)	290.121(10)
10 % V	10.30262(22)	5.98984(13)	4.69563(10)	289.772(11)
15 % V	10.27589(25)	5.97117(14)	4.69939(11)	288.350(12)
25 % V	10.24307(34)	5.95064(19)	4.70406(14)	286.726(16)

The formation of an Fe impurity indicates that there may be Fe vacancies in the structure, which is consistent with the shrinking unit cell volume. It is important to reiterate that Fe_3O_4 impurity formed despite careful analysis ensuring that stoichiometric amounts of precursors were mixed in stoichiometric ratios to prepare samples according

¹ The XRD patterns were collected after grinding approximately 10 wt. % Si with the samples such that the intensity of most intense peak of the Si phase was similar to the most intense olivine peak. A pure Si powder sample was refined first to obtain lattice parameters. The lattice parameters found from this Si refinement were used for all of the other samples. During refinement of the olivine sample, the Si phase was first refined to fix the zero position. Then the olivine phase was added to the refinement. The atomic displacement parameters were generally reasonable without any constraints with rare exception, and it was usually possible to refine W, V, Y, and U (full width half maximum and shape parameters) for the olivine phase in most files.

to the formula $\text{LiFe}_{1-x}(\text{VO})_x\text{PO}_4$, as discussed in the previous section. Fe vacancies could be present to balance excess charge on V if it is not present as $(\text{VO})^{2+}$. After the Fe_3O_4 was removed, ICP data further confirms iron deficiency, suggesting that V does likely substitute for Fe, but also that the samples are cation deficient, as shown in Table 3.2. Substitution of more than 5 mole percent of V for Fe results in consistently lower Fe/P ratios than expected. Conversely, Table 3.2 clearly shows that the V/P and Li/P ratios are nominally equal to the expected ratios for the intended samples.

Table 3.2. *Elemental ratios obtained from ICP analysis of samples prepared according to $\text{LiFe}_{1-x}(\text{VO})_x\text{PO}_4$ with $0 \leq x \leq 0.25$.*

Compound	Fe/P	V/P	Li/P
LiFePO₄	0.99	-----	1.00
5 % V	0.96	0.05	0.99
10 % V	0.86	0.10	0.97
15 % V	0.77	0.16	1.02
25 % V	0.70	0.24	0.99

Since XRD and ICP results suggest that $\text{LiFe}_{1-x}(\text{VO})_x\text{PO}_4$ may not be the correct formula for these samples, the olivine structure was examined more closely. The structure consists of a hexagonal close-packed oxygen array, and it would likely be difficult to accommodate $(\text{VO})^{2+}$ ions in the octahedral sites due to the large size of the vanadyl ion and the electrostatic repulsion associated with adding an extra oxygen ion into the Fe site. Therefore, because of these structural considerations and the results that indicate cation deficiency, doping of aliovalent vanadium ions for iron was considered. Although there is still skepticism regarding aliovalent doping in LiFePO_4 , many recent reports support this is possible [37, 41-50, 96]. If V^{3+} or V^{4+} rather than $(\text{VO})^{2+}$ substituted for Fe^{2+} , the

expected formula would be $\text{LiFe}_{1-2x}\text{V}_x\Box_x\text{PO}_4$ for V^{4+} or $\text{LiFe}_{1-3x/2}\text{V}_x\Box_{x/2}\text{PO}_4$ for V^{3+} (where \Box indicates Fe vacancies) rather than $\text{LiFe}_{1-x}(\text{VO})_x\text{PO}_4$. Both of these formulas could account for the presence of Fe vacancies, which are postulated to exist in these samples due to the formation of Fe_3O_4 impurity and the ICP data which suggests Fe deficiency after Fe_3O_4 is removed.

To examine the possibility of synthesizing materials with the formula $\text{LiFe}_{1-2x}\text{V}_x\Box_x\text{PO}_4$, precursors were mixed stoichiometrically to prepare $\text{LiFe}_{1-2x}\text{V}_x\Box_x\text{PO}_4$ with $x = 0.05, 0.10$, and 0.15 . The $\text{LiFe}_{0.80}\text{V}_{0.10}\Box_{0.10}\text{PO}_4$ and $\text{LiFe}_{0.90}\text{V}_{0.05}\Box_{0.05}\text{PO}_4$ materials formed phase-pure olivine samples with no detectable impurities. However, attempts to prepare $\text{LiFe}_{0.70}\text{V}_{0.15}\Box_{0.15}\text{PO}_4$ resulted in Li_3PO_4 impurity (Figure 3.2). Since this material was clearly deficient in Fe, the amount of Fe precursor was then increased while keeping the V, P, and Li stoichiometry constant until the Li_3PO_4 impurity disappeared. A phase pure sample formed (with no Li_3PO_4 or Fe_3O_4) when Fe/P was approximately 0.78 - 0.79. Furthermore, the ICP data shown in Table 3.3 indicates that all of the samples prepared according to $\text{LiFe}_{1-2x}\text{V}_x\Box_x\text{PO}_4$ had higher Fe contents than expected from the precursor stoichiometry. These results are more consistent with an oxidation state closer to V^{3+} rather than V^{4+} . A V^{3+} oxidation state implies $\text{LiFe}_{1-3x/2}\text{V}_x\Box_{x/2}\text{PO}_4$. After washing the samples with isopropyl alcohol (in addition to washing with acetone which was done for all other samples), the Li content found by ICP decreased a few percent to below the expected value, which may indicate slight lithium deficiency in the olivine structure. The lithium hydroxide starting material is not very soluble in the solvent (TEG) used in synthesis at room temperature or in the acetone typically used to wash the samples, though it does have limited solubility in isopropyl alcohol.

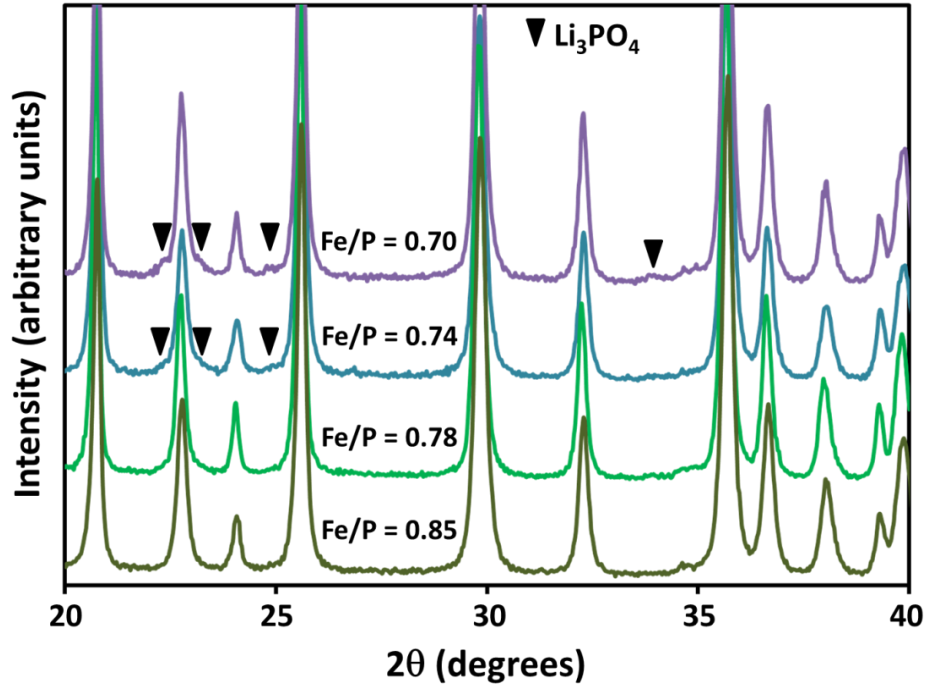


Figure 3.2. XRD of 15 % V-doped LiFePO_4 with varying Fe/P ratio in the precursor solution.

Table 3.3. ICP data for V-doped samples prepared according to $\text{LiFe}_{1-x}(\text{VO})_x\text{PO}_4$, $\text{LiFe}_{1-2x}\text{V}_x\text{PO}_4$, and $\text{LiFe}_{1-3x/2}\text{V}_x\text{PO}_4$.

Intended Sample	Impurity ⁺	Li/P [*]	Fe/P [*]	V/P [*]
$\text{LiFe}_{0.90}\text{V}_{0.05}\text{PO}_4$	none	0.99	0.92	0.05
$\text{LiFe}_{0.80}\text{V}_{0.10}\text{PO}_4$	none	1.00	0.83	0.10
$\text{LiFe}_{0.70}\text{V}_{0.15}\text{PO}_4$	Li_3PO_4	1.00	0.74	0.15
$\text{LiFe}_{0.775}\text{V}_{0.15}\text{PO}_4^{\#}$	none	0.97	0.79	0.15
$\text{LiFe}_{0.85}(\text{VO})_{0.15}\text{PO}_4$	Fe_3O_4 (removed)	1.02	0.77	0.16

*Errors in ratios are estimated to be around 2 - 3 %. [#]Sample was washed with isopropyl alcohol. ⁺“None” means no impurities were detected by XRD or magnetic stirring.

Upon adding excess Li to the precursor solution for LiFePO_4 , ICP reveals excess Li in these samples. Since more than one Li^+ cannot be inserted into LiFePO_4 , these

results indicate that excess Li precursor does not wash out completely in acetone after a reaction. Therefore, lithium deficiency in the V-doped samples may not be adequately detected by elemental analysis.

Determination of transition-metal oxidation states

Initially XPS was used to determine the oxidation states of the transition-metal ions. The binding energies for V^{3+} , V^{4+} , and V^{5+} differ by only about 1.5 eV and the literature values vary significantly. The difficulty in interpreting XPS data is compounded further by the fact that some researchers shift their peaks so that the carbon 1s peak is at 284.5 eV, some shift the carbon peaks to 285.0 eV, and others shift the oxygen peaks to standardize the measurements. Silversmit *et al.* [98] compared several V oxidation states among various studies and included the respective standardization conditions. The average value among the studies they examined were 517.2 eV for V^{5+} in V_2O_5 , 516.0 eV for V^{4+} in VO_2 , and 515.6 eV for V^{3+} in V_2O_3 .

It is more difficult to find standardized data for vanadium in phosphates, so XPS measurements were taken for the MW-ST V-doped $LiFePO_4$ sample prepared according to $LiFe_{0.85}(VO)_{0.15}PO_4$ as well as for $LiVOPO_4$ (V^{4+}) and $Li_3V_2(PO_4)_3$ (V^{3+}) as standards.² The $LiVOPO_4$ and $Li_3V_2(PO_4)_3$ standards both showed multiple oxidation states in initial measurements, so the samples were sputtered to remove the surface layer. Vanadium

² Note that many of the characterization experiments presented here were performed with the samples prepared according to $LiFe_{1-x}(VO)_xPO_4$ because much characterization work was performed before the correct formula was determined. Subsequent characterization of a subset of the samples prepared according to the correct formula ($LiFe_{1-3x/2}V_x\Box_{x/2}PO_4$) did not significantly differ from that for samples prepared according to $LiFe_{1-x}(VO)_xPO_4$ after Fe_3O_4 was removed.

measurements for the sputtered samples are shown in Figure 3.3(a). It is clear that the peaks for all three samples are in very similar locations, despite the fact that the LiVOPO_4 and $\text{Li}_3\text{V}_2(\text{PO}_4)_3$ have different oxidation states which should affect the peak positions.

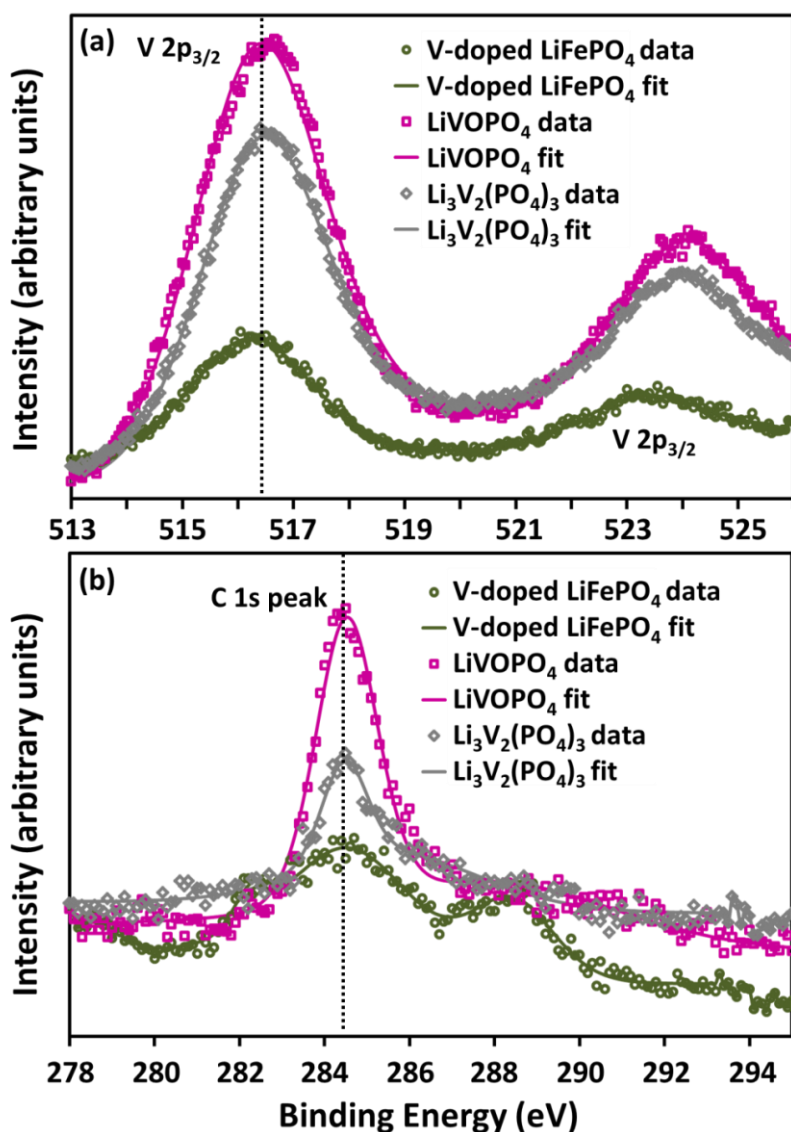


Figure 3.3. XPS (a) V 2p and (b) C 1s core lines for sample prepared according to $\text{LiFe}_{0.85}(\text{VO})_{0.15}\text{PO}_4$.

These results indicate that it is not possible to distinguish between V^{3+} and V^{4+} in these samples. XPS analysis is complicated by the fact that the samples are insulating, so charge compensation must be used during data collection. Charge compensation shifts the peak locations, so all of the peaks were adjusted such that the C 1s peak was at 284.5 eV, as shown in Figure 3.3(b). However, since the samples and standards were prepared by different methods, different carbon sources may be present which could lead to inaccurate peak shifting. Also, most samples have several carbon peaks, further complicating analysis.

Although the oxidation state of V could not be determined by the XPS measurements, XPS could be used to calculate elemental ratios. The V/P ratio on the surface of the V-doped sample was found to be $V/P = 0.16$ for the sample prepared according to $LiFe_{0.85}(VO)_{0.15}PO_4$. This value agrees well with the intended V/P ratio and also agrees well with the bulk V/P ratio determined by the ICP analysis. This shows that the V is not a surface coating; rather, the V substitutes uniformly for Fe in the olivine lattice.

To determine the oxidation state of V without the difficulties associated with XPS, the samples were tested with XANES. As shown in Figure 3.4, XANES spectra were collected on samples prepared according to $LiFe_{1-x}(VO)_xPO_4$ ($x = 0.05, 0.10, 0.15$), $LiFe_{1-2x}V_x\Box_xPO_4$ ($x = 0.05$ and 0.10), and $LiFe_{1-3x/2}V_x\Box_{x/2}PO_4$ ($x = 0.15$). These samples are compared to $LiVOPO_4$ and $Li_3V_2(PO_4)_3$ standards. Oxide standards were also used, but phosphate standards are a more relevant comparison, so only the phosphate standards are shown in Figure 3.4.

The phosphate standards match those found in the literature well [60]. The pre-edge feature, detailed for a few samples by the inset in Figure 3.5, arises because of

the $1s \rightarrow 3d$ transition for vanadium and is possible due to V 3d / V 4p and O 2p mixing. The LiVOPO_4 sample has a much larger pre-edge peak than the $\text{Li}_3\text{V}_2(\text{PO}_4)_3$ sample. The pre-edge feature is indicative of distortion in the VO_6 octahedra, and the V=O bond in LiVOPO_4 leads to significant distortion, whereas $\text{Li}_3\text{V}_2(\text{PO}_4)_3$ has much more symmetric octahedra. In $\text{Li}_3\text{V}_2(\text{PO}_4)_3$, there is a double peak which arises due to crystal field splitting of the V 3d orbitals into t_{2g} and e_g states [67].

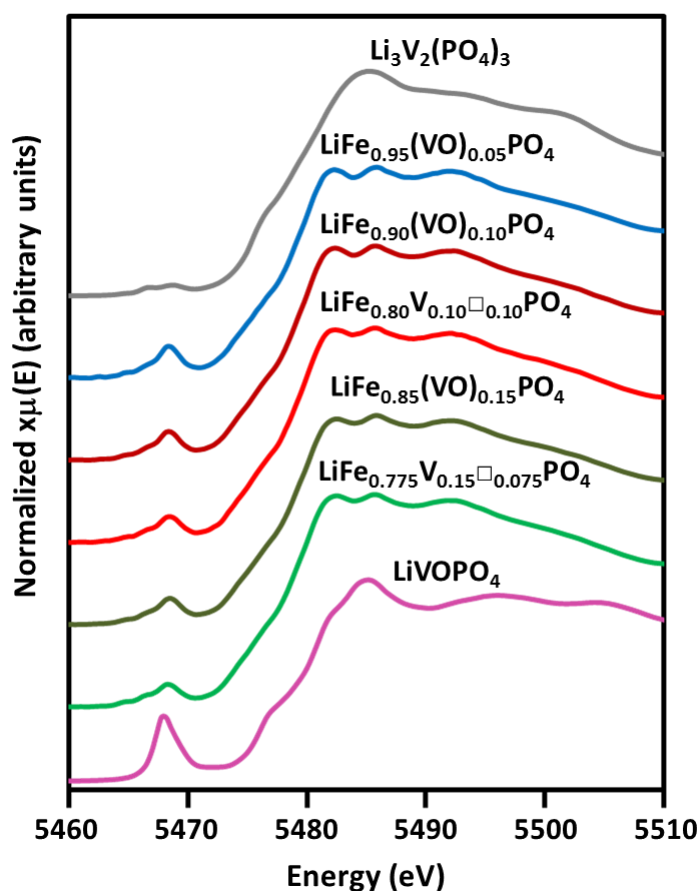


Figure 3.4. *V edge XANES data of V-doped LiFePO_4 samples and $\text{Li}_3\text{V}_2(\text{PO}_4)_3$ and LiVOPO_4 standards. With the exception of $\text{LiFe}_{0.775}\text{V}_{0.15}\square_{0.075}\text{PO}_4$, the formulas for the V-doped LiFePO_4 samples reflect the intended sample compositions and the precursor ratios that were used for synthesis, rather than the actual compositions.*

The V-doped LiFePO_4 samples show larger pre-edge peaks than $\text{Li}_3\text{V}_2(\text{PO}_4)_3$ but smaller pre-edge peaks than LiVOPO_4 , indicating that the VO_6 octahedra are less distorted than in LiVOPO_4 with a strong $\text{V}=\text{O}$ bond, but more distorted than in $\text{Li}_3\text{V}_2(\text{PO}_4)_3$. It is also notable that there is a slight decrease in pre-edge intensity with increasing V-doping levels, indicating that less distortion occurs for the more highly doped samples. This trend has been demonstrated previously for V-doped LiFePO_4 samples [45]. The V oxidation state can be estimated by least squares fitting of the standards. The estimated V oxidation states for the samples are presented in Table 3.4. The fit (detailed in Figure 3.6) suggests a mixed oxidation state consisting of 77 to 88 % V^{3+} and 12 to 23 % V^{4+} .

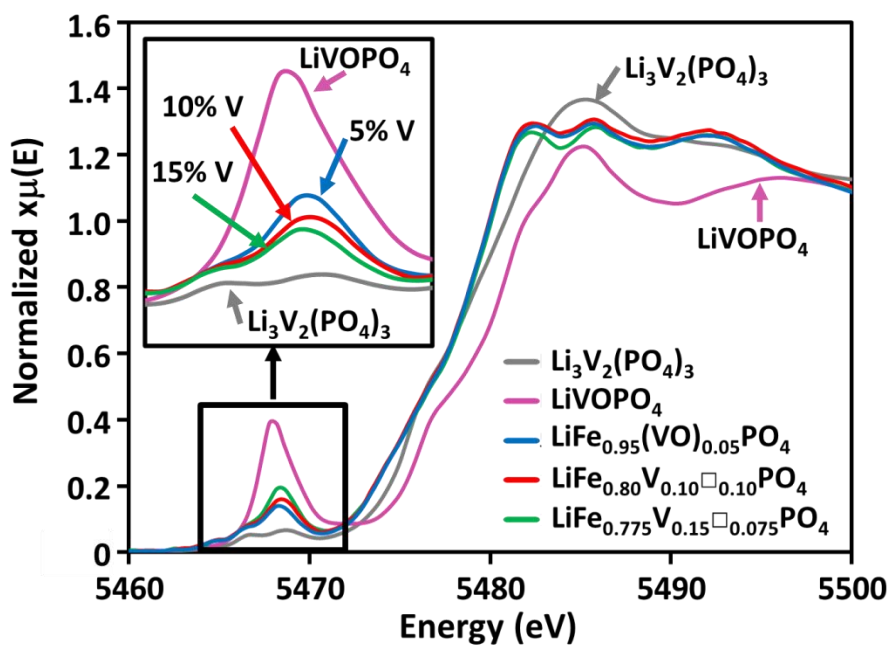


Figure 3.5. XANES of V-doped LiFePO_4 samples and standards with inset close up of V pre-edge region. With the exception of $\text{LiFe}_{0.775}\text{V}_{0.15}\square_{0.075}\text{PO}_4$, the formulas for the V-doped LiFePO_4 samples represent the intended sample compositions and the precursor ratios that were used for synthesis, rather than the actual compositions.

Table 3.4. Vanadium oxidation state analysis from XANES least squares fit (± 0.03).

Intended Sample	Intended Cation Dopant	V ³⁺ Content	V ⁴⁺ Content	Oxidation State
LiFe _{0.95} (VO) _{0.05} PO ₄	(VO) ²⁺	0.77	0.23	3.23
LiFe _{0.90} (VO) _{0.10} PO ₄	(VO) ²⁺	0.85	0.15	3.15
LiFe _{0.80} V _{0.10} □ _{0.10} PO ₄	V ⁴⁺	0.88	0.12	3.12
LiFe _{0.85} (VO) _{0.15} PO ₄	(VO) ²⁺	0.75	0.25	3.25
LiFe _{0.775} V _{0.15} □ _{0.075} PO ₄	V ³⁺	0.84	0.16	3.16

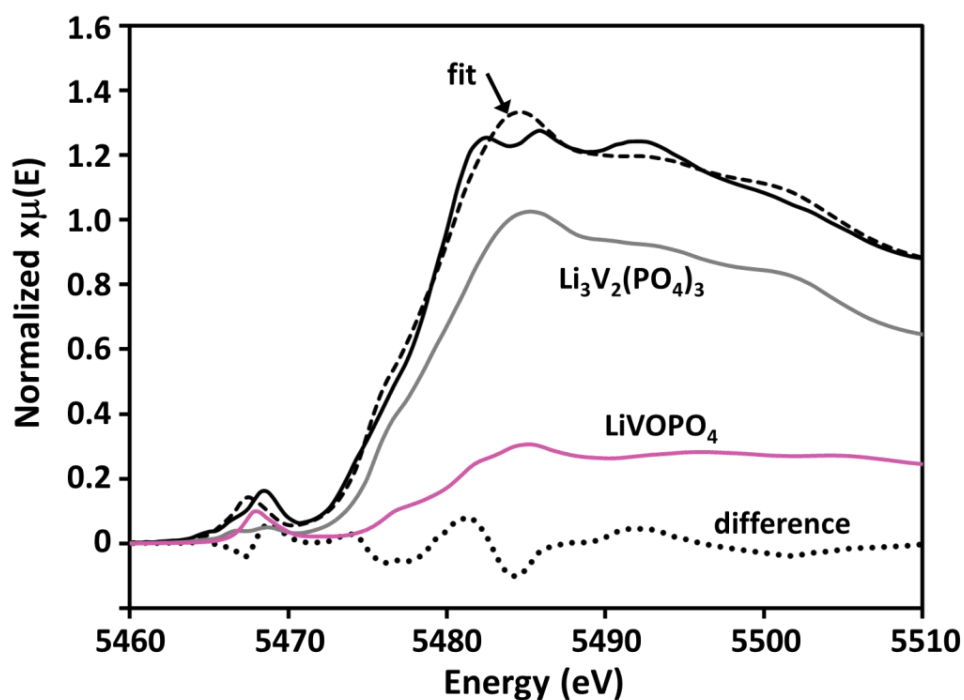


Figure 3.6. Representative XANES absorption spectrum least squares fit for sample prepared according to LiFe_{0.85}(VO)_{0.15}PO₄. The Li₃V₂(PO₄)₃ and LiVOPO₄ curves are scaled by their relative contributions to the fit.

XANES spectra (Figure 3.7) were also taken on the Fe edges and were compared to a commercial FePO₄·xH₂O sample, MW-ST LiFePO₄, and conventionally prepared LiFePO₄. The edge position and pre-edge regions for the V-

doped samples and LiFePO_4 (Fe^{2+} standards) are almost identical, and are distinctly different from the spectrum for the FePO_4 (Fe^{3+}) standard.

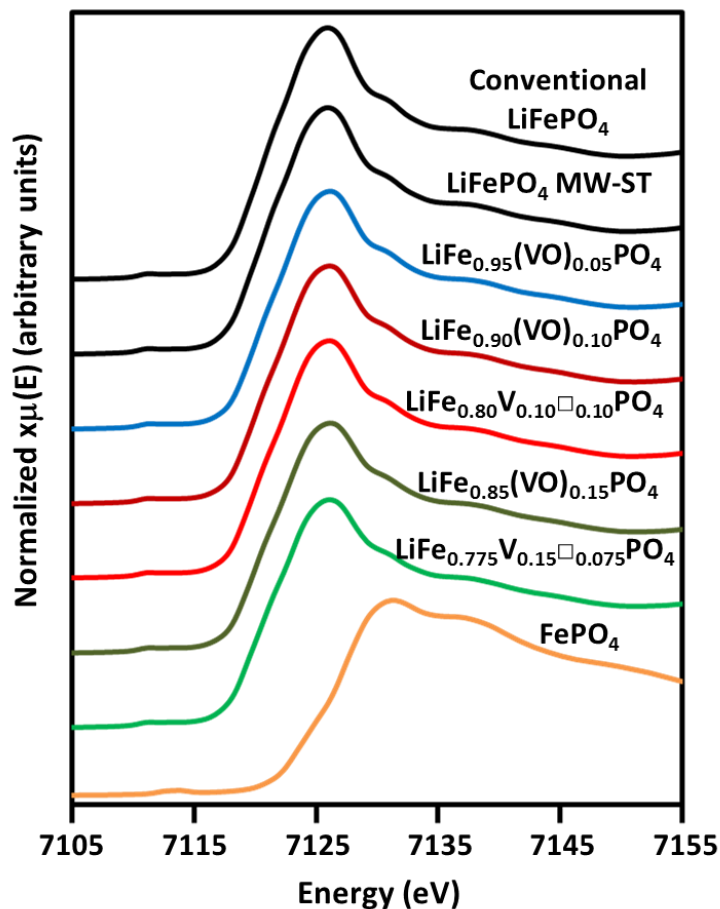


Figure 3.7. *Fe edge XANES data of V-doped LiFePO_4 samples as well as FePO_4 , conventional LiFePO_4 , and MW-ST LiFePO_4 standards. With the exception of $\text{LiFe}_{0.775}\text{V}_{0.15}\square_{0.075}\text{PO}_4$, the formulas for the V-doped LiFePO_4 samples represent the intended sample compositions and the precursor ratios that were used for synthesis, rather than the actual compositions.*

A subset of the data is overlaid in Figure 3.8 to show that the curves all fall on top of one another. The pre-edge region, also detailed in Figure 3.8, shows no differences between the V-doped samples and the pristine LiFePO_4 standards,

indicating that the FeO_6 octahedra are not significantly distorted by the V doping. This has been previously demonstrated for V-doped LiFePO_4 samples [45].

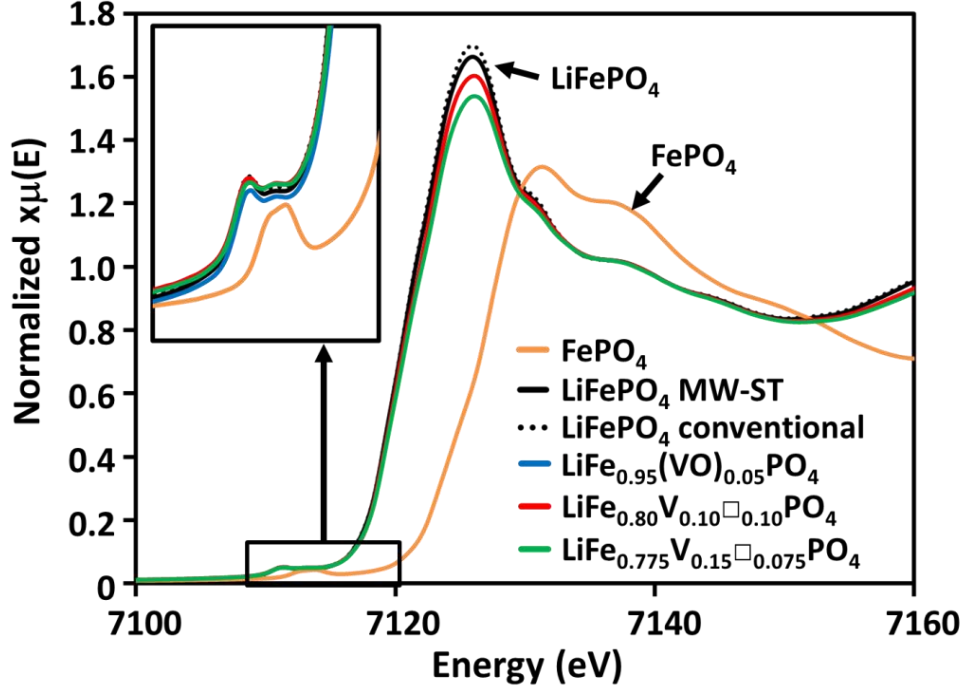


Figure 3.8. XANES of V-doped LiFePO_4 samples and standards with the inset showing the Fe pre-edge region. With the exception of $\text{LiFe}_{0.775}\text{V}_{0.15}\square_{0.075}\text{PO}_4$, the formulas for the V-doped LiFePO_4 samples represent the intended sample compositions and the precursor ratios that were used for synthesis, rather than the actual compositions.

Figure 3.8 also illustrates that the Fe edge data for the LiFePO_4 sample prepared by MW-ST process are almost identical to that prepared conventionally at 725°C in 5 % H_2 – 95 % Ar, indicating that there is not any Fe^{3+} in the pristine MW-ST LiFePO_4 sample or the V-doped samples. Although it has been previously shown that low-temperature synthesis can lead to $\sim 10\%$ Li deficiency in LiFePO_4 [34], the pristine MW-ST LiFePO_4 sample shows no indication of Fe^{3+} , which means that it

should not be Li deficient (as charge balance would dictate Fe^{3+} should be present with Li deficiency). This is noteworthy because Fe_3O_4 forms if excess Fe precursor is added to the reaction precursor solution, which implies that both Fe^{2+} and Fe^{3+} can be stable in TEG. Conversely, these data demonstrate only Fe^{2+} is present in LiFePO_4 .

It is worth mentioning that Zhao *et al.* [93] determined that LiFePO_4 could not be doped with V in the Fe site because their XRD patterns showed an impurity and XANES fits deviated significantly from their experimental spectra, appearing more like $\text{Li}_3\text{V}_2(\text{PO}_4)_3$. The XRD patterns shown here do not have any impurities and the XANES spectra are distinctly different than $\text{Li}_3\text{V}_2(\text{PO}_4)_3$ in the pre-edge region. Their difficulty may have been substitution of V for Fe in a 1:1 ratio without considering the vacancy formation due to different valence states of the two ions (Fe^{2+} and V^{3+}).

Determination of transition-metal occupancies

To confirm further the presence of iron vacancies and the presence of V on the Fe site, the occupancies of V and Fe were estimated from the XRD data with Rietveld refinement, (Table 3.5) and a representative refinement fit is shown in Figure 3.9. Convergence could not be reached through attempts to restrain the total cation charge to be equal to 3+ (to balance with PO_4^{3-}). Since X-rays are not sensitive to Li, it would be difficult to determine the lithium content through refinement of XRD patterns, so the Li occupancy was assumed to be unity and all of the V was assumed to be on the Fe site. A restraint was placed such that the total charge on the Fe site had to add up to 2+ (including Fe, V, and vacancies). The oxidation state of V was assumed to be 3.2+ for this analysis based on the average oxidation state found from the XANES samples.

Table 3.5. *Rietveld refinement occupancy results of XRD data for undoped and V-doped LiFePO_4 (with fit parameter χ^2 shown).*

Sample	Fe_{occ}	V_{occ}	χ^2
LiFePO_4	-----	-----	1.55
'$\text{LiFe}_{0.85}\text{PO}_4$'	-----	-----	2.66
$\text{LiFe}_{0.925}\text{V}_{0.05}\square_{0.025}\text{PO}_4$	0.933(18)	0.042(11)	1.92
$\text{LiFe}_{0.85}\text{V}_{0.10}\square_{0.05}\text{PO}_4$	0.823(17)	0.111(11)	1.70
$\text{LiFe}_{0.775}\text{V}_{0.15}\square_{0.075}\text{PO}_4$	0.764(18)	0.149(11)	1.40
$\text{LiFe}_{0.625}\text{V}_{0.25}\square_{0.125}\text{PO}_4$	0.689(17)	0.195(11)	1.44

Attempts to add analogous restraints on the Li site (such that V was allowed on the Li site and the total charge on the Li site was restrained to 1+) resulted in very high isotropic displacement parameters ($B_{\text{iso}} \sim 8$), indicating likely non-physical results. Therefore, the refinement is not improved by placing V on the Li site and assuming that charge is balanced, supporting the assumption that there is not significant V doping on the Li site. However, restraining the total charge on the Li site to 1+ or the total charge on the Fe site to 2+ are just two possibilities. It is also possible that the charge is not perfectly balanced on each site as is the case when there are anti-site defects in LiFePO_4 .

Rietveld refinement results of the XRD data shown in Table 3.5 supports the conclusion that the V and Fe occupancies are similar to the expected values from ICP as well as the claim that these samples are highly doped. The V occupancy of the 25 % V-doped sample was found to be a little lower than expected, suggesting that it may only be possible to achieve ~ 20 % V doping on the Fe site. Since the refined Fe occupancy matches the ICP Fe/P ratio well for most samples, the results suggest that the restraint provides an appropriate model of the Fe/V site occupancy. The

possibility exists that there could be some V on the Li site or Li vacancies such that the total charge on the Fe site may not be exactly 2+, as mentioned above. Due to the complexity of accounting for these possibilities in the refinement, it was not possible to determine if the assumptions made could be responsible for the slight disagreement between the V occupancy and the ICP results for the 25 % V-doped sample. Although the refinement shows the V occupancy to be lower than expected with the described restraint, the lattice parameters show larger shifts from the 15 % V-doped samples than are consistent with only 20 % doping. Therefore, it is possible that the restraint used may not be appropriate for this sample, and there may be more cation disorder in this sample.

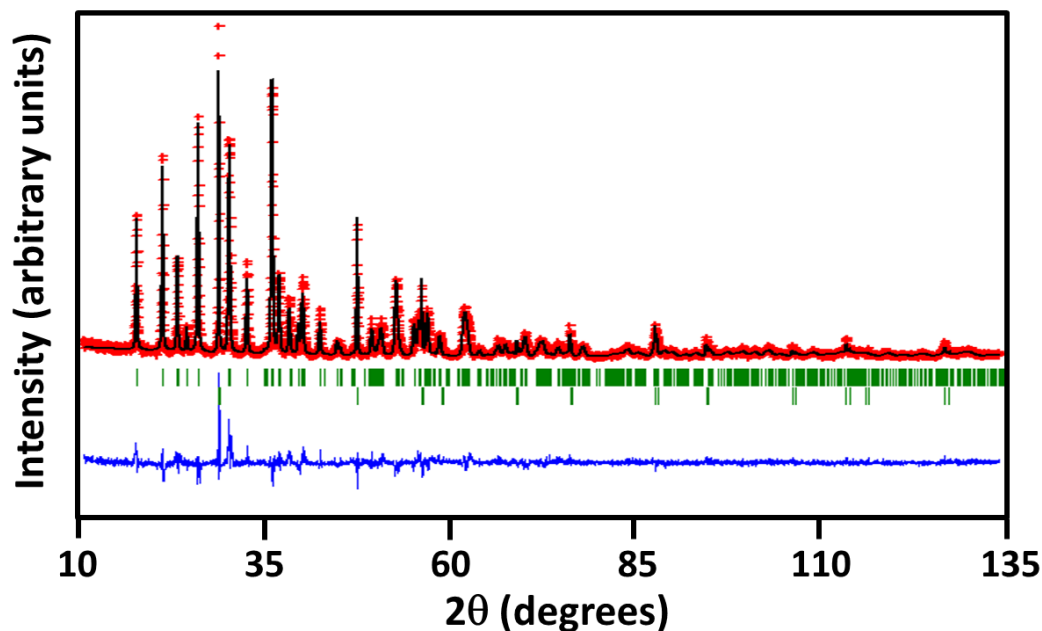


Figure 3.9. Representative XRD Rietveld refinement fit for 15 % V-doped sample.

Because XRD is sensitive to V and Fe, but insensitive to Li, it can be useful to estimate the relative V and Fe occupancies. Contrastingly, because powder neutron

diffraction is sensitive to Fe and Li, but not V, it can be used to estimate the Fe and Li occupancies. PND was performed for 5, 10, and 15 % V-doped samples and Table 3.6 shows a summary of the results. It should be noted that the 25 % V sample is difficult to synthesize in the large amounts required for neutron diffraction due to the high pressure generated by the low boiling point V precursor used in the MW-ST synthesis. Therefore, the 25 % V-doped sample was not included in the neutron analysis.

The lattice parameters found by PND are similar to those found from XRD. Fits to the neutron data with no chemical constraints and the V occupancies set at the nominal (intended) values are physically reasonable, with the implication that the occupancies are consistent with Fe^{2+} and V^{3+} within error (close to V^{3+}). The large Li displacement parameter (Uiso) may relate in part to static disorder, which suggests the possibility that lithium may displace off-site from the standard (0,0,0) position. After off-site displacement, the thermal parameter decreases rapidly to near zero within error, and there is an improvement in the fit quality as may be expected with the addition of three (x,y,z) parameters for Li. Refinement off-site produces in the case of 15 % vanadium sample a negative thermal parameter, which is not physically reasonable. Overall, there is an indication that some displacement in the lithium position is real, but which may be difficult to adequately model by Rietveld refinement of the available data.

Attempts to refine with the vanadium oxidation state constrained to V^{4+} produced unphysical results, suggesting physically reasonable results obtained from unconstrained refinement of the Fe occupancy (Table 3.6) to be more appropriate. It is also worth noting that the neutron refinement results suggest a small amount of Li

deficiency in these samples, which implies that there is either a small amount of V on the Li site or that the overall charge balance on the Fe site could be slightly higher than 2+. Either of these possibilities could explain why the V occupancy on the Fe site found for the 25 % V-doped sample was a little lower than expected from ICP data. A representative neutron refinement fit is shown in Figure 3.10.

Table 3.6. *Rietveld refinement results of the neutron diffraction data for samples prepared according to $\text{LiFe}_{1-x}(\text{VO})_x\text{PO}_4$.*

	Samples [Li at (0,0,0)]			Samples (Li off position)		
	5 % V	10 % V	15 % V	5 % V	10 % V	15 % V
a (Å)	10.3122(7)	10.2986(7)	10.2826(8)	10.3115(7)	10.2980(7)	10.2820(8)
b (Å)	5.9963(4)	5.9840(4)	5.9714(5)	5.9959(4)	5.9838(4)	5.9712(4)
c (Å)	4.6982(4)	4.7003(3)	4.7018(4)	4.6979(4)	4.7001(3)	4.7016(4)
V (Å³)	290.51(6)	289.67(6)	288.70(7)	290.46(6)	289.63(6)	288.66(6)
U_{iso}Li	2.4(3)	2.4(3)	2.1(4)	1.0(3)	0.3(4)	-0.6(4)
Li_{occ}	1.04(3)	0.98(3)	0.94(3)	1.04(3)	0.92(3)	0.92(3)**
Fe_{occ}	0.916(5)	0.855(5)	0.801(6)	0.923(5)	0.860(5)	0.808(6)
V_{occ}	0.05	0.10	0.15	0.05	0.10	0.15
Ox_{Fe}	1.97	2.01	2.01	1.96	2.02	2.02
Ox_V	2.52	3.12	3.05	2.28	3.20	3.12
χ²	2.24	2.98	3.43	2.17	2.92	3.30
wRp	0.0334	0.0313	0.0374	0.0329	0.0309	0.0367

* For the “Fe oxidation state” calculation, V³⁺ was assumed. For the “V oxidation state” calculation, Fe²⁺ was assumed. ** For the Li off-position refinements, the refined occupancy has been multiplied by a factor of 2 for comparison with the refinements with Li at (0,0,0). The multiplicity of Li off-position is 8, rather than 4 at (0,0,0).

Further structural insight can be provided from STEM and EELS characterization studies. High-angle annular dark-field STEM images (Figure 3.11) show clear interstitial defects in the V-doped LiFePO₄ samples. Because of the high contrast observed in the images, the species in the interstitial sites should be either V or Fe. This is surprising

because although Li interstitial (Frenkel) defects in LiFePO_4 are calculated to require relatively low energy to form, Fe interstitial defects are expected to require high energy to form, reducing the likelihood of formation in pristine LiFePO_4 [40]. However, the high doping levels and large quantities of vacancies may change the formation energy for these defects. Interstitial defects and vacancies could explain why neutron refinement data were better fit by allowing Li to be off-site.

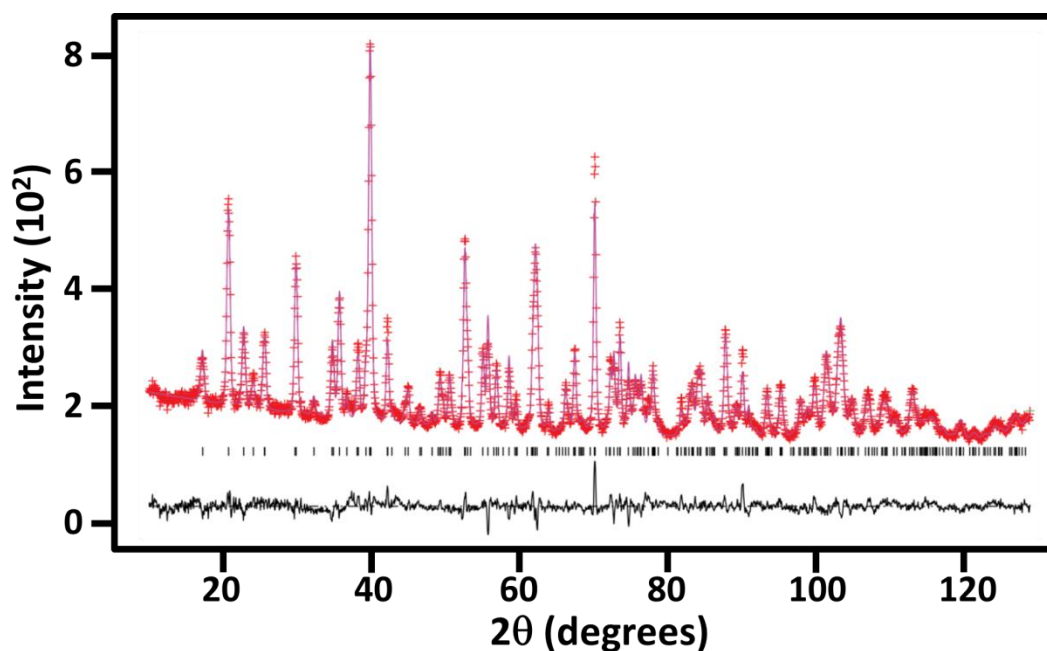


Figure 3.10. Representative neutron diffraction refinement fit for sample synthesized according to $\text{LiFe}_{0.85}(\text{VO})_{0.15}\text{PO}_4$ with Li at $(0,0,0)$.

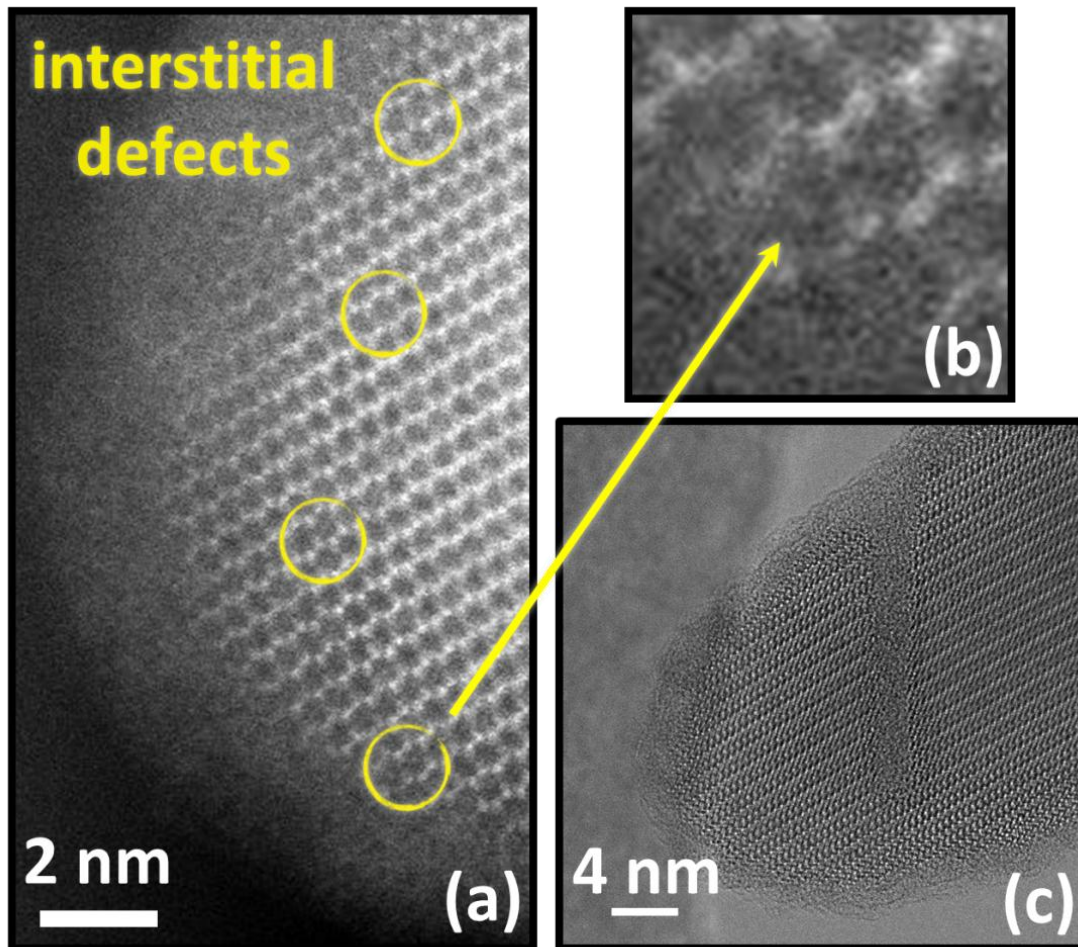


Figure 3.11. STEM Z-contrast images depicting interstitial defects ((a) and (b)) and bright field image (c) of a nanorod for 15 % V-doped LiFePO₄.

EELS data collected on the V-doped LiFePO₄ nanorods are shown in Figure 3.12. The vanadium L₃/L₂ ratio was found to be 1.61 +/-0.08, which further confirms an oxidation state that is closer to V³⁺ than V⁴⁺ [99, 100], in agreement with the XANES measurements.

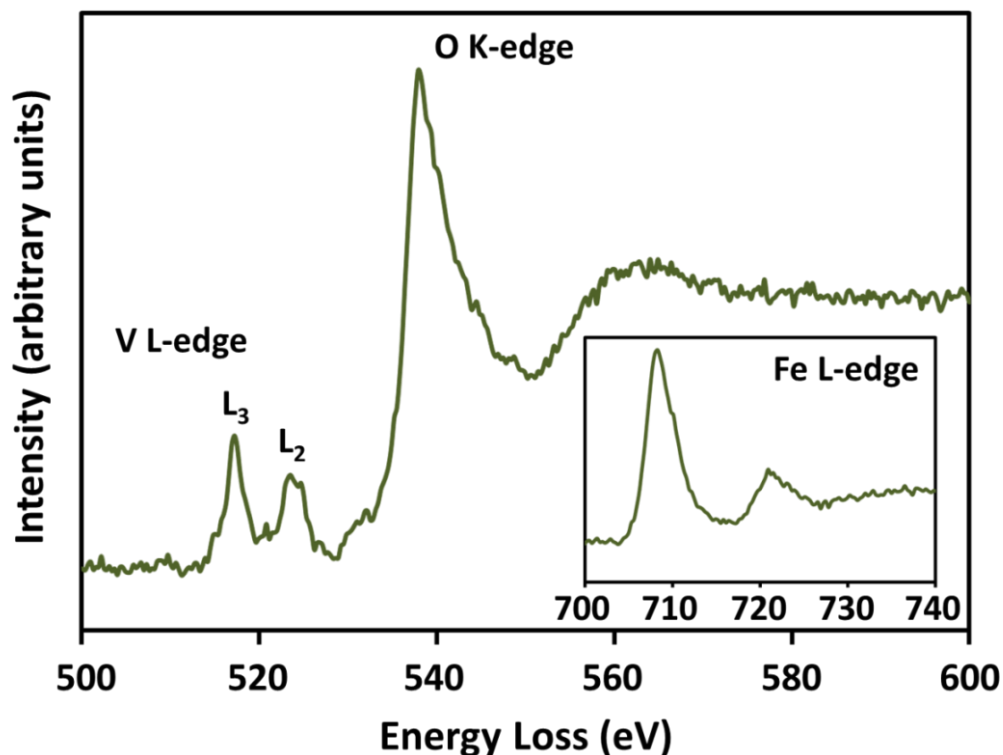


Figure 3.12. EELS data taken on a 15 % V-doped LiFePO_4 nanorod.

Spectroscopic characterization

FTIR measurements can also provide insight regarding the V-doped LiFePO_4 samples. FTIR spectra are shown in Figure 3.13 below for several samples including LiVOPO_4 and $\text{Li}_3\text{V}_2(\text{PO}_4)_3$ standards. The FTIR data for LiFePO_4 , LiVOPO_4 , and $\text{Li}_3\text{V}_2(\text{PO}_4)_3$ are consistent with the spectra found in the literature [101-104]. IR spectra of the V-doped samples closely resemble the LiFePO_4 spectrum. It should be noted that early literature suggested that it might also be possible for V^{5+} to substitute in the anion site for P^{5+} rather than the cation site [44], leading to VO_4^{3-} ions. Because the FTIR spectra are so dominated by the polyanion group, large differences in the spectra would be expected if $\text{LiFeP}_{1-x}\text{V}_x\text{O}_4$ is formed, rather than only the small shifts evident in Figure

3.13. For example, the FTIR spectra of LiCoVO_4 and LiNiVO_4 look very different from that of LiFePO_4 [105, 106]. Therefore, the small shifts evident from Figure 3.13 are more consistent with cation substitution than with anion substitution.

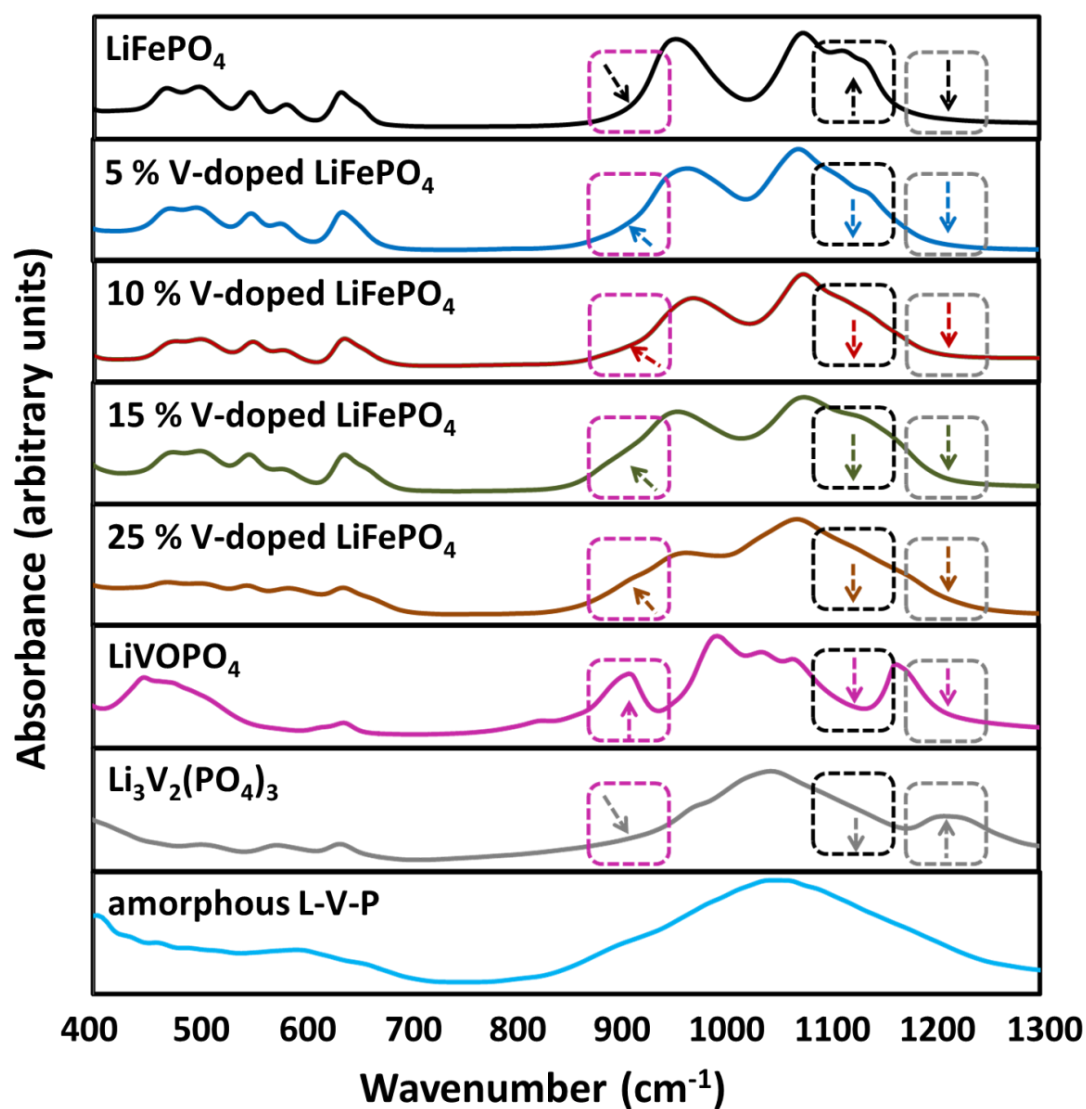


Figure 3.13. FTIR spectra for LiFePO_4 and V-doped LiFePO_4 compared to standards. Also shown is an amorphous product formed when performing MW-ST synthesis with Li, V, and P precursors in the absence of Fe.

Despite the similarity between the pristine and V-doped LiFePO_4 spectra, there are notable differences. The black dashed-line boxes in Figure 3.13 indicate sharp ν_3 P-O stretching mode peaks for the LiFePO_4 sample, but these features become less distinct in the V-doped samples, which indicates disruption or suppression of these modes. Also, a distinguishing feature between the LiFePO_4 and LiVOPO_4 spectra is the presence of a peak for V=O at $\nu = 909 \text{ cm}^{-1}$. LiFePO_4 has anti-symmetric stretching modes of the P-O bond at $\nu_3 = 1078 - 1134 \text{ cm}^{-1}$ and symmetric stretching modes at $\nu_1 = 944 - 962 \text{ cm}^{-1}$, but these peaks drop off sharply in the region near 909 cm^{-1} . Contrastingly, the V-doped samples show a shoulder to lower wavenumbers on the ν_1 peak around 900 cm^{-1} , corresponding with the location of the V=O bond in LiVOPO_4 , as illustrated by pink dashed boxes. The intensity of this shoulder increases with increasing V doping level. Although V=O bond peaks generally occur at a higher wavenumbers near 1000 cm^{-1} , there are many examples of vanadium-based phosphates in the literature that exhibit V=O bond peaks near 900 cm^{-1} , as is the case for LiVOPO_4 [73, 74, 101, 107-110].

As V^{3+} is not expected to form V=O and because there is a relatively small amount of V^{4+} in the V-doped samples, it is unlikely that the FTIR shoulder around 900 cm^{-1} is indicative of V=O. To examine this point further, Raman spectroscopy measurements are presented in Figure 3.14. It is difficult to obtain a clear pattern from Raman spectroscopy because of iron fluorescence; therefore, very low power had to be used to avoid burning and decomposing the samples. Spectra were obtained for LiFePO_4 , 15 % V-doped LiFePO_4 , and LiVOPO_4 . It is clear that there is no peak around 882 cm^{-1} , which would correspond to the V=O bond in LiVOPO_4 . Thus, the shoulder around 900 cm^{-1} seen in the FTIR patterns is not indicative of a V=O bond in

these samples. However, this FTIR peak is inconsistent with common impurities, including Li_3PO_4 , Fe_3O_4 , FePO_4 , LiOH , $\text{Li}_3\text{Fe}_2(\text{PO}_4)_3$, and LiFeP_2O_7 .

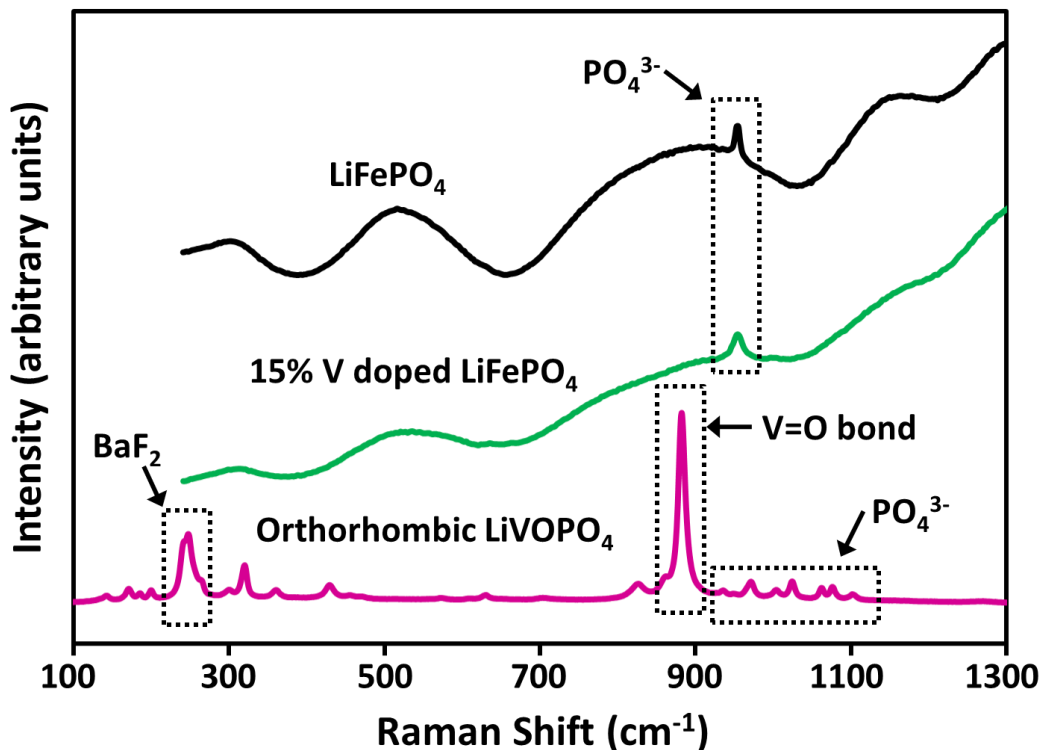


Figure 3.14. Raman spectroscopy of LiFePO_4 , 15 % V-doped LiFePO_4 prepared according to $\text{LiFe}_{0.775}\text{V}_{0.15}\square_{0.075}\text{PO}_4$, and LiVOPO_4 .

It is unknown what the shoulder at around 900 cm^{-1} represents in the V-doped samples. To investigate this further, the FTIR spectrum was recorded for the amorphous sample resulting from mixing precursors with a Li:V:P ratio of 1:1:1 and running a microwave reaction under the same conditions as for the V-doped LiFePO_4 samples. It would be possible for this species to be present as an impurity that would not be detectable by XRD but may show FTIR peaks. This was deemed unlikely due to the X-ray and neutron diffraction results, which indicate clear changes in lattice

parameters and cation occupancies consistent with doping. Regardless, the FTIR spectrum for the amorphous sample was examined anyway. The amorphous sample does not reveal an FTIR peak around 900 cm^{-1} (as shown in Figure 3.13), so the FTIR shoulders in the V-doped samples are not the result of an amorphous V-based impurity. Moreover, the FTIR pattern for the amorphous phase resembled that of $\text{Li}_3\text{V}_2(\text{PO}_4)_3$.

It is worth mentioning that the most distinguishing feature between the LiFePO_4 and $\text{Li}_3\text{V}_2(\text{PO}_4)_3$ spectra is the presence of peaks around 1220 cm^{-1} in the $\text{Li}_3\text{V}_2(\text{PO}_4)_3$ spectrum, outlined by a gray dashed-line boxes, arising from stretching vibrations of the terminal PO_4 units [104]. These peaks are not present in the V-doped samples, further confirming the absence of a $\text{Li}_3\text{V}_2(\text{PO}_4)_3$ impurity phase.

Electrochemical characterization

Since electrochemical measurements can be dependent on particle size and morphology, the morphologies of LiFePO_4 and 15 % V-doped LiFePO_4 were also characterized by SEM, as shown in Figure 3.15. LiFePO_4 forms uniform nanorod particles which have been analyzed by TEM in previous work, in which they were shown to be single crystals with an average size of about 40 nm by 100 nm [31, 33]. Conversely, the morphology of 15 % V-doped LiFePO_4 consisted of several types of shapes including rods, plate-like particles, and spheres. The particle size is less uniform as well, but the particles are still at the nano scale with similar average size.

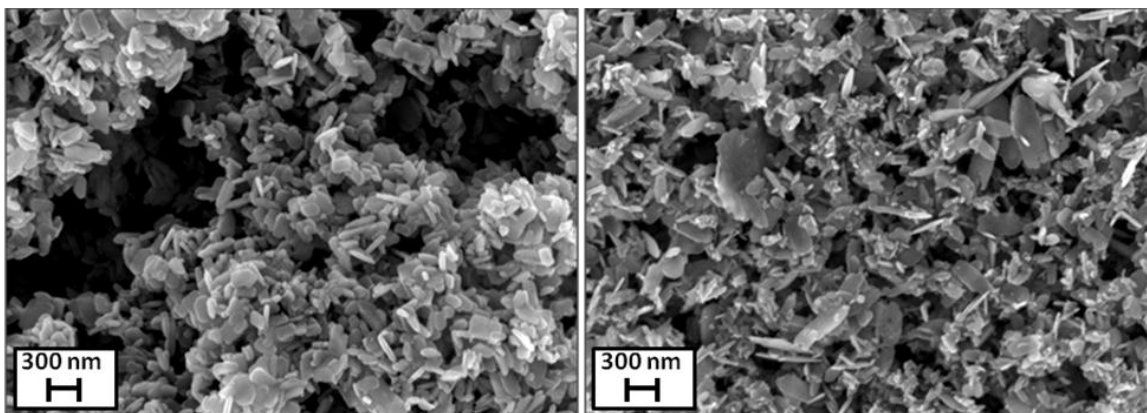


Figure 3.15. SEM micrographs of LiFePO_4 (left) and 15 % V-doped LiFePO_4 prepared according to $\text{LiFe}_{0.85}(\text{VO})_{0.15}\text{PO}_4$ (right).

The V-doped samples were also characterized electrochemically by cyclic voltammetry to determine the activity of the Fe and V redox couples. The CV curves are shown in Figure 3.16, and a summary of the charge and discharge peak locations are presented in Table 3.7. The second CV cycle is analyzed in detail because the CV peak locations stabilize after one cycle. LiFePO_4 has charge and discharge peaks centered around 3.45 V vs. Li/Li^+ [27]. LiVOPO_4 has peaks centered around 4.0 V for the $\text{V}^{4+/5+}$ couple [71], and $\text{Li}_3\text{V}_2(\text{PO}_4)_3$ has several sets of peaks between 3.5 and 4.3 V [111]. In $\text{Li}_3\text{V}_2(\text{PO}_4)_3$, the extraction of the first Li^+ occurs in two steps from 3.5 and 3.8 V ($\text{V}^{3+/4+}$ couple). There is an additional charge plateau around 4.1 V, which corresponds to the second Li^+ ion extraction ($\text{V}^{3+/4+}$). Peaks for the third Li^+ extraction ($\text{V}^{4+/5+}$) occur around 4.6 V (not shown here due to the 4.3 V cutoff).

The V-doped samples all have peaks centered around 3.45 V, which correspond to the activity of the $\text{Fe}^{2+/3+}$ couple. The peaks centered at 3.45 V in the V-doped samples are closer together in voltage and less broad than those in LiFePO_4 , indicating reduced polarization (Table 3.7). The V-doped samples also exhibit very broad peaks between 3.9 and 4.3 V that increase in size with increasing doping. These peaks are illustrated in more

detail to the right of the CV profiles. Increasing the doping level leads to decreasing iron-peak intensity for the peaks centered at 3.45 V and increasing current density in the region between 4.0 and 4.3 V. The latter current density can be attributed to the redox activity of the $V^{3+/4+}$ since the oxidation state in these samples was found to be $V^{3.2+}$ from XANES. Because of this activity in the region between 3.9 and 4.3 V, V is concluded to be redox active.

The $LiVOPO_4$ and $Li_3V_2(PO_4)_3$ curves also have small peaks close to 2 V. Because this is difficult to see from the scale in the plot, the region between 2.0 and 2.6 V has been expanded to the left of each CV plot. $LiVOPO_4$ has been cycled between 2.0 and 4.3 V in this study to be consistent with $LiFePO_4$ and the other samples tested, but typically $LiVOPO_4$ is cycled between 3.0 and 4.5 V. The activity seen near 2 V in $LiVOPO_4$ can be attributed to oxidation and reduction of the $V^{3+/4+}$ couple. When cycled in this voltage range, $LiVOPO_4$ can accept a second Li^+ ion to form Li_2VOPO_4 , which has activity near 2 V [60, 112-119]. Similarly, there is slight activity around 2 V for the $Li_3V_2(PO_4)_3$ sample (note changes of scale), which has recently been shown to be attributable to the $V^{2+/3+}$ couple [120] and will be described in more detail subsequently. It is clear that as the V-doping increases, the samples have a small amount of activity near 2 V, *i.e.*, the separation between charge and discharge CV curves increases in size with increasing V-doping. Like the activity between 3.9 and 4.3 V, there are not sharp peaks between 2.0 and 2.5 V. However, the CV measurements demonstrate that there is likely some reduction of V^{3+} to V^{2+} .

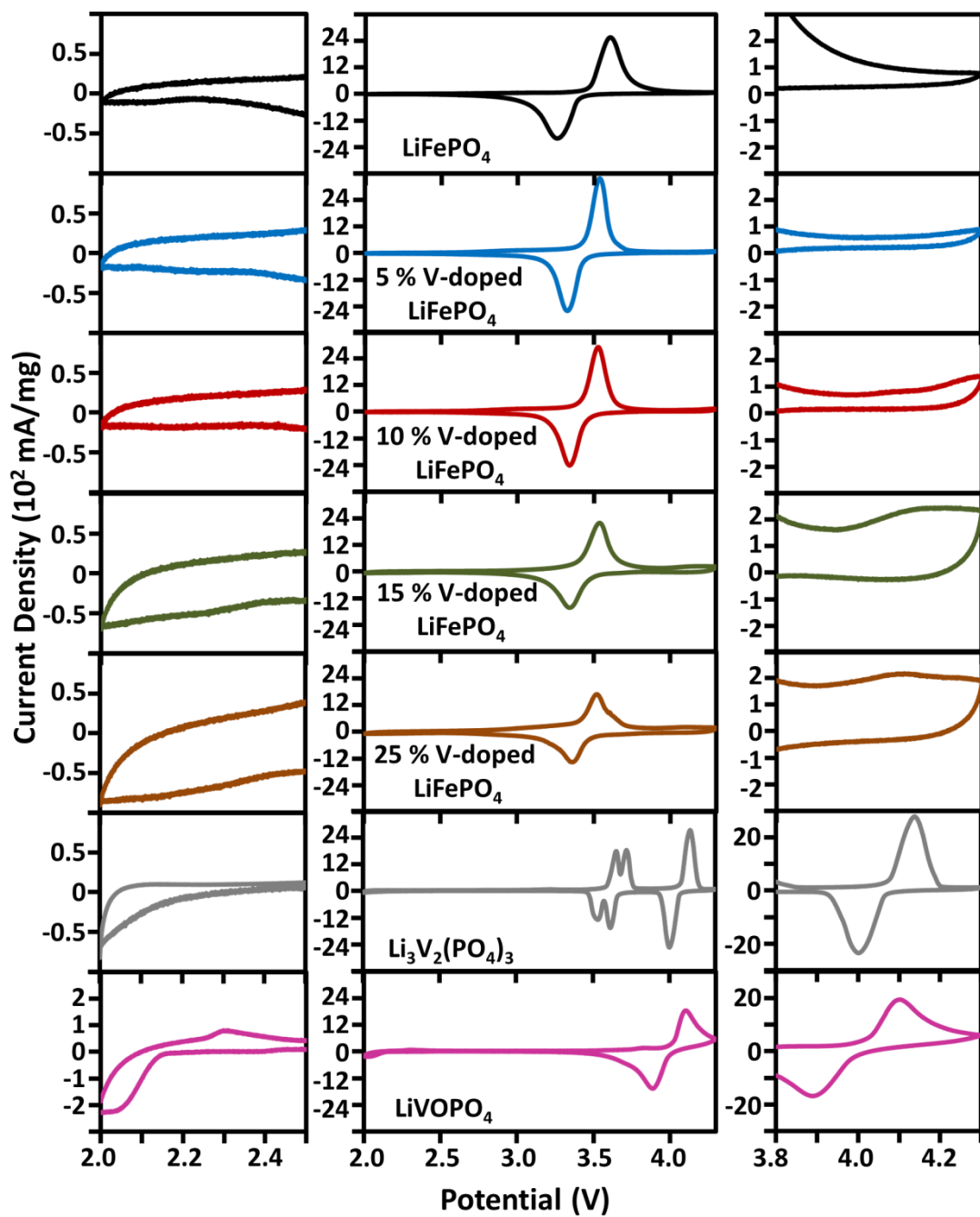


Figure 3.16. Second CV cycle at a rate of 0.1 mV/s in the range of 2.0 to 4.3 V for LiFePO_4 and V-doped LiFePO_4 prepared according to $\text{LiFe}_{1-x}(\text{VO})_x\text{PO}_4$ with $0 \leq x \leq 0.25$ compared to vanadium phosphate standards (note changes of scale for the vanadium phosphate standards).

Table 3.7. *Second CV cycle charge and discharge peak voltages at a 0.05 mV/s rate for samples prepared according to $\text{LiFe}_{1-x}(\text{VO})_x\text{PO}_4$ with $0 \leq x \leq 0.25$.*

Compound	$\text{Fe}^{2+/3+}$ Charge Peak Voltage (V)	$\text{Fe}^{2+/3+}$ Discharge Peak Voltage (V)
LiFePO_4	3.62	3.27
5 % V-doped LiFePO_4	3.54	3.33
10 % V-doped LiFePO_4	3.54	3.33
15 % V-doped LiFePO_4	3.53	3.34
25 % V-doped LiFePO_4	3.52	3.36

To investigate further the activity at low and high voltage, CV was also performed in the voltage range between 1.5 – 4.8 V for a subset of the samples, as shown in Figure 3.17. The pristine LiFePO_4 material has little activity in the 3.8 – 4.8 V and 1.5 – 2.5 V regions since the $\text{Fe}^{2+/3+}$ couple operates at 3.45 V vs. Li, but the 15 % V-doped sample has obvious activity in both of these regions that can be assigned to V oxidation and reduction. Besides the peaks between 4.0 – 4.4 V for the V-doped sample that can be assigned to the $\text{V}^{3+/4+}$ couple, there is no evidence of a second higher voltage peak corresponding to $\text{V}^{4+/5+}$ in this sample, which would be analogous to the $\text{V}^{4+/5+}$ couple in $\text{Li}_3\text{V}_2(\text{PO}_4)_3$.

In the lower voltage range, it has recently been shown that 2 more Li^+ can be reversibly inserted into $\text{Li}_3\text{V}_2(\text{PO}_4)_3$ upon discharge to form $\text{Li}_5\text{V}_2(\text{PO}_4)_3$ [120]. This insertion occurs in four steps between 1.5 and 2.0 V and results from the $\text{V}^{2+/3+}$ couple in $\text{Li}_3\text{V}_2(\text{PO}_4)_3$. V-doped LiFePO_4 also shows significant activity below 2 V, and since the oxidation state of the pristine V-doped samples is close to V^{3+} , the activity below 2 V can be assigned to a $\text{V}^{2+/3+}$ couple analogous to $\text{Li}_3\text{V}_2(\text{PO}_4)_3$.

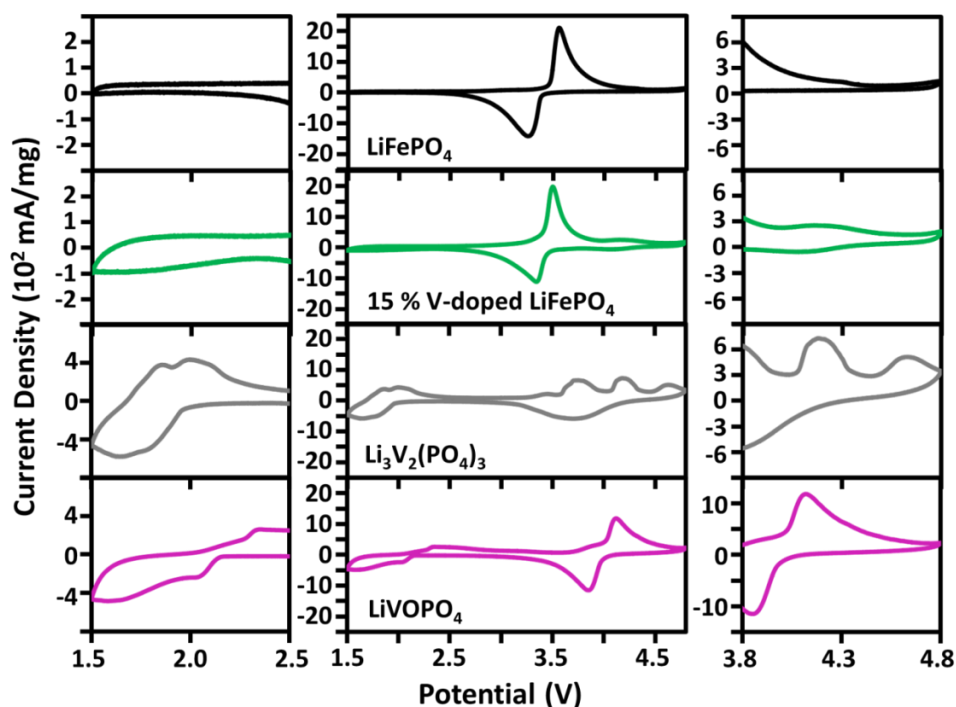


Figure 3.17. Second CV cycle at a 0.1 mV/s rate in the range between 1.8 and 4.8 V for LiFePO_4 and $\text{LiFe}_{0.775}\text{V}_{0.15}\square_{0.075}\text{PO}_4$ synthesized under the same MW-ST conditions. The data are compared to vanadium phosphate standards (note the changes of scale for the vanadium phosphate standards).

Further evidence of V redox activity is apparent from the first charge-discharge curves (Figure 3.18) with rates of C/10, C/2, and 2C. LiVOPO_4 and $\text{Li}_3\text{V}_2(\text{PO}_4)_3$ are also presented. The V-doped LiFePO_4 curves generally exhibit behavior characteristic of LiFePO_4 . The capacity is shown to decrease with increasing V doping owing to the Fe vacancies. The charge curves exhibit a change in slope around 4 V. They flatten out at higher voltage and this feature increases in extent with increasing doping levels. The capacity at 4 V is present due to the activity of the $\text{V}^{3+/4+}$ couple, as described in the CV discussion. It is also clear that the discharge curves for the V-doped samples have a change in slope at around 2.5 V and flatten out between 2.0 and 2.5 V. This activity can be attributed to the activity of the $\text{V}^{2+/3+}$ couple, analogous to the activity in $\text{Li}_3\text{V}_2(\text{PO}_4)_3$.

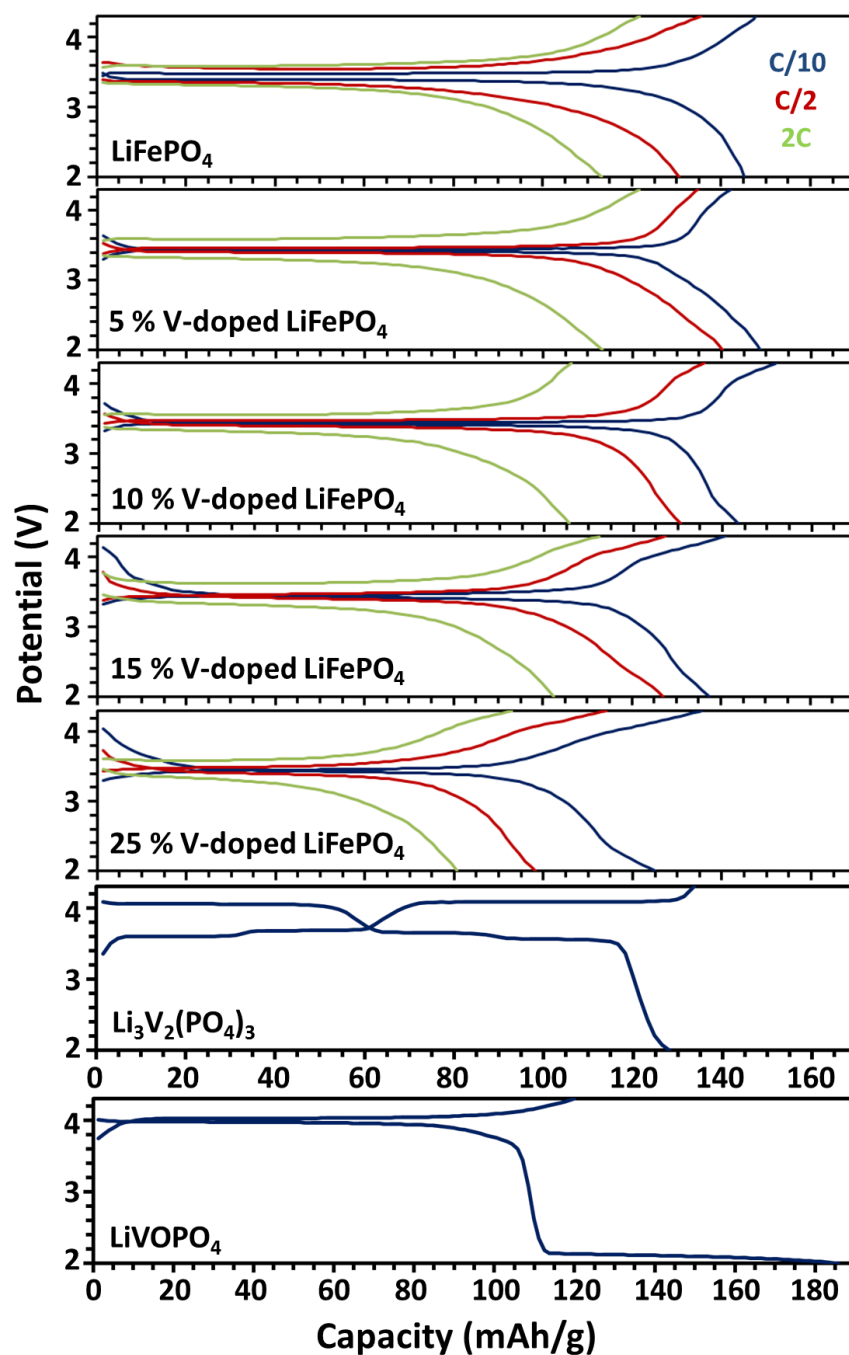


Figure 3.18. First charge-discharge curves between 2 and 4.3 V for LiFePO_4 and V-doped LiFePO_4 prepared according to $\text{LiFe}_{1-x}(\text{VO})_x\text{PO}_4$ with $0 \leq x \leq 0.25$ compared to vanadium phosphate standards (note change of scale for LiVOPO_4).

Because there are Fe vacancies (total occupancy on Fe site is 0.925) in the V-doped olivine structure, the V ions can operate on multiple valence states without the insertion of more than one Li^+ ion. It is also possible that some of the Fe vacancies could be filled by Li^+ ions. Because of the vacancies in the lattice it may be possible for Li^+ to diffuse by different paths than the normal 1D channel diffusion, and increased Li diffusion has been demonstrated previously for doped samples [42, 95]. The overall contribution of V to the electrochemical behavior of the V-doped samples can be described by high voltage (~ 4.1 V) and low voltage (~ 1.5 V – 2.5 V) activity corresponding to the $\text{V}^{3+/4+}$ and $\text{V}^{2+/3+}$ couples, with the defects on the Fe/V site playing a role in lithium diffusion and redox behavior.

As doping levels increase, the samples also show gradual suppression of the two-phase behavior that is typical for LiFePO_4 . For LiFePO_4 , the two-phase plateau begins almost immediately upon discharge, so there is only a very small single-phase region. For the sample with 25 % V, however, there is considerable single-phase behavior at the beginning of the discharge curve, and the two-phase region is decreased greatly. The suppression of the two-phase behavior is best demonstrated through examination of the open-circuit voltage curve for the 25 % V-doped sample, shown in Figure 3.19. LiFePO_4 is notorious for its very flat voltage curve at 3.45 V. In contrast, the 25 % V-doped sample exhibits a continuously sloping open-circuit voltage (OCV) curve. A sloping OCV curve suggests a single-phase reaction mechanism, rather than a two-phase mechanism. The sloping voltage curve could be caused by the disorder associated with V doping or due to iron vacancies in the samples disrupting the phase transition. A single sloping voltage curve for LiFePO_4 has been reported previously for a sample with small particle size and cation vacancies, indicating that non-stoichiometry combined with small

particles size may lead to single-phase behavior [34]. Single-phase charging and discharging is of interest because it allows for greater coexistence of Fe^{2+} and Fe^{3+} species in the lattice without the presence of a phase boundary. This has rate implications since electronic conductivity in LiFePO_4 is achieved by small polaron hopping of Fe^{3+} holes or Fe^{2+} electrons. These charge carriers increase in concentration in a single-phase system [21, 22]. Also, although battery materials with flat voltage curves are beneficial because they can supply power at a constant voltage, sloping charge-discharge curves make state-of-charge determination easier for batteries [34].

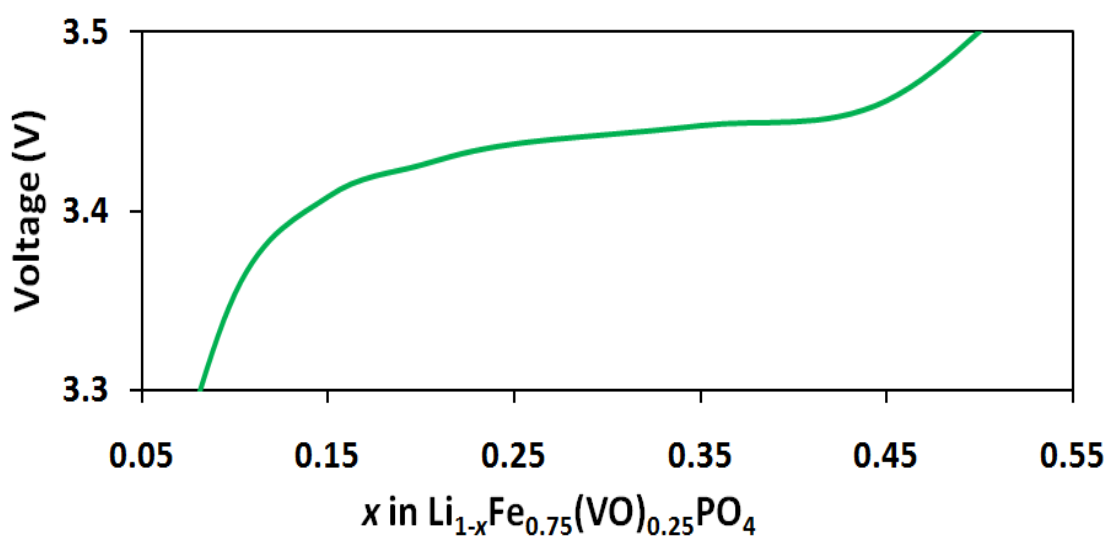


Figure 3.19. Open-circuit voltage curve for 25 % V-doped LiFePO_4 sample prepared according to $\text{LiFe}_{0.75}(\text{VO})_{0.25}\text{PO}_4$.

It should be noted that the XANES data does not show a mixed Fe oxidation state, indicating that the suppression of the distinct two-phase plateau behavior characteristic of LiFePO_4 does not result from $\text{Fe}^{2+/3+}$ mixing in these samples. Instead, the iron vacancies or presence of V^{3+} appear to be responsible for increasing

the solid solubility of FePO_4 and LiFePO_4 . It has also been previously suggested that doping can lead to increased solid solution between LiFePO_4 and FePO_4 [42]. This improved solubility could be the reason for the decreased polarization demonstrated in the CV data for the V-doped samples since the phase change is kinetically limiting.

Although the capacity decreases with increasing V-doping due to Fe vacancies, the capacity retention during extended cycling improves for all of the V-doped samples compared to LiFePO_4 , as shown in Figure 3.20. It is possible that the improved cyclability could be due to the Fe vacancies in the samples; the Fe vacancies may suppress anti-site disorder between Li and Fe, and thereby enhance the lithium diffusivity or create new paths for Li^+ diffusion.

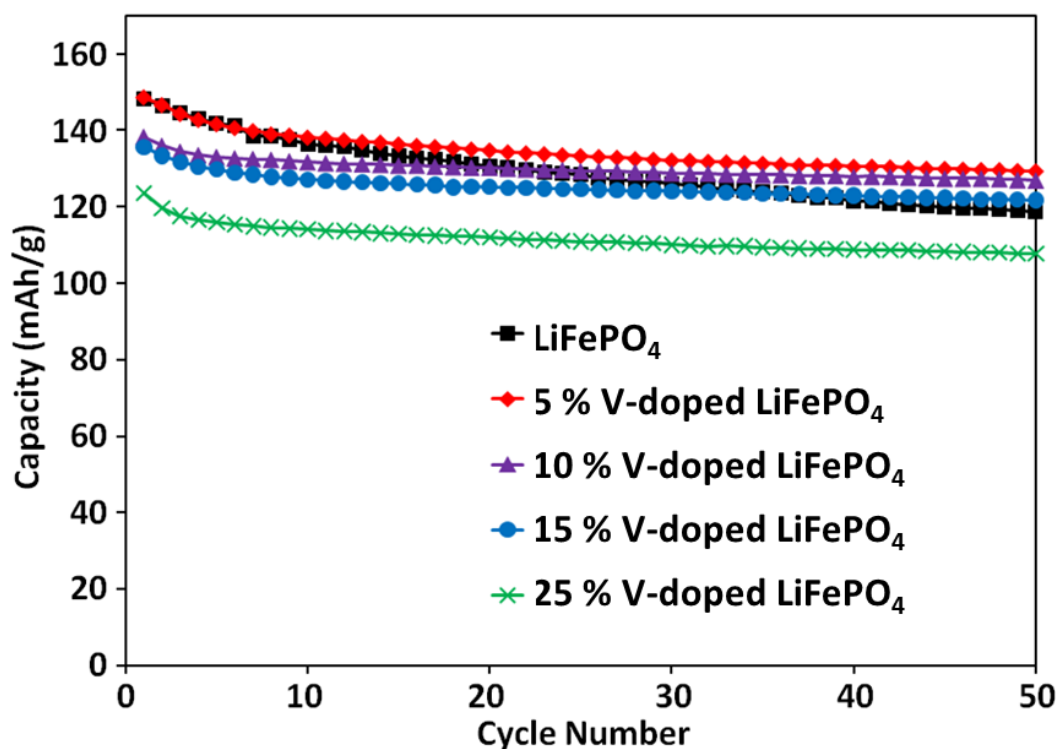


Figure 3.20. Cycle performance data at a C/10 rate for LiFePO_4 and V-doped LiFePO_4 samples prepared according to $\text{LiFe}_{1-x}(\text{VO})_x\text{PO}_4$ with $0 \leq x \leq 0.25$.

By 50 cycles, the capacities of all of the V-doped samples (except the 25 % V-doped sample) exceed the capacity of pristine LiFePO_4 and are fairly stable. Because of redox activity at higher voltage and the increased capacity, the energy densities of the V-doped samples are also higher than for LiFePO_4 after 50 cycles. It should be noted that all of the data presented here are for samples without any carbon coating, and MW-ST LiFePO_4 with carbon coating has been shown before to exhibit very good capacity retention [31]. Therefore, the trend in the cyclability results shown here may differ in the presence of carbon coating.

3.4 CONCLUSIONS

A rapid microwave-assisted solvothermal synthesis method was developed to prepare V-doped LiFePO_4 cathodes with the formula $\text{LiFe}_{1-3x/2}\text{V}_x\text{PO}_4$ (x at least 0.2) at 300 °C. The oxidation state of V was found consistently to be $\sim \text{V}^{3.2+}$ by XANES. Neutron and X-ray Rietveld refinements show clear evidence of Fe vacancies in these materials, with the X-ray data confirming that at least 20 % V can be doped into the Fe site and that the olivine structure can accommodate significant cation vacancies. This is in sharp contrast to other studies that employed conventional, high-temperature synthetic approaches and demonstrated a maximum of 10 % V doping without formation of impurity phases.

CV and charge-discharge curves show that the $\text{V}^{2+/3+}$ and $\text{V}^{3+/4+}$ redox couples are both electrochemically active, and the typical two-phase plateau behavior characteristic of LiFePO_4 is suppressed in the vanadium ion substituted samples. Although the capacities and rate capabilities decrease with increasing V doping due to Fe vacancy formation and corresponding capacity loss, the cycle life improves; however, the samples examined are not coated with carbon, which affects cyclability.

Chapter 4: Phase Stability of $\text{LiFe}_{1-3x/2}\text{V}_x\text{PO}_4$ Cathodes

4.1 INTRODUCTION

In the previous Chapter, the low-temperature microwave-assisted solvothermal synthesis and characterization of V-doped LiFePO_4 cathodes was detailed. Although previous studies have been able to demonstrate a maximum of 10 % V doping [43-51], accommodation of at least 20 % V in the olivine lattice is demonstrated here. In this Chapter, these remarkably high doping levels are shown to be possible only because of the low-temperature MW-ST synthesis method which leads to formation of a metastable phase. This is demonstrated by heating the 15 % V-doped LiFePO_4 sample in reducing and inert atmospheres at various temperatures to show that the olivine lattice loses vanadium and forms $\text{Li}_3\text{V}_2(\text{PO}_4)_3$ at high temperatures. For comparison, attempts were also made to prepare V-doped samples by a conventional ball milling and heating method. As found in previous studies, at conventional synthesis temperatures, only about 10 % V can be accommodated in the olivine lattice. Therefore, the low temperature MW-ST method is demonstrated here to yield a metastable phase with higher dopant levels than can be achieved by conventional methods.

4.2 EXPERIMENTAL

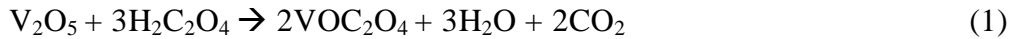
Microwave Synthesis

The microwave-synthesized samples were prepared as described in the previous Chapter. To determine the stability of the V-doped samples at synthesis temperatures conventionally used for LiFePO_4 type phases, the pristine MW-ST sample prepared according to $\text{LiFe}_{0.775}\text{V}_{0.15}\text{PO}_4$ was ground and heated in flowing 5 % H_2 – 95 % Ar or 100 % Ar environments at various elevated temperatures (525 °C – 25 °C) and for various times (6 h and 15 h), similar to the

methods used in the conventional high-temperature synthesis of pristine and V-doped LiFePO_4 [23, 25-27, 35- 38, 43-51].

Conventional synthesis

Attempts were also made to synthesize $\text{LiFe}_{0.775}\text{V}_{0.15}\square_{0.075}\text{PO}_4$ directly by solid-state reaction. The V precursor was first prepared by reaction (1):



The water was evaporated while stirring the solution on a hot plate at 70 °C and finally the powder was dried in a vacuum oven at 100 °C. ICP analysis was used to determine and adjust for the water content of VOC_2O_4 . Subsequently, the VOC_2O_4 was ball milled in acetone for 5 days with stoichiometric amounts of iron oxalate (Fisher), ammonium dihydrogen phosphate (Fisher), and lithium hydroxide monohydrate (Fisher) in stoichiometric ratios to prepare $\text{LiFe}_{0.775}\text{V}_{0.15}\square_{0.075}\text{PO}_4$. The products were dried, ground, and then heated in flowing 5 % H_2 – 95 % Ar and 100 % Ar atmospheres for 3 h at 350 °C followed by 6 h at temperatures ranging from 525 °C - 725 °C. This is similar to previously described conventional methods used for LiFePO_4 and V-doped LiFePO_4 synthesis [23, 25-27, 35-38, 43-51].

Additionally, LiFePO_4 was prepared by the same ball milling and heating method with stoichiometric amounts of precursors. For a comparison, $\text{Li}_3\text{V}_2(\text{PO}_4)_3$ and LiVOPO_4 were also prepared, as described in the previous Chapter. A naming scheme will be employed to refer to the pristine and heated samples, defined by: “synthesis method – sample – furnace heating atmosphere – furnace heating temperature – furnace heating time.” For example, MW-ST V-doped LiFePO_4 that is then heated at 525 °C in 5% H_2 and 95 % Ar for 6 h will be referred to as MW-LFVP- H_2 -525-6h. The corresponding conventionally prepared sample will be referred to as

CONV-LFVP-H₂-525-6h. LiFePO₄ samples will be described with "LFP" rather than "LFVP." The relevant samples are summarized in Table 4.1

Table 4.1. Summary of as-prepared and post-heated samples of undoped and V-doped LiFePO₄.

Sample	Intended Product	Synthesis Method	MW Temp.	MW Time	Furnace Temp.	Furnace Time	Furnace Atmosphere
MW-LFP-unheated	LiFePO ₄	MW	300 °C	30 min	N/A	N/A	N/A
MW-LFPdef-unheated	LiFe _{0.85} PO ₄	MW	300 °C	30 min	N/A	N/A	N/A
MW-LFP-H ₂ -725-6h	LiFePO ₄	MW	300 °C	30 min	725 °C	6 h	5 % H ₂
MW-LFVP-unheated	LiFe _{0.775} V _{0.15} PO ₄	MW	300 °C	30 min	N/A	N/A	N/A
MW-LFVP-H ₂ -525-6h	LiFe _{0.775} V _{0.15} PO ₄	MW, heat	300 °C	30 min	525 °C	6 h	5 % H ₂
MW-LFVP-H ₂ -625-6h	LiFe _{0.775} V _{0.15} PO ₄	MW, heat	300 °C	30 min	625 °C	6 h	5 % H ₂
MW-LFVP-H ₂ -725-6h	LiFe _{0.775} V _{0.15} PO ₄	MW, heat	300 °C	30 min	725 °C	6 h	5 % H ₂
MW-LFVP-Ar-525-6h	LiFe _{0.775} V _{0.15} PO ₄	MW, heat	300 °C	30 min	525 °C	6 h	Ar
MW-LFVP-Ar-625-6h	LiFe _{0.775} V _{0.15} PO ₄	MW, heat	300 °C	30 min	625 °C	6 h	Ar
MW-LFVP-Ar-725-6h	LiFe _{0.775} V _{0.15} PO ₄	MW, heat	300 °C	30 min	725 °C	6 h	Ar
MW-LFVP-Ar-525-15h	LiFe _{0.775} V _{0.15} PO ₄	MW, heat	300 °C	30 min	525 °C	15 h	Ar
MW-LFVP-Ar-625-15h	LiFe _{0.775} V _{0.15} PO ₄	MW, heat	300 °C	30 min	625 °C	15 h	Ar
MW-LFVP-Ar-725-15h	LiFe _{0.775} V _{0.15} PO ₄	MW, heat	300 °C	30 min	725 °C	15 h	Ar
CONV-LFP-Ar-725-6h	LiFePO ₄	ball mill, heat	N/A	N/A	725 °C	6 h	Ar
CONV-LFPdef-Ar-725-6h	LiFe _{0.85} PO ₄	ball mill, heat	N/A	N/A	725 °C	6 h	Ar
CONV-LFP-H ₂ -525-6h	LiFePO ₄	ball mill, heat	N/A	N/A	525 °C	6 h	Ar
CONV-LFP-H ₂ -625-6h	LiFePO ₄	ball mill, heat	N/A	N/A	625 °C	6 h	Ar
CONV-LFP-H ₂ -725-6h	LiFePO ₄	ball mill, heat	N/A	N/A	725 °C	6 h	Ar
CONV-LFVP-H ₂ -525-6h	LiFe _{0.775} V _{0.15} PO ₄	ball mill, heat	N/A	N/A	525 °C	6 h	5 % H ₂
CONV-LFVP-H ₂ -625-6h	LiFe _{0.775} V _{0.15} PO ₄	ball mill, heat	N/A	N/A	625 °C	6 h	5 % H ₂
CONV-LFVP-H ₂ -725-6h	LiFe _{0.775} V _{0.15} PO ₄	ball mill, heat	N/A	N/A	725 °C	6 h	5 % H ₂
CONV-LFVP-Ar-525-6h	LiFe _{0.775} V _{0.15} PO ₄	ball mill, heat	N/A	N/A	525 °C	6 h	Ar
CONV-LFVP-Ar-625-6h	LiFe _{0.775} V _{0.15} PO ₄	ball mill, heat	N/A	N/A	625 °C	6 h	Ar
CONV-LFVP-Ar-725-6h	LiFe _{0.775} V _{0.15} PO ₄	ball mill, heat	N/A	N/A	725 °C	6 h	Ar
Li ₃ V ₂ (PO ₄) ₃	Li ₃ V ₂ (PO ₄) ₃	ball mill, heat	N/A	N/A	725 °C	6 h	5 % H ₂
LiVOPO ₄	LiVOPO ₄	sol-gel, heat	N/A	N/A	500 °C	4 h	Air

4.3 RESULTS AND DISCUSSION

Structural characterization

XRD patterns are shown in Figure 4.1 for the as-prepared MW-LFP-unheated and MW-LFVP-unheated samples as well as the MW-ST samples subsequently heated in 5 % H₂ – 95 % Ar at various temperatures. A Si internal standard was used during data collection, as discussed in the previous chapter to obtain more accurate lattice parameters. The pattern for Li₃V₂(PO₄)₃ is also shown for a comparison. Results for the samples heated in Ar were very similar to those heated in 5 % H₂ – 95 % Ar, so only the samples heated in 5 % H₂ – 95 % Ar are presented for brevity. The XRD patterns for MW-LFVP-H₂-525-6h and MW-LFVP-H₂-625-6h closely resemble that for MW-LFVP-unheated with no detectable impurity phases. Conversely, the MW-LFVP-H₂-725-6h sample has impurity peaks that can be identified as monoclinic Li₃V₂(PO₄)₃. Several studies have shown that that Li₃V₂(PO₄)₃ impurity forms when doping V into the olivine lattice at levels above 5 – 10 % by conventional high temperature synthesis methods [44, 45-47, 50, 96]; therefore, this result was anticipated.

XRD patterns for the post-heated microwave-synthesized samples can be compared to the LiFe_{0.775}V_{0.15}□_{0.075}PO₄ samples synthesized by a conventional ball milling and heating process. The XRD patterns for these materials (CONV-LFVP) are shown in Figure 4.1 for the samples heated in 5 % H₂ – 95 % Ar. Li₃V₂(PO₄)₃ peaks are detectable in the samples at all three heating temperatures in contrast to the MW-ST synthesized and heated samples. Again, similar results were obtained when heating in Ar and in 5 % H₂ – 95 % Ar.

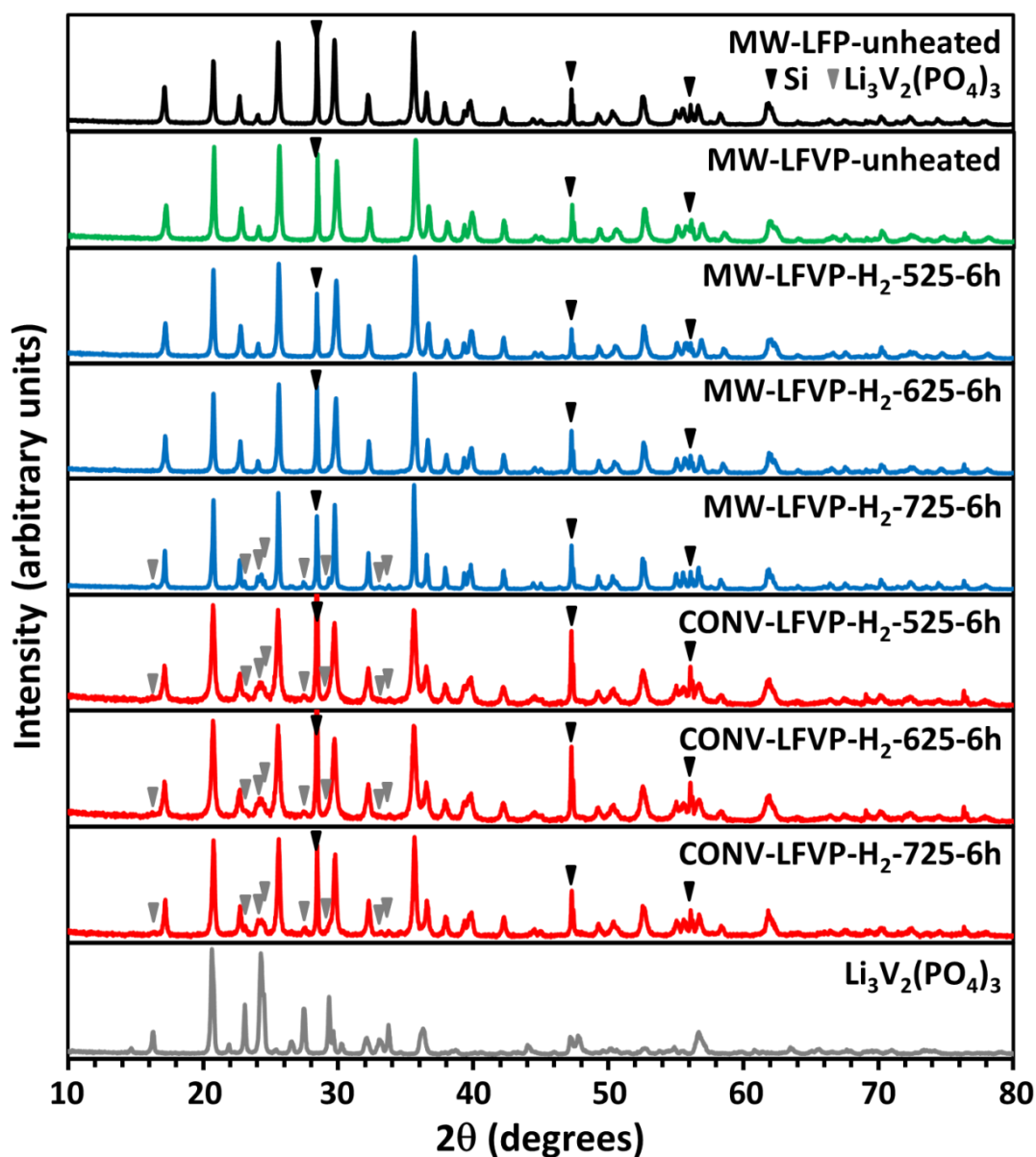


Figure 4.1. XRD patterns of as-prepared and post-heated samples of undoped and V-doped LiFePO_4 with an internal Si standard.

To eliminate any possibility that different heating conditions were responsible for the difference in $\text{Li}_3\text{V}_2(\text{PO}_4)_3$ formation, the microwave-synthesized sample and

the precursors for the conventionally doped samples were heated in the same tube furnace in adjacent crucibles. This result was repeatable, which confirms that MW-ST synthesis provides a product with higher doping levels that is somewhat kinetically stable at elevated temperatures. If the V had been present, for example, as an amorphous impurity rather than within the olivine lattice, the V should have formed $\text{Li}_3\text{V}_2(\text{PO}_4)_3$, as occurs in the conventionally prepared samples. Furthermore, even after 15 h of heating in Ar, the microwave-synthesized LFVP sample showed phase pure patterns at 525 °C and 625 °C.

As shown in the previous Chapter, there is a systematic decrease in unit cell volume, in addition to an increase in the length of the *c* axis, with increasing V doping. Therefore, an increase in unit cell volume and decrease in *c* axis length is expected if heating results in vanadium being leached from the olivine lattice. Table 4.2 shows that the MW-LFVP-H₂-525-6h, MW-LFVP-Ar-525-6h, and MW-LFVP-Ar-525-15h samples have similar unit cell volumes, indicating only a slight increase (approximately within error) from pristine MW-LFVP-unheated. At higher temperatures, there is a systematic increase in unit cell volume with increasing temperature, with the most significant increase in the unit cell volume present for the samples heated at 725 °C. In addition, there is a systematic decrease in the length of the *c* axis. However, the lattice parameters do not shift all the way back to those for MW-LFP-unheated, suggesting that some vanadium remains present in the olivine lattice even at 725 °C. The unit cell volumes for the conventionally heated LFVP samples are shown to be similar for all heating conditions, and the unit cell volumes are all lower than for the conventional LiFePO_4 samples, indicating V doping. Furthermore, the unit cell volumes are similar to those for the microwave-synthesized

samples heated at 725 °C, and have a volume similar to LiFePO₄ doped with V in the range of 5 – 10 %.

Table 4.2. *Summary of the lattice parameters of the as-prepared and post-heated undoped and V-doped LiFePO₄ (obtained by Rietveld refinement of XRD data with fit parameter χ^2 shown).*

Sample	a (Å)	b (Å)	c (Å)	V (Å ³)	χ^2
MW-LFP-unheated	10.32093(20)	6.00127(12)	4.69262(9)	290.655(10)	1.55
MW-LFPdef-unheated	10.32392(14)	5.99971(8)	4.69249(6)	290.655(7)	2.66
MW-LFP-H ₂ -700-6h	10.32653(8)	6.00370(5)	4.69084(4)	290.820(4)	2.44
MW-LFVP-unheated	10.27589(25)	5.97117(14)	4.69939(11)	288.350(12)	1.40
MW-LFVP-H ₂ -525-6h	10.28668(14)	5.97441(8)	4.69636(6)	288.623(7)	1.94
MW-LFVP-H ₂ -625-6h	10.29490(14)	5.98145(9)	4.69423(6)	289.063(7)	2.21
MW-LFVP-H ₂ -725-6h	10.31397(10)	5.99741(6)	4.69195(5)	290.230(5)	2.67
MW-LFVP-Ar-525-6h	10.28145(15)	5.97428(9)	4.69722(7)	288.523(7)	1.88
MW-LFVP-Ar-625-6h	10.28643(14)	5.97664(9)	4.69590(6)	288.696(7)	2.24
MW-LFVP-Ar-725-6h	10.31407(10)	5.99812(6)	4.69239(5)	290.295(5)	2.52
MW-LFVP-Ar-525-15h	10.28433(16)	5.97423(9)	4.69697(7)	288.586(8)	1.85
MW-LFVP-Ar-625-15h	10.28678(14)	5.97686(8)	4.69540(6)	288.686(7)	2.11
MW-LFVP-Ar-725-15h	10.31685(8)	6.00016(5)	4.69230(4)	290.466(4)	2.70
CONV-LFVP-H ₂ -525-6h	10.3097(3)	6.00242(17)	4.69601(14)	290.604(14)	1.84
CONV-LFVP-H ₂ -625-6h	10.30809(27)	6.00045(15)	4.69596(12)	290.461(13)	1.85
CONV-LFVP-H ₂ -725-6h	10.31044(20)	5.99990(12)	4.69530(9)	290.459(10)	1.95
CONV-LFVP-Ar-525-6h	10.31085(30)	6.00156(16)	4.69548(13)	290.562(14)	1.68
CONV-LFVP-Ar-625-6h	10.30902(25)	5.99882(14)	4.69585(11)	290.400(12)	1.74
CONV-LFVP-Ar-725-6h	10.30636(21)	5.99633(12)	4.69407(10)	290.095(10)	2.52
CONV-LFP-Ar-725-6h	10.32494(8)	6.00591(5)	4.69161(4)	290.930(4)	1.80
CONV-LFPdef-Ar-725-6h	10.32681(11)	6.00602(6)	4.69043(5)	290.915(5)	1.95
CONV-LFP-H ₂ -525-6h	10.32535(15)	6.00610(9)	4.69367(7)	291.079(7)	2.27
CONV-LFP-H ₂ -625-6h	10.32441(13)	6.00614(7)	4.69241(6)	290.975(6)	2.40
CONV-LFP-H ₂ -725-6h	10.32507(9)	6.00606(5)	4.69162(4)	290.941(4)	3.64

Since the precursor for these doped samples all have deficient amounts of Fe relative to Li and P, samples were also synthesized with Fe deficiency but without V, i.e., 'LiFe_{0.85}PO₄' as the intended formula, both conventionally and by the MW-ST process. These samples are referred to as CONV-LFPdef-Ar-725-6h and MW-LFPdef-unheated, respectively, and the lattice parameters are shown. In both cases, the deficient iron samples have similar unit cell volumes as their stoichiometric counterparts. This shows that Fe vacancies do not occur without vanadium doping and the lower lattice parameters in the doped samples are due to V presence in the olivine lattice. It is worth noting that the MW-LFP-unheated sample has a slightly lower unit cell volume than the conventionally prepared LiFePO₄ samples. However, upon heating, the lattice parameters are similar, as indicated in Table 4.2 by the MW-LFP-H₂-725-6h sample. It is unclear why this is the case; it could be related to defects in the structure, but could also have to do with particle size effects giving rise to lattice strain from surface tension [26, 121, 122].

To estimate the amount of vanadium remaining in the lattice after heating, the V and Fe occupancies were also refined with a restraint that the total charge on the Fe site must be 2+. Oxidation states were assumed to be Fe²⁺ and V³⁺. The MW-LFVP-unheated sample was found to have a slightly higher V oxidation state (V^{3.2+}), but the heated samples were assumed to consist of V³⁺ since the conventional V-doped samples have Li₃V₂(PO₄)₃ impurity, indicating V³⁺ is the stable oxidation state. The oxidation state might be slightly higher than V³⁺ in some of the samples (especially when heated at lower temperature), but an assumption had to be made and this seemed most reasonable. A representative refinement fit is shown in Figure 4.2 for a sample with olivine, Si, and Li₃V₂(PO₄)₃. It was difficult to refine the Li₃V₂(PO₄)₃

phase in the samples since it was only a small impurity phase. Therefore, a pure $\text{Li}_3\text{V}_2(\text{PO}_4)_3$ sample was first refined and all of the parameters from that refinement were used for the $\text{Li}_3\text{V}_2(\text{PO}_4)_3$ impurity phase in the olivine samples. Only the lattice parameters and the overall isotropic displacement parameter were refined for the $\text{Li}_3\text{V}_2(\text{PO}_4)_3$ phase in the olivine samples.

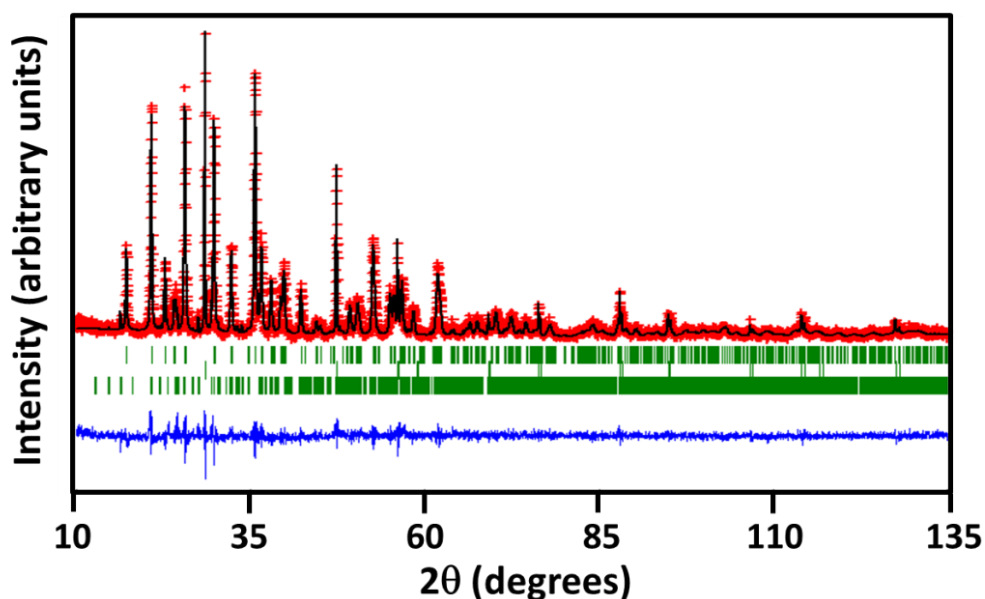


Figure 4.2. Representative XRD Rietveld refinement fit of V-doped LiFePO_4 , $\text{Li}_3\text{V}_2(\text{PO}_4)_3$, and Si phases.

As shown in Table 4.3, the refinement suggests that the samples heated at 525 °C and 625 °C still have around 15 % V doping, but the samples heated at 725 °C lose V from the olivine lattice. These values agree well with existing literature and with the conventionally prepared samples, which indicate doping levels of ~10 % or less can be achieved [43-51, 93, 94]. The doping levels in the conventional samples are slightly higher than in the MW-ST samples at 725 °C, which could be related to the

slightly different stoichiometry in the microwave samples (i.e., possible lithium deficiency as discussed in the previous Chapter).

Table 4.3. *Fractional occupancy and phase fraction results for as-prepared and post-heated samples of undoped and V-doped LiFePO_4 from Rietveld refinement.*

Sample	$\text{Fe}_{\text{occupancy}}$	$\text{V}_{\text{occupancy}}$	$\text{V}_{\text{occupancy}}$ from % LVP*	% LVP
MW-LFVP-unheated	0.764(18)	0.149(11)	-----	-----
MW-LFVP- H_2 -525-6h	0.765(14)	0.156(9)	-----	-----
MW-LFVP- H_2 -625-6h	0.798(14)	0.135(10)	-----	-----
MW-LFVP- H_2 -725-6h	0.875(14)	0.084(9)	0.0883(16)	9.50(33)
MW-LFVP-Ar-525-6h	0.777(13)	0.148(9)	-----	-----
MW-LFVP-Ar-625-6h	0.763(14)	0.158(10)	-----	-----
MW-LFVP-Ar-725-6h	0.878(14)	0.082(10)	0.0802(18)	10.61(36)
MW-LFVP-Ar-525-15h	0.767(14)	0.155(9)	-----	-----
MW-LFVP-Ar-625-15h	0.769(14)	0.154(9)	-----	-----
MW-LFVP-Ar-725-15h	0.895(15)	0.070(10)	0.0668(21)	12.39(41)
CONV-LFVP- H_2 -525-6h	0.843(35)	0.098(40)	0.1168(15)	5.36(31)
CONV-LFVP- H_2 -625-6h	0.839(17)	0.107(12)	0.1144(15)	5.72(30)
CONV-LFVP- H_2 -725-6h	0.805(19)	0.130(13)	0.0975(19)	8.24(39)
CONV-LFVP-Ar-525-6h	0.842(20)	0.105(13)	0.1175(14)	5.26(30)
CONV-LFVP-Ar-625-6h	0.824(18)	0.117(12)	0.1171(14)	5.33(29)
CONV-LFVP-Ar-725-6h	0.830(17)	0.113(11)	0.1035(17)	7.36(35)

*Errors for “ V_{occ} from % LVP” were estimated by the method of sequential perturbation because an iterative solution was required.

To corroborate the V occupancies as a function of temperature that were determined by direct refinement of site occupancies, the amount of V remaining in the olivine lattice after heating was also indirectly estimated from the phase fractions. By assuming the V is all present in either the crystalline olivine phase or $\text{Li}_3\text{V}_2(\text{PO}_4)_3$,

one can estimate the amount of V remaining in the olivine lattice from the phase fraction of $\text{Li}_3\text{V}_2(\text{PO}_4)_3$ that forms. This indirect analysis reveals similar V occupancies (within error) as the direct Fe site refinement, as shown in Table 4.3.

The only data that do not agree well are for the conventional sample synthesized at 725 °C in 5 % H_2 – 95% Ar (the strongest reducing environment). In this case, the V occupancy found by restraining the total charge on the Fe site is significantly higher than for the occupancy found from the phase fraction of $\text{Li}_3\text{V}_2(\text{PO}_4)_3$. The higher V occupancy in this sample is inconsistent with the trends from the other samples and from other literature. This implies that the restraint on the Fe-site charge is not valid for this sample or that V is present in a phase other than the olivine and $\text{Li}_3\text{V}_2(\text{PO}_4)_3$ phases. The maximum V doping demonstrated in the olivine lattice is summarized as a function of temperature in Figure 4.2 and compared to other studies. In general, all of the results indicate the trend that the maximum achievable doping levels before impurity formation decreases with increasing temperature.

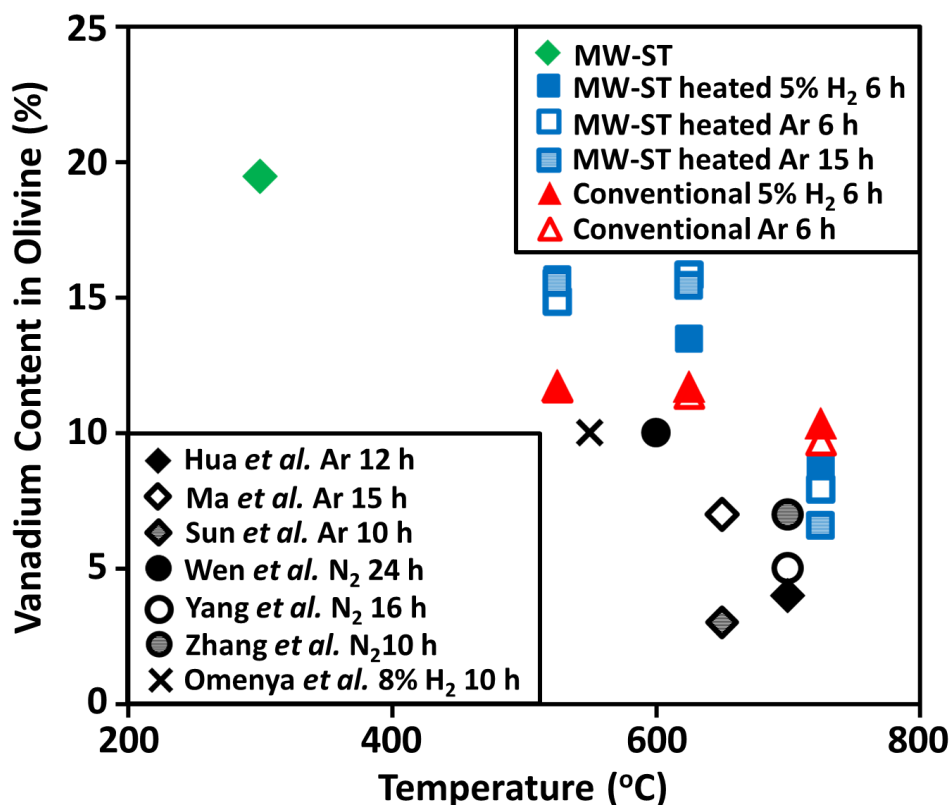


Figure 4.3. Maximum V content demonstrated versus temperature. Heated MW-ST V-doped LiFePO₄ samples are compared to conventionally prepared V-doped LiFePO₄ samples from this study (red triangles) and from other literature (black symbols). The legends indicate the heating environment and heating time. The values used here are ' $V_{\text{occupancy}}$ from % LVP' from Table 4.3 where applicable. The MW-ST data point is the $V_{\text{occupancy}}$ value found for the Fe site in the '25 %' V-doped sample.

STEM and EDS analysis

To confirm the assumption made in the Rietveld analysis that the monoclinic Li₃M₂(PO₄)₃ phase consists of M = V rather than M = Fe, electron microscopy data were collected in conjunction with elemental analysis. As both M are possible, it would be difficult to distinguish whether M = Fe or V with XRD for the small impurity amounts present in the samples. M = V is expected because V³⁺ and Fe²⁺ should be stable under these heating conditions, rather than Fe³⁺, especially as no Fe³⁺

was discovered in the pristine MW-ST samples (Figure 3.8). However, to confirm this assumption, several samples were imaged by STEM with an EDS elemental mapping capability. Figure 4.4(a) shows a MW-LFVP-unheated nanorod and corresponding elemental dot maps for Fe, V, and P. It is clear that the V and Fe are evenly distributed along the nanorod imaged. Since the morphology of this sample includes nanorods as well as other shapes, a range of different particle sizes and shapes were imaged. Images of all particles yielded similar results, and no evidence of any V-rich or Fe-poor regions was found.

Figure 4.4(b) shows an STEM image of MW-LFVP-H₂-725-6h with corresponding elemental dot maps. It is clear that there are V-rich, Fe-poor particles present in this sample, indicating clear phase separation. This confirms that the Li₃M₂(PO₄)₃ impurity is likely Li₃V₂(PO₄)₃ with little Fe incorporated since the particle clearly shows both V and P but not Fe. Another interesting point is that there is still a significant amount of V in the Fe-rich particles indicating that they remain significantly doped, which agrees with the refinement results. STEM/EDS was also performed for MW-LFVP-H₂-525-6h (not shown in Figure 4.4), and no V-rich or Fe-poor particles were discovered. These microscopy results suggest that phase segregation to form Li₃V₂(PO₄)₃ only occurs above 500 °C in the MW-ST LFVP samples.

STEM/EDS was also performed on the CONV-LFVP-H₂-525-6h and CONV-LFVP-H₂-725-6h samples, as shown in Figure 4.5(a) and Figure 4.5(b), respectively. In both of these samples, there was clear evidence of V-rich particles and Fe-poor particles. This is in contrast to MW-LFVP-H₂-525-6h. Similar to the STEM/EDS shown in Figure 4.4 for MW-LFVP-H₂-725-6h, there is still a significant amount of V

in the Fe-rich particles (presumably the olivine structured phase). Clearly, at higher doping levels the conventional synthesis produces V-rich impurities at all temperatures, though some V remains in the olivine lattice.

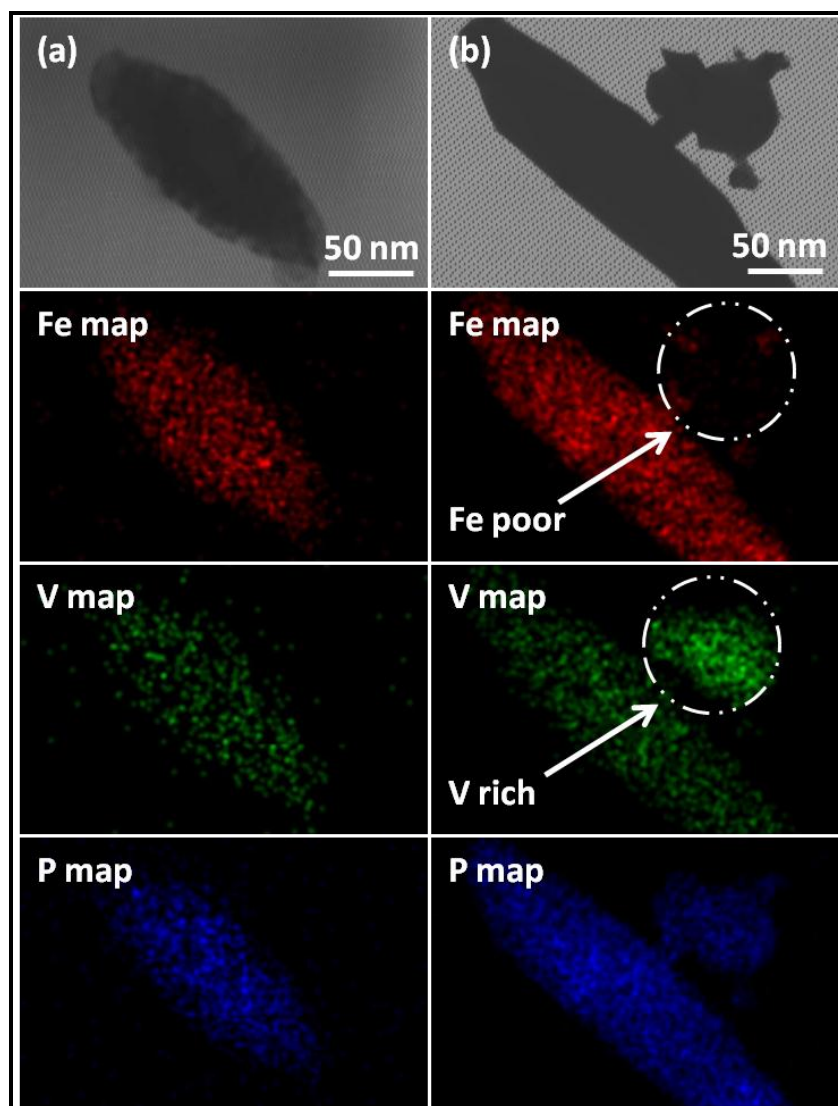


Figure 4.4. STEM images and corresponding elemental dot maps of (a) MW-LFVP-unheated and (b) MW-LFVP-H₂-725-6h. Note that (b) was obtained for a sample previously heated at 700 °C rather than 725 °C, but this is not anticipated to change the result.

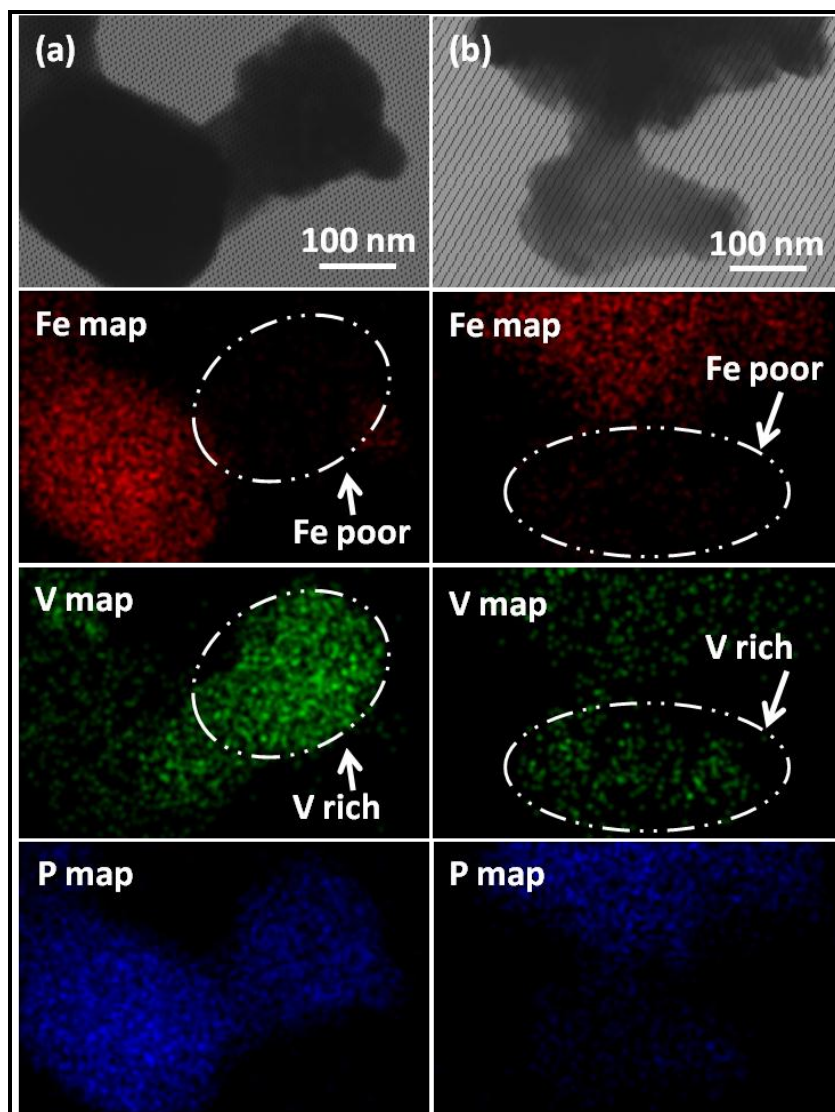


Figure 4.5. STEM images and corresponding elemental dot maps of (a) CONV-LFVP- H_2 -525-6h and (b) CONV-LFVP- H_2 -725-6h. Note that images were obtained for samples previously heated at 500 °C and 700 °C rather than 525 °C and 725 °C, but this is not anticipated to change the results.

Spectroscopic characterization

In addition to diffraction and imaging techniques, spectroscopy can also provide insight regarding the phases formed upon heating the samples. Figure 4.6 shows FTIR spectra for several samples. As discussed in greater detail in the previous

Chapter, the largest distinction between the spectra for the doped and undoped LiFePO_4 samples prepared by MW-ST is the shoulder at around 900 cm^{-1} , which agrees with the previously documented position of the V=O bond in LiVOPO_4 [101] and is outlined in a dashed-line pink box. Pink dashed-line boxes around the same location for the heated MW-ST V-doped samples show a decreasing shoulder in this location with increasing heating temperature. Since Raman spectroscopy showed no evidence of a vanadyl bond, this peak cannot correspond to V=O . However, it remains a noteworthy feature because it is present in the MW-ST doped samples, but not in MW-LFP-unheated or in the conventionally doped samples, which show no peak in the pink box region at any heating temperature.

The black dashed line boxes in Figure 4.6 indicate another feature that changes with V doping, related to P-O bonds. Sharp peaks for ν_3 P-O stretching modes [102, 103] are not distinct in the unheated V-doped samples, but these peaks return after heating at $625\text{ }^\circ\text{C}$ and $725\text{ }^\circ\text{C}$, albeit slightly broadened (black dashed line boxes). These peaks are present in the conventionally prepared V-doped samples, but are broader than in the pristine LiFePO_4 sample. Finally, it is also informative to compare the heated materials to pure $\text{Li}_3\text{V}_2(\text{PO}_4)_3$, while noting that the results were again similar for the samples heated in Ar and 5 % H_2 – 95% Ar. The spectra are roughly similar to that of MW-LFVP-unheated, but for some of the samples, there are extra peaks around 1220 cm^{-1} , outlined by a gray dashed-line box, as expected for $\text{Li}_3\text{V}_2(\text{PO}_4)_3$ [104]. Contrastingly, the 1220 cm^{-1} peaks are not present in the doped or undoped pristine MW-ST samples, or for the MW-LFVP- H_2 -525-6h and MW-LFVP- H_2 -625-6h samples. However, the peak is present for the MW-LFVP- H_2 -725-6h and all of the conventionally heated samples, which further confirms the presence of

$\text{Li}_3\text{V}_2(\text{PO}_4)_3$ impurities.

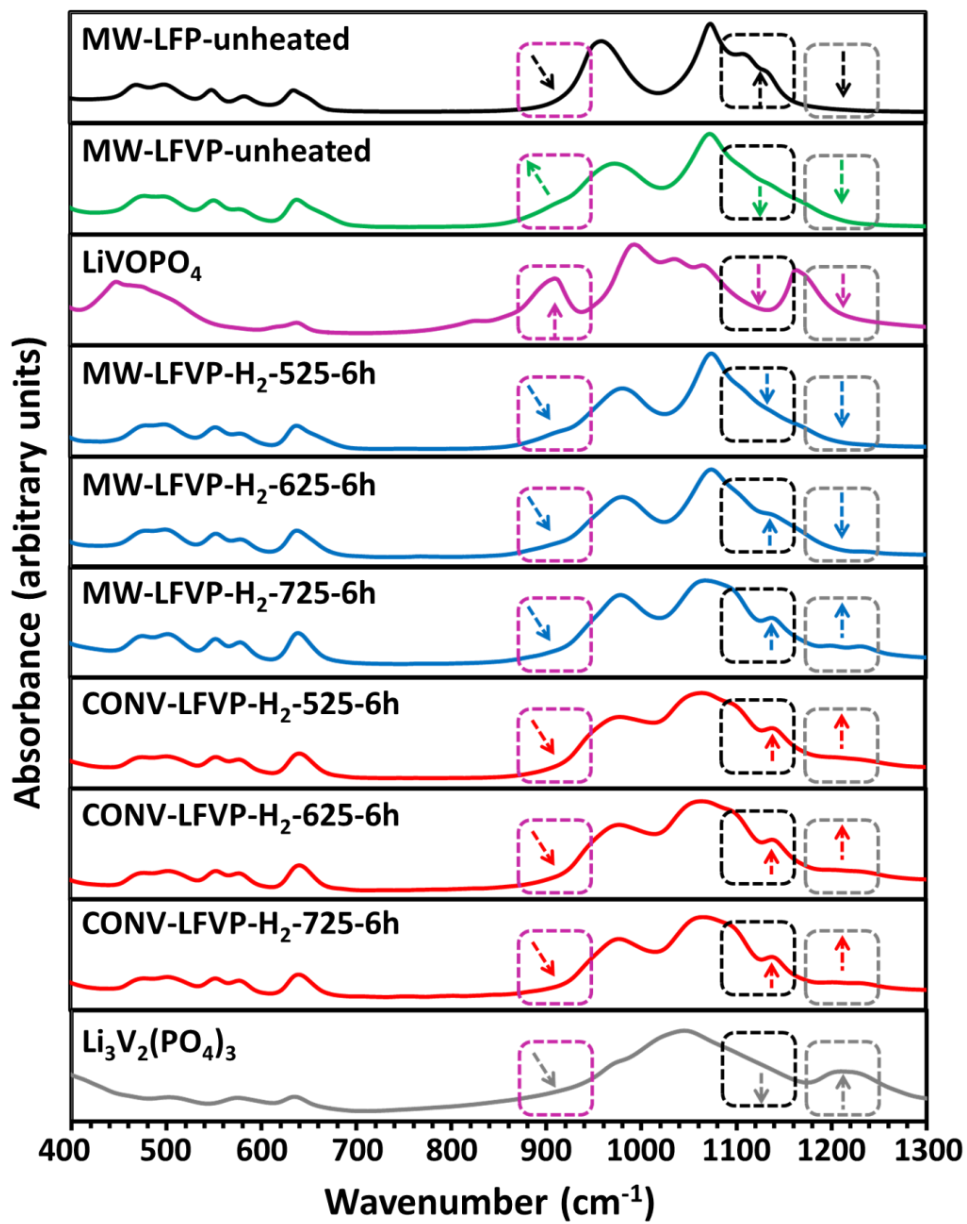


Figure 4.6. FTIR absorbance spectra for as-prepared and post-heated samples of undoped and V-doped LiFePO_4 , conventionally prepared V-doped LiFePO_4 , and reference compounds.

Electrochemical characterization

It is useful to examine electrochemical data for V-doped samples in consideration of the structural and compositional analysis that has been presented. Electrochemical data can be instructive in terms of understanding redox couples and for examining the presence of multiple phases. Figure 4.7 shows first charge-discharge curves for various samples in the voltage range from 1.5 - 4.8 V. Although it is common to test LiFePO_4 between limits of 2.0 – 4.3 V (which is shown in Figure 4.8 for reference), the range is expanded here to look for additional redox couples that could be assigned to different vanadium plateaus. As discussed in more detail in the previous Chapter, LiFePO_4 has little capacity in the 3.8 – 4.8 V and 1.5 – 2.5 V regions, but the 15 % V-doped LiFePO_4 sample has significant capacity in both of these regions that can be assigned to activity of the $\text{V}^{3+/4+}$ and $\text{V}^{2+/3+}$ couples, respectively, by comparison to the redox couples in $\text{Li}_3\text{V}_2(\text{PO}_4)_3$.

Further evidence of phase separation into LiFePO_4 and $\text{Li}_3\text{V}_2(\text{PO}_4)_3$ in the conventionally heated materials can also be established through electrochemical measurements due to the different redox energies of the Fe and V redox couples. After heating the MW-LFVP-pristine sample at 525 and 625 °C, the capacity between 3.8 and 4.8 V (corresponding to $\text{V}^{3+/4+}$) decreases slightly, but the capacity between 1.5 and 2.5 V (corresponding to $\text{V}^{2+/3+}$) decreases more significantly, as shown in Figure 4.7. This decrease is particularly obvious for the sample heated at 625 °C, indicating that the $\text{V}^{2+/3+}$ couple is no longer accessible in this sample.

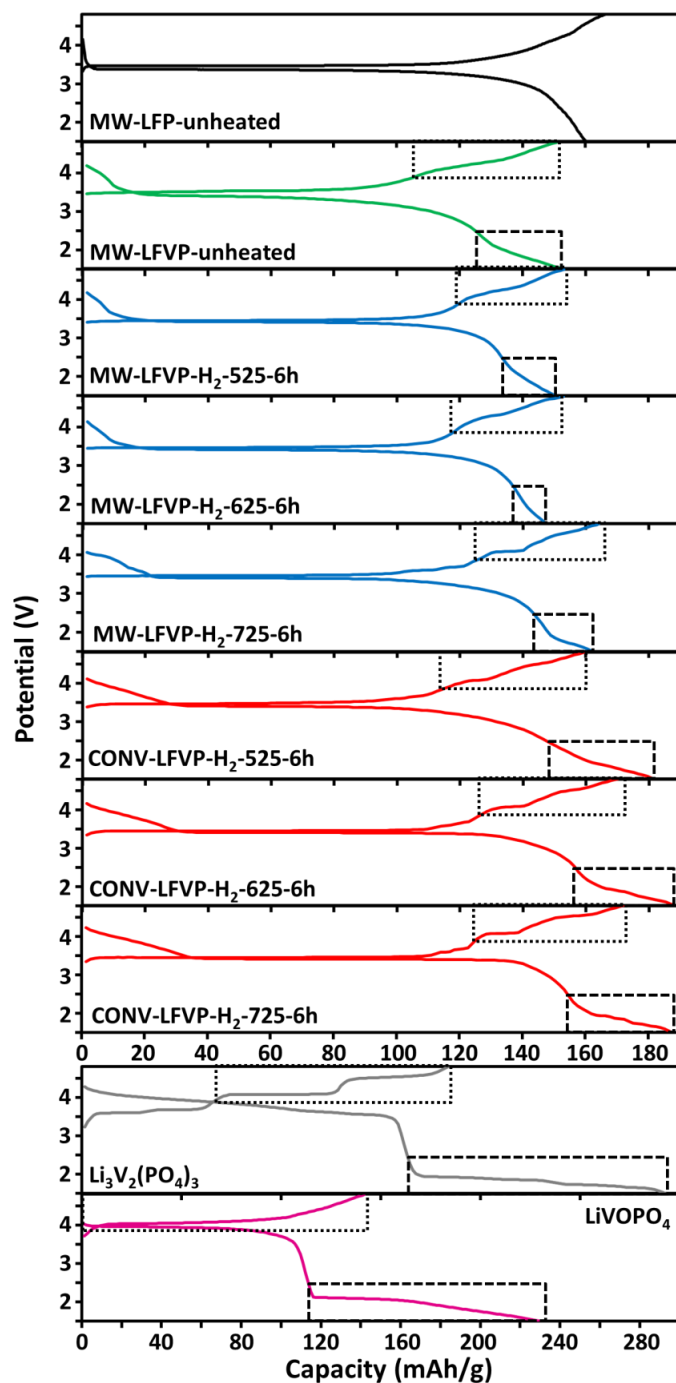


Figure 4.7. First charge-discharge curves at a C/10 rate for MW-ST LiFePO₄, heated and unheated MW-ST V-doped LiFePO₄ samples, conventionally prepared V-doped LiFePO₄ samples, as well as Li₃V₂(PO₄)₃ and LiVOPO₄ for a comparison.

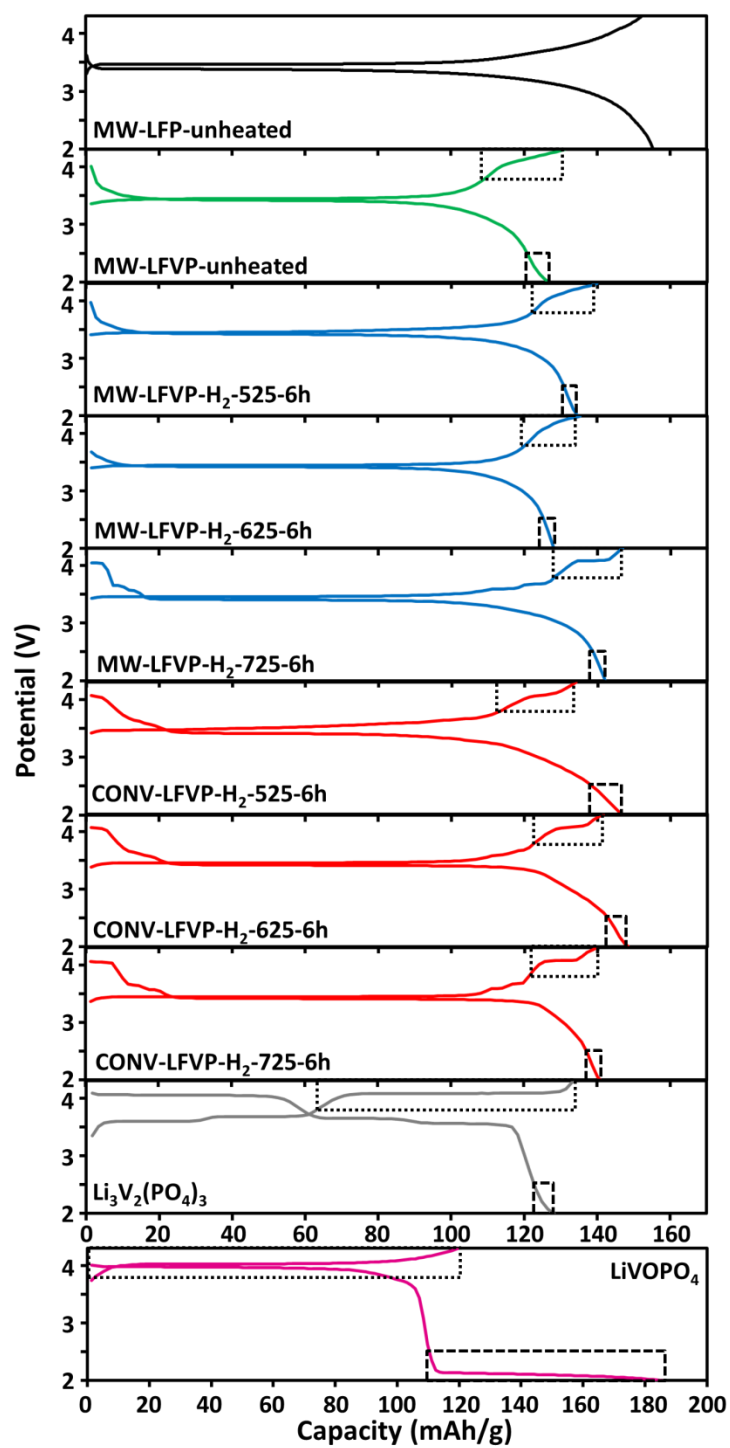


Figure 4.8. Charge-discharge data at a C/10 rate in the voltage range from 2.0 – 4.3 V, which is the typical range for LiFePO_4 .

Cyclic voltammetry (Figure 4.9) data show that small peaks arise in the 3.8 to 4.8 V region that were not present in the pristine sample, indicating that a small amount of a new phase has formed. Although the peaks in the MW-ST V-doped sample heated at 600 °C are shifted from the locations for the peaks in $\text{Li}_3\text{V}_2(\text{PO}_4)_3$, Figure 4.10 shows that (for the same sample heated at 600 °C) these peaks align well with $\text{Li}_3\text{V}_2(\text{PO}_4)_3$ when cycled from 2.0 – 4.3 V. Thus, even though $\text{Li}_3\text{V}_2(\text{PO}_4)_3$ was not detected by XRD or FTIR, it is likely that there is a small amount of $\text{Li}_3\text{V}_2(\text{PO}_4)_3$ in the MW-ST V-doped sample heated at 625 °C. The presence of this impurity is consistent with reduced V occupancy found through Rietveld refinement for this sample in Table 4.3.

Heating the pristine sample at 725 °C led to clear peaks in the CV (Figure 4.9) and a plateau around 4.6 V in the charge-discharge measurements that corresponds to $\text{V}^{4+/5+}$ in $\text{Li}_3\text{V}_2(\text{PO}_4)_3$ (Figure 4.7). Similarly, distinct peaks arise in the 1.5 – 2.5 V region corresponding to $\text{V}^{2+/3+}$ in $\text{Li}_3\text{V}_2(\text{PO}_4)_3$, as is expected since $\text{Li}_3\text{V}_2(\text{PO}_4)_3$ was detected by XRD and FTIR for this sample. There are also distinct fingerprint plateaus and peaks for $\text{Li}_3\text{V}_2(\text{PO}_4)_3$ in all of the conventionally heated samples, also in agreement with the XRD and FTIR measurements.

The capacities and CV peaks are higher for the conventionally prepared samples. The higher capacities exhibited by the conventionally prepared samples likely result because of carbon coating from the organic oxalate precursors used in the synthesis. The MW-ST samples are a light gray color with a pink tint. Contrastingly, the conventional materials are all dark gray in color, consistent with carbon coated samples.

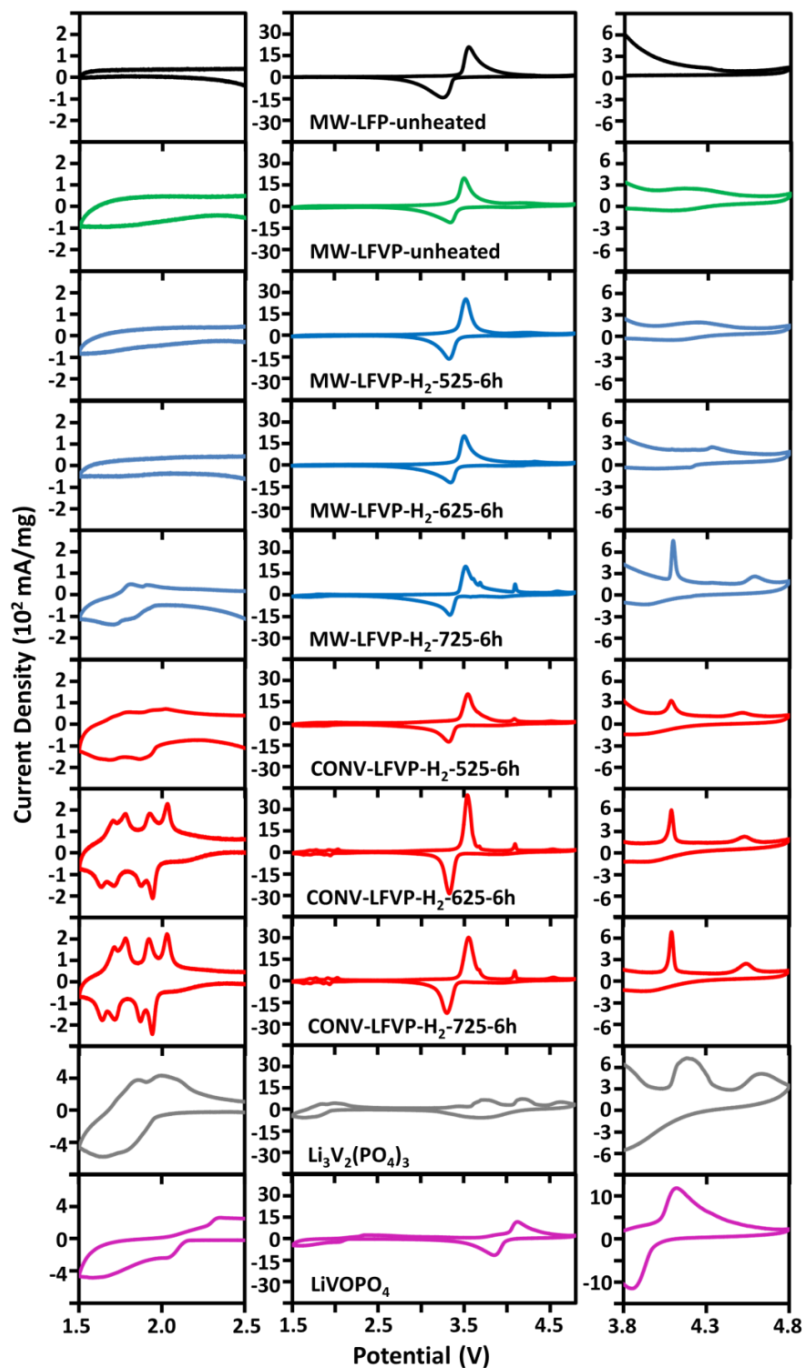


Figure 4.9. Second cycle CV data at a 0.1 mV/s rate for MW-ST LiFePO_4 , heated and unheated MW-ST V-doped LiFePO_4 samples, conventionally prepared V-doped LiFePO_4 samples, as well as $\text{Li}_3\text{V}_2(\text{PO}_4)_3$ and LiVOPO_4 for comparison.

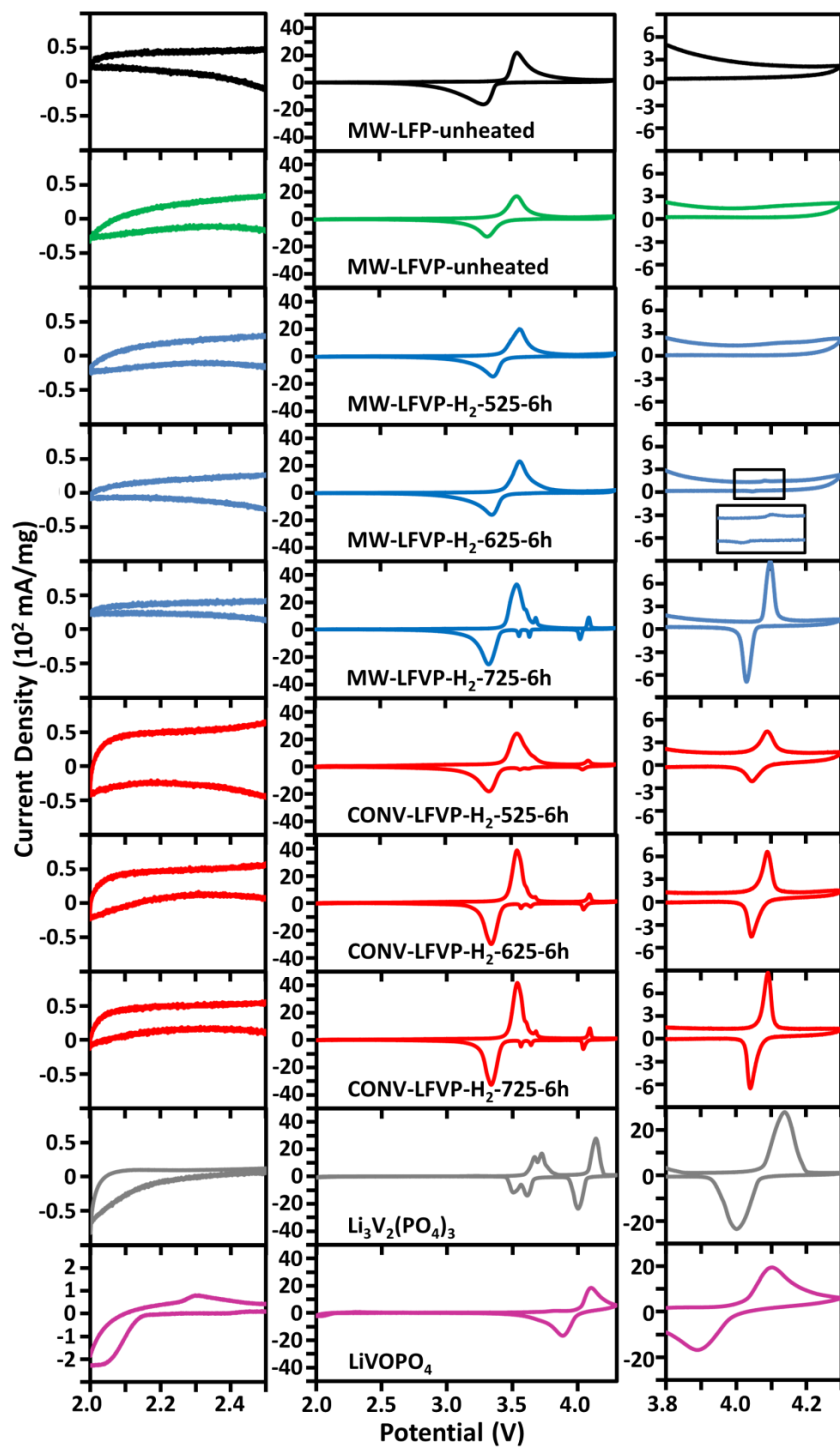


Figure 4.10. Second cycle CV data at a 0.1 mV/s rate in the voltage range of 2.0 - 4.3 V, which is a more typical range for LiFePO₄ than the range of 1.5 - 4.8 V.

It is worth mentioning that the capacities for the conventionally prepared samples are higher than the theoretical capacity of LiFePO_4 . However, since the theoretical capacity of $\text{Li}_3\text{V}_2(\text{PO}_4)_3$ is ~ 329 mAh/g when cycled in this range with 5 Li^+ inserted and extracted, even 5-10 % $\text{Li}_3\text{V}_2(\text{PO}_4)_3$ impurity could approximately account for this increased capacity. It also may be possible that some additional Li ions can be inserted into vacancies on the Fe site, as discussed in the previous Chapter, since the presence of Fe vacancies may allow Li^+ to access diffusion paths that are not possible in undoped LiFePO_4 [42, 95].

4.4 CONCLUSION

The metastability of V-doped LiFePO_4 samples prepared by a rapid, low-temperature microwave-assisted solvothermal synthesis method has been examined by heating the pristine 15 % V-doped LiFePO_4 in 100 % Ar and 5 % H_2 – 95 % Ar over a range of heating temperatures and times. Heating the samples led to clear $\text{Li}_3\text{V}_2(\text{PO}_4)_3$ impurities at 725 °C, but the samples were relatively stable at 525 °C and 625 °C. The limited stability of the samples heated at 525 and 625 °C was demonstrated by subtle changes in lattice parameters and vanadium occupancies determined through Rietveld refinement, FTIR spectra, and electrochemical measurements relative to the pristine microwave-synthesized V-doped LiFePO_4 sample. STEM/EDS data showed no evidence of $\text{Li}_3\text{V}_2(\text{PO}_4)_3$ for the sample heated at 525 °C or the pristine sample, but clear evidence of $\text{Li}_3\text{V}_2(\text{PO}_4)_3$ for the sample heated at 725 °C. Contrastingly, attempts to synthesize 15 % V-doped LiFePO_4 samples by a conventional method resulted in impurities at all temperatures. Therefore, the pristine MW-ST V-doped LiFePO_4 samples with > 10 % doping are metastable phases only accessible at low temperature, which exhibit moderate kinetic stability up to 625 °C.

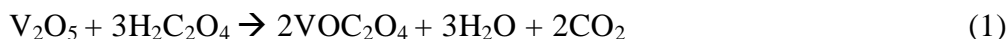
Chapter 5: Microwave-assisted Solvothermal Synthesis and Characterization of Various Polymorphs of LiVOPO₄ Cathodes

5.1 INTRODUCTION

Recently, the Manthiram group has shown the ability to tune particle size and obtain useful particle morphologies for LiFePO₄ with microwave-assisted hydrothermal and solvothermal (in tetraethylene glycol) synthesis methods [29-33]. LiVOPO₄ is a cathode material with higher energy density than LiFePO₄ due to its 4.1 V redox plateau, but similar limitations in ionic and electronic conductivity. The electrochemical performances of the three LiVOPO₄ polymorphs vary widely with different synthesis methods. Since particle size and morphology can greatly influence the electrochemical performance of LiVOPO₄ as in the case of LiFePO₄ [61, 62], it is of interest to develop a microwave-assisted synthesis method for LiVOPO₄ in an attempt to control the particle size and morphology by varying synthesis parameters. Here MW-ST methods are presented for the first time to synthesize all three phases of LiVOPO₄ under various conditions. The triclinic polymorph (α -LiVOPO₄) formed with the most stoichiometric elemental ratios, so this work focuses on optimizing the electrochemical performance of the triclinic phase. The orthorhombic (β -LiVOPO₄) and tetragonal (α_1 -LiVOPO₄) polymorphs will be further optimized in the future.

5.2 EXPERIMENTAL

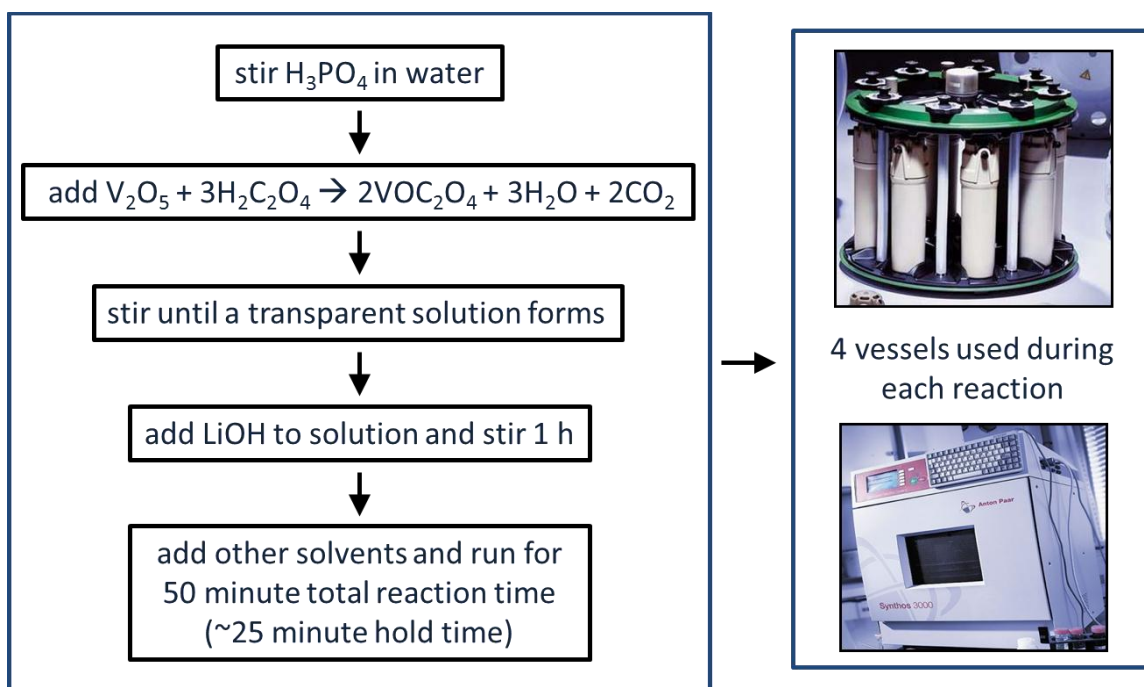
Various ratios of vanadium (V) oxide (Alfa Aesar), oxalic acid (Fisher), and phosphoric acid (Fisher) precursors were dissolved in water and stirred overnight until the solutions were transparent. Oxalic acid was added according to reaction (1):



Then lithium hydroxide monohydrate (Fisher) was added and the solutions were

stirred for an additional hour. In some syntheses, various amounts of alcohols (methanol, ethanol, isopropanol, butanol, octanol, tetraethylene glycol (TEG), and polyethylene glycol (PEG)) were added just before transferring the solutions to 100 mL polytetrafluoroethylene (PTFE) microwave reaction vessels. The total amount of solution was always 15 mL and the concentration was kept at 0.067 M in V unless otherwise noted. These vessels were inserted into ceramic liners and sealed such that autogenous pressure could be generated during the reaction. These vessels were secured on a rotor, which was placed on a turntable in a microwave reaction system (Anton Paar Synthos 3000). To ensure uniform microwave heating and reaction mixing, each vessel was equipped with a stir bar and the turntable was spun during synthesis. Four vessels were always used in a given synthesis run, and the power during the temperature ramp time was set to 600 W. The temperature and pressure of each vessel was monitored during the reactions.

In order to screen many different combinations of reaction conditions quickly, four different solutions were run simultaneously with a maximum pressure set to 40 bar and the total reaction time set to 50 min. This included approximately 25 min ramping time to the final temperature. The ratios of precursors and solvents were varied to test many different conditions, as will be subsequently discussed. After each synthesis run, the microwave convectively cooled the vessels to 50 °C. The precipitates were washed with water and acetone and centrifuged several times. The products were then dried overnight in a vacuum oven at 150 °C. The α -LiVOPO₄ and α_1 -LiVOPO₄ polymorphs were green in color and the β -LiVOPO₄ polymorph was brown. A schematic of the synthesis process is depicted in Schematic 5.1 for a representative synthesis condition leading to the α -LiVOPO₄ polymorph.



Schematic 5.1. Schematic summarizing the typical synthesis conditions for α -LiVOPO₄.

5.3 RESULTS AND DISCUSSION

Synthesis of LiVOPO₄ polymorphs

Conventional hydrothermal methods have been demonstrated in the literature for synthesizing all three polymorphs of LiVOPO₄; thus, it seemed likely that microwave-assisted hydrothermal methods for LiVOPO₄ could be developed. The conventional hydrothermal method for β -LiVOPO₄ consists of a Li:V:P = 1:1:3.3 mixture of precursors heated at 450 °C for 7 days [68]. The hydrothermal method in the literature for synthesizing α -LiVOPO₄ consists of a Li:V:P mixture of 9:3:1 heated at 250 °C for 48 h with the addition of N₂H₄·H₂O as a reducing agent [70]. The α_1 polymorph of LiVOPO₄ has been synthesized by a two-step process. First, LiVOPO₄·2H₂O was synthesized by a conventional hydrothermal process at 120 °C for 48 h with stoichiometric precursors and oxalic acid as a reducing agent. The hydrothermal step was followed by dehydration at

300 °C under vacuum [65]. Since the existing methods indicate that sometimes non-stoichiometric ratios of precursors are required to obtain LiVOPO_4 , synthesis attempts were made with stoichiometric precursors, excess P, excess Li, and both excess P and excess Li.

The effectiveness of the volumetric dielectric and ohmic heating employed during a microwave reaction is dependent on the dissolved species in solution, so adjustment of the precursor ratios causes significantly varying temperature and pressure relationships during the reactions. It is difficult to predict the maximum possible temperature that can be reached before actually running a reaction. On account of this difficulty and the desire to test many different reaction conditions, initial experiments to screen for promising conditions were all performed with a maximum pressure set to 40 bar rather than with a maximum temperature. The maximum temperature reached typically varied between 215 and 235 °C for these reactions with the exception of one sample that only achieved 180 °C. Under these conditions, no LiVOPO_4 polymorphs formed, as shown in the first column of Table 5.1. The temperature was increased to 250 °C for the reactions with the same precursor ratios used in the conventional hydrothermal methods [65, 68, 70], but LiVOPO_4 still did not form (although the precursors were not all exactly the same as in the conventional hydrothermal reactions).

Because obtaining LiVOPO_4 in water did not appear promising from initial results, the solvent was varied. V_2O_5 does not dissolve in alcohols easily even with the addition of oxalic acid, so water and ethanol were mixed in 3:1, 1:1, and 1:3 ratios, and microwave reactions were performed for the various precursor ratios with a maximum pressure of 40 bar. The results are outlined in Table 5.1, which shows the dominant phase that formed (impurities also formed) during each reaction. The maximum temperature

reached in these reactions was between 200 and 225 °C. In contrast to the reactions run in water, which led to no LiVOPO₄ formation at 40 bar, many different conditions in the mixed solvent reactions produced LiVOPO₄, and the products formed at lower temperatures.

Table 5.1. Dominant products from MW-ST synthesis in water or mixed water and ethanol solvent with various ratios of Li:V:P. All reactions were run to a maximum pressure of 40 bar for a total reaction time of 50 minutes with a V concentration of 0.067 M.

water : ethanol	1:0	3:1	1:1	1:3
Li:V:P = 1:1:1	amorphous	no precipitate	amorphous	β + α_1 -LiVOPO ₄
Li:V:P = 1:1:2	VPO ₄ ·H ₂ O	HVOPO ₄ ·0.5H ₂ O	HVOPO ₄ ·0.5H ₂ O	β -LiVOPO ₄
Li:V:P = 1:1:3	HVOPO ₄ ·0.5H ₂ O	HVOPO ₄ ·0.5H ₂ O	HVOPO ₄ ·0.5H ₂ O + α -LiVOPO ₄	β -LiVOPO ₄
Li:V:P = 1:1:4	HVOPO ₄ ·0.5H ₂ O	HVOPO ₄ ·0.5H ₂ O	HVOPO ₄ ·0.5H ₂ O	β -LiVOPO ₄
Li:V:P = 2:1:1	no precipitate	amorphous	α_1 -LiVOPO ₄	Li ₃ PO ₄
Li:V:P = 3:1:1	Li ₃ PO ₄	no precipitate	Li ₃ PO ₄	Li ₃ PO ₄
Li:V:P = 4:1:1	Li ₃ PO ₄	Li ₃ PO ₄	Li ₃ PO ₄	Li ₃ PO ₄
Li:V:P = 5:1:1	Li ₃ PO ₄	Li ₃ PO ₄	Li ₃ PO ₄	Li ₃ PO ₄
Li:V:P = 2:1:2	amorphous	amorphous	α -LiVOPO ₄	unknown
Li:V:P = 3:1:3	no precipitate	α_1 -LiVOPO ₄	α -LiVOPO ₄	unknown
Li:V:P = 4:1:4	unknown	α_1 -LiVOPO ₄	α -LiVOPO ₄	unknown
Li:V:P = 5:1:5	amorphous	α_1 -LiVOPO ₄	α -LiVOPO ₄	Li ₃ PO ₄
Li:V:P = 4:1:3	no precipitate	Li ₃ PO ₄	α -LiVOPO ₄	Li ₃ PO ₄
Li:V:P = 6:1:3	Li ₃ PO ₄	Li ₃ PO ₄	HVOPO ₄ ·0.5H ₂ O	Li ₃ PO ₄
Li:V:P = 9:1:3	Li ₃ PO ₄	Li ₃ PO ₄	Li ₃ PO ₄	Li ₃ PO ₄
Li:V:P = 12:1:3	Li ₃ VO ₄	Li ₃ PO ₄	HVOPO ₄ ·0.5H ₂ O	Li ₃ PO ₄
Li:V:P = 3:1:2	no precipitate	Li ₃ PO ₄	α -LiVOPO ₄	Li ₃ PO ₄
Li:V:P = 4:1:2	Li ₃ PO ₄	Li ₃ PO ₄	Li ₃ PO ₄	Li ₃ PO ₄
Li:V:P = 5:1:2	Li ₃ PO ₄	Li ₃ PO ₄	Li ₃ PO ₄	Li ₃ PO ₄
Li:V:P = 6:1:2	Li ₃ PO ₄	Li ₃ PO ₄	Li ₃ PO ₄	Li ₃ PO ₄

Since impurities also formed for the reactions summarized in Table 5.1, the reaction conditions (temperature and precursor ratios) had to be further varied to obtain

more phase-pure materials. Figure 5.1 shows XRD patterns for the resulting materials. The synthesis conditions and elemental ratios determined by ICP are shown in the insets of the XRD patterns. It is clear that only the α phase gives stoichiometric elemental ratios. Patterns for the α_1 and α polymorphs show no impurities, but the peak intensity ratios for the α_1 polymorph are different than expected. Specifically, the peak at 20 degrees has a lower intensity than is typically observed. The varied peak intensity could be due to defects, since the ICP data indicate something of the form $\text{Li}_{1.16}(\text{VO})_{0.91}\text{PO}_4$, which is approximately charge balanced assuming all V^{4+} , but the deviations from the expected stoichiometry could also indicate amorphous impurities.

The β polymorph also showed unexpected peak intensity ratios in addition to lithium deficiency and some slight impurities, including a small amount of α - LiVOPO_4 . Conversely, the α polymorph is phase pure, stoichiometric, and shows no obvious peak intensity ratio variations from the expected patterns. Lattice parameters found from Rietveld refinement of the three polymorphs are presented in Table 5.2. The lattice parameters for the α - LiVOPO_4 polymorph agree well with the literature values [75], and the refinement fit is very good. The fit was worse for the β - LiVOPO_4 and α_1 - LiVOPO_4 polymorphs, which is not surprising because of the non-stoichiometry of the samples. The unit cell volumes were larger than some literature values for both the β - LiVOPO_4 and α_1 - LiVOPO_4 polymorphs, although there is a fairly large range [68, 58].

Table 5.2. *Lattice parameters for LiVOPO_4 determined by Rietveld refinement.*

Polymorph	a (Å)	b (Å)	c (Å)	α	β	γ	V (Å ³)	χ^2
α	6.7872(3)	7.2153(3)	7.8857(3)	89.902(2)	88.575(2)	62.835(3)	343.45(2)	1.42
α_1	6.3166(8)	6.3166(8)	4.4337(4)	90	90	90	176.90(4)	5.19
β	7.467(2)	6.338(2)	7.172(2)	90	90	90	339.38(15)	5.25

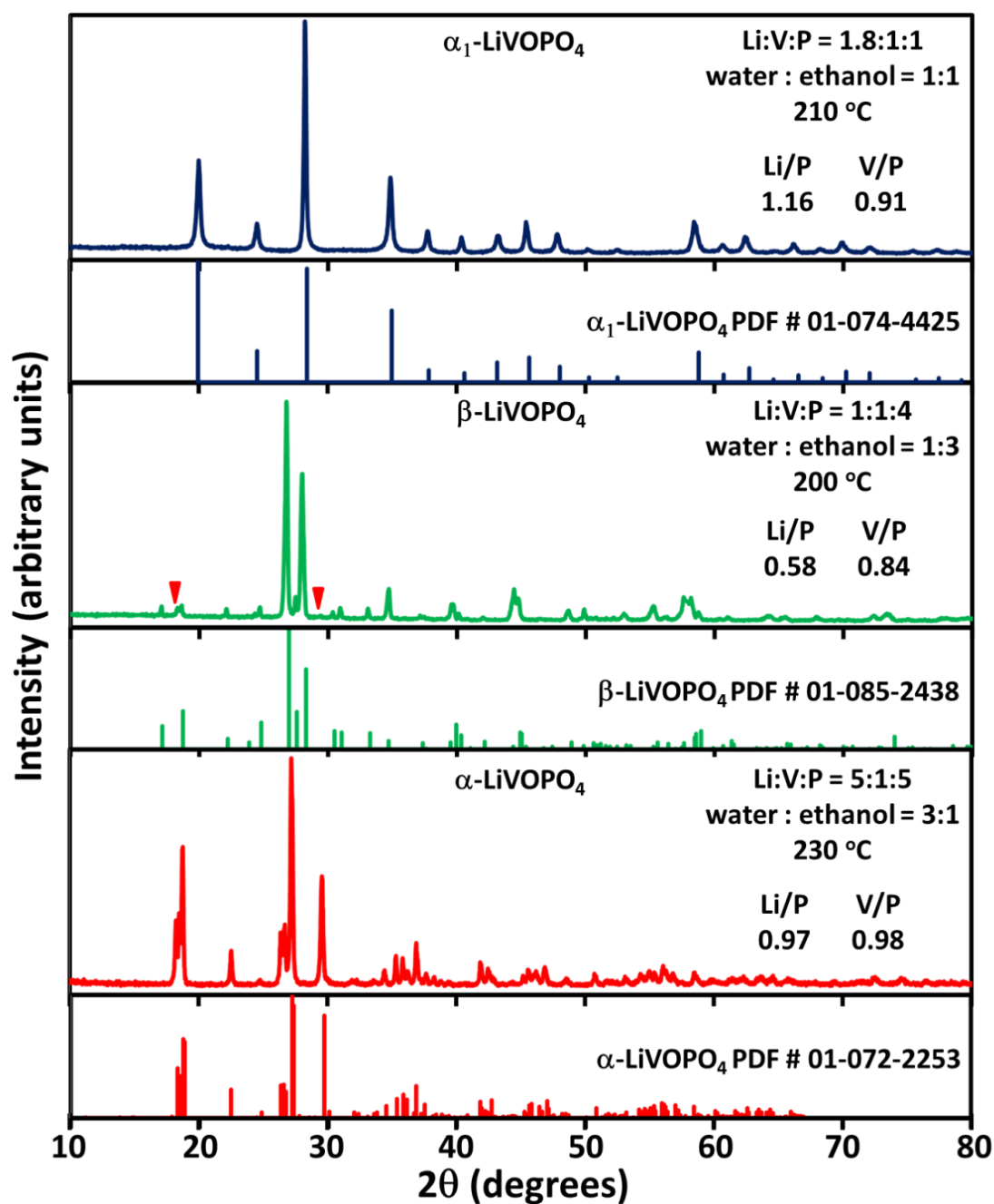


Figure 5.1. XRD patterns for the three polymorphs of LiVOPO_4 compared to the database patterns [58, 68, 75]. All three syntheses were run for a total reaction time of 50 minutes (~ 25 min hold time) with a concentration of 0.067 M in V. Slight impurities for $\beta\text{-LiVOPO}_4$ are indicated with red arrows.

When varying the temperatures in an attempt to obtain phase pure polymorphs, it was common for the other phases to transition into the triclinic phase as the temperature and pressure was increased, which indicates that the other phases form as intermediates and may be metastable under these reaction conditions. Several examples that show the transition to the triclinic polymorph with increasing temperature are shown in Table 5.3. Because the triclinic phase was the easiest to synthesize and formed the most stoichiometric product, it was selected for further optimization.

Table 5.3. *Examples of transition to α polymorph with increased pressure (which equates to increased temperature). All tests were run to a maximum of either 40 or 50 bar with a V concentration of 0.067 M.*

precursor ratio	water : ethanol ratio	dominant product at 40 bar	dominant product at 50 bar
Li:V:P = 1:1:1	1 : 3	β -LiVOPO ₄ + α_1 -LiVOPO ₄	α_1 -LiVOPO ₄
Li:V:P = 1:1:2	1 : 3	β -LiVOPO ₄	α -LiVOPO ₄
Li:V:P = 1:1:3	1 : 3	β -LiVOPO ₄	β -LiVOPO ₄ + α -LiVOPO ₄
Li:V:P = 1:1:4	1 : 3	β -LiVOPO ₄	β -LiVOPO ₄ + α -LiVOPO ₄
Li:V:P = 5:1:5	3 : 1	α_1 -LiVOPO ₄	α -LiVOPO ₄
Li:V:P = 5:1:5	1 : 3	Li ₃ PO ₄	α -LiVOPO ₄

FTIR was also used to characterize the α -LiVOPO₄ sample, as shown in Figure 5.2. The spectrum matches the literature well with no detectable impurities [74, 101], further confirming the phase purity of the sample. The ν_1 and ν_3 peaks arise from symmetric and asymmetric bending vibrations of the PO₄ tetrahedra, respectively, and the ν_2 and ν_4 peaks arise from bending vibrations of PO₄.

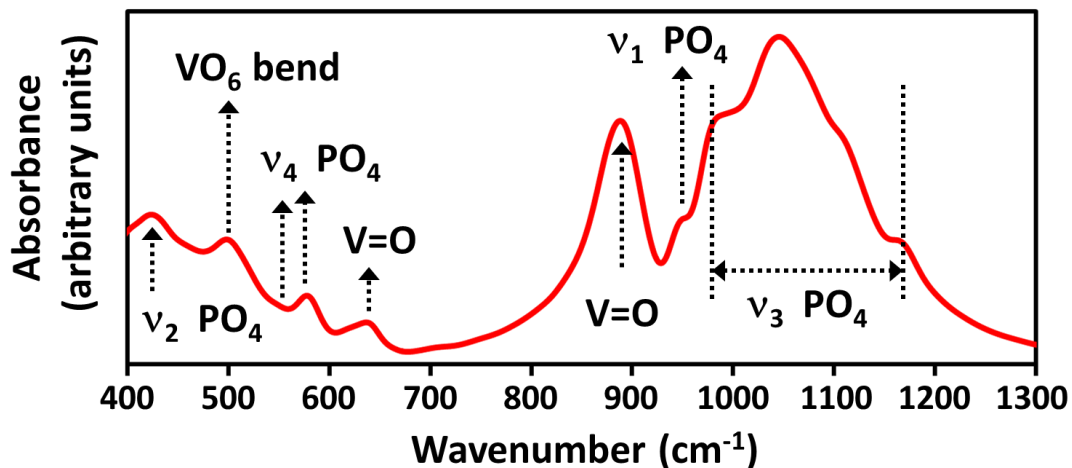


Figure 5.2. FTIR absorbance spectrum for α -LiVOPO₄ synthesized at 230 °C with a *V* concentration of 0.067 M and a total reaction time of 50 min.

Effects of the solvent

Because a maximum pressure was used as the limit in the initial reactions, the temperatures were not constant for all of the samples. Phase-pure α -LiVOPO₄ was synthesized at 230 °C in 3:1 water:ethanol, so it was of interest to determine whether a phase-pure material could be synthesized in the other solvent mixtures at the same temperature and with the same precursor ratio. The reactions in pure water, 1:1 water:ethanol, and 1:3 water:ethanol were repeated at 230 °C with Li:V:P = 5:1:5 to see how critical the solvent mixture was to obtain the pure phase; the XRD results are shown in Figure 5.3.

It is clear that impurities form for all conditions except the 3:1 mixture of water:ethanol, so the ratio of ethanol to water is critical. It was possible to obtain phase-pure α -LiVOPO₄ with 100 % water as the solvent and Li:V:P = 5:1:5, but the temperature had to be elevated to 240 °C. ICP data for the sample synthesized in water at

240 °C revealed nearly stoichiometric elemental ratios, as shown in the inset on the XRD pattern.

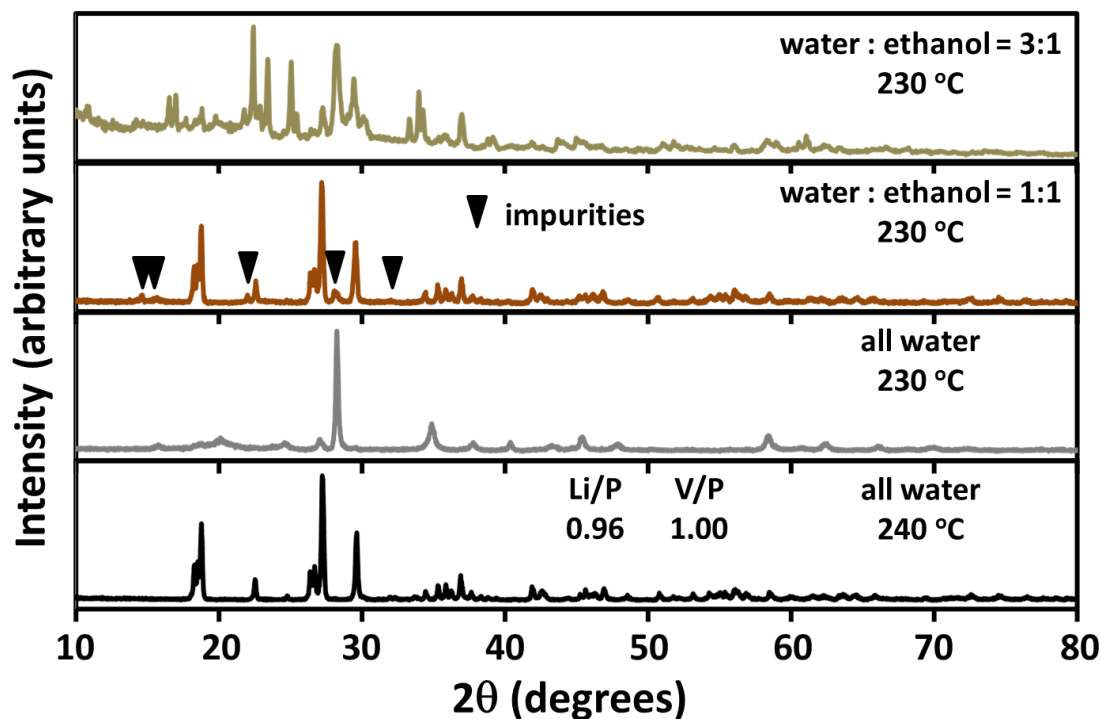


Figure 5.3. XRD of α -LiVOPO₄ synthesized with a V concentration of 0.067 M for a 50 min total reaction time and Li:V:P = 5:1:5 in various solvent mixtures.

Because α -LiVOPO₄ could be synthesized in mixtures of ethanol and water, it seemed reasonable that it may also be synthesized in other alcohols. To see whether the alcohol had an effect on the products, α -LiVOPO₄ was synthesized at 230 °C with Li:V:P = 5:1:5 and 3:1 mixtures of water and methanol, ethanol, isopropanol, butanol, octanol, PEG, or TEG. The XRD patterns are shown in Figure 5.4 for the products resulting from each of these solvent mixtures. Single-phase α -LiVOPO₄ formed for all of these samples, except for the samples synthesized in mixtures of water with octanol and methanol.

Synthesis in a mixture octanol and water did not lead to a decipherable phase, and synthesis in methanol and water mixture led to just a slight impurity. Elemental ratios for the samples which formed pure or nearly pure phases are indicated in the insets of the XRD patterns. The samples generally showed close to stoichiometric elemental ratios, with slight Li deficiency in some of the samples.

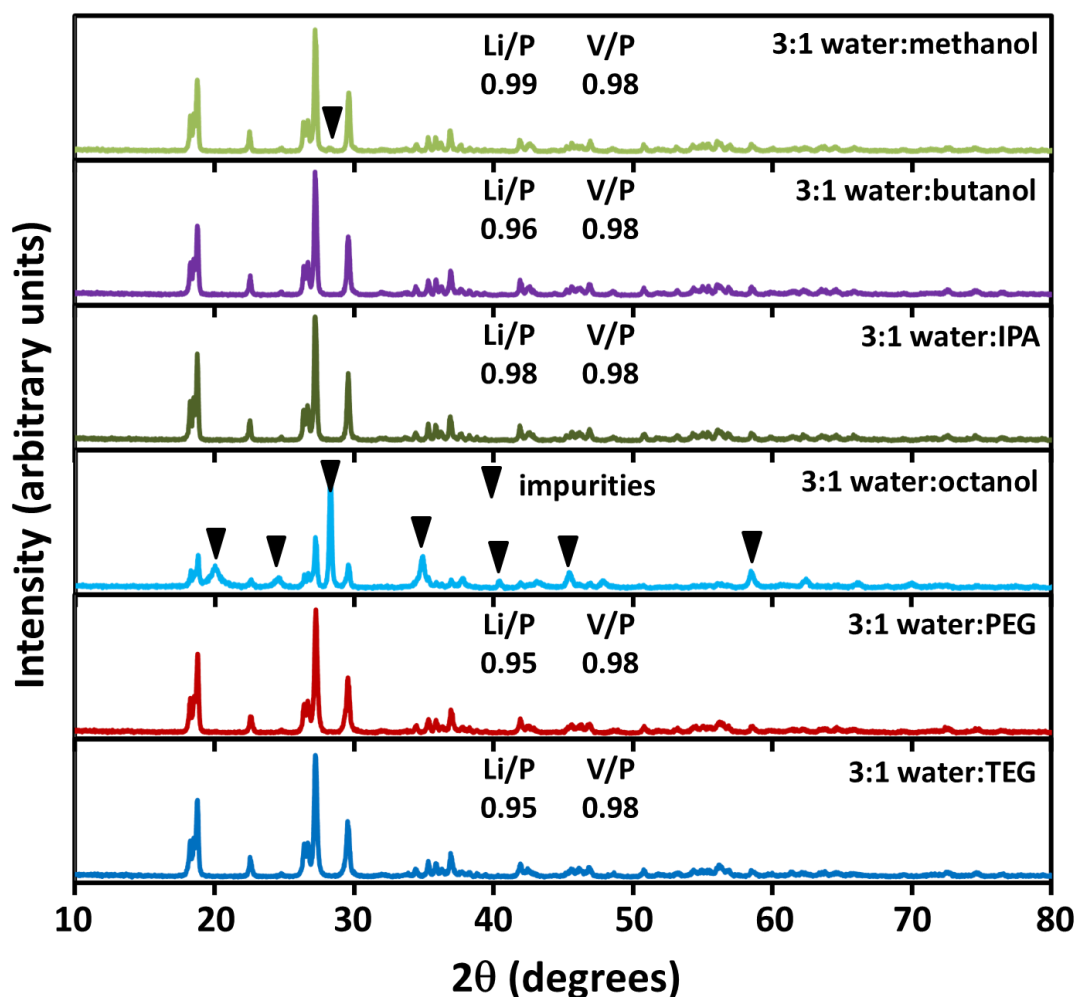


Figure 5.4. XRD of α -LiVOPO₄ synthesized at 230 °C with a V concentration of 0.067 M for a 50 min total reaction time (~25 min hold time) and Li:V:P = 5:1:5 in various solvent mixtures.

SEM images for the materials synthesized in various water and alcohol mixtures are shown in Figure 5.5. The materials form into microflower-like morphologies with similar sizes for most of the simple alcohols. The samples synthesized in 3:1 mixtures of water : butanol, water : PEG, or water : TEG showed smaller particle sizes. The smallest and most uniform particles were synthesized in mixtures of water and PEG.

To determine the effect of the solvent on the electrochemical performance, coin cells were fabricated, and the performance at C/20 is shown in Figure 5.6. The highest capacities are achieved for mixtures of water with the two glycols. This correlates well with the smaller particle sizes (Figure 5.5) obtained during synthesis. Small particle size has been previously demonstrated as a means to improve electrochemical performance for LiVOPO_4 due to its poor conductivity [61, 62]. The sample synthesized in butanol and water also showed slightly higher performance, but much lower still than the samples synthesized in the glycols, despite similar particle size. Therefore, it is likely that the glycols may have an effect beyond simply particle size control.

The glycols are very reducing, which could be useful since it is necessary to keep V in the V^{4+} state. However, the ICP ratios shown in Figure 5.4 indicate slight lithium deficiency for the samples synthesized in water and glycol mixtures. Lithium deficiency suggests that there may be a small amount of V^{5+} in the samples to maintain charge balance, but this is clearly inconsistent with the glycols being good reducing agents. Therefore, it is unclear how to rationalize these observations that the samples with lithium deficiency exhibited the highest capacities. Note also that the sample synthesized in pure water showed lower capacity than any of the samples prepared in the mixed solvents despite similar particle size and the higher reaction temperatures used.

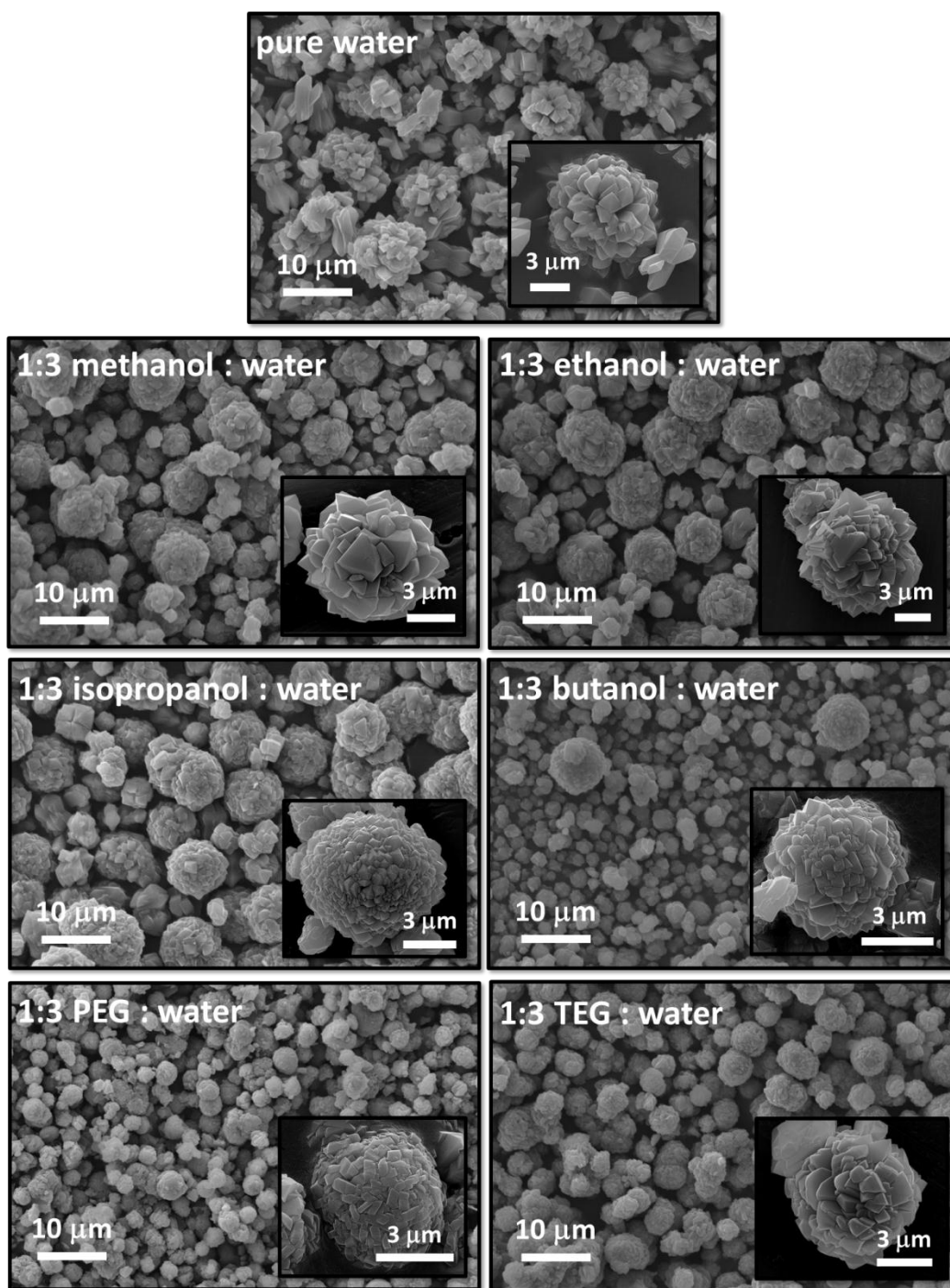


Figure 5.5. SEM images of α -LiVOPO₄ synthesized at 230 °C with a V concentration of 0.067 M for a 50 min total reaction time (~ 25 min hold time) in various solvents.

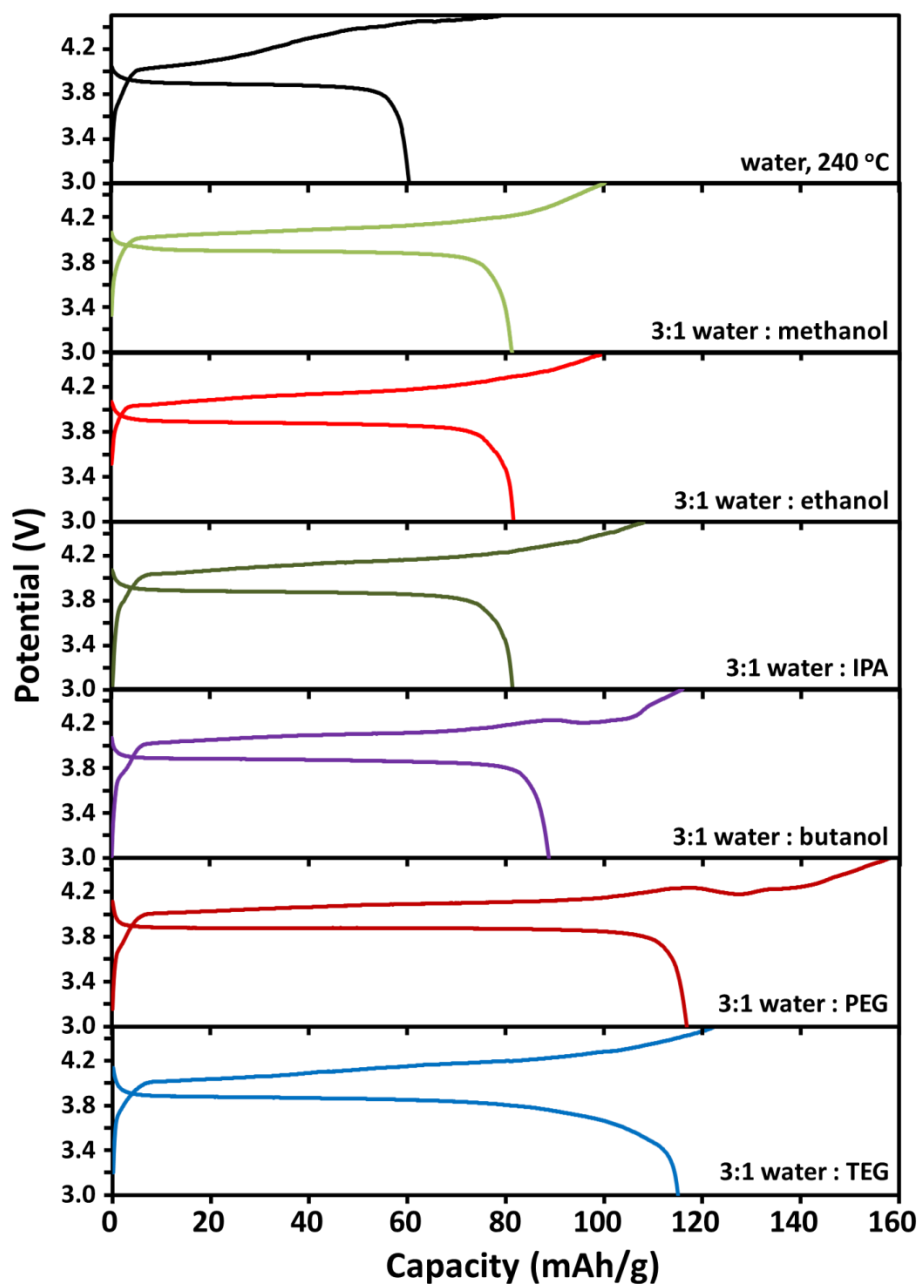


Figure 5.6. First charge-discharge curves at 3.0 - 4.5 V with a C/20 rate for α - LiVPO_4 synthesized. All solutions contained a V concentration of 0.067 M for a 50 min total reaction time in different solvents. All samples were prepared at 230 °C except for the sample prepared in water, which was held at 240 °C.

It has been suggested in the literature that a second Li can be inserted into LiVOPO_4 to form Li_2VOPO_4 [60, 112-119]. The second Li ion insertion occurs between 2.0 and 2.5 V and increases the theoretical capacity to 318 mAh/g, though this extra capacity is not generally fully realized. First charge-discharge curves are shown in Figure 5.7 for the voltage range of 2 – 4.5 V to allow access to the $\text{V}^{3+/4+}$ couple corresponding to the second lithium insertion/extraction. Although there are large differences in capacity in the range between 3 – 4.5 V, the differences are not as large in the range from 2 – 4.5 V. Furthermore, high capacity in the 3 - 4.5 V range did not necessarily correlate to high capacity in the 2 – 4.5 V range. For example, the sample synthesized in pure water showed the lowest capacity for the $\text{V}^{4+/5+}$ couple at ~ 4 V (~ 60 mAh/g), but showed the highest capacity for the $\text{V}^{3+/4+}$ couple at ~ 2 V (~ 135 mAh/g). Similarly, the samples prepared in glycols and water showed high capacity at ~ 4 V (~ 120 mAh/g), but showed relatively low capacity at ~ 2 V (~ 90 mAh/g). The capacities in the 2 – 4.5 V range also did not show a strong correlation to the particle size.

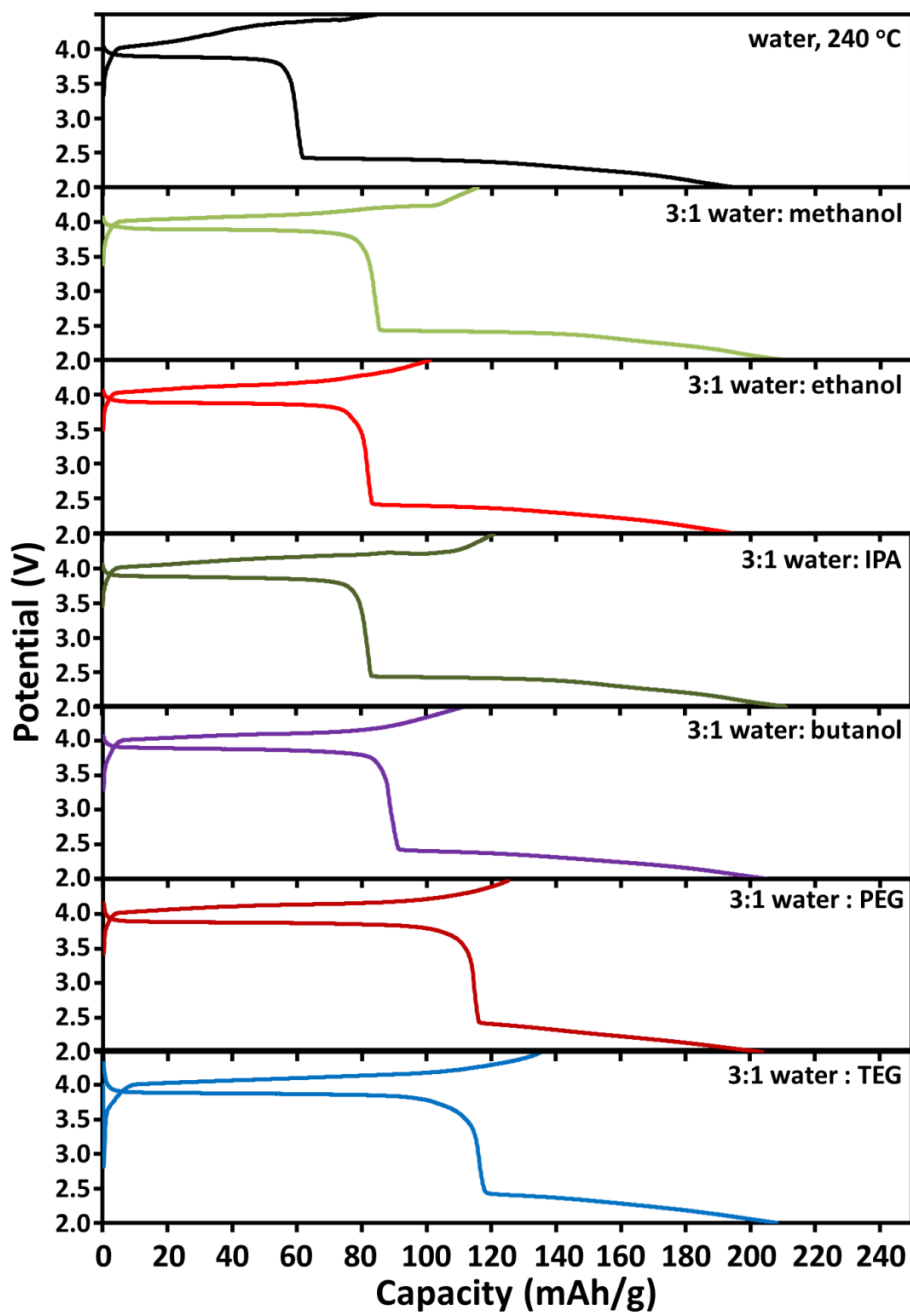


Figure 5.7. First charge-discharge curves at 2.0 - 4.5 V with a C/20 rate for α -LiVPO₄ synthesized. All solutions contained a V concentration of 0.067 M for a 50 min total reaction time in different solvents. All samples were prepared at 230 °C except for the sample prepared in water, which was held at 240 °C.

Optimization of particle size

Initially, a very long hold time (~ 25 min) was used to ensure that products would form (50 min total reaction time with a 25 min ramp time), but the long hold time led to large particles, which contributes to poor capacities. Therefore, the hold time was varied from 5 to 45 min for the sample synthesized in water and ethanol to determine the effect of reaction time on particle growth and electrochemical performance. A hold time of at least ten minutes was necessary to obtain pure phase α -LiVOPO₄. The particle size was found to decrease with decreasing reaction time as indicated in Figure 5.8, and the particle size correlated inversely with improved electrochemical performance (Figure 5.9 and Figure 5.10).

Decreasing the precursor concentration also decreased particle size and improved electrochemical performance for constant reaction time, as has been previously demonstrated for microwave synthesized LiFePO₄ [32]. However, the performance improvement was very modest for the sample prepared with lower precursor concentration. The concentration may need to be decreased further to see a more appreciable effect, but attempts to decrease the concentration to significantly lower values led to amorphous products. Furthermore, it is preferable to control particle size with reaction time rather than concentration to maximize product yield.

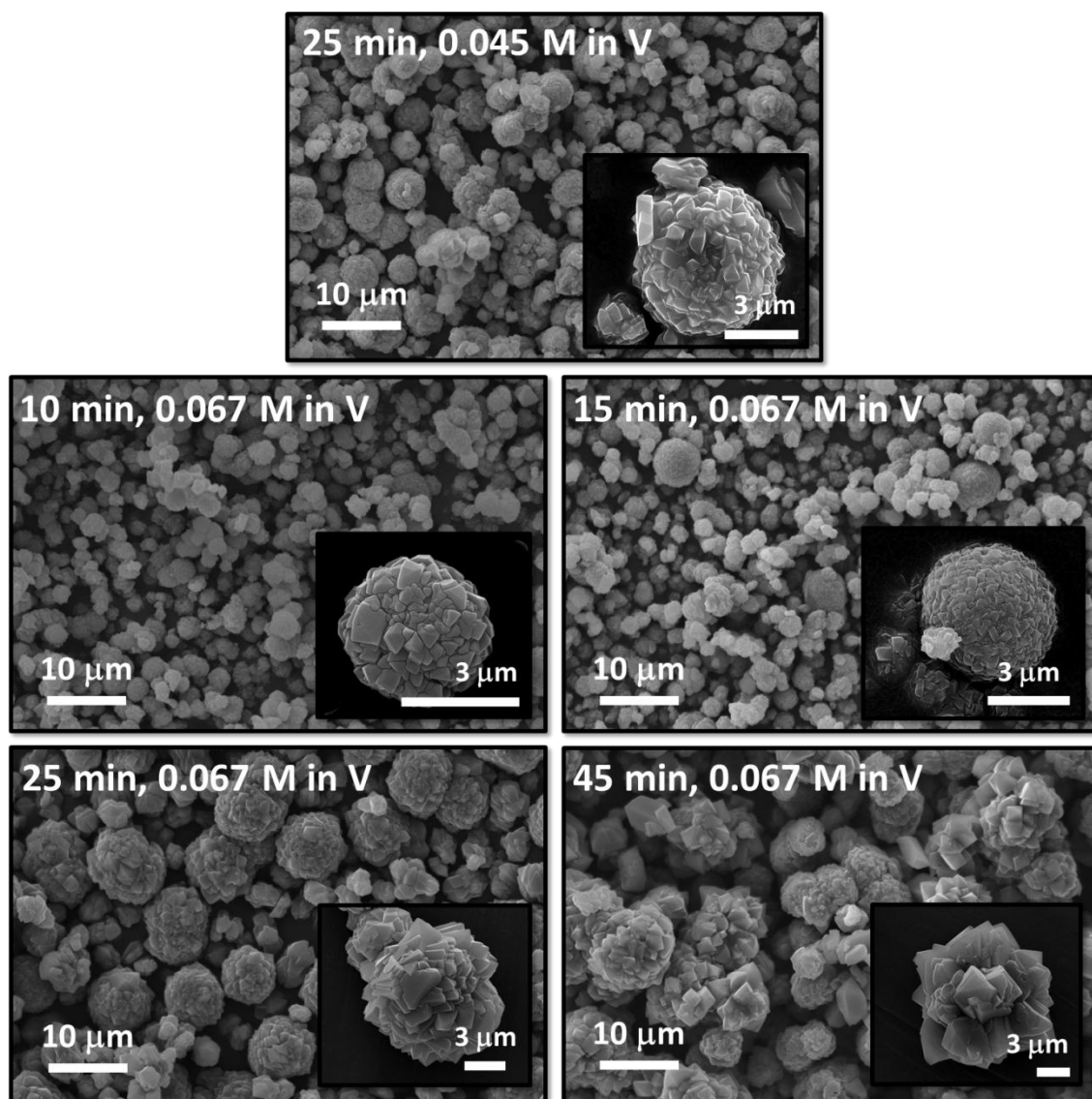


Figure 5.8. SEM of α -LiVOPO₄ synthesized in 3:1 water:ethanol. All samples were prepared at 230 °C with varied concentration and reaction time.

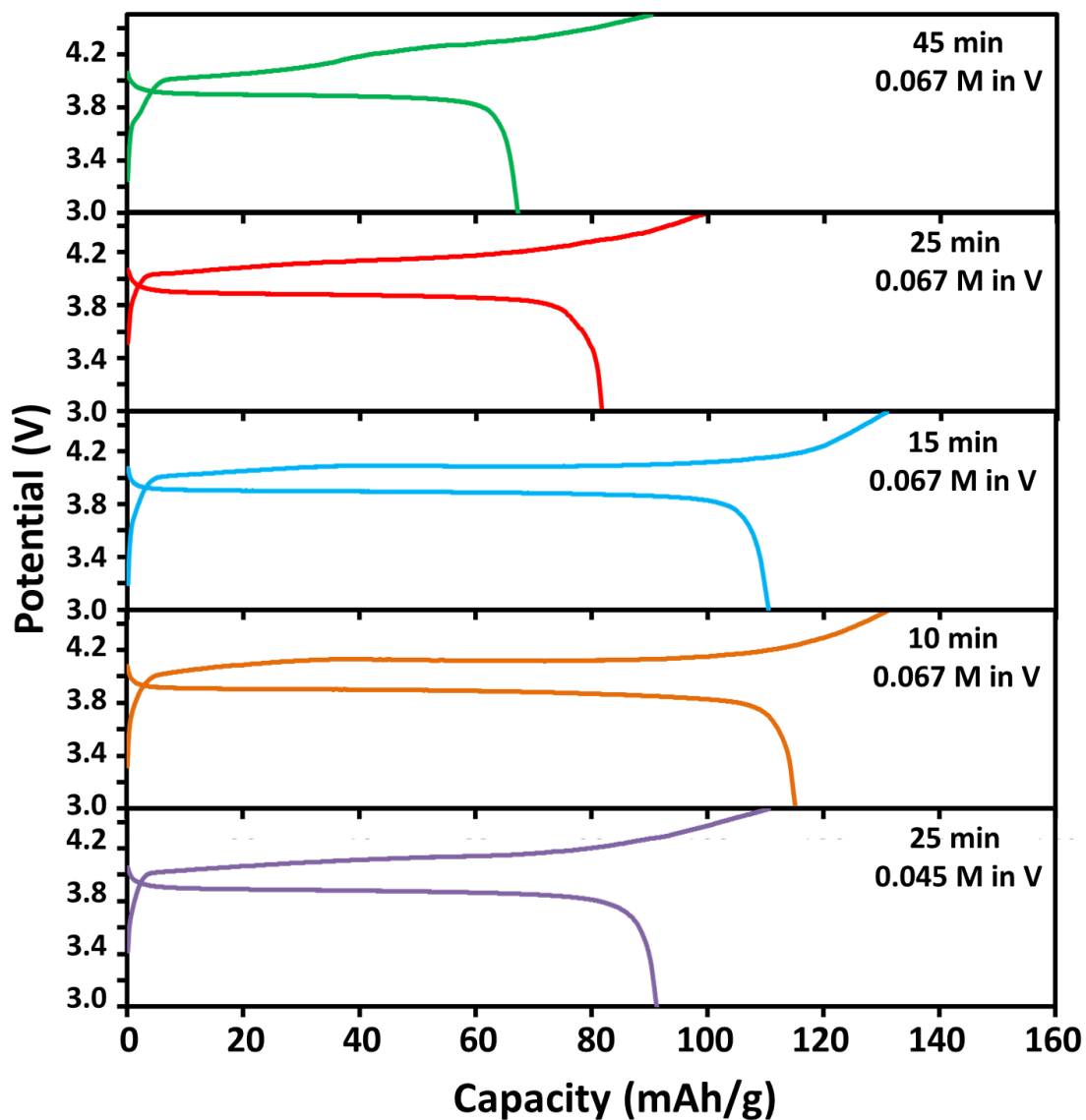


Figure 5.9. First charge-discharge curves at 3.0 - 4.5 V with a C/20 rate for α - LiVOPO_4 synthesized in 3:1 water:ethanol at 230 °C with varied reaction time and concentration.

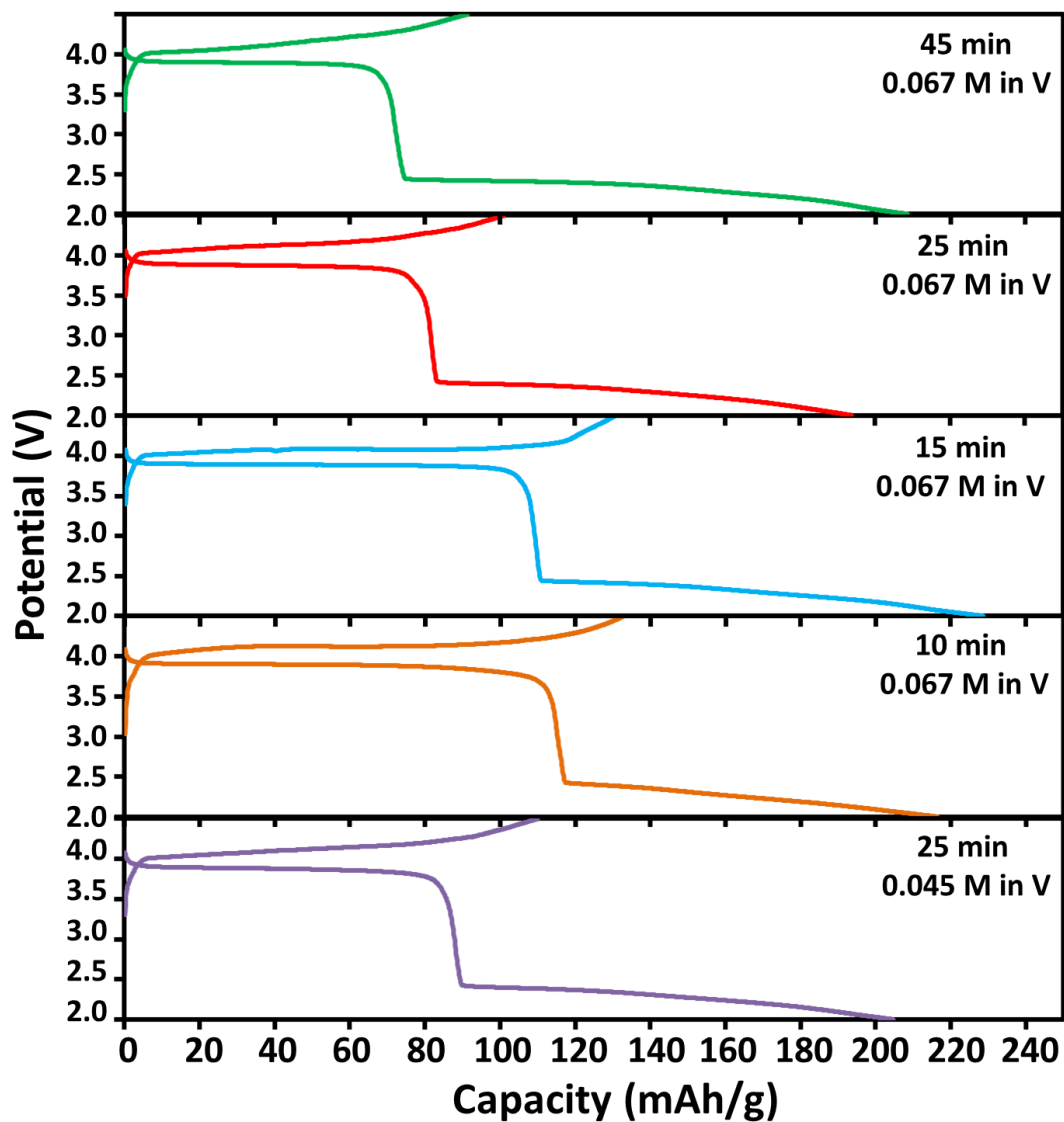


Figure 5.10. First charge-discharge curves at 2.0 - 4.5 V at C/20 rate for α -LiVOPO₄ synthesized in 3:1 water:ethanol at 230 °C with varied reaction time and concentration.

In an attempt to decrease particle size further, a surfactant (cetyl trimethylammonium bromide (CTAB)) was used to prevent particle growth and agglomeration. 0.5 – 1.5 mL of CTAB extraction solution (Teknova 2 % CTAB, 100 mM HCL pH 8.0, 20 mM EDTA pH 8.0, and 1.3 M NaCl) was substituted for water in the precursor solutions such that there was still a 3:1 mixture of water + CTAB solution : ethanol. The sample with 1.5 mL CTAB was amorphous, but the samples prepared with 0.5 and 1.0 mL CTAB solution were pure phase α -LiVOPO₄.

The particle size decreased with increasing CTAB for the same reaction time, as shown in Figure 5.11, and smaller particle sizes were obtained than for the samples prepared with water and glycol mixtures as well as the samples prepared with short reaction times and lower precursor concentrations. The sample synthesized with 0.5 mL of CTAB solution still showed micro-flower like morphology, but the samples synthesized with 1.0 mL CTAB showed more irregular particles.

The electrochemical performance improved for the sample prepared with 0.5 mL CTAB solution in the 3 – 4.5 V range, as shown in Figure 5.12, but the capacity in the 2 – 3 V range was quite limited. The cause of this observed phenomenon is not clear. The sample prepared with 1.0 mL CTAB solution showed lower capacity than the sample prepared with 0.5 mL CTAB solution in the 3-4.5 V range despite smaller particles, but higher capacity in the 2-4.5 V range. As discussed for other samples, high capacity at ~ 4 V does not always correlate well with high capacity at ~ 2 V.

To try to understand the discrepancy that the sample prepared with 1.0 mL CTAB solution consisted of smaller particles but showed lower capacity than the sample prepared with 0.5 mL CTAB solution, ICP was done to determine the elemental ratios. These ratios are presented in Table 5.4 and show that the sample prepared with 1.0 mL

CTAB solution had significant Li deficiency compared to the other samples. The elemental ratios suggest that the sample may have defects or impurities, so more experiments are necessary to optimize the amount of CTAB added to the solution to obtain small particles but the expected stoichiometry. All attempts to further reduce the particle size led to amorphous products.

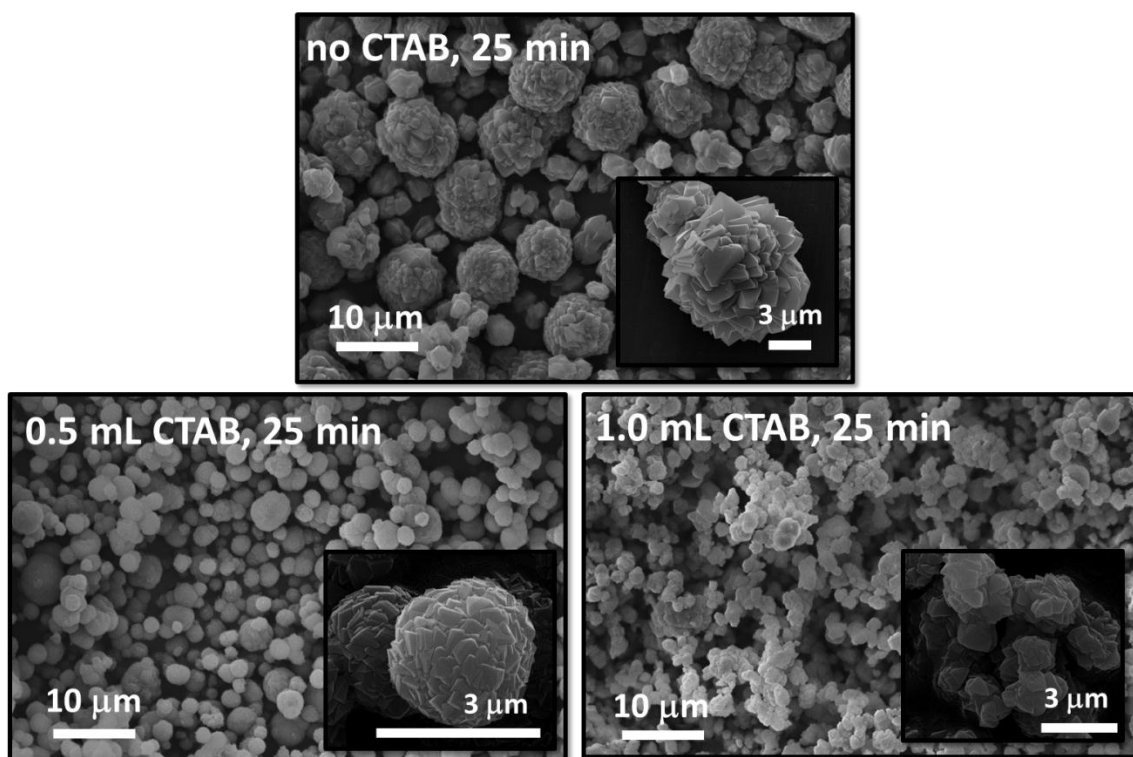


Figure 5.11. SEM of α -LiVOPO₄ synthesized in 3:1 water:ethanol at 230 °C. The reactions were run with a V concentration of 0.067 M with varied reaction time and amounts of CTAB solution substituted for water.

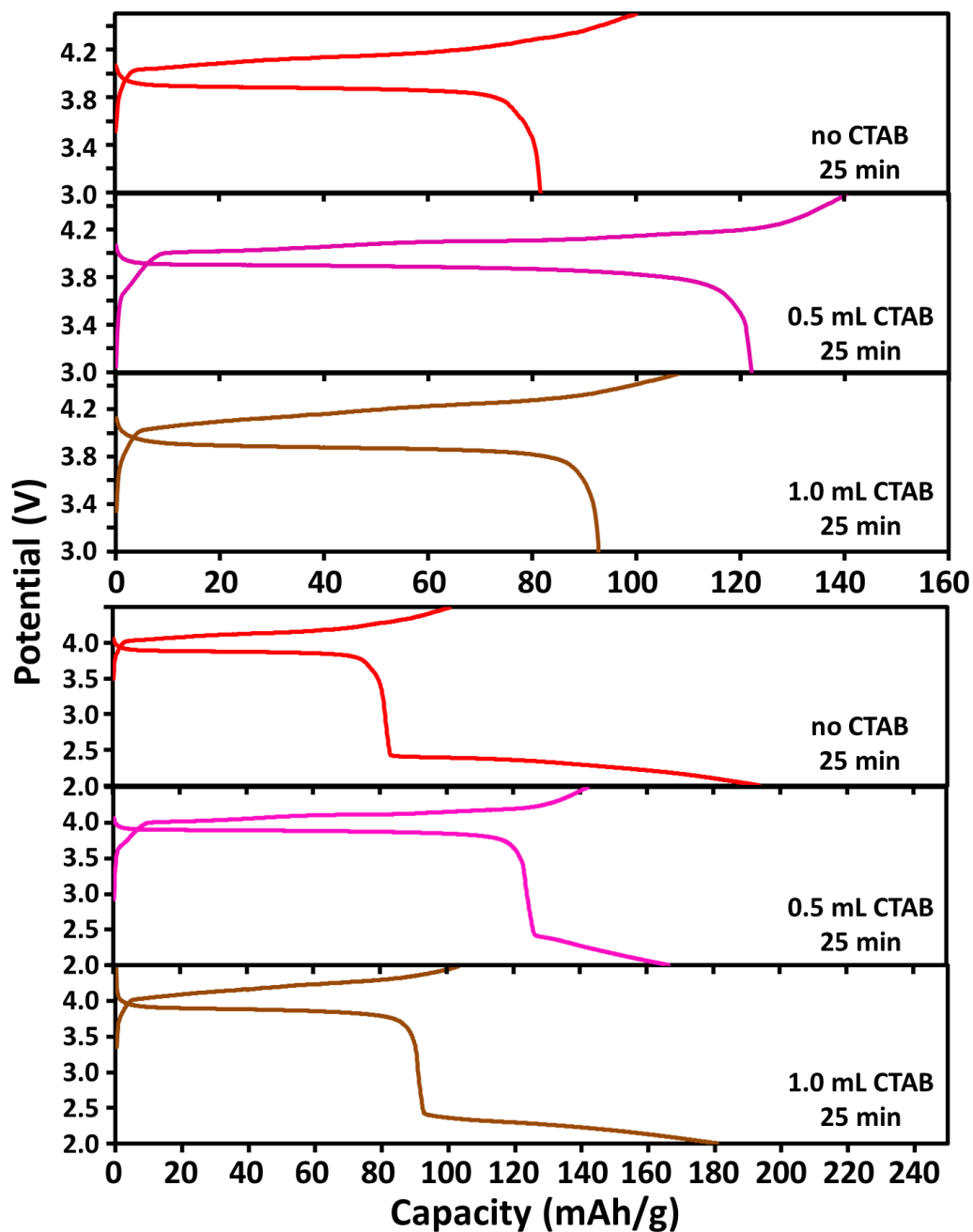


Figure 5.12. First charge-discharge curves at 3.0 - 4.5 ad 2.0 - 4.5 V at C/20 rate for α - LiVOPO_4 synthesized in 3:1 water:ethanol at 230 °C. The reactions were run with a V concentration of 0.067 M with varied amounts of CTAB solution substituted for water.

Table 5.4. *Elemental analysis of samples prepared at 230 °C in 3:1 water:ethanol with varying amounts of CTAB solution substituted for water. All samples were synthesized with a V concentration of 0.067 M.*

CTAB solution content	V/P	Li/P
none	0.98	0.97
0.5 mL	0.95	0.99
1.0 mL	0.97	0.86

Cycling performance

The cycling performance for the samples with varied solvents is shown in Figure 5.13 and Figure 5.14 shows the cycling performance for the samples with varied reaction time and CTAB concentration (all with solvent mixtures of water and ethanol). It is clear that the cycle performance is poor for most samples. Furthermore, the cycle performance does not generally correlate well to high initial capacity. For example, the sample prepared in pure water showed the lowest initial capacity of all the samples, but the capacity was more stable than the samples prepared in mixed solvents. Similarly, the sample prepared with a 45 min hold time exhibited good cycle performance, but poor initial capacity. The samples prepared in short reaction times and with CTAB solution (small particles) showed high initial capacities, but there was rapid capacity fade in these samples such that after 20 cycles, the capacity was equivalent or lower than the samples prepared with longer reaction times (larger particles).

The correlation between particle size (exposed surface area) and performance degradation during cycling suggests that the degradation in cycle performance may be related to reactions at the surface of the particles. Especially since these samples are cycled up to 4.5 V, which is a potential at the limits of stability for the electrolyte window, the degradation could be related to side reactions with the electrolyte. Thus, it seemed likely that coating the particles might improve the cycling performance.

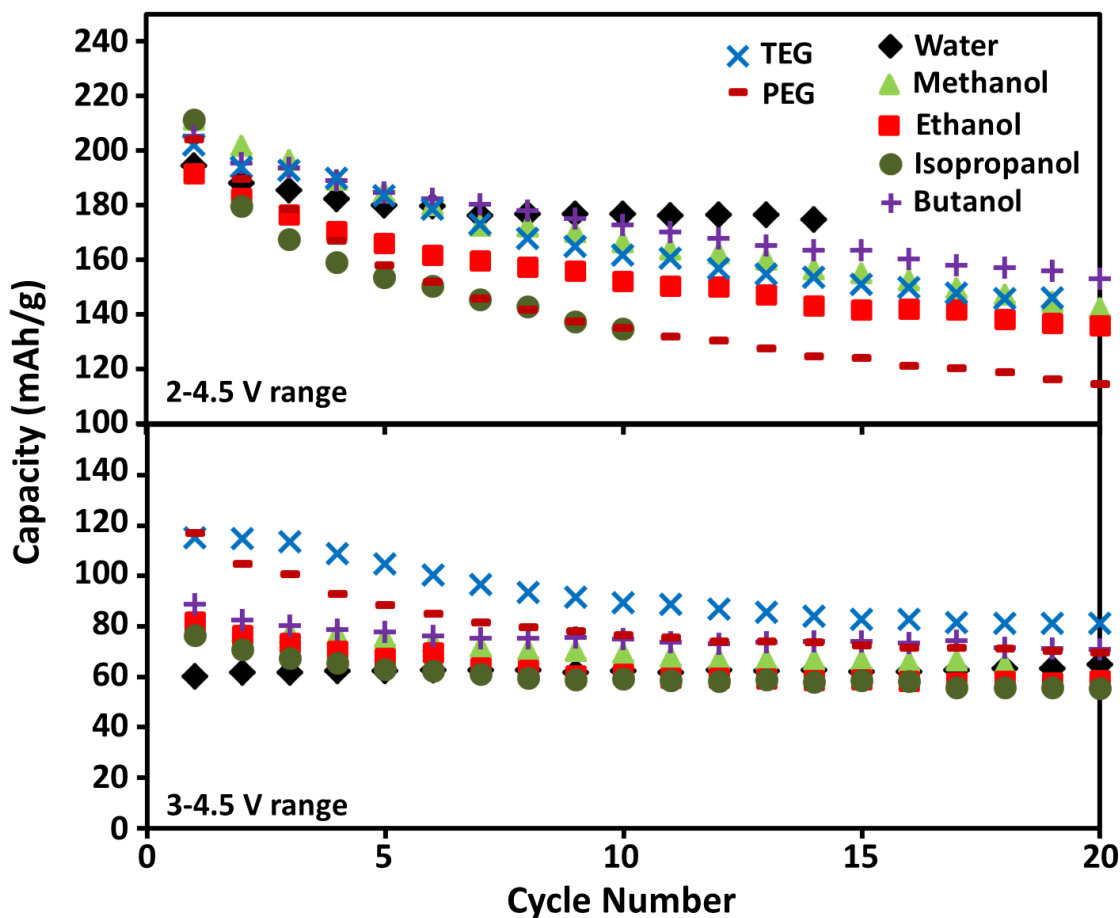


Figure 5.13. Cycle performance of samples synthesized in mixtures of water and various solvents with a V concentration of 0.067 M and a temperature of 230 °C (except for the sample synthesized in water at 240 °C) for a reaction time of 50 min.

The sample prepared in 3:1 water:ethanol with a 10 min reaction hold time was coated with PEDOT:PSS (poly(3,4-ethylenedioxythiophene) poly(styrenesulfonate), Clevios™ P VP AI 4083 with resistivity 500 - 5000 Ω -cm). This was accomplished by mixing the PEDOT:PSS solution with 10 mL of water and adding 0.1 g of the α -LiVOPO₄ sample. Enough PEDOT:PSS solution was added to incorporate about 5 wt. % PEDOT:PSS into the final product. The mixture was stirred on a hot plate at 85 °C until

the water evaporated and then the material was ground and dried in a vacuum oven at 150 °C before making electrodes. This process is similar to a previously described PEDOT coating procedure for LiFePO_4 [32].

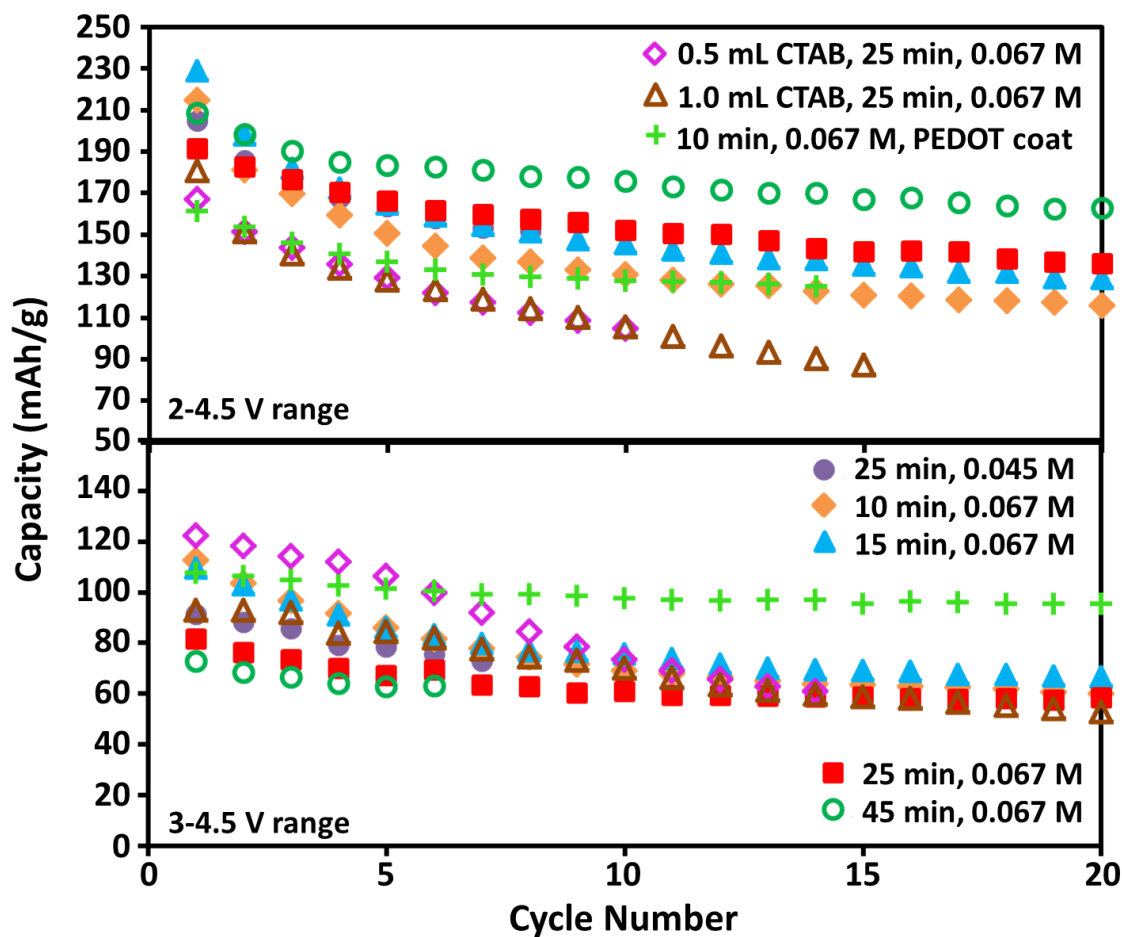


Figure 5.14. Cycle performance of samples synthesized in mixtures of water and ethanol with a temperature of 230 °C for varied reaction time, concentration, and CTAB and PEDOT additives.

The cycling performance of the PEDOT:PSS coated sample is compared to the other samples in Figure 5.14. The PEDOT:PSS-coated sample shows improved

cyclability compared to the pristine sample prepared in water and ethanol with a 10 min microwave reaction time before coating. However, much lower initial capacity is exhibited. Also interesting is that there is a change in the shape of the charge-discharge profile with PEDOT:PSS addition, but more analysis is necessary to understand this change. Overall, coating shows promise for improving the cycling performance for these samples, but the coating procedure needs to be optimized.

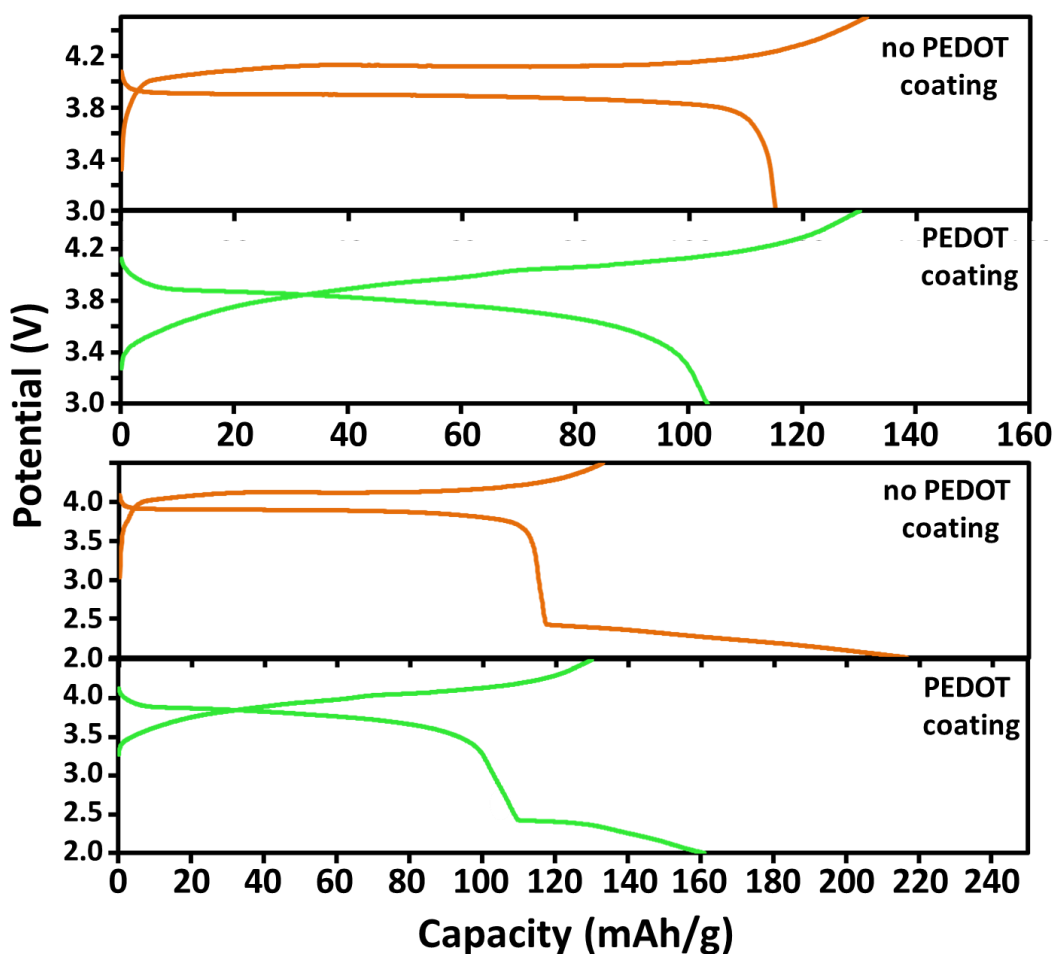


Figure 5.15. First charge-discharge curves of the PEDOT:PSS-coated sample compared to the sample before coating (prepared in 3:1 water:ethanol with a reaction time of 10 min) with voltage windows of 2 – 4.5 and 3 – 4.5 V.

5.4 CONCLUSIONS

Three polymorphs of LiVOPO_4 were synthesized with a facile, low-temperature microwave-assisted solvothermal approach. By varying the ratios of ethanol and water as the solvent as well as the precursor ratios and temperature, the three known polymorphs of LiVOPO_4 could be stabilized. Formation of the triclinic phase ($\alpha\text{-LiVOPO}_4$) was favored at high temperature and formed the most stoichiometric product, whereas the other two polymorphs showed non-stoichiometric elemental ratios and atypical XRD peak intensity ratios.

The effects of synthesis conditions on the particle size/morphology and the electrochemical performance of the $\alpha\text{-LiVOPO}_4$ were studied in detail. The ratio between water and alcohol as the solvent was found to be critical for formation of a phase pure sample. Several different alcohols and glycols could be used to synthesize this phase, with the smallest particles and best electrochemical performance resulting from synthesis in mixtures of water and glycols. The reaction time and concentration were also varied to show that the particle size could be controlled by these factors. Higher initial capacity was generally found to be linked to reduced particle size.

The particles formed into a micro-flower like morphology. To further control the particle size, CTAB was added to the precursor solution, which helped to prevent particle growth and agglomeration, reduced particle size, and improved electrochemical performance. The cycling performance was improved by coating the particles with PEDOT:PSS.

Chapter 6: Chemical and Electrochemical Lithiation of LiVOPO_4 Cathodes

6.1 INTRODUCTION

As shown in the previous Chapter, more than one Li^+ ion can be inserted into LiVOPO_4 . There have been a few papers that have mentioned this. Pozas et al. [119] synthesized orthorhombic $\text{Li}_{1.6}\text{VOPO}_4$ by reaction of $\alpha\text{-VOPO}_4$ with $\text{LiNO}_3\cdot\text{H}_2\text{O}$, and confirmed the Li content by emission spectroscopy. The Whittingham group showed that $\varepsilon\text{-VOPO}_4$ can be synthesized by heating monoclinic H_2VOPO_4 [112, 115-118]. Since the structures of $\varepsilon\text{-VOPO}_4$, H_2VOPO_4 , and $\alpha\text{-LiVOPO}_4$ are closely related, the authors hypothesized that a second Li could be inserted electrochemically into $\varepsilon\text{-VOPO}_4$. They found that ~ 1.6 Li (discharge capacity of 250 mAh/g) could be inserted into $\varepsilon\text{-VOPO}_4$ electrochemically and the insertion of the second Li occurred between 2.0 and 2.5 V. They mention that the extra 1.6 lithium inserted is accompanied by larger lattice parameters but do not show XRD patterns or detail the structural change.

Similarly, Ren et al. [70, 114] discovered that $\alpha\text{-LiVOPO}_4$ and $\beta\text{-LiVOPO}_4$ could be cycled as anode materials. The first step in their proposed reaction mechanism involved a second Li insertion into LiVOPO_4 to form Li_2VOPO_4 . Further reaction involves irreversible phase separation into V metal and Li_3PO_4 , which undergoes the reversible reaction $\text{V} + \text{Li}_3\text{PO}_4 \leftrightarrow \text{VPO}_4 + 3\text{Li}^+ + 3\text{e}^-$. Davis et al. [113] conducted an NMR study on Li_2VOPO_4 which was synthesized from $\alpha\text{-LiVOPO}_4$ by chemical lithiation, but no diffraction or elemental analysis are provided for the Li_2VOPO_4 phase.

Perhaps the most detailed study of the second lithium insertion is provided by Allen et al. [60]. They synthesized $\alpha\text{-LiVOPO}_4$ and $\beta\text{-LiVOPO}_4$ and electrochemically lithiated the materials at slow rates to obtain $\alpha\text{-Li}_{1.76}\text{VOPO}_4$ and $\beta\text{-Li}_{1.47}\text{VOPO}_4$. Again,

no XRD patterns were presented, but they show very detailed XANES/EXAFS measurements at various states of charge and discharge. Their results suggest that the short bond in LiVOPO_4 increases in length with increasing Li^+ insertion as the vanadium is reduced to V^{3+} . This is expected since V^{3+} does not form $\text{V}=\text{O}$ bonds. Because of this, there is likely a structural rearrangement with the second lithium insertion, which has not been detailed in the literature. There is a diffraction database entry for $\alpha\text{-Li}_{1.75}\text{VOPO}_4$, but the reference for the data is an ICDD Grant in Aid report with no details accessible [123].

Although several reports suggest it is possible to insert more than one lithium ion into $\alpha\text{-LiVOPO}_4$ and $\beta\text{-LiVOPO}_4$, none of the studies detail the phase transformation that occurs and it is unclear how much lithium can actually be inserted. To this end, $\alpha\text{-LiVOPO}_4$ and $\beta\text{-LiVOPO}_4$ are synthesized here and both chemical and electrochemical lithiation on the starting materials are performed. The materials are chemically lithiated to $\text{Li}_{1.5}\text{VOPO}_4$ and Li_2VOPO_4 and electrochemically lithiated at steps of 0.1 Li^+ for Li_xVOPO_4 with $1 \leq x \leq 2$. ICP, FTIR, and XRD data are used to evidence the chemical lithium insertion, and *ex situ* XRD measurements are presented to show the structural changes that occur at various stages during the lithiation process. Although the second voltage plateau is below 2.5 V, which may be too low to be ideal for high energy density lithium-ion batteries, the second voltage plateau is helpful for determining state of charge with certainty and preventing over-discharge even if the extra capacity is not used directly [60, 115].

6.2 EXPERIMENTAL

Synthesis of LiVOPO_4

The $\alpha\text{-LiVOPO}_4$ polymorph was synthesized as described in Chapter 5 by a

microwave reaction in a 3:1 mixture of water:ethanol. The reaction was held at 230 °C for 10 min and the concentration was 0.067 M in V. A sol-gel method used to synthesize β -LiVOPO₄ was described in Chapter 3.

Chemical Lithiation

Chemical lithiation was performed with *n*-butyllithium (Acros) and the standard Schlenk technique under an atmosphere of dry nitrogen. Hexanes (Fischer) were dried and degassed by a Vacuum Atmospheres Company solvent purification system (model number 103991-0319). 1.6 mmol (0.27 g) of pristine LiVOPO₄ was added to each of two flame-dried 50 mL Schlenk flasks (one for each polymorph) equipped with stir bars for preparation of the α and β Li_{1.5}VOPO₄ samples. Slightly less (1.56 mmol) pristine LiVOPO₄ was added to each of the two additional flasks (one for each polymorph) for preparation of the Li₂VOPO₄ samples. The flasks were sealed with rubber septa and then evacuated and backfilled with dry nitrogen. Hexanes (10 mL for Li_{1.5}VOPO₄ products and 20 mL for Li₂VOPO₄ products) was added to the flasks via a syringe. Then 0.5 mL or 1.0 mL (0.8 or 1.6 mM, 1.6 M in hexanes) of *n*-butyllithium were added in one portion to the flasks at ambient temperature to obtain Li_{1.5}VOPO₄ and Li₂VOPO₄, respectively. It should be noted that slightly less LiVOPO₄ was added to the flasks for the samples prepared according to Li₂VOPO₄ such that there would be a slight excess of *n*-butyllithium, but 1.0 mL could still be easily measured with a syringe.

Adding the *n*-butyllithium resulted in rapid color changes of the solid from light green to varying shades of grayish green/blue. The color of the solution before and after adding *n*-butyllithium is shown in Figure 6.1. The mixtures were then stirred for 48 h under nitrogen, at which time the solids were allowed to settle and the supernatant was removed by syringe. The residual solids were washed with two 25 mL portions of

hexanes and then dried under vacuum. The samples were then transferred to an Ar-filled glove box for storage. Pictures of the powders before and after lithiation are shown in Figure 6.1, indicating the clear color changes in the products.

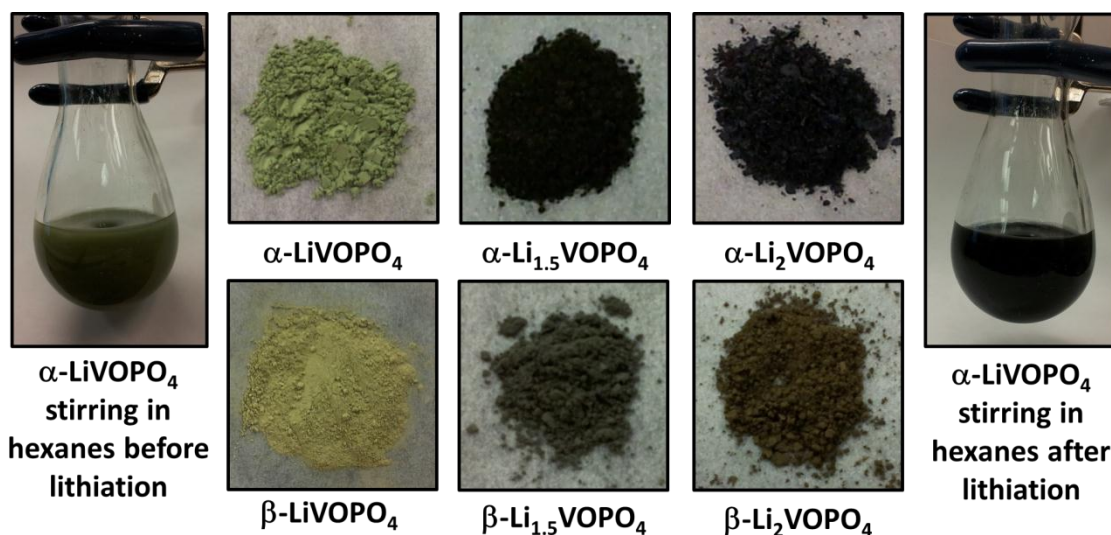


Figure 6.1. Pictures of LiVOPO_4 products before and after chemical lithiation. The color change was immediate upon addition of *n*-butyllithium.

6.3 RESULTS AND DISCUSSION

Chemical lithiation

$\alpha\text{-LiVOPO}_4$ and $\beta\text{-LiVOPO}_4$ were chemically lithiated with enough *n*-butyllithium to synthesize approximately $\text{Li}_{1.5}\text{VOPO}_4$ and Li_2VOPO_4 . ICP results are shown in Table 6.1 for the $\alpha\text{-LiVOPO}_4$ and $\beta\text{-LiVOPO}_4$ materials before and after chemical lithiation. The elemental analysis confirms that lithium is present in approximately the intended amounts. Secondly, the estimated oxidation states of vanadium were also calculated based on charge balance assuming that all of the lithium present is incorporated into the structure. Clearly, there is a slight lithium excess in the $\beta\text{-Li}_2\text{VOPO}_4$ sample, which could be present in another phase.

Table 6.1. *Elemental analysis of pristine and chemically lithiated LiVOPO₄.**

Intended Sample	Li/P	V/P	Formula	estimated V oxidation state
pristine α -LiVOPO ₄	0.97	0.98	Li _{0.97} (VO) _{0.98} PO ₄	4.07+
α -Li _{1.5} VOPO ₄	1.49	0.97	Li _{1.49} (VO) _{0.97} PO ₄	3.56+
α -Li ₂ VOPO ₄	1.92	0.97	Li _{1.92} (VO) _{0.97} PO ₄	3.11+
pristine β -LiVOPO ₄	0.98	0.99	Li _{0.98} (VO) _{0.99} PO ₄	4.04+
β -Li _{1.5} VOPO ₄	1.53	1.01	Li _{1.53} (VO) _{1.01} PO ₄	3.47+
β -Li ₂ VOPO ₄	2.06	1.00	Li _{2.06} (VO) _{1.00} PO ₄	2.94+

* Errors in ICP results are expected to be ~2-3%.

Since V in LiVOPO₄ transitions to V³⁺ when the second Li is inserted, the V=O bond should no longer be present after lithiation to Li₂VOPO₄. To evidence the reduction of V and the vanishing of the V=O bond, FTIR spectra were collected for the pristine and chemically lithiated samples, as shown in Figure 6.2. The pristine samples match the literature values well and the V=O bond is depicted near 900 cm⁻¹ in both the structures [74, 101]. It is clear that the V=O bond peak shifts to lower wavenumbers (weaker bond) with increasing Li content for α -Li_{1.5}VOPO₄ and α -Li₂VOPO₄ compared to pristine α -Li₂VOPO₄. This is consistent with the reduction of V⁴⁺ to V³⁺ because V³⁺ should form weaker bonds with oxygen than V⁴⁺ and because short V=O bonds do not form for V³⁺. The shifting of the V=O bond peak suggests that for both the chemically lithiated samples, there is a phase with mixed V^{3+/4+} oxidation state which is consistent with longer V-O bonds being present. If lithium intercalation occurs by a two-phase reaction mechanism such that all the extra lithium is accommodated only in a second phase in the α -Li_{1.5}VOPO₄ and α -Li₂VOPO₄ samples, then the V=O bond peaks would be in the same locations as in the pristine sample. The V=O bond peak almost disappears for the fully lithiated sample, further confirming that vanadium has been reduced and the sample has

been chemically lithiated. There is still a slight V=O bond peak for the ‘ α - Li_2VOPO_4 ’ sample, which is consistent with the elemental analysis results that show only 1.92 Li were actually inserted into the α - Li_2VOPO_4 sample (Table 6.1). The FTIR data complements previous detailed *ex situ* EXAFS measurements that show the short V-O bond in α - Li_xVOPO_4 increases in length with $0 \leq x \leq 1.76$ [60].

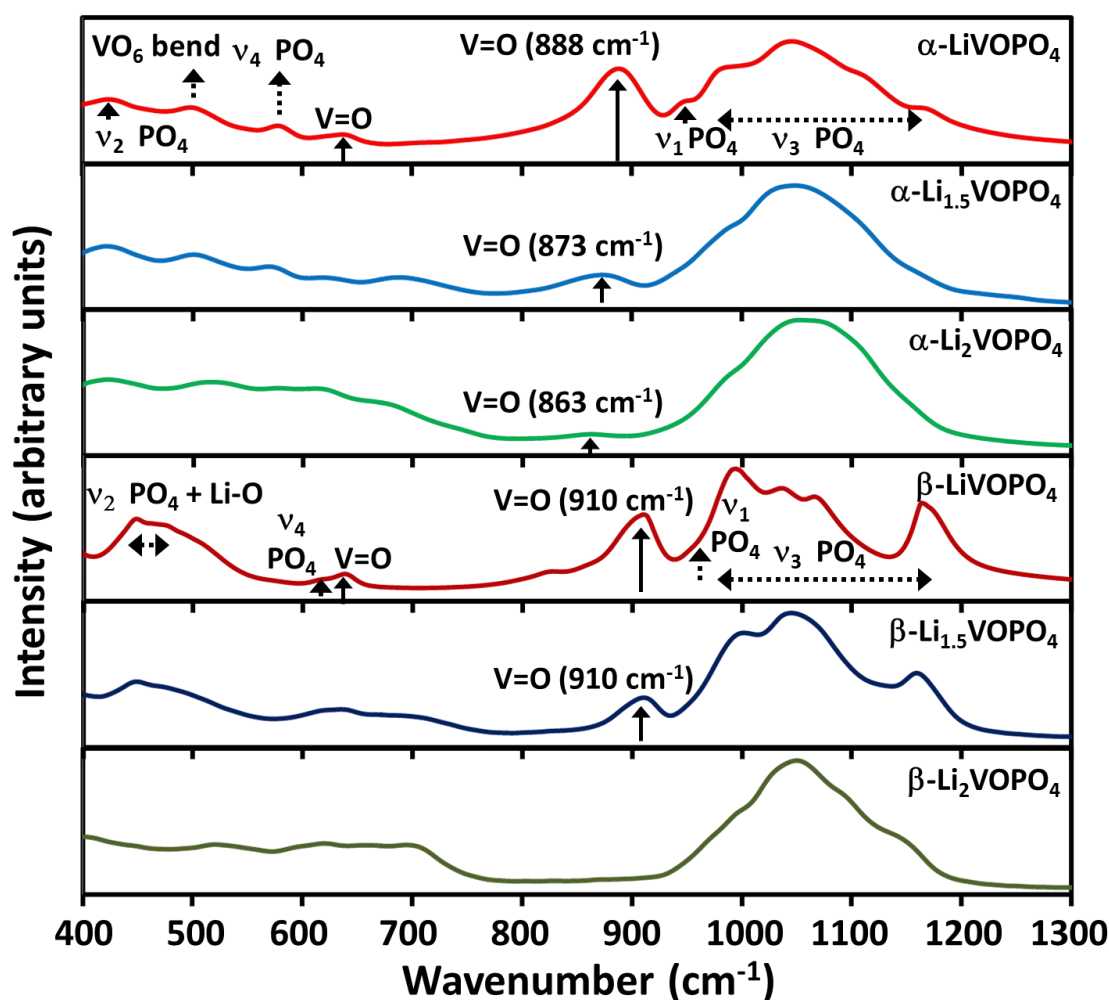


Figure 6.2. FTIR spectra of α - LiVOPO_4 and β - LiVOPO_4 before and after chemical lithiation.

In contrast to the α -Li_{1.5}VOPO₄ sample, which showed a shift in the V=O bond peak location with increasing lithium content, the β -Li_{1.5}VOPO₄ sample has a V=O bond peak at the same wavenumber as that for pristine β -LiVOPO₄. However, the peak for the V=O bond decreases in intensity for β -Li_{1.5}VOPO₄ relative to that of the pristine β -LiVOPO₄, indicating that the V=O bond is the same length but the species containing the V=O bond is less prevalent. This likely indicates a two-phase reaction mechanism in which there is a mixture of a species very closely related to β -LiVOPO₄ and another species which does not contain a V=O bond (presumably something like β -Li₂VOPO₄) with little solid solution between the two phases. If that were the case, the V=O bond length (and therefore the peak location) would not change, but the intensity would diminish due to the influence of β -Li₂VOPO₄. Clearly β -Li₂VOPO₄ has no V=O bond peak (Figure 6.2), as expected for the fully lithiated sample, in agreement with the elemental analysis (Table 6.1), which shows there should be no V⁴⁺ left in this sample.

Previous *ex situ* EXAFS measurements suggested that the V=O bond in β -Li_xVOPO₄ increases in length with lithiation between $0 \leq x \leq 1.47$, which is inconsistent with the results here [60]. The cause of this disagreement is unclear. However, their pristine sample was not stoichiometric (β -Li_{1.16}(VO)_{0.92}PO₄), which may affect the lithiation process. Also, with EXAFS it may be difficult to distinguish between the average bond length between a mixture of phases (one with and one without a V=O bond) and a single phase with a changing short V-O bond length, especially since there are already three distinct V-O bond lengths in the VO₆ octahedra for LiVOPO₄ (a short V=O bond, a long V-O bond opposite to the short V-O bond, and four equal V-O bonds) [68].

XRD patterns for the chemically lithiated materials are shown in Figure 6.3. There are clear changes in the XRD patterns after chemical lithiation. It should be noted that these patterns are distinctly different from database patterns for $\beta\text{-Li}_{1.6}\text{VOPO}_4$ and $\alpha\text{-Li}_{1.75}\text{VOPO}_4$ (although not at exactly the same lithium contents, which will be addressed later). The database pattern for the $\alpha\text{-Li}_{1.75}\text{VOPO}_4$ phase, synthesized by chemical lithiation, is very similar to the pristine pattern for $\alpha\text{-LiVOPO}_4$ [123]. The database pattern for $\beta\text{-Li}_{1.6}\text{VOPO}_4$, synthesized by mixing precursors in acetone and then heating in N_2 , does not resemble the pristine or chemically lithiated products presented here [119], indicating that a different phase forms through chemical lithiation. The phases formed here have not been previously presented.

Although refinement of the exact structures formed by chemical lithiation has not yet been achieved, several observations can be made by examining the XRD patterns in the low-angle region (Figure 6.4). The $\alpha\text{-Li}_{1.5}\text{VOPO}_4$ sample exhibits many of the same peaks as the pristine $\alpha\text{-LiVOPO}_4$ pattern, but several peaks in the $\alpha\text{-Li}_{1.5}\text{VOPO}_4$ pattern are shifted, missing, or new relative to the pristine $\alpha\text{-LiVOPO}_4$ pattern (most notably the peaks at ~ 22.5 , 27.3 , 29.6 , and 34.5 degrees).

Similarly, the $\alpha\text{-Li}_{1.5}\text{VOPO}_4$ pattern peaks do not align well with the peaks for $\alpha\text{-Li}_2\text{VOPO}_4$. It is clear that the $\alpha\text{-Li}_{1.5}\text{VOPO}_4$ sample is not simply a mixture of the $\alpha\text{-LiVOPO}_4$ and the $\alpha\text{-Li}_2\text{VOPO}_4$ patterns. The peak shifts suggest that there is some solid solution between the $\alpha\text{-LiVOPO}_4$ and the $\alpha\text{-Li}_2\text{VOPO}_4$ phases or between these phases and intermediate phases. This supports the observation made in the FTIR data which suggests that the short V-O bond weakens with increasing lithiation, indicating that at least some lithium is inserted into the $\alpha\text{-LiVOPO}_4$ in accompaniment with the formation of a new phase.

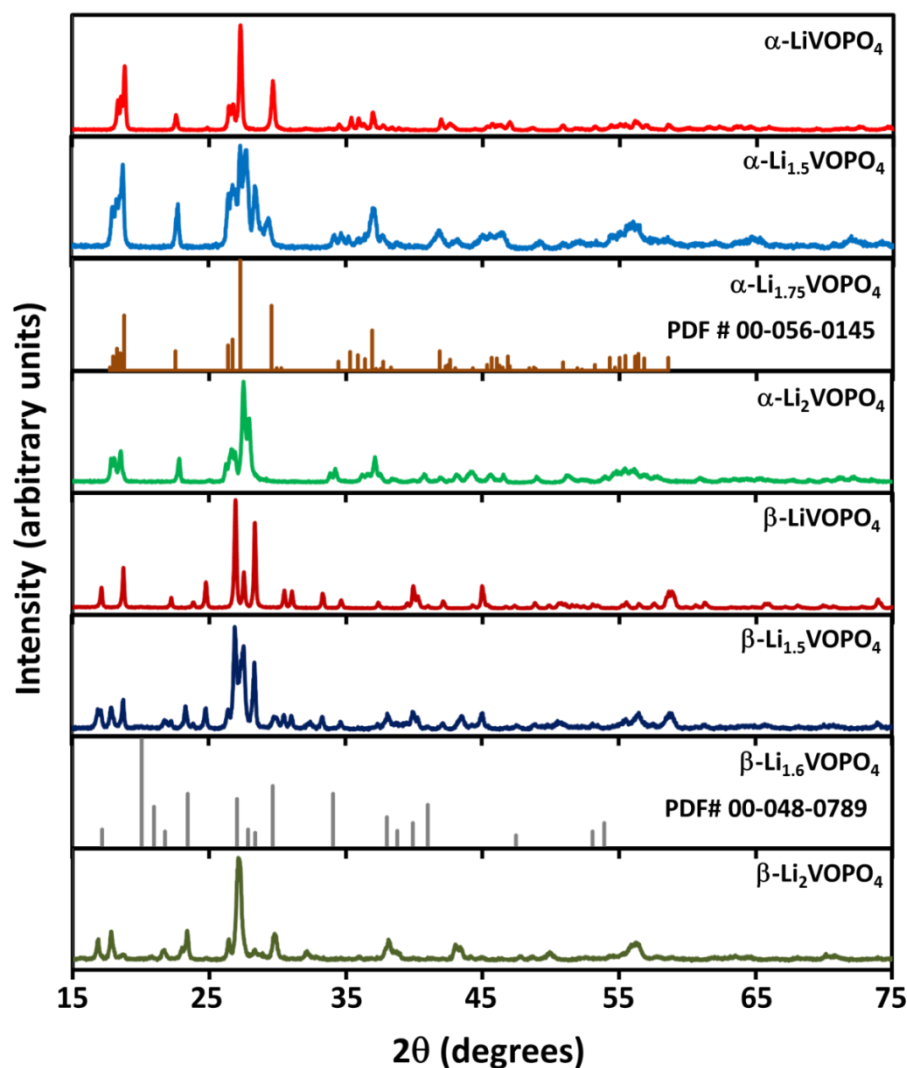


Figure 6.3. XRD patterns of α -LiVOPO₄ and β -LiVOPO₄ before and after chemical lithiation compared to database patterns.

Conversely, all of the peaks for β -LiVOPO₄ phase are present in the β -Li_{1.5}VOPO₄ pattern at the same angles. The presence of the un-shifted β -LiVOPO₄ peaks indicates that there is likely little lithium inserted into pristine β -LiVOPO₄. Instead, a new phase is likely formed to accommodate the lithium. The second phase in the β -Li_{1.5}VOPO₄ pattern is consistent with the β -Li₂VOPO₄ pattern with some small shifts for

a few peaks. Thus, the β -Li_{1.5}VOPO₄ sample is a phase mixture between the pristine and fully lithiated samples with very little solid solution between β -LiVOPO₄ and β -Li₂VOPO₄. These observations are again consistent with the FTIR results, which suggest no change in V=O bond length for the β -LiVOPO₄ polymorph with insertion of a second lithium. This implies that a new phase forms to accommodate the extra lithium during chemical lithiation and this new lithium-rich phase consists of V³⁺ with no V=O bond.

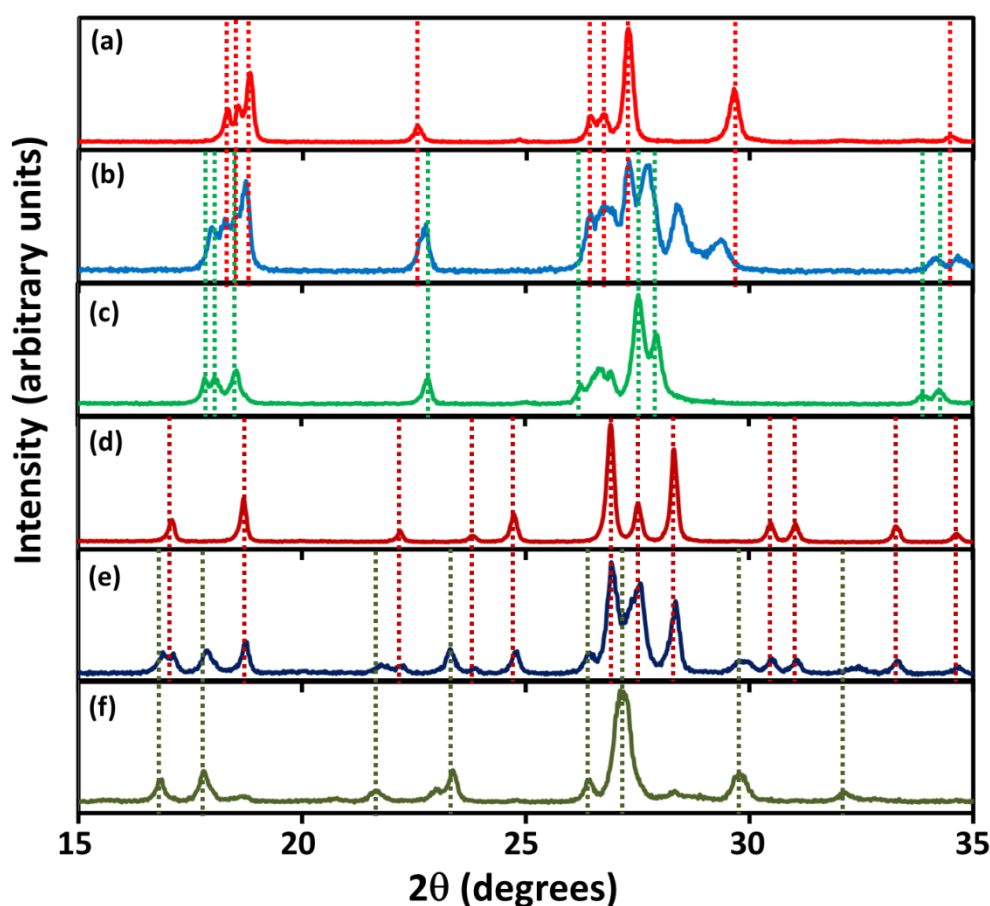


Figure 6.4. XRD patterns in a small range of angles for (a) pristine α -LiVOPO₄, (b) chemically lithiated α -Li_{1.5}VOPO₄, (c) chemically lithiated α -Li₂VOPO₄, (d) pristine β -LiVOPO₄, (e) chemically lithiated β -Li_{1.5}VOPO₄, and (f) chemically lithiated β -Li₂VOPO₄.

Electrochemical lithiation

Since the XRD patterns of the chemically lithiated materials do not resemble previously published patterns for LiVOPO_4 samples hosting more than one lithium ion per formula unit, it was of interest to investigate the structural transformation that occurs during electrochemical lithiation for comparison to the chemical lithiation products. Thus, pouch cells of pristine $\alpha\text{-LiVOPO}_4$ and $\beta\text{-LiVOPO}_4$ were constructed and discharged at a C/100 rate to various states of discharge for *ex situ* XRD measurements. The cells were then opened in an Ar-filled glove box so that the electrodes could be removed and sealed in Kapton film and tape. The discharge curves are shown in Figure 6.5, and the states of discharge that were accessed for *ex situ* XRD are indicated.

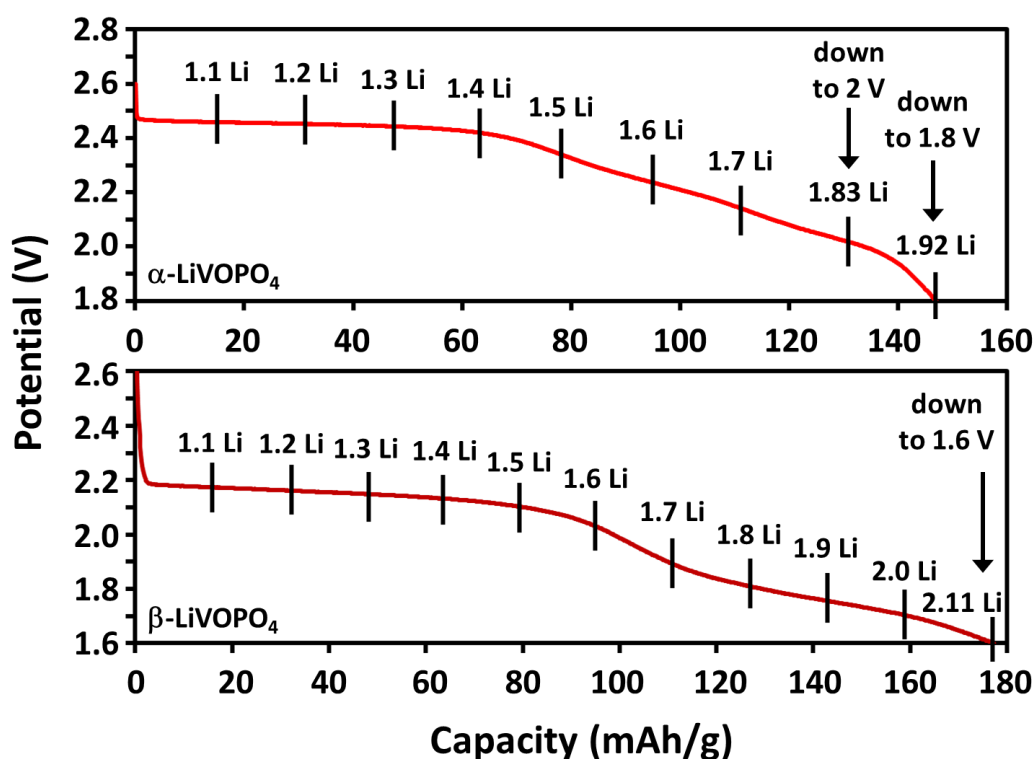


Figure 6.5. Discharge curves for $\alpha\text{-LiVOPO}_4$ and $\beta\text{-LiVOPO}_4$ with states of discharge used for *ex situ* XRD indicated (note changes in scale).

Because the α -LiVOPO₄ curve was still somewhat flat at 2 V (which has been used as a potential cutoff in previous studies [60, 115]), the cells were also cycled down to 1.8 V to lithiate the material a little further. By cycling down to 1.8 V, 1.92 Li can be incorporated into the structure. Just above this point, the slope of the curve changes such that it is clear that discharging to lower potential would not increase the capacity significantly. Also, elemental analysis of the chemically lithiated “ α -Li₂VOPO₄” sample showed only about 1.92 Li per formula unit (Table 6.1). Because the *ex situ* measurements were undertaken for comparison to the chemical lithiation products, discharging down to 1.8 V with 1.92 Li total Li per formula unit is reasonable.

The discharge profile for α -LiVOPO₄ shows that there is a relatively flat region (up to about 1.4 Li), followed by a continuously sloping region. By Gibbs phase rule, the plateau region would imply that there is a two-phase mixture during Li insertion up to about 1.4 Li⁺ and then a single phase after that point. At the point in the discharge curve that would correspond to α -Li_{1.5}VOPO₄, the curve is transitioning to a single phase, so one would expect that the emerging new phase would have a mixture of V³⁺ and V⁴⁺. This is consistent with shifts in the V=O bond peak locations in the FTIR measurements and shifts in the XRD peaks for the chemically lithiated α -LiVOPO₄ samples.

The capacity for the second lithium insertion into the β -LiVOPO₄ polymorph occurs at slightly lower voltage (2.2 V versus 2.4 V), so the cells were discharged down to lower voltage. Discharging down to 1.8 V led to a capacity equivalent to lithiation with ~1.8 Li per formula unit. The discharge curve was still fairly flat at 1.8 V, so electrodes were also discharged down to 1.6 V, resulting in capacity corresponding to ~ β -Li_{2.10}VOPO₄. There was a change in slope just above 1.6 V implying that discharging

further would not lead to significant increases in capacity. Also, since chemical lithiation results indicate $\beta\text{-Li}_{2.06}\text{VOPO}_4$, 1.6 V is a reasonable cutoff voltage for comparison.

The chemical and electrochemical lithiation results for $\beta\text{-Li}_2\text{VOPO}_4$ show slightly higher lithium content than expected, which could mean that more than 2 lithium ions can be incorporated into the new phase that forms upon lithiation of pristine $\beta\text{-LiVOPO}_4$, especially since both the chemical and electrochemical lithiation results show similar values. However, this could also imply that there is a lithium-rich impurity phase present or could indicate that side reactions occur during electrochemical lithiation. It is worth noting that the chemical lithiation product was washed with hexanes to remove excess leftover *n*-butyllithium, but it is also possible that a small impurity is present. Furthermore, this could indicate that the initial oxidation state of V was a little higher and the lithium content was a little lower in the starting material than is implied by the formula $\beta\text{-LiVOPO}_4$, although the elemental analysis suggested ratios consistent with $\beta\text{-LiVOPO}_4$ within error and no detectable impurities are present in the XRD pattern.

Ren *et al.* [114] showed that discharging $\beta\text{-LiVOPO}_4$ down to 0.01 V resulted in irreversible decomposition of $\beta\text{-LiVOPO}_4$ into Li_2O , V metal, Li_3PO_4 , and VPO_3 . Their CV curve shows a continuous discharge peak between about 1.6 and 2.1 V (presumably for $\text{V}^{3+/4+}$ corresponding to the second lithiation in $\beta\text{-LiVOPO}_4$) and then a flat region until approximately 1.1 V, after which there are a series of other peaks. This agrees with the assumption made here that lithiation of $\beta\text{-LiVOPO}_4$ occurs down to about 1.6 V and the material irreversibly decomposes only at lower voltage. As will be discussed in more detail at the end of this Chapter, discharging $\beta\text{-LiVOPO}_4$ down to 1.6 V was reversible and pristine $\beta\text{-VOPO}_4$ was recovered upon charging to 4.5 V.

It is also worth examining the shape of the discharge profile for β -LiVOPO₄ in more detail. There is a relatively flat region up to the insertion of ~ 1.6 Li, which implies a possible two-phase mixture over that range. A two-phase mixture is consistent with the FTIR results that indicate that the V=O bond does not shift with lithiation and with XRD of the chemically lithiated β -Li_{1.5}VOPO₄ sample, which suggests that this sample is a phase mixture with little solid solution between β -LiVOPO₄ and β -Li₂VOPO₄. After ~ 1.6 Li, the discharge curve slopes continuously, which indicates a likely single-phase region. Because these discharge curves are measured under load (although a slow rate is used), it is difficult to draw decisive conclusions from the discharge curves. Open-circuit voltage discharge curves are needed to make more definitive arguments about the discharge curve shapes than can be made from examining the discharge curves under load.

Figure 6.6 shows *ex situ* XRD patterns at various states of discharge, and Figure 6.7 details the low-angle range. There is a clear structural transition that occurs as more Li is inserted into the structure. Most notably, the peaks around 22.5 and 27.3 degrees shift to higher angles with lithiation, and the peak at 29.6 degrees shifts to lower angle with lithiation. For the sample with ≥ 1.4 Li, new peaks arise. The strong peak at 28.5 degrees in the α -Li_{1.4}VOPO₄ pattern shifts to lower angles with increased lithiation, but many other peaks remain in similar locations. The shifting of peaks in the samples with 1.1 – 1.3 Li provides evidence that lithium has been intercalated into the structure, as opposed to simply forming a phase mixture. Because the voltage plateau is relatively flat in the region between α -LiVOPO₄ and α -Li_{1.4}VOPO₄, there still may be a two-phase mixture in this range, but open-circuit voltage curves are needed to confirm this. However, the peak shifting suggests that the α -LiVOPO₄ phase can also accommodate some extra lithium in addition to formation of a new phase.

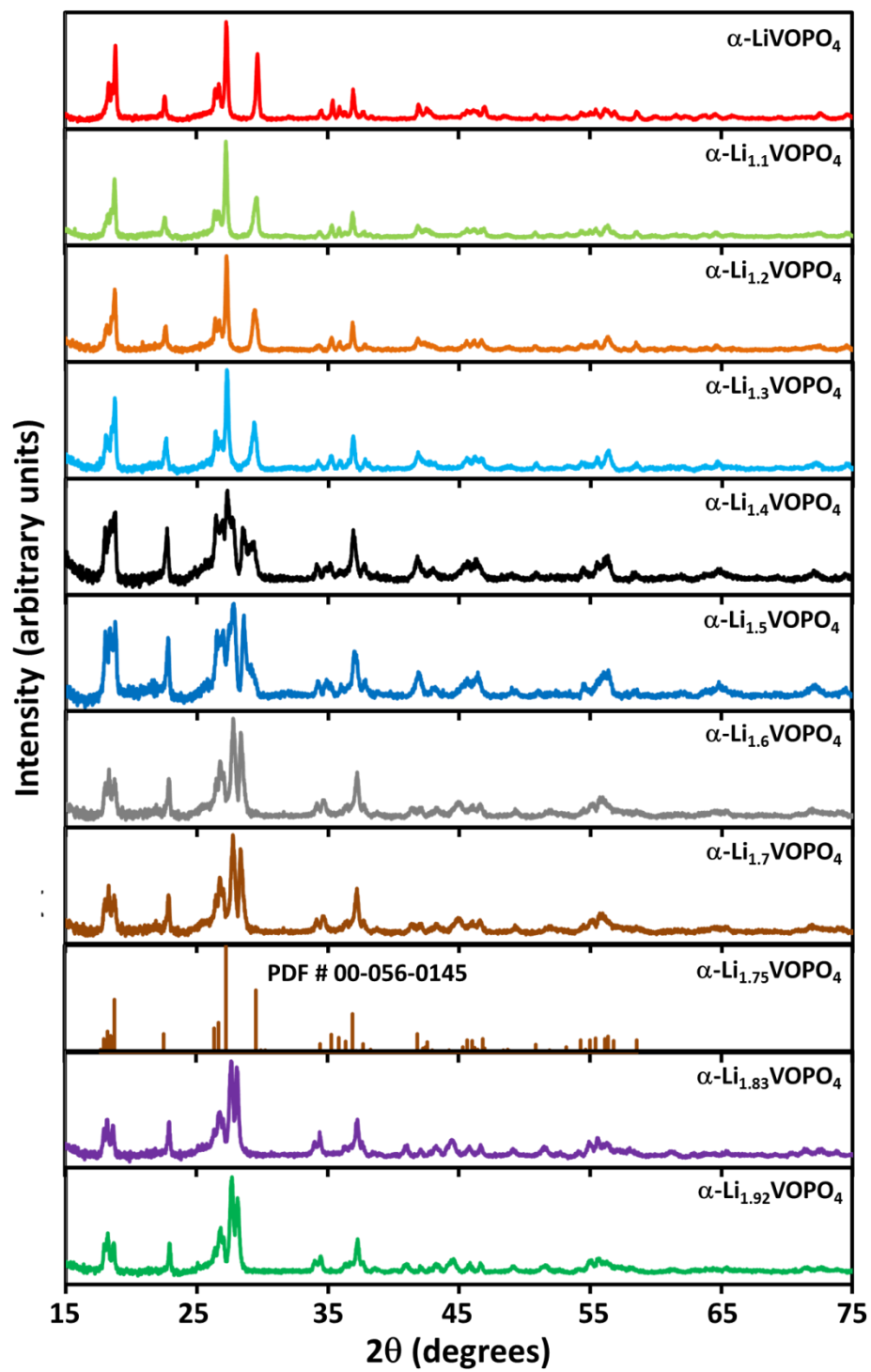


Figure 6.6. *Ex situ* XRD patterns of α -LiVOPO₄ at various states of discharge.

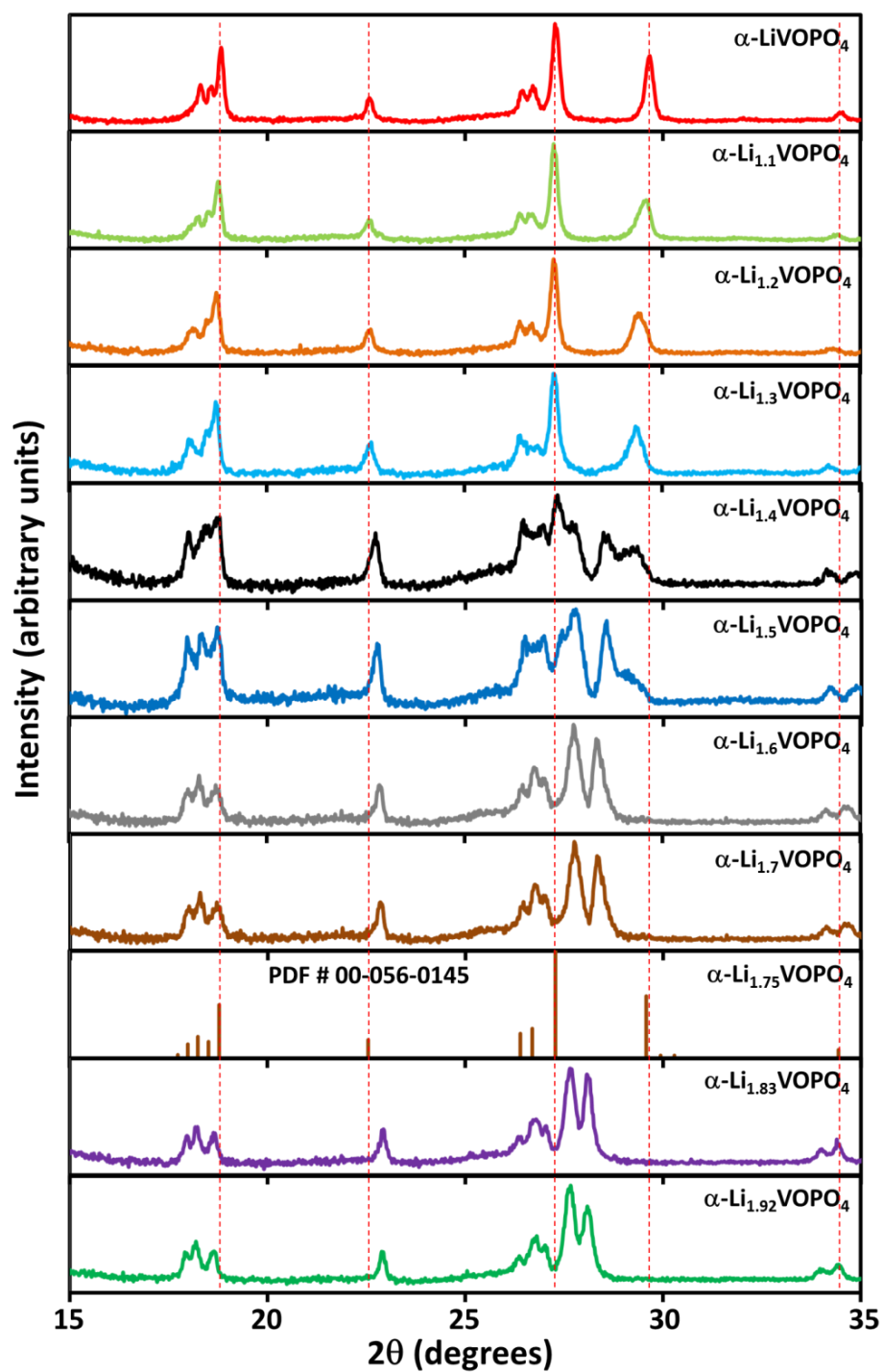


Figure 6.7. *Ex situ* XRD patterns of α - LiVOPO_4 at various states of discharge, detailing the low-angle region.

The voltage plateau for the samples with ≥ 1.5 Li was shown to be continuously sloping, suggesting a single phase is present. The sloping curve also explains why the peaks for the pristine α -LiVOPO₄ phase disappear for samples with lithium contents of approximately ≥ 1.5 Li and only shifts in the peaks are observed with increased lithiation, consistent with a single phase.

A database pattern for α -Li_{1.75}VOPO₄ is shown again for comparison, and it is distinctly different from the electrochemically lithiated materials obtained in this study as well. Again, this database pattern resembles the pristine α -LiVOPO₄ material much more closely than the α -Li_{1.7}VOPO₄ or α -Li_{1.8}VOPO₄ samples shown here.

It is helpful to compare the chemically and electrochemically lithiated materials to see whether the same structural transformation occurs. Figure 6.8 shows such a comparison for the α -Li_{1.5}VOPO₄ and α -Li₂VOPO₄ samples. It is clear that the chemically and electrochemically lithiated materials match well, which indicates that the structural transformation that occurs during electrochemical lithiation can be replicated by chemical lithiation. The electrochemically and chemically lithiated α -Li_{1.5}VOPO₄ have slightly different peak intensities, but overall show similar peak locations. The small differences are likely because the α -Li_{1.5}VOPO₄ sample has a lithium content corresponding to an inflection point in the discharge curve, so small changes in the state of charge may change the XRD pattern significantly. Since lithiation to 1.5 Li is around the region where a plateau transitions to a sloping region, it is likely that a two-phase mixture is transitioning to a single phase, making this region particularly difficult to characterize. The patterns for the electrochemically and chemically lithiated α -Li₂VOPO₄ materials are almost identical, indicating that the same structural transformation occurs during chemical and electrochemical lithiation.

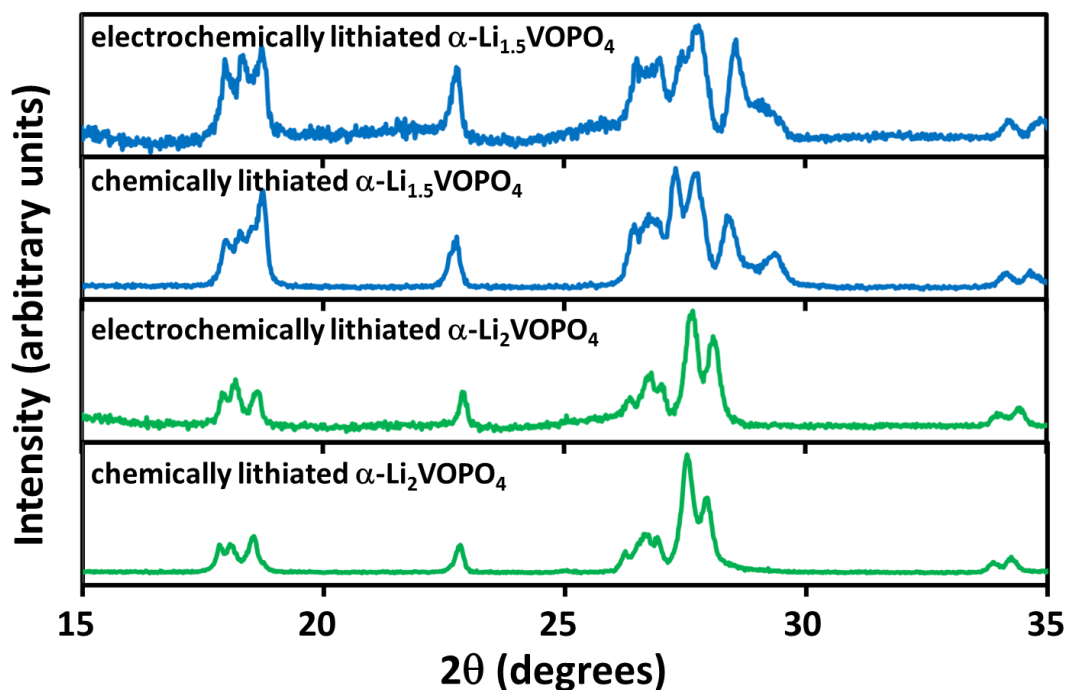


Figure 6.8. Comparison between chemically lithiated and electrochemically lithiated α - LiVOPO_4 samples.

Similarly, *ex situ* XRD patterns at various states of discharge are shown in Figure 6.7 and Figure 6.10 for the β - LiVOPO_4 sample. Again, there are clear changes in the XRD patterns as more lithium is inserted, but the changes are more subtle at lower states of discharge. At states of discharge ≥ 1.4 Li, there are not any obvious systematic shifts in the peak locations, again indicating that little additional lithium can be inserted into β - LiVOPO_4 without a phase change occurring. Starting at around β - $\text{Li}_{1.4}\text{VOPO}_4$, though, a shoulder becomes visible on the peak around 26.5 degrees. As the lithium content increases further, there are more drastic changes in the patterns and the peaks between ~ 27.0 and ~ 28.4 merge into a single peak. Similarly, several small new peaks arise.

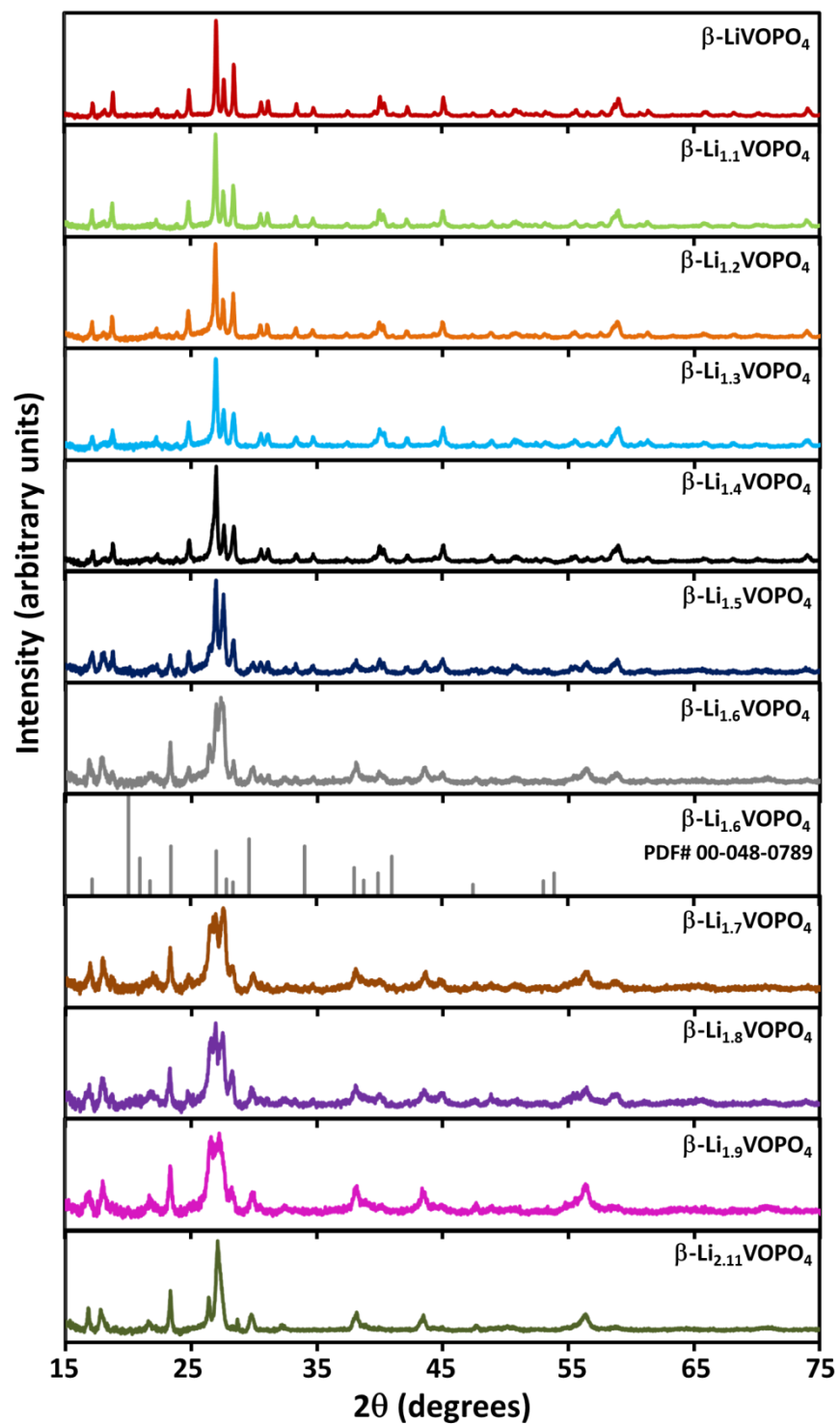


Figure 6.9. *Ex situ* XRD patterns of β -LiVOPO₄ at various states of discharge.

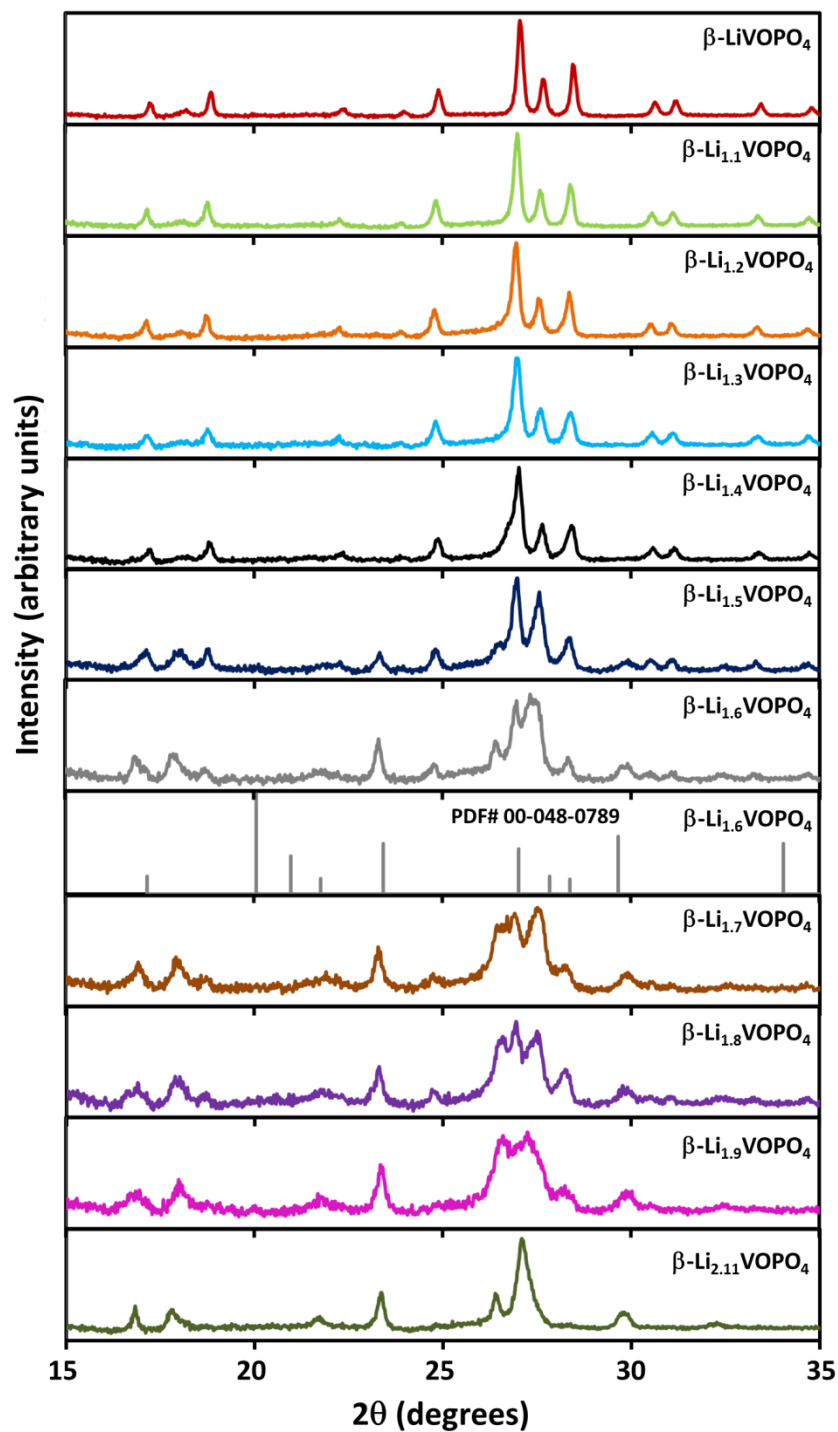


Figure 6.10. Ex situ XRD Patterns of β -LiVOPO₄ at various states of discharge, detailing the low-angle region.

The discharge curve for the β -LiVOPO₄ sample exhibits a sloping curve after an initial voltage drop occurs at around 1.6 V (Figure 6.5), indicating that there is likely a single phase. Again, open-circuit voltage measurements are needed to exactly analyze where the single phase region begins. Finally, it is worth pointing out that there is no similarity between the *ex situ* XRD pattern for β -Li_{1.6}VOPO₄ and the database pattern synthesized by mixing precursors in acetone and then firing in N₂ [119]. Clearly this solid state procedure does not result in the same phase as occurs during electrochemical lithiation of β -LiVOPO₄.

A comparison is shown between the chemically and electrochemically lithiated β -LiVOPO₄ polymorph in Figure 6.11. The chemically and electrochemically lithiated β -Li₂VOPO₄ samples agree well. The pattern for the chemically lithiated β -Li_{1.5}VOPO₄ sample is very similar to that for the electrochemically lithiated sample with some slight peak intensity differences. Again, this is at a point in the discharge curve where a two-phase region is transitioning to a single-phase region, which means that small changes in the lithium content could change the XRD patterns significantly. Regardless, it is clear that the chemical and electrochemical lithiation data at these two stages of lithiation agree for both polymorphs, indicating that the structural transformations that occur electrochemically are replicated here by chemical lithiation.

Finally, it is important to establish that the α -LiVOPO₄ and β -LiVOPO₄ structures remain stable after insertion of close to 2 Li. After cycling the materials down to 1.8 and 1.6 V, respectively, the cells were then charged to 4.5 V and *ex situ* XRD patterns were collected. These patterns were compared to pristine cells charged to 4.5 V (without discharging first). The *ex situ* XRD results are shown in Figure 6.12, and it is clear that charging the fully discharged α -LiVOPO₄ material to 4.5 V results in the same

VOPO₄ phase as charging the pristine material to 4.5 V. The α -LiVOPO₄ material showed a similar trend. The *ex situ* XRD patterns obtained by charging the β -LiVOPO₄ and α -LiVOPO₄ polymorphs can be indexed to β -VOPO₄ (orthorhombic) and η -VOPO₄ (monoclinic), respectively.

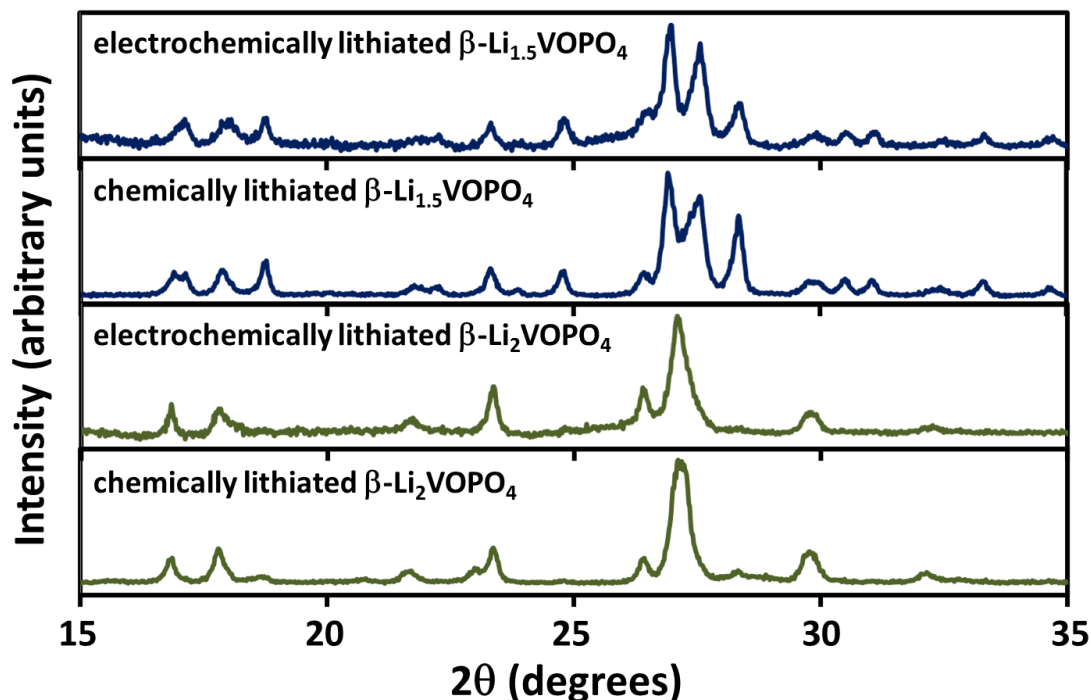


Figure 6.11. Comparison of the chemically and electrochemically lithiated β -LiVOPO₄ samples.

Thus, inserting 1.92 Li into the α -LiVOPO₄ structure and ~ 2.1 Li into the β -LiVOPO₄ structure does not cause an irreversible structural change. This structural reversibility supports the argument that the capacities and structures presented here are the result of lithiation of the respective LiVOPO₄ polymorphs rather than due to structural decomposition and resulting impurity formation. The structures that form after

lithiation need to be analyzed by neutron diffraction in order to determine the lithium positions in the structure.

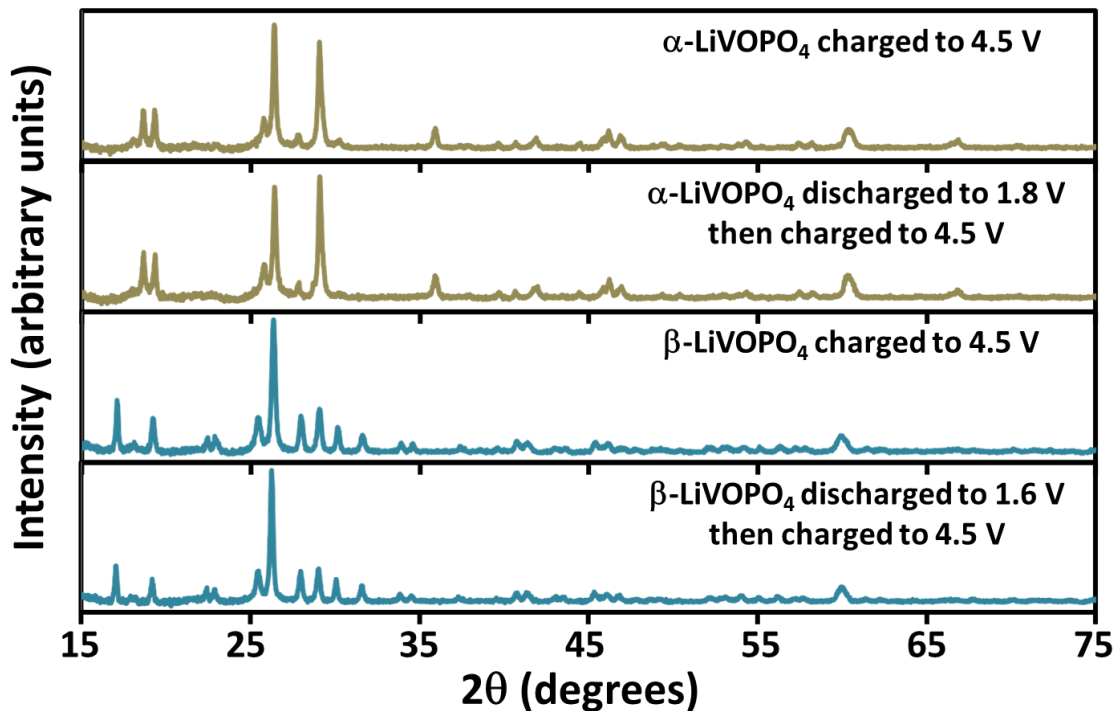


Figure 6.12. *Ex situ* XRD patterns of LiVOPO_4 after the pristine material is charged to 4.5 V and after the fully discharged material is charged to 4.5 V.

6.4 CONCLUSIONS

A second lithium ion can be inserted into LiVOPO_4 , increasing its theoretical capacity to 318 mAh/g (albeit half of that capacity occurs at potentials less than 2.5 V), but this process has not been detailed in the literature. To address this, $\alpha\text{-LiVOPO}_4$ and $\beta\text{-LiVOPO}_4$ were synthesized and the lithium insertion process was studied. The materials were chemically lithiated to obtain α and β $\text{Li}_{1.5}\text{VOPO}_4$ as well as α and β Li_2VOPO_4 , and the materials were also electrochemically lithiated for *ex situ* XRD. The

XRD patterns show clear changes from the starting materials and are also significantly different from patterns available in the literature. FTIR and XRD measurements on the chemically lithiated phases suggest that lithiation into the α -LiVOPO₄ polymorph proceeds such that some excess Li can be accommodated in the structure before a phase change occurs at which point there is a large single-phase region. Lithiation of the β -LiVOPO₄ polymorph is more consistent with the formation of a two-phase mixture with little solid solution between the two phases. More analysis needs to be done to determine the structures of the new phases that form upon lithiation.

Chapter 7: Microwave-assisted Solvothermal Synthesis of TiO₂ Thin Films

7.1 INTRODUCTION

Thin-film synthesis is of interest for many applications ranging from solar cells, thin-film batteries, electronics, photochemical water splitting, and sensors. Conventional techniques for growing thin films typically require expensive, time consuming, and energy intensive processes such as sputtering and vacuum deposition, which then require high-temperature heating to crystallize the materials. These conventional deposition and heating methods are a major hurdle for certain applications. For example, synthesizing anatase-phase TiO₂ thin films on indium tin oxide (ITO)-coated substrates is necessary for some types of solar cells such as inorganic-organic hybrid cells [124]. However, anatase films are conventionally grown by spin coating a Ti sol-gel precursor onto ITO and then heating above 450 °C [125]. This precludes the use of flexible plastic substrates since they will melt at temperatures above 100 - 300 °C. Therefore, this application requires innovative new synthesis methods allowing films to be grown at low temperature in order for flexible solar cells to be fabricated directly on plastic substrates.

Thin-film batteries are another example of an application that is limited by existing high-temperature synthesis methods. Conventional thin film electrode deposition methods for thin-film batteries such as chemical vapor deposition, spray pyrolysis, pulsed laser deposition, vacuum evaporation, and sputtering [76-79] also can be problematic because they are expensive, slow, and stoichiometry control of the electrode materials is difficult [126, 127]. This is especially challenging for ternary element cathode materials for which the performance is intimately linked to the stoichiometry. Furthermore, the deposition has to be performed at high temperatures or the films need to be post-heated to obtain crystalline phases [76, 126, 127]. There is speculation in the literature that low-

temperature processing methods could reduce manufacturing cost, but there are very few low-temperature deposition methods and generally these methods lead to poor performance compared to materials synthesized at conventional temperatures [76, 128-132]. In response to difficulties obtaining crystalline and stoichiometric electrode films by traditional deposition methods, a few sol-gel methods have been developed during which the sol-gel is spin-coated onto the substrate and sintered at high temperature to obtain crystalline phases, as is necessary for high capacity and cyclability in batteries [126, 127, 133]. To deposit thick films, this process sometimes is repeated several times.

TiO₂ is an attractive candidate electrode material for lithium-ion thin film batteries owing to its good lithium intercalation reversibility and safety advantages [79, 134]. As the low-temperature deposition of TiO₂ thin films is of interest for several different energy applications, including solar cells and thin-film batteries, among others, a low-temperature microwave-assisted solvothermal method (MW-ST) is developed here to grow thin films of TiO₂ on ITO-coated glass. ITO on glass is not a traditional substrate for thin-film batteries because it is too expensive to be used as a current collector and is not flexible. However, ITO has been used previously in the literature as the current collector to evaluate TiO₂ for thin-film battery applications [79]. Thus, growing thin films of TiO₂ on ITO serves as a demonstration that the microwave-assisted solvothermal method can be used to deposit electrode films for use in solar cells and thin-film batteries. As will be discussed, TiO₂ on ITO is only one example to demonstrate that thin films can be deposited at low temperatures by a MW-ST process, and other materials/substrates may prove more useful for thin-film batteries.

Thin-film growth in solution is inherently a difficult process because there is a competition between the bulk homogeneous nucleation of particles in solution and

heterogeneous nucleation on a substrate inside of a growth solution. In order to grow thin films in solution, the conditions must be tuned to favor heterogeneous nucleation. Microwave irradiation has previously been shown to create an environment that can favor heterogeneous nucleation [135, 136]. However, the mechanism by which this process occurs has not been adequately understood. The results presented here indicate that the films grow on ITO because the ITO layer absorbs microwaves more readily than the solution, which leads to ohmic heating of the ITO layer. Consequently, the hot surface acts to catalyze nucleation of the TiO_2 film, leading to preferential nucleation and growth on the surface. Therefore, it is likely that many different materials can be grown on a variety of microwave absorbing layers including metal and highly conducting oxides like ITO. The MW-ST process should make it possible to deposit crystalline, stoichiometry-controlled thin films, thus reducing film deposition and sintering into a single, rapid step performed at low temperatures. This could provide a means for depositing thin films on plastics and other low-melting-temperature substrates.

Furthermore, the MW-ST process is of interest because it demonstrates the importance of the ‘specific’ microwave effect known as ‘selective heating’ [82, 83, 84]. It is well-known that microwave-assisted synthesis processes can drastically reduce reaction times compared to conventional solvothermal processes carried out using acid digestion vessels in a furnace, as has been demonstrated in previous chapters. However, there are also sometimes other anomalous results that cannot always easily be explained by simple thermal effects such as the fast ramp rates achieved during microwave synthesis [82-84]. There is much controversy regarding whether anomalous results are directly caused by microwave interaction with the material in question. Since materials have differing abilities to absorb microwaves, they will heat (‘selectively’) at different

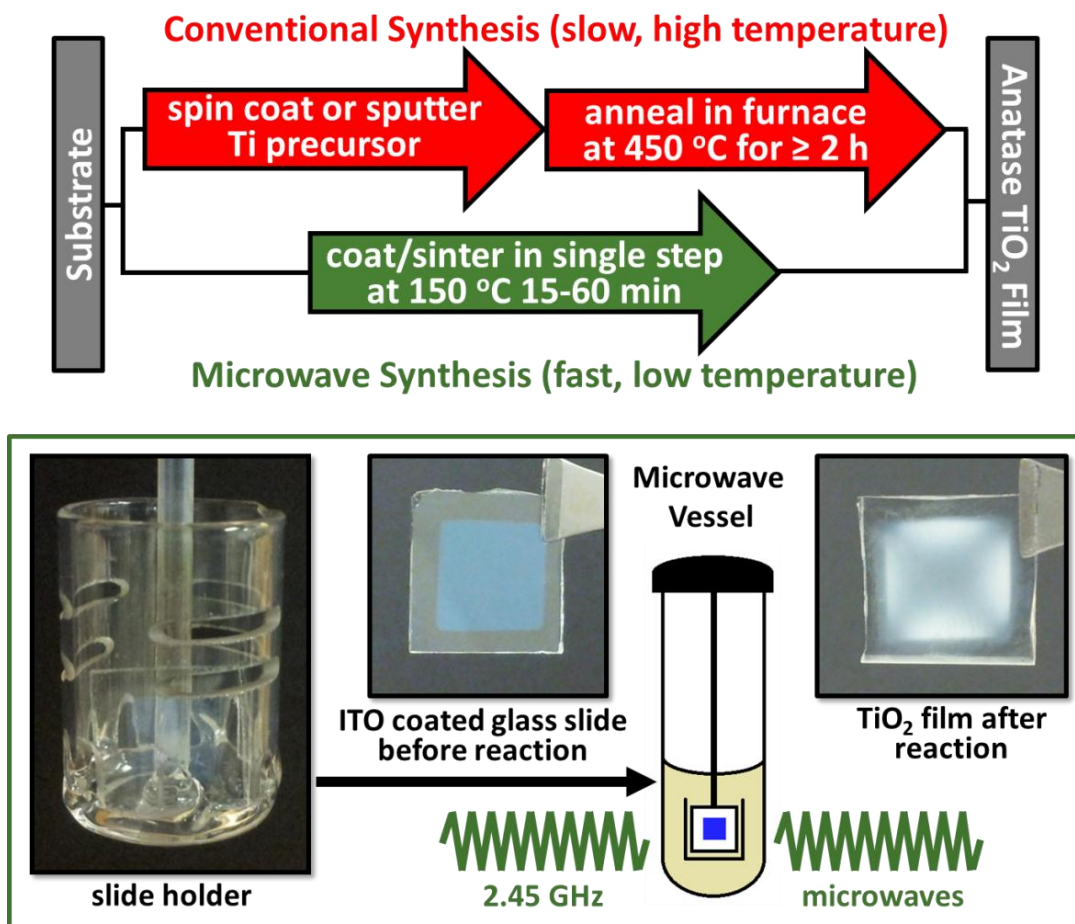
rates under microwave radiation. Although selective heating is recognized as a reality in microwave synthesis, whether the selective heating directly has an effect on the product is controversial. It is shown that growth of the TiO_2 thin films demonstrated here is critically dependent on selective heating of the microwave absorbing ITO layer.

7.2 EXPERIMENTAL

A typical experiment involved mixing 20 mL of tetraethylene glycol (TEG) and 5 mL of a Ti containing sol-gel in 80 mL quartz vessels. The sol-gel consisted of a mixture of 10:1:1:1:1 ethanol : tetrabutyl orthotitanate (TBT) : acetic acid : acetylacetone : deionized water [137]. The sol-gel was aged for one week before using. Indium tin oxide (ITO)-coated glass slides (sheet resistance $\sim 10 \text{ } \Omega/\square$) and polyethylene terephthalate (PET) slides (sheet resistance $\sim 30 \text{ } \Omega/\square$) were purchased from Nanocs (New York, NY), cut into $\sim 1 \text{ cm}$ by 1 cm squares, and patterned as described elsewhere [138]. Deposition of Al metal (150 nm) was prepared by thermal evaporation also as described elsewhere [138]. Deposition of high resistance ITO (sheet resistance $\sim 450 \text{ } \Omega/\square$) layers on glass substrates was achieved by magnetron sputtering of an In_2O_3 : SnO_2 (10 wt. % SnO_2) sputtering target (99.99% purity, Kurt J. Lesker company) onto soda-lime glass substrates with an RF power supply of 75 W with an Ar working pressure of 3 mTorr under a base pressure of 8.75×10^{-5} Torr for 60 min.

The ITO and metal-coated substrates were then hung from the vessel caps in custom-designed glass baskets, as is shown in Schematic 7.1. The vessels were positioned on a rotor (4 vessels at a time) that was spun on a turntable inside an Anton Paar Synthos 3000 microwave reactor operated at 2.45 GHz. Stir bars were added to ensure efficient mixing and the vessels were sealed. The solution temperature was measured with infrared sensors, which were calibrated to an internal temperature probe.

Reactions were ramped with a power rate of 10 W/min until the temperature reached 150 °C, and that temperature was held for 60 min in a typical experiment. However, these conditions were widely varied, as will be discussed. After the reaction, the solutions were convectively cooled, and the resulting TiO₂ films were washed and sonicated in deionized water, acetone, and ethanol to remove leftover solvent and precursors.



Schematic 7.1. Comparison of the MW-ST synthesis to conventional thin film deposition (top) with a summary of synthesis method and resulting TiO₂ thin films (bottom). The blue square shown on the glass slide is ITO that was patterned onto the slide by chemical etching.

7.3 RESULTS AND DISCUSSION

Synthesis condition optimization and film growth mechanism

Heterogeneous growth of a thin film selectively onto a substrate requires extensive optimization of synthesis conditions. One of the first steps in optimizing the film growth was selecting an appropriate additive for the growth solution so as to dilute the Ti sol-gel precursor. The growth solution always consisted of 5 mL sol-gel and 20 mL of solvent additive. The solvent additives used in the reaction vessels were ethanol and tetraethylene glycol (TEG) in varying amounts. Initial tests were performed with ethanol as an additive, but anatase formation was found to be favored by using TEG instead. Figure 7.1 shows GIXRD patterns for films grown with using various ratios of TEG and ethanol as additives at 140 °C. Films grown in solutions containing more TEG led to small peaks beginning to form at around 25 degrees, which corresponds to the largest peak for anatase TiO₂.

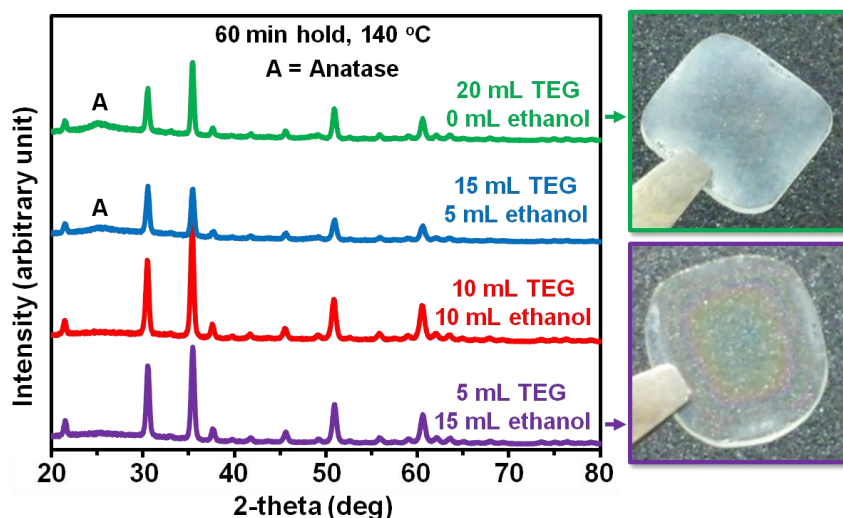


Figure 7.1. GIXRD patterns for films grown with a 60 min hold time at 140 °C. Films are grown with varying amounts of TEG and ethanol as additives, but all growth solutions contained 5 mL of Ti sol-gel.

Because adding TEG to the sol-gel led to anatase formation at lower temperatures than with ethanol as an additive, the sol-gel recipe was then prepared with TEG as the solvent rather than ethanol. Attempts to grow films with a TEG-based precursor led to thin and non-uniform films. Thus, it was concluded that the optimum films are grown with a mixture of an ethanol based sol-gel and TEG as an additive in the microwave vessels.

Initial testing was also performed at a variety of temperatures to determine the temperature range at which anatase formed. Figure 7.2 shows GIXRD patterns for films grown in solutions consisting of 5 mL sol-gel, 15 mL ethanol, and 5 mL TEG. It is clear that films grow even at 120 °C, as indicated by the rainbow fringe pattern on the slide. However, no anatase formation is detected in GIXRD patterns at low temperatures. As the temperature increases, the films become white in color, and the anatase phase (at 25°) is detected in the GIXRD patterns. The anatase peak at 25° was strongest for the film grown at 150 °C. At higher temperatures, the films become thick and begin to chip off. At lower temperatures, the films are thin and amorphous. At 180 °C, additional rutile peaks appeared, and the slide cracked into several pieces, which will be discussed in more detail in a subsequent section. It should be noted that this test was run with 5 mL sol-gel and 20 mL of ethanol, in contrast to the rest of the slides in Figure 7.2. For safety reasons, the test at 180 °C was not repeated with different ratios of additives.

Some ITO-coated slides were also patterned with smaller square ITO layers chemically etched onto them, as shown below in Schematic 7.1. The slides were patterned because in device applications, films need to be patterned into a variety of shapes. Also, patterning the slides was found to be useful to avoid cracking of the films. The edges of the glass are jagged due to rough cutting of the slides. The rough edges lead

to small cracks on the edges of the ITO film, which can propagate during the rapid heating occurring in the MW-ST process. The effect of temperature on film growth is shown in Figure 7.3 for patterned ITO-coated glass slides. Similar to the non-patterned slides, the optimum film growth occurred at 150 °C. It is also noteworthy that the TiO₂ films form only on the ITO layer and not on the surrounding glass, which will be further discussed in a subsequent section. Conventional thin-film growth, in contrast, requires an additional patterning step after the thin film has been deposited and sintered.

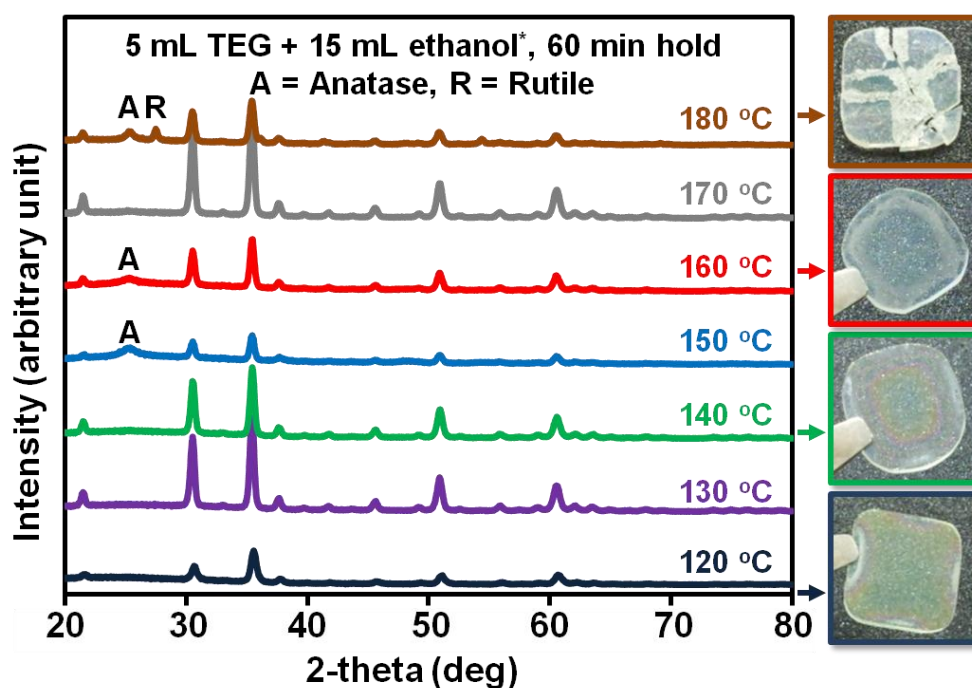


Figure 7.2. GIXRD patterns of films grown with a 60 minute hold time at various temperatures with 5 mL sol-gel, 15 mL ethanol, and 5 mL TEG *except for the film at 180 °C, which was grown in 5 mL sol-gel and 20 mL ethanol.

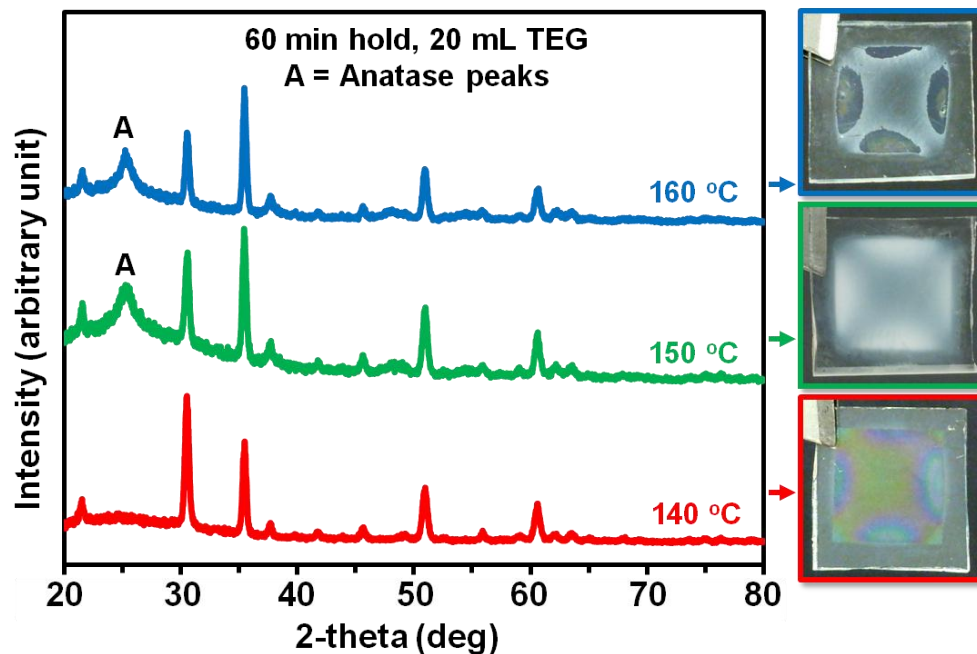


Figure 7.3. GIXRD patterns of patterned films grown with a 60 minute hold at various temperatures. Films are grown with 5 mL sol-gel and 20 mL TEG.

The dependence of reaction time on thin-film growth for the patterned and non-patterned slides was also studied, as shown in Figure 7.4 and Figure 7.5. It is clear that the most uniform films are grown for reaction times of 60 min or less. For non-patterned slides, the anatase peaks become larger with increased reaction time until the films begin to flake off after 75 – 90 min, but anatase peaks can be detected for all reaction times. GIXRD of the patterned slides (Figure 7.5) shows similar trends, but the films were found to be amorphous if only allowed short reaction times. It should also be noted that at higher temperatures, shorter reaction times were required to obtain crystalline films, although only the effects of time variation at 150 °C are shown here.

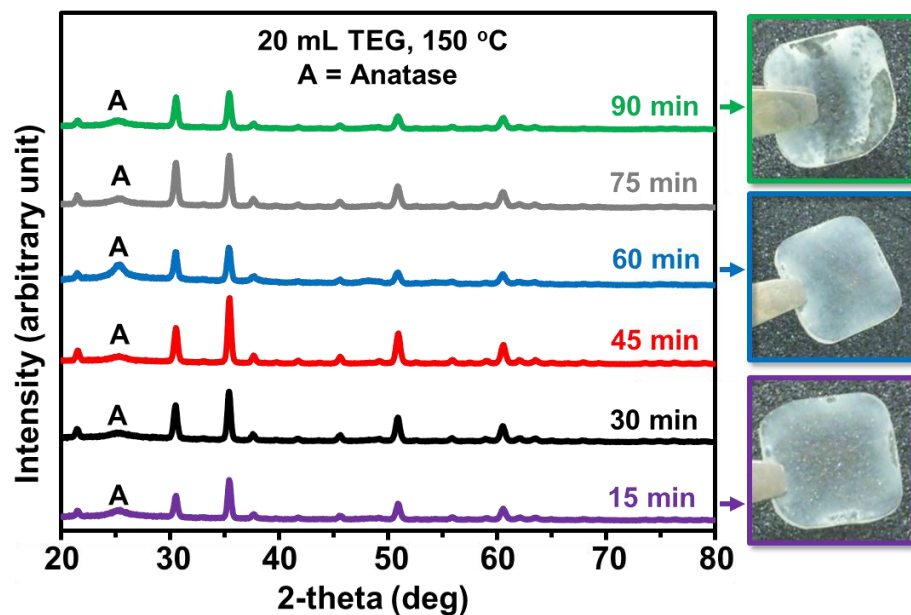


Figure 7.4. GIXRD patterns of films grown at 150 °C for various hold times. Films are grown with 5 mL sol-gel and 20 mL TEG.

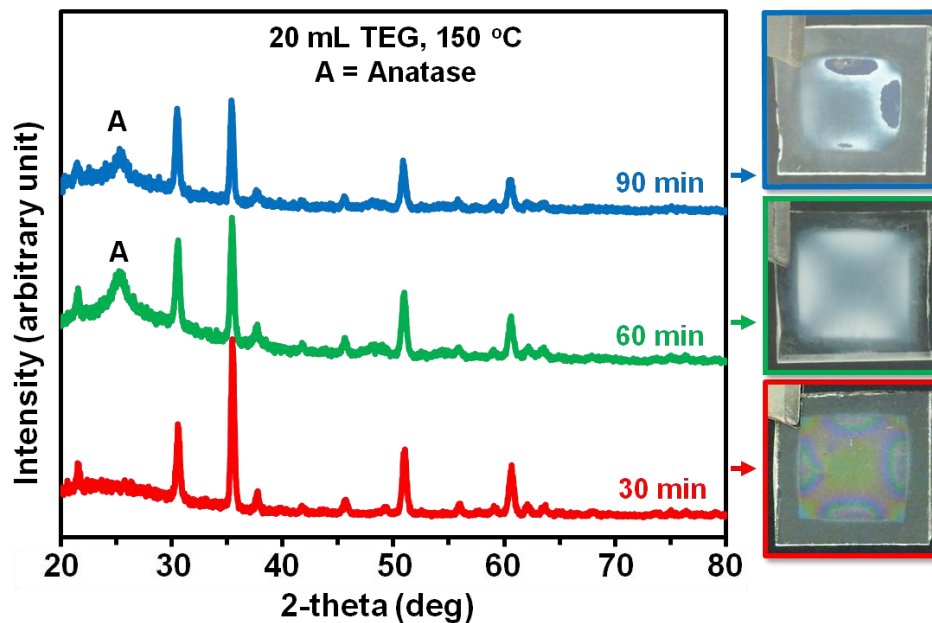


Figure 7.5. GIXRD patterns of patterned films grown at 150 °C for various hold times. Films are grown with 5 mL sol-gel and 20 mL TEG.

The ITO-coated glass slide orientation proved to have a dramatic effect on TiO_2 film growth. GIXRD patterns of films grown in vertical and horizontal orientations are shown in Figure 7.6, along with pictures of the custom-designed glass holders with the slide positions depicted. Clearly the anatase peaks are much stronger for the films grown in the vertical orientation. The anatase peaks agree with visual inspection of the films, which suggests very thin films form in the horizontal orientation. Similar results were observed for the patterned and non-patterned ITO-coated slides. Cross-sectional SEM confirms that the films grown oriented horizontally are much thinner than the vertically oriented films, as described elsewhere [138]. Also shown elsewhere are high-resolution transmission electron microscopy (TEM) imaging and Raman spectroscopy data for the optimized films, which further confirm formation of anatase [138].

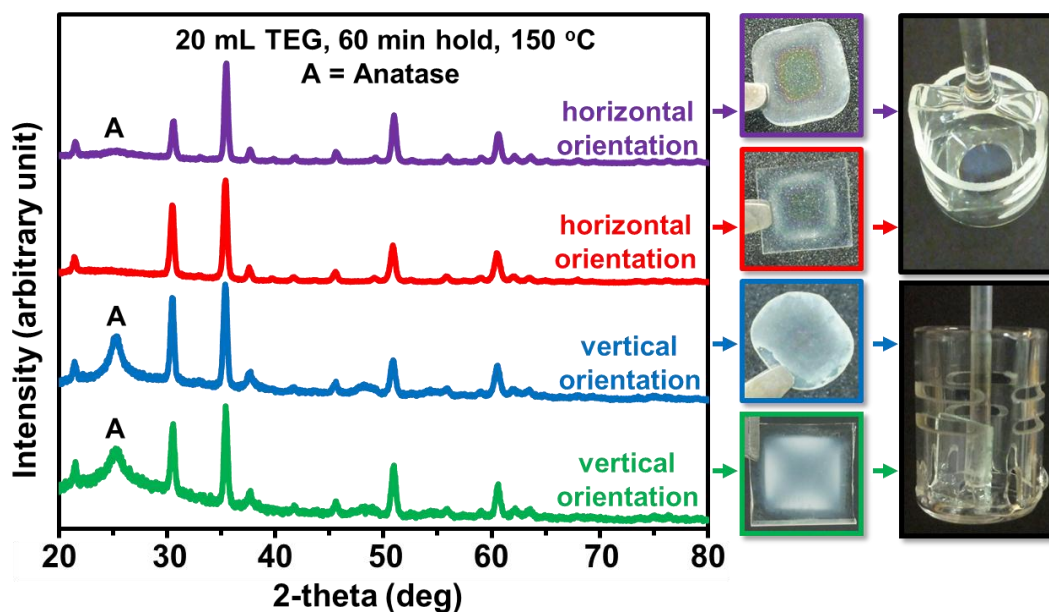


Figure 7.6. GIXRD of films grown on ITO-coated glass slides at 150 °C with a 60 minute hold time in solutions consisting of 20 mL TEG and 5 mL sol-gel.

The morphology of these films was also examined, as shown by SEM micrographs in Figure 7.7. The films are very dense, flat, and uniform, with few features. Films grown under optimized conditions were found to strongly adhere to the ITO, likely due to the strong oxide-oxide bonding between TiO_2 and ITO. Sonicating the films for 10 min in various solvents did not damage them. Cross-sectional SEM was used to determine the film thickness, which was found to be one the order of 1-2 μm for slides grown at 150 $^\circ\text{C}$ with a 60 min reaction time. Many cross-sectional SEM micrographs [138] were imaged for many different conditions, and the micrographs confirmed that the films grown at low temperature or short times were thinner and those grown at high temperature and long reaction time were thicker, as expected from visual inspection and by GIXRD measurements. The cross sectional SEM results provide evidence that there is a very dense and strongly adhered underlayer with a less dense outerlayer (dense underlayer shown here in Figure 7.7) [138].

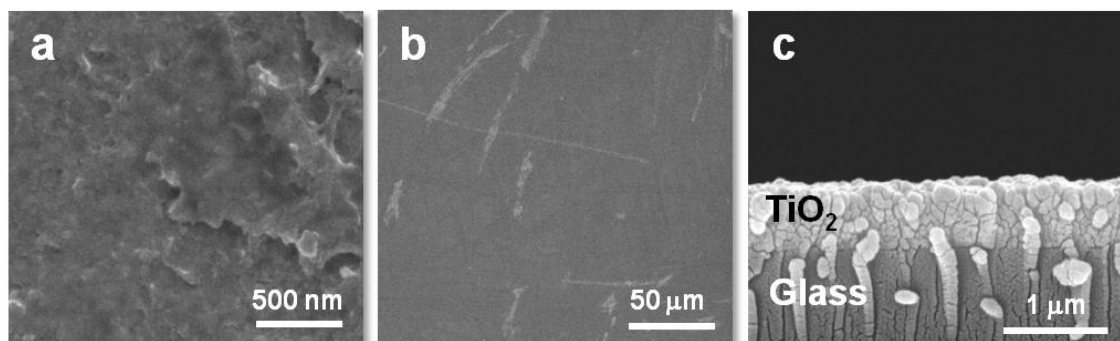


Figure 7.7. TiO_2 film grown at 150 $^\circ\text{C}$ for 60 min reaction inside microwave reactor with 10 W/m power ramp rate. A large area SEM view is shown in (b), and a magnified region is shown in (a). A cross sectional image reveals a thickness of approximately 800 nm in (c).

Selective heating of the ITO layer

Several observations from the results shown in the preceding section can provide insight into how and why these films grow. The first of these observations is that the film grown at 180 °C, shown in Figure 7.2, cracked into several pieces. Glass substrates heated under the same conditions without the ITO layer did not crack at 180 °C or any other temperature tested, so one can conclude that the presence of the ITO layer causes the cracking. ITO is a strong microwave absorber resulting in rapid ohmic heating during the microwave process. Contrastingly, glass does not absorb microwaves, so it heats slowly by thermal convection from other microwave absorbing species in the vessel (solution and ITO layer). Therefore, it is reasonable to theorize that the ITO selectively absorbs microwaves and heats, thereby providing a hot surface to catalyze TiO₂ film nucleation and growth. As the temperature is ramped (by increasing the microwave power), it is likely that there is a large thermal gradient between the microwave absorbing ITO layer and the insulating glass substrate during this non-equilibrium process. This, in turn, could cause significant thermal expansion mismatch at the interface between the glass and ITO layer, which could cause the slide to crack due to the corresponding mechanical strain. Alternatively, this could be a thermal shock phenomenon.

The patterned slides further support the argument that the ITO selectively absorbs microwaves and acts as a hot nucleation site for the TiO₂. If the ITO layer acts as a nucleation site for the film to grow because it absorbs microwaves and heats faster than other surfaces in the vessel, then the films should grow only on the patterned ITO. This is indeed what occurs; the films form selectively on the square ITO layer (Figure 7.3, Figure 7.5, and Figure 7.6) and not on the surrounding glass from which the ITO has been etched away chemically. Furthermore, the TiO₂ films did not form at any temperature tested for glass slides suspended in the growth solution without an ITO layer.

For the MW-ST films, once the TiO_2 nucleates on the ITO, it is likely easy to form a well-adhered film due to oxide-oxide bonding between the TiO_2 and ITO.

Another interesting observation regarding these films is that they are non-uniform. The films are thickest at the edges and thinnest in the middle, as has been confirmed by cross-sectional SEM. The thickness variation is obvious upon visual inspection, as is demonstrated in Figure 7.8 for a variety of chemically etched ITO patterns and the resulting films after microwave reaction. Collaboration with a computational group specializing in electromagnetic simulation provided insight regarding the film growth pattern. The experimental setup was simulated with the integral form of Maxwell's equations. The electric field, conduction current density, and the absorbed power can all be calculated from the model (see [139]).

Simulations showing the time-averaged absorbed microwave power density (in units of dB) are shown in Figure 7.8. It is clear that the model independently predicts increased microwave power absorption on the edges of the ITO layers. Despite the large wavelength of the microwaves (> 10 cm), there is still a distinguishable field interaction with the small ITO patterns (~ 1 cm) such that current and power absorption are highest at the edges. This occurs because the incident microwaves are distorted by the ITO layer, but the perpendicular components of the electric and magnetic fields must be continuous at the boundaries between the ITO layer and the solution or glass. As a result of the mismatch in the properties between the conductive ITO and the dielectric solution/glass at the boundary, the electromagnetic field and the current density will be highest near the edges. Another way to think about this is that currents tend to repel one another. In the middle of the slide, there are currents coming from all directions, so the currents can effectively repel one another. At the boundary between the ITO and the glass, there is

current density on the ITO side of the boundary, but not on the glass side, so the current density can collect at the ITO edges.

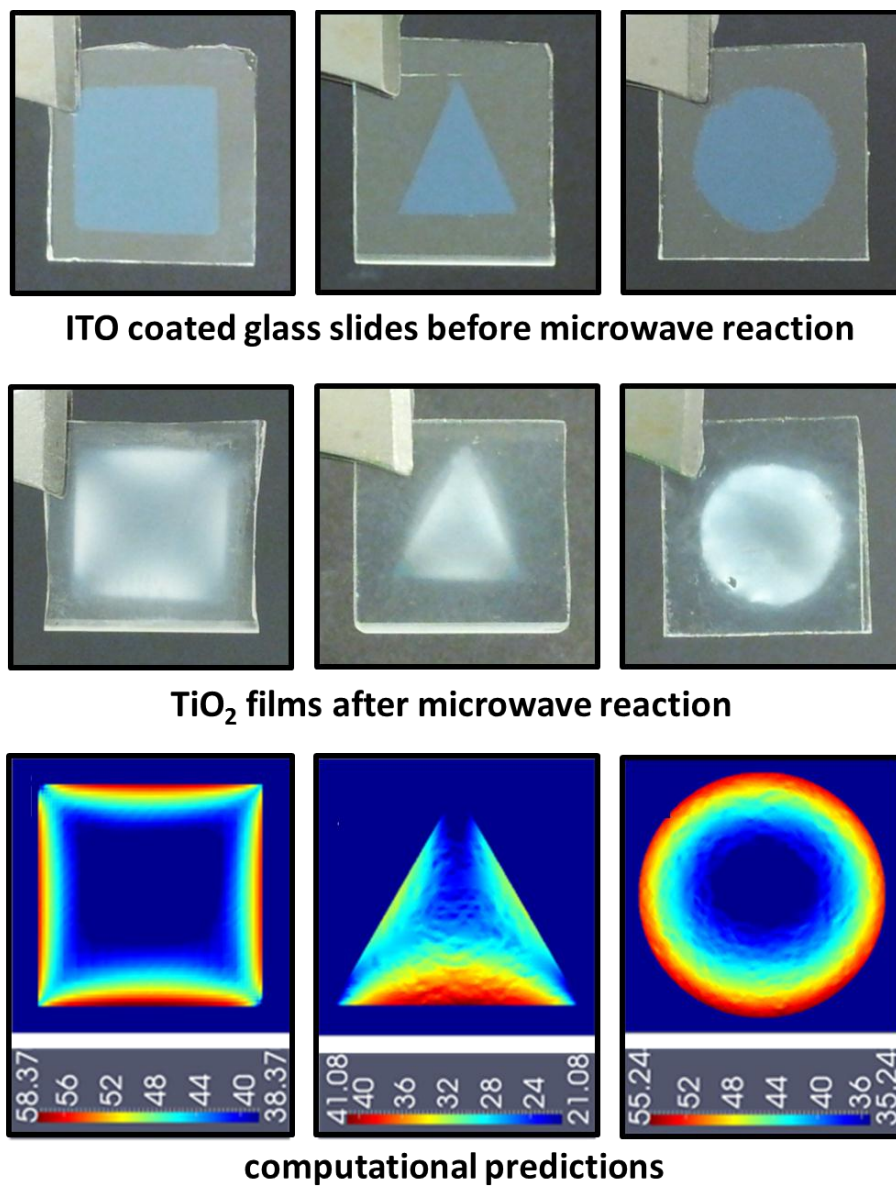


Figure 7.8. Various ITO patterns before the microwave reactions, TiO_2 films grown on ITO after microwave reactions, and computational predictions showing the time-averaged absorbed power density in the ITO layer (units of dB).

The absorbed power distributions correlate well with the experimentally observed film growth patterns. Although the model does not explicitly calculate heat transfer, the absorbed power will be converted to heat by ohmic heating. The edge effects shown in Figure 7.8 are likely to be smeared to some degree by thermal conduction in the ITO layer, which is not included in the model.

Another important observation that can be explained by the simulations is that the patterned slides do not show anatase peaks in the GIXRD patterns for films grown at 140 °C for 60 min or at 150 °C for 30 min (Figure 7.3 and Figure 7.5) in contrast to the comparable non-patterned slides (Figure 7.1 and Figure 7.4). TiO₂ films form on the ITO for the patterned slides as well, as indicated by visual inspection of the films and confirmed by EDS, but the films are amorphous. These differences between the GIXRD patterns for the patterned and non-patterned slides held at 140 °C for 60 min and 150 °C for 30 min were theorized to be due to the different sizes of the ITO layers.

To test this theory, the ITO was patterned with four squares that were approximately half the dimensions of the typical ITO square size (pictured in Figure 7.9), keeping the total area of the ITO layer constant. Attempts to grow films on this substrate were unsuccessful under normal reaction conditions (150 °C for 60 min). In order to grow films on the smaller ITO features, the power had to be increased significantly, which equated to a temperature of 170 °C rather than 150 °C. Furthermore, each of the four small squares was found to have edge effects similar to the larger squares. The simulations confirmed that the smaller ITO patterns absorb less power, in agreement with the experimental observations that the power had to be increased to grow films.

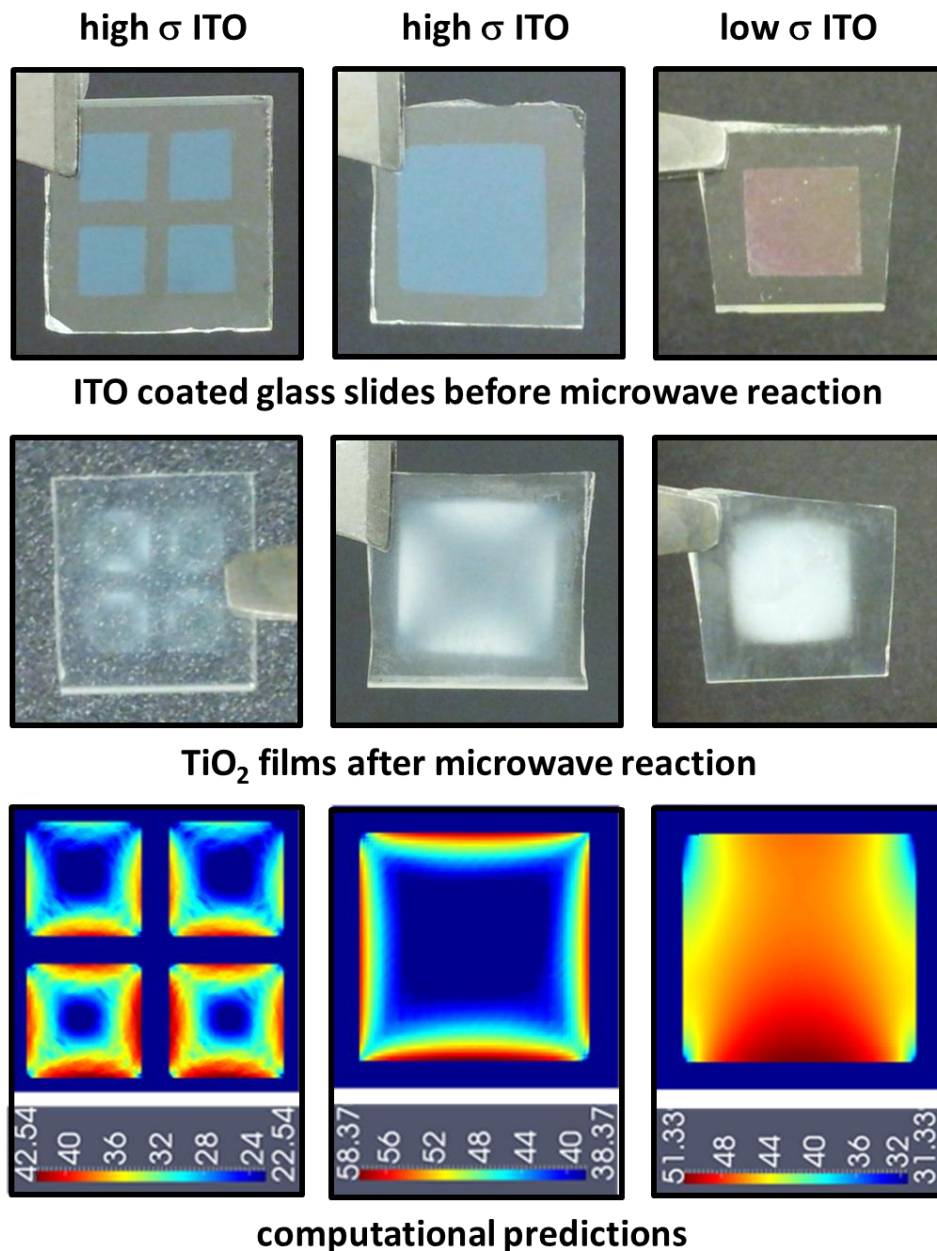


Figure 7.9. Simulations of the time-averaged absorbed power density in the ITO layer (units of dB) compared to experiments detailing the effects of ITO pattern size and ITO sheet resistance. Note that the sheet resistance of the ITO for the left and middle columns is $10 \Omega/\square$ for simulations and experiments. The resistivity of the ITO on the right is $1000 \Omega/\square$ for the simulations and 450 ohm/sq for the experiments.

The size effect is expected if selective microwave heating is important because as the microwave absorbing layer becomes smaller, there is a larger difference between the effective microwave wavelength and the ITO layer dimensions, reducing the efficiency of the absorption between the microwaves and the small ITO patterns. The film formation shown here is found to be dependent on the size of the patterned features, which further suggests that direct interaction with the microwave field is responsible for film growth.

Since the model was found to agree well with experimental observations, the model was then used to identify conditions that could lead to more uniform films, which would be more desirable for device applications. The simulations predicted that more uniform films could be obtained by lowering the microwave frequency or increasing the sheet resistance of the ITO layer, as is discussed in more detail elsewhere [139]. The effect of conductivity on absorption of microwave power is complex. As the conductivity increases, so does the absorption coefficient, but the reflectivity also increases at the boundaries, so the microwave field is largely rejected by the conducting material. However, if the conductivity is too low, the material only weakly absorbs microwave power because electrons cannot be effectively excited by the field. Thus, there exists an optimum conductivity where maximum microwave power absorption occurs throughout the layer. Also, if the conductivity is too low, there is less difference in the properties between the conductive layer and the surrounding dielectric materials (solution and glass), so there is not as strong of an edge effect and microwave power is absorbed more evenly.

Based on the predictions suggesting that lower conductivity would lead to more uniform films, films were grown on ITO with a sheet resistance of approximately $450 \text{ } \Omega/\square$ and are compared to films grown on $10 \text{ } \Omega/\square$ slides in Figure 7.9. Clearly, more

uniform films are grown on higher resistance ITO as predicted. It also took less time to obtain these films, which is in further accordance with the predictions. The simulations predict higher power absorption for the higher resistance ITO, and higher power absorption should lead to more pronounced selective heating and consequently higher temperature and less time to obtain crystalline films.

Attempts to grow films by conventional solvothermal method

The non-uniformity of the films (edge effects), the orientation effects, the size dependence on film growth, and the effect of conductivity on the film growth all support the argument that the films grow due to specific microwave interaction (selective heating) with the ITO layer. This is further confirmed by excellent agreement between simulations and experimental observations. Since the film growth was found to be dependent on interaction with the microwave field, it was of interest to attempt to grow films by conventional solvothermal experiments for comparison with the microwave-assisted solvothermal experiments.

To see whether the film growth could be replicated without the microwave field, 5 mL of sol-gel was mixed with 20 mL of TEG in 45 mL Paar 4744 acid digestion vessels. ITO-coated glass slides were positioned on custom-made glass holders to keep the slides in vertical orientations similar to the microwave experiments. The vessels were then sealed and placed in a preheated furnace to achieve the fastest ramp rate possible. The reactions were held at 150 °C and 180 °C for 2 - 72 h. Because reaction times for conventional solvothermal synthesis are generally much longer than for microwave synthesis reactions, the reaction time was varied over a wide range. The results are summarized in Table 7.1.

At 150 °C, the ITO-coated glass slide did not change in any detectable way. The resistance of the ITO was the same before and after the reaction and the ITO showed no color change. However, an anatase phase precipitate formed in solution after the 8 h, 24 h, and 72 h experiments at 150 °C, although the patterns were weakly crystalline at shorter times. During the microwave reaction, only the solution temperature can be measured. Since the ITO selectively absorbs microwaves, it is likely that the temperature of the ITO is warmer than the temperature of the glass and the surrounding solution (which is the temperature measured in the microwave). Note that the temperature of the slide cannot be too much warmer than 150 °C during the microwave reaction because films were also grown on plastic substrates (which will be discussed later) without melting or deforming the substrates.

Table 7.1. *Summary of results for conventional solvothermal synthesis tests. ITO-coated glass slides were placed in acid digestion vessels containing 5 mL sol-gel and 20 mL TEG for times ranging from 2-72 h at 150 and 180 °C.*

Temperature (°C)	Time (h)	Change in ITO Resistance (Ω/\square)	ITO Color After Synthesis	GIXRD of Slide	XRD Solution Precipitate
150	2	none	blue	no anatase	no precipitate
150	8	none	blue	no anatase	anatase
150	24	none	blue	no anatase	anatase
150	72	none	blue	no anatase	anatase
180	2	none	blue	no anatase	amorphous
180	8	none	blue	no anatase	anatase
180	24	16 \rightarrow 23	yellow and pink	no anatase	anatase
180	72	16 \rightarrow 24	yellow and pink	no anatase	anatase

To see whether a higher temperature was needed, the conventional solvothermal tests were also run at 180 °C. After 2 and 8 h, the slide results were similar to the results

at 150 °C. After 24 h, the slide had copious amounts of white precipitate loosely bound to both sides (the ITO and glass surfaces), as shown in Figure 7.10. However, the powder fell off easily when cleaning the slide with a deionized water squirt bottle.

The results summarized in Figure 7.10 are in striking contrast to the microwave synthesized slides, which can be washed and even sonicated for 10 minutes without damaging the films. Furthermore, the film forms selectively on the ITO layer in the microwave process rather than powder from solution loosely bound to both sides of the slide, as was seen in the conventional solvothermal samples at 180 °C. Also notable was an increase in the ITO resistance and color change of the ITO layer for the slides held at 180 °C for 24 and 72 h. Since the color change could be indicative of a TiO₂ film, the films were analyzed by GIXRD (Figure 7.11) and EDS (Figure 7.12). No anatase was detected by GIXRD. Correspondingly, EDS shows no Ti signals in contrast to the large Ti peaks for the microwave deposited films.

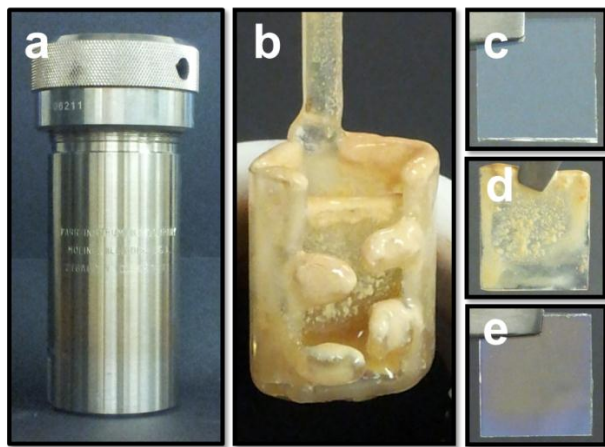


Figure 7.10. Conventional solvothermal reactions were performed in the vessel shown in (a) on ITO-coated glass slides (c). After the reaction at 180 °C for 72 h, the glass holder and slide were covered with off-white precipitate (b and d). This was easily washed to produce the slide shown in (e).

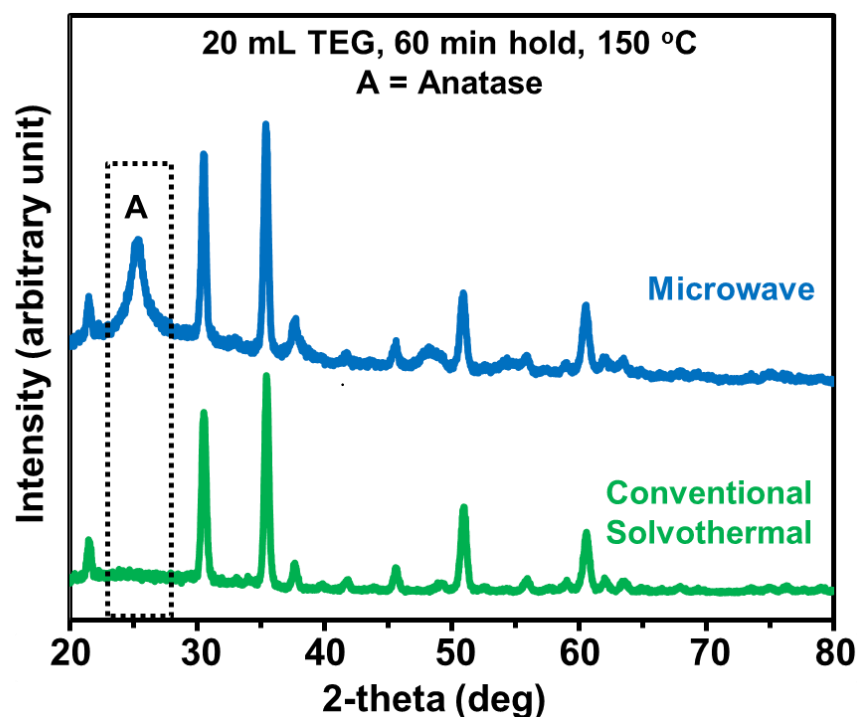


Figure 7.11. GIXRD of the ITO-coated glass slide (pictured in Figure 7.10) after the 180 °C reaction held for 72 h compared to a microwave-synthesized film.

Another important observation is that the solution precipitate was identified as anatase TiO_2 for almost all of the conventional solvothermal reactions, so the temperature was definitely high enough and the time was long enough to form crystalline anatase. Furthermore, there was little change between the results after 24 and 72 h, indicating that holding the time for longer would likely not change the results. The color change of the slide may be due to sol-gel sticking to the slide. Even letting a small amount of the sol-gel dry on glass at room temperature leads to hydrolysis of the sol-gel and a very thin Ti film. However, the sol-gel will not lead to anatase unless annealed.

The color change and increase in resistance could also be due to indium diffusion in the ITO layer due to the prolonged hold time at 180 °C. In summary, heating the

solution conventionally did not lead to film growth. These results support the argument that growth of the TiO_2 thin films is dependent on the selective heating of the ITO layer by direct interaction with the microwave field.

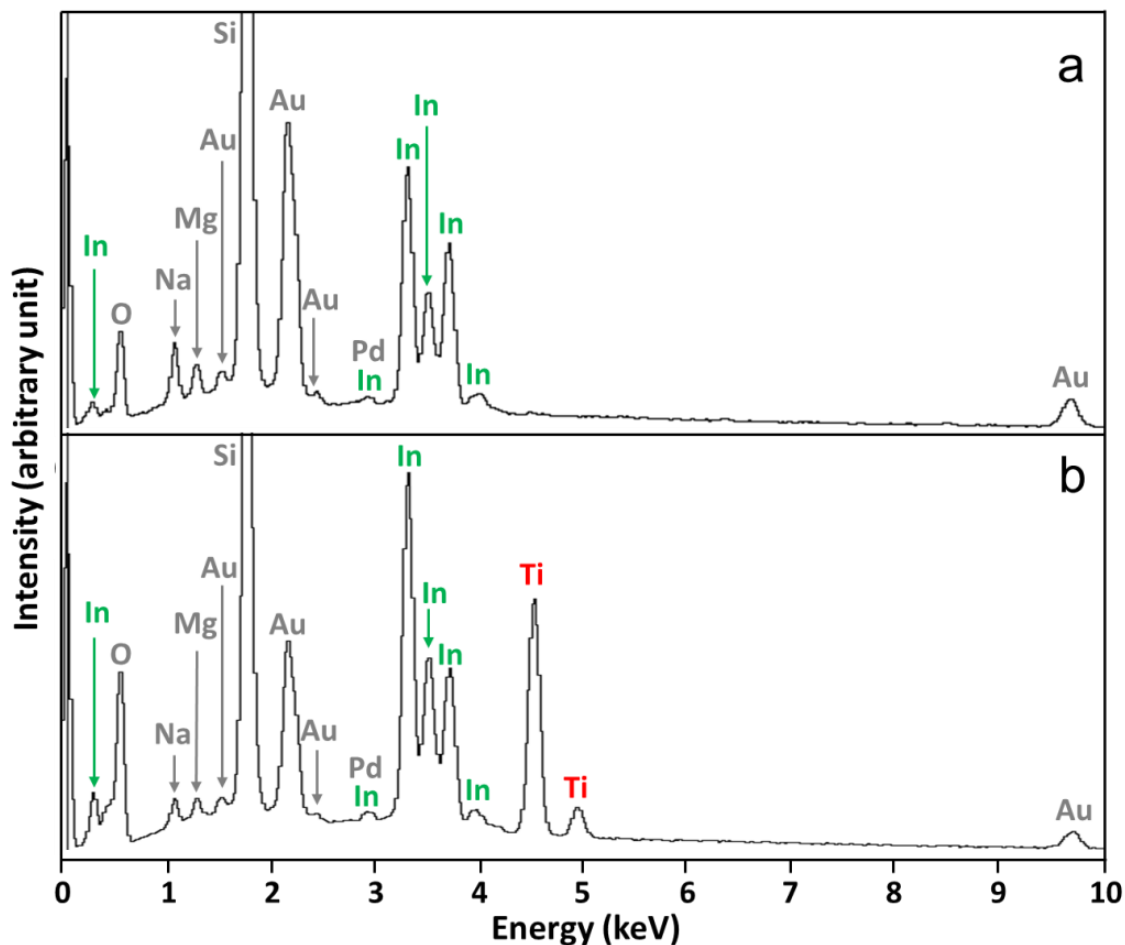


Figure 7.12. EDS results of the ITO-coated glass slides (a) after solvothermal reaction at 180°C for 72 h and (b) after microwave solvothermal deposition at 150°C for 60 min with a 10 W/min power ramp rate. Both growth solutions contained 5 mL sol-gel and 20 mL TEG.

Film growth in other microwaves

All films discussed thus far were grown in an Anton Paar Synthos 3000 microwave reactor, a multi-mode reactor in which four or eight vessels can be used during a single reaction. There are two magnetrons located on two adjacent walls, which supply the microwaves. The vessels are placed on a rotor, which spins during the reaction to ensure uniform exposure of the vessels to the microwave field. Because there are essentially two microwave fields that interact with vessels rotating within the resulting field, this setup is very complex. In order to study film growth in a simpler microwave reactor, the synthesis conditions were modified and reactions were run in two mono-mode microwaves (CEM Discover and Anton Paar Monowave). These microwaves are much simpler, each with only one magnetron and only one stationary vessel being irradiated during the reaction.

TiO₂ films were grown with both mono-mode microwaves. Because the software and scale of reaction in these microwaves are different than in the Synthos 3000, the ramping condition had to be changed. In the Synthos 3000, a linear power ramping condition of 10 W/min (corresponding to ~30 min ramping time to 150 °C) was used and the best films were grown after a 60 minute hold time. In the Discover microwave, a constant power of 50 – 70 W was set during the temperature ramping portion of the synthesis, which corresponded to a 5 – 10 min ramp time up to 150 °C. Once the temperature reached 150 °C, the power was then adjusted to maintain the constant temperature. Similarly, in the Monowave, a constant power of 20 – 60 W was set during a 2 – 10 min ramping time to get to 160 °C and the temperature was held at 160 °C for 60 minutes. The Monowave reactions were run at a higher temperature because the ITO patterned squares were etched smaller than in the Synthos and CEM microwave reactions due to the small size of the Monowave vessels.

The films grown in the Synthos 3000 were highly optimized and hundreds of films were grown to test various conditions. Many fewer films were grown in the two mono-mode reactors, so the conditions would require further optimization to obtain highly crystalline films similar to those grown in the Synthos 3000. Regardless, it is interesting to examine the results from initial testing in the mono-mode microwave reactors to demonstrate that the synthesis technique can be adapted to other reactors.

The film growth patterns in the mono-mode microwave reactors appeared visually different than films grown in the Synthos 3000. As shown in Figure 7.13, the films grown in the Synthos 3000 showed thicker regions on all four edges and the thinnest regions at the center and corners. Contrastingly, the films grown in the mono-mode microwave reactors showed thick regions only on two edges. The pattern is difficult to see on the Monowave slide at 160 °C with a 60 min hold time, so a picture of a film grown after a shorter time is shown to the right.

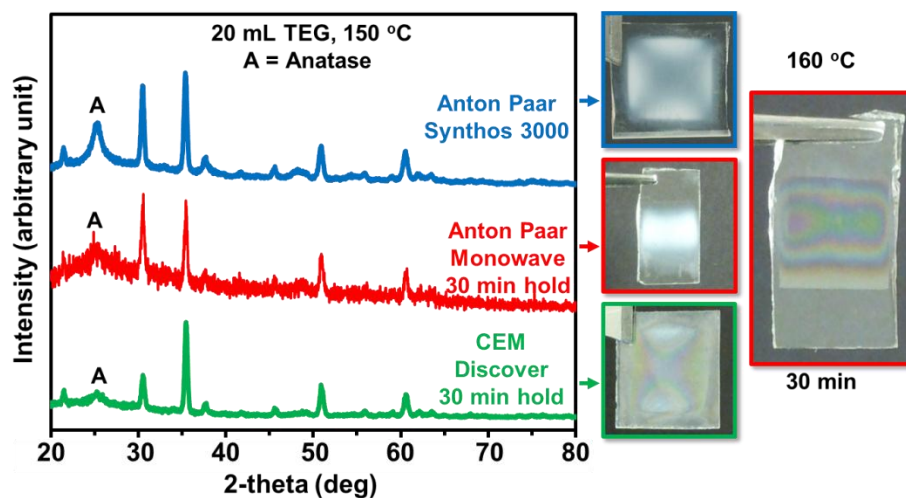


Figure 7.13. Pictures and GIXRD of TiO_2 films grown in three different microwaves. The film grown in the Monowave is a different size because smaller vessels used cannot accommodate larger slides.

The thinnest regions form on the top and bottom of the ITO layer and there are horizontal rainbow patterned fringes showing different thicknesses. Although the thickness variation is difficult to see in the picture, the edges on the left and the right show thicker regions than the middle. The differences in the film growth patterns are likely due to the differences in the electric field generated by the microwaves due to different geometry and whether the vessels are stationary or rotate. The angle of the ITO-coated slide relative to the field was found to greatly affect the power absorption and the edge effects on the ITO in computational simulations.

MW-ST synthesis comparison in SiC and glass vessels

The conventional solvothermal experiments in acid digestion vessels suggest that the microwave irradiation and subsequent selective heating of the ITO layer is critical for film growth, but the vessel geometry and temperature ramp rates are not constant between the conventional and microwave-assisted solvothermal experiments, and these factors could also affect the results. To further confirm the dependence of film growth on the microwave field, reactions were run in glass and SiC vessels in an Anton Paar Monowave microwave reactor. Glass is a poor microwave absorber, so when an ITO-coated glass slide is suspended in TiO_2 growth solution within a glass vessel, the microwave field can interact directly with the solution and ITO layer since the glass vessel does not appreciably absorb microwaves. Contrastingly, SiC is a very good microwave absorber, so if an ITO-coated glass slide is suspended in TiO_2 growth solution within a SiC vessel, the SiC absorbs the microwaves very effectively and prevents microwave absorption by the solution and ITO layer [140]. In the glass vessel, heating occurs by selective ohmic heating of the ITO layer and dielectric/ohmic heating of the solution. In the SiC vessel, the SiC absorbs microwaves and heats through ohmic heating.

The solution and ITO layer are then in turn heated by thermal convection of heat from the hot vessel walls.

A common argument used to dismiss specific microwave effects is that the conditions during microwave heating are difficult to replicate by conventional methods (such as the temperature ramping time) [82- 84, 140]. Because of the small size of the vessels (10 mL) and the very high power available in the Monowave, the solution can be heated very quickly by thermal convection even in the SiC vessel. It has been previously demonstrated that even very poor microwave absorbers can be heated very quickly with the SiC vessel and that the SiC vessel effectively shields the solution from direct interaction with the microwave field [140].

To compare directly heating of the ITO layer by selective heating (in the glass vessel) and by thermal convection (in the SiC vessel), microwave reactions were run with the same heating conditions in the two different microwave vessels. The ramp time, heating temperature, and reaction hold time were the same in both reactions (Figure 7.14). The only difference was the vessel material. In both vessels, an ITO-coated glass slide was suspended from the top of the vessel with a custom made basket tied to the vessel cap by Teflon tape. The reaction temperature was measured directly within the growth solution via a thermometer inside an immersion tube. The thermometer was located directly behind the glass slide in these reactions. The temperature was ramped to 160 °C in approximately 3 min and held for 60 min. Note that the required temperature was slightly higher than in other microwave reactors because of the limited size of the Monowave reaction vessels (and therefore small ITO patterns), as discussed previously.

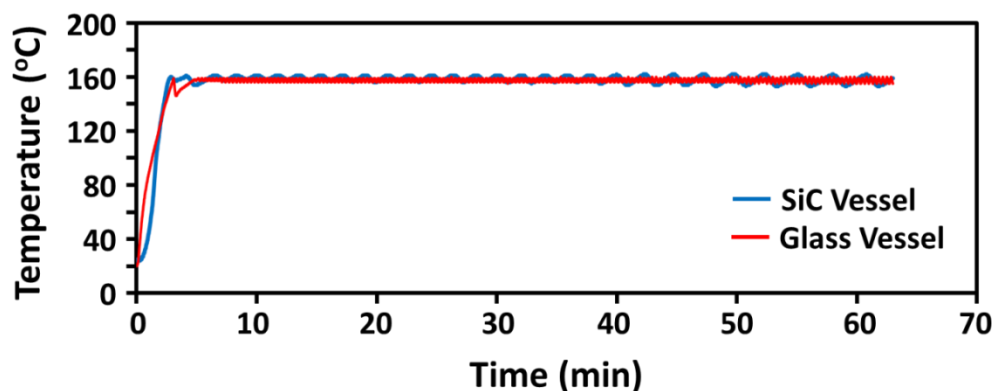


Figure 7.14. Comparison of the thermal profiles in glass and SiC vessels. The ramp time, temperature, and hold time were nearly identical in both vessels. There is slightly more temperature variation during the hold time in the SiC vessel, because it is more difficult to control the temperature. This is because thermal convection is a slow heat transfer process relative to direct dielectric heating of the solvent and ohmic heating of the ITO layer.

The results from the reactions in the SiC and glass vessels are shown in Figure 7.15. Clearly, no film forms when reactions are run in the SiC vessel and films do form during reactions under the same conditions in the glass vessel. Even after varying the ramp time and temperature, films never grew in the SiC vessel. In contrast, films could be grown in the glass vessels for a wide variety of temperatures and ramp times. The ITO layer is only heated indirectly by thermal convection in the SiC vessel, rather than by direct selective heating, which occurs due to interaction with the microwave field. This further demonstrates that film growth is critically dependent on the selective heating of the ITO layer, which results from direct interaction with the microwave field.

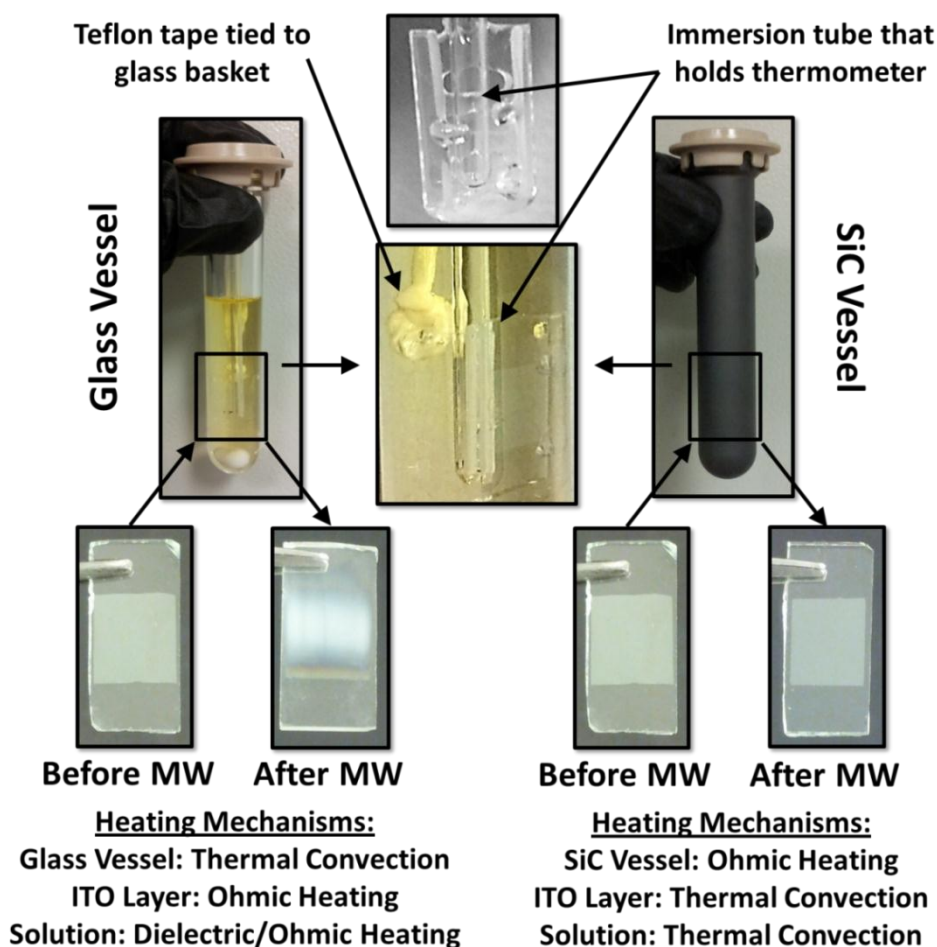


Figure 7.15. Comparison of ITO slides before and after microwave reactions in glass and SiC vessels for a reaction ramped to 160 °C in approximately 3 min and held for 60 minutes. Only reactions in the glass vessel led to film formation. The color of the ITO layer (square patterned in center of slides) is different than previously shown slides, because the slides were from a different batch with a slightly higher resistance. It should be noted that different temperatures and different ramp times did not change these results.

Cyclic voltammetry of thin films

The utility of these films for thin-film battery applications can also be demonstrated. Anatase TiO₂ is currently being studied as a candidate anode material for thin-film Li-ion batteries because it is safer than Li metal anodes and can withstand

solder-reflow conditions, the common process for attaching thin-film batteries to circuit boards [76, 79-81, 134].

CV results for anatase thin films on ITO-coated glass grown by the MW-ST method are shown in Figure 7.16. The CV experiments were performed by constructing coin cells with 1:1 ethylene carbonate and diethyl carbonate as the electrolyte (LiPF_6 salt). This is not a typical configuration for thin-film batteries since thin-film batteries are completely solid state and typically are grown on flexible substrates. Also, ITO is not a practical current collector for thin-film batteries due to cost. Despite these considerations, CV of TiO_2 on ITO has previously been used to demonstrate the electrochemical response of anatase for thin-film battery applications [79]. Future work will focus on adapting these films to be grown in more traditional thin-film battery configurations. It should be noted that the thicknesses of the films grown here are more on the order of those for thin-film batteries than for Li-ion batteries. Furthermore, they are grown with no binder or carbon additives, also consistent with thin-film batteries and not consistent with lithium-ion batteries.

The CV results show sharp peaks centered around 1.75 V for the most crystalline film pictured, as is typical of anatase. A thin amorphous film is also shown in which there are no TiO_2 peaks and there is little current density. The CV curves for the amorphous sample were found to show only slightly more separation between charge and discharge curves than CV curves for cells fabricated with just Cu metal versus Li metal (not shown here). The peaks below 1.5 V and above 2.2 V are present for cells made with just Cu metal versus Li metal, indicating that these peaks result from side reactions with the cell components.

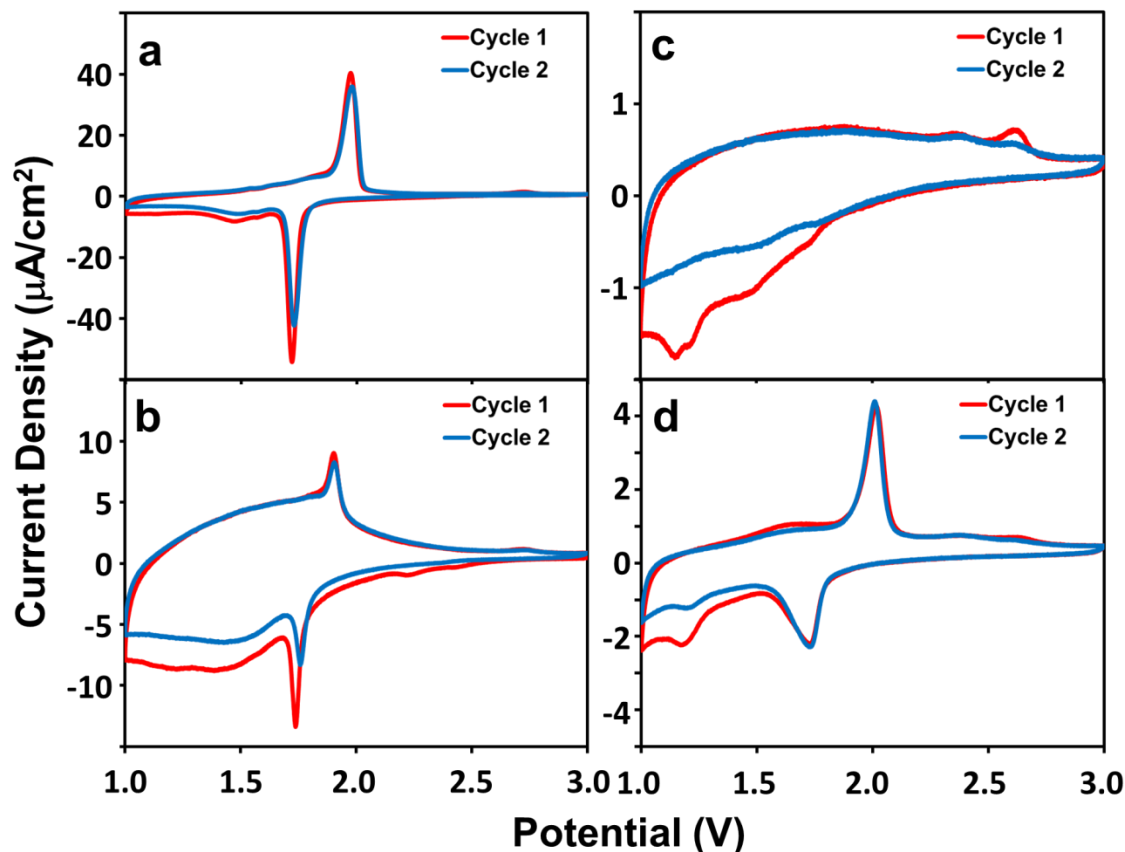


Figure 7.16. CV of (a) a very crystalline microwave-grown TiO_2 film on ITO-coated glass, (b) a more weakly crystalline TiO_2 film, (c) an amorphous TiO_2 film, and (d) TiO_2 film on ITO-coated glass grown by conventional spin coating of Ti sol-gel and subsequent furnace heating at 450°C . Note changes in current density scale.

Representative CV curves are also shown for more weakly crystalline TiO_2 films in which there are TiO_2 peaks present but also large broad separation between the charge and discharge curves at low voltage, which is likely attributable to amorphous TiO_2 or impurities. Only the most crystalline films showed sharp peaks like those in Figure 7.16(a) and most films tested exhibited an electrochemical response more like that shown in Figure 7.16(b), indicating that the conditions have to be very well optimized in order to

obtain good electrochemical performance. These results can also be compared to a conventionally prepared TiO_2 thin film synthesized by spin coating Ti sol-gel onto ITO-coated glass and firing in air at 450 °C. This procedure is used to grow TiO_2 films for use in inorganic-organic hybrid solar cells, as discussed in more detail elsewhere [138]. There are clear crystalline anatase peaks for this sample as well. The current density is lower than for the crystalline microwave-grown films because the conventionally prepared film is much thinner than the microwave-grown films, and the current density is scaled per unit area rather than per unit thickness.

Although this demonstrates that it may be possible to grow anode films for lithium-ion thin-film batteries, this process may prove more useful for cathode materials. Conventional deposition methods cannot control stoichiometry well, which is a particularly difficult challenge for ternary cathode materials. In response to difficulties obtaining crystalline and stoichiometric electrode films by traditional deposition methods, a few sol-gel methods have been developed in which the sol-gel is spin coated onto the substrate and sintered at high temperature to obtain crystalline phases [126, 127, 133]. To deposit thick films, this process is sometimes repeated several times. In future work, growing films of other materials relevant for batteries will be attempted on microwave absorbing substrates. This film growth method will likely have economic advantages, and may lead to better stoichiometry control than is possible for current methods.

Because devices for many applications require films to be grown on other substrates, attempts have been made to grow films on ITO-coated plastic and on Al-coated glass. Although the conditions for these reactions are not optimized, Figure 7.17 shows film growth on both substrates. The films on Al-coated glass appear to be more

weakly adhered than the films on ITO, possibly due to the absence of oxide-oxide bonding, and thus far, only amorphous films have been grown.

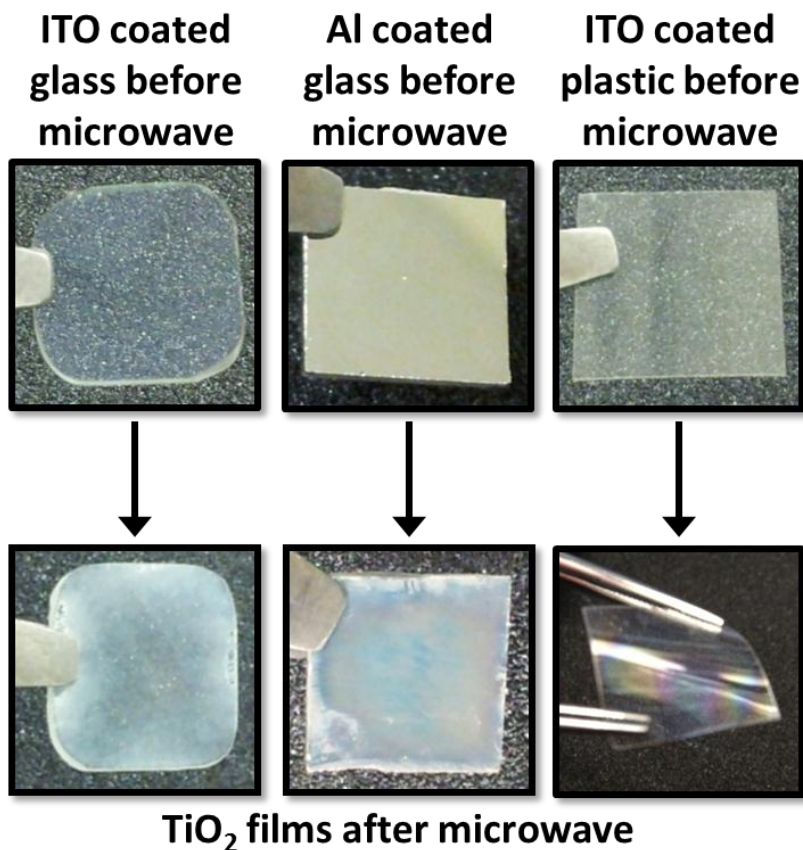


Figure 7.17. Films grown on Al-coated glass and ITO-coated plastic compared to films grown on ITO-coated glass.

Films grown on ITO-coated plastic also present challenges because of the thin flexible nature of the substrates. High temperatures and long times lead to cracks in the films. The crystallinity of the films on plastic could not be tested with GIXRD because the PET substrate has a very strong peak that overlaps the anatase peak, but Raman spectroscopy revealed spectra similar to that of the crystalline films on ITO-coated glass

[138]. More optimization needs to be done to obtain strongly adhered, crystalline films on flexible and metal substrates, but initial results suggest that this is likely possible. The film growth mechanism described here, which is strongly dependent on selective heating of a microwave-absorbing substrate to catalyze film growth, may be adaptable to many different materials grown on many substrates.

Summary of results from collaborators

This project is the result of much collaboration. My contributions have been outlined here, but there are significant contributions from collaborators. In addition to preparing ITO-coated glass slides before microwave synthesis and collecting many of the GIXRD patterns, B. Reeja-Jayan did extensive characterization of the films with TEM, Raman spectroscopy, XPS, and conductive AFM. She also put together a movie of the film formation from a camera that recorded the film growth *in situ* in the CEM Discover microwave. This showed that the film grew on the ITO before it grew in solution. Additionally, she fabricated photodetectors and solar cells out of the films and compared their performance to conventionally synthesized thin films. More extensive discussion can be found in her dissertation [138]. Chih-Liang Wang also helped prepare substrates for use in the microwave synthesis reactions, including developing a method to deposit high-resistance ITO on glass. He also imaged many samples with cross-sectional SEM to study the thickness of the films grown under various conditions. These images are presented elsewhere [138]. Finally Kai Yang developed an extensive computational model of the microwave interaction with the ITO layer and performed many simulations of different conditions varying the microwave absorbing layer conductivity, the size and shape of the patterns, the microwave frequency, and many other parameters. A few of the

results are presented here, but more details and results can be found in his dissertation [139].

7.4 CONCLUSIONS

Thin films of anatase TiO_2 were grown on ITO-coated glass substrates at 150 °C by a facile, single step MW-ST synthesis technique. Attempts to grow these films by conventional solvothermal heating mechanisms (both in a furnace and with SiC vessels in a microwave) were unsuccessful, indicating that this process is critically dependent on the presence of a microwave absorbing layer like ITO on the substrate, which heats selectively and catalyzes thin-film growth. This argument is further supported by simulations, which show excellent agreement with experimental observations.

This process is likely adaptable to growing thin films on other microwave absorbing substrates, including metals and other conducting oxides. The temperature used is low enough that it could be possible to deposit films on ITO-coated plastic substrates without melting the plastic, although more optimization is necessary before this becomes a reality. With more optimization, these films have potential applications in many other areas including ultracapacitors, dye-sensitized solar cells, hydrogen production, photocatalytic water splitting, functional biomaterials, medical devices, and self-cleaning and anticorrosion coatings.

Chapter 8: Summary

Inorganic materials for energy applications are commonly synthesized by solid-state methods, which require long reaction times at high temperatures, sometimes in specialized gas environments. These processes consume large amounts of energy, which increases manufacturing cost. Solvothermal synthesis methods can greatly reduce reaction temperatures, but generally require very long reaction times (often several days). Microwave-assisted solvothermal (MW-ST) synthesis methods can reduce reaction times to mere minutes, and often result in nanoparticles with tunable sizes and useful morphologies. To this end, this dissertation outlines a variety of contributions, which involve the development of microwave-assisted solvothermal synthesis methods for inorganic materials that are relevant to energy applications focusing on batteries and solar cells.

First, a MW-ST method was developed to dope vanadium into LiFePO_4 at $300\text{ }^\circ\text{C}$ in a reaction time of 5-10 min, such that a cathode material of the form $\text{LiFe}_{1-3x/2}\text{V}_{x/2}\text{PO}_4$ with at least $x = 0.2$ was prepared. The doping onto the iron site was evidenced by Rietveld refinement of powder neutron and X-ray diffraction patterns. XANES was used to calculate the oxidation state of vanadium, which was $\sim 3.2+$. Electrochemical measurements suggest that the $\text{V}^{3+/4+}$ and $\text{V}^{2+/3+}$ couples are active in the doped samples, and open-circuit voltage measurements suggest a single phase charge-discharge mechanism (solid-solution) rather than the two-phase behavior typical of LiFePO_4 . The cycling performance was also found to improve with doping.

The phase stability of the 15 % V-doped LiFePO_4 was also assessed by heating the pristine material in reducing and inert environments at conventional synthesis temperatures. After heating, Rietveld refinement of the X-ray diffraction patterns showed

clear evidence of $\text{Li}_3\text{V}_2(\text{PO}_4)_3$ impurity at high temperatures, and the vanadium occupancies in the olivine phase decreased with increasing heating temperature. At lower temperatures, no impurity formed, but changes in the FTIR spectra and electrochemical data indicated that the samples exhibited only moderate kinetic stability after heating, even at low temperatures. Furthermore, direct synthesis of 15 % V-doped LiFePO_4 was attempted by conventional heating methods. Rietveld refinement of these materials indicated less vanadium doping than that in the microwave-prepared samples. These results agree with previous studies, which indicate only about 10 % vanadium can be accommodated in the olivine lattice at conventional temperatures, whereas at least 20 % can be accommodated by the MW-ST method presented here. These observations confirm that the MW-ST method allows formation of a metastable phase at low temperatures, which can accommodate higher doping levels than can be achieved in conventional synthesis.

A MW-ST method was also developed to synthesize all three polymorphs of LiVOPO_4 at $\leq 230^\circ\text{C}$ in ≤ 25 min using a mixed solvent (water and a variety of alcohols/glycols) approach. By varying the mixture of solvents, the precursor ratios, and the temperature, the various polymorphs could be isolated. The α - LiVOPO_4 polymorph was the most stoichiometric phase, as determined by elemental analysis, so this phase was further optimized by varying the reaction conditions. The morphology was found to consist of micro-flower-like structures and particle size was shown to be tunable by varying the solvent mixture, reaction time, and concentration. Smaller particles were found to greatly improve electrochemical performance. The particle size and resulting electrochemical performance was further controlled by adding a surfactant (CTAB) to the

reaction solution. The capacities of the as-synthesized materials faded with cycling, so the material was coated with PEDOT to improve cyclability.

The process of inserting a second lithium ion into two of the LiVOPO_4 polymorphs was also studied here by electrochemical and chemical lithiation of pristine $\alpha\text{-LiVOPO}_4$ and $\beta\text{-LiVOPO}_4$. Chemical lithiation of the material was confirmed by elemental analysis, and FTIR measurements revealed the V=O bonds present in both the polymorphs disappeared with increasing lithium content, in agreement with expectations. *Ex situ* XRD measurements of the electrochemically lithiated material detailed the phase transition that occurs during discharge. XRD patterns for the electrochemically and chemically lithiated products agreed well, indicating that the same phase forms during these processes. *Ex situ* measurements of the fully charged materials (fully delithiated) before and after full discharge to Li_2VOPO_4 showed that the structural transformation that occurs by insertion of a second lithium ion is reversible. Furthermore, the products synthesized here have not been presented before in the literature and do not resemble previously recognized phases.

In addition to isolation of metastable phases and the ability to tune particle size and electrochemical performance for lithium-ion batteries, a MW-ST method was also developed to grow thin films of anatase TiO_2 on indium tin oxide (ITO)-coated glass. The ITO coating selectively absorbs microwaves, leading to rapid ohmic heating of the ITO, as is confirmed through electromagnetic simulations. This, in turn, provides a favorable site for thin-film nucleation and growth. Film growth was found to be critically dependent on direct microwave interaction with the ITO coating, as evidenced by failure to grow films without the presence of the microwave field in conventional solvothermal and SiC microwave reaction vessels.

ITO-coated glass was chosen as a substrate because the initial goal of this project was to develop a low-temperature method to grow TiO_2 on ITO-coated plastic, which is of particular interest for use in flexible inorganic-organic hybrid solar cells. Since TiO_2 is normally synthesized at temperatures of at least 450 °C, thin films cannot be grown on ITO-coated plastic due to the low melting temperature of the available plastics. Although film growth was optimized on ITO-coated glass, preliminary results reveal that this method could likely be adapted to ITO-coated plastic substrates. TiO_2 is also of interest for thin-film battery applications. Although ITO-coated glass is not an ideal substrate for thin-film batteries, cyclic voltammetry tests of the TiO_2 films demonstrate encouraging electrochemical activity. Initial attempts to grow films on more appropriate metal substrates were successful, but these initial experiments led to amorphous films. More optimization is required to adapt these films to be grown on substrates appropriate for thin-film batteries. Regardless, the MW-ST method is a promising approach, which has been only minimally explored for thin-film deposition.

Overall, MW-ST synthesis methods are advantageous for reducing manufacturing energy, cost, and time. It is also shown here that MW-ST methods can access regions unexplored and inaccessible with conventional approaches. The materials resulting from these synthesis methods can be useful for a variety of energy applications, especially owing to the ability to vary reaction parameters with MW-ST so as to tune material properties.

Appendices

A. SYNTHESIS OF BULK TiO_2 POWDER FOR LITHIUM-ION BATTERIES

Chapter 7 described synthesis of anatase phase TiO_2 thin films on ITO-coated glass substrates. In addition to use in thin-film batteries, TiO_2 is also an anode material under investigation for lithium-ion batteries [141, 142]. For lithium-ion batteries, bulk powder must be synthesized for electrodes rather than thin films. Thus, it was relevant to adapt the thin-film TiO_2 procedure from Chapter 7 to synthesize bulk TiO_2 powder. Because anatase formation was favored by addition of tetraethylene glycol (TEG) to the precursor solutions (Figure 7.1), the sol-gel recipe [137] described in Chapter 7 was adapted such that the ethanol was replaced by TEG. Also, the TiO_2 powder resulting from the synthesis described in Chapter 7 was light yellow in color, whereas TiO_2 is generally white. Since the precursor solution turns yellow upon addition of acetylacetone, it seemed likely that the acetylacetone may be causing the color change by possibly not washing out after synthesis, so the acetylacetone was left out of the precursor solutions for bulk powder synthesis.

In a typical reaction, 10 mL of tetrabutyl orthotitanate (TBT) was added to 100 mL of TEG and stirred for 30 min. Then, 10 mL of acetic acid was added and the solution was stirred for 1 h. 20 mL of the solution was transferred to each of four polytetrafluoroethylene (PTFE) microwave reaction vessels. Reactions were run using a power of 600 W until final temperatures between 150 °C and 300 °C were reached. At that point, the reaction was held for 20 min and then convectively cooled. The other details about reaction conditions are similar to those described in previous Chapters.

Low yields were obtained at lower temperatures, so a reaction temperature of 200 °C seemed most optimal. An XRD pattern of the as-synthesized material is shown in

Figure A.1. The peaks can all be indexed to anatase phase TiO_2 . The SEM image in Figure A.2 shows nano-particle morphology with some particle agglomeration. Initial electrochemical performance is promising, as shown in Figure A.3, and is similar to literature values [141, 142]. Future work will focus on optimizing the synthesis conditions by changing the temperature, time, solvent, and solution composition.

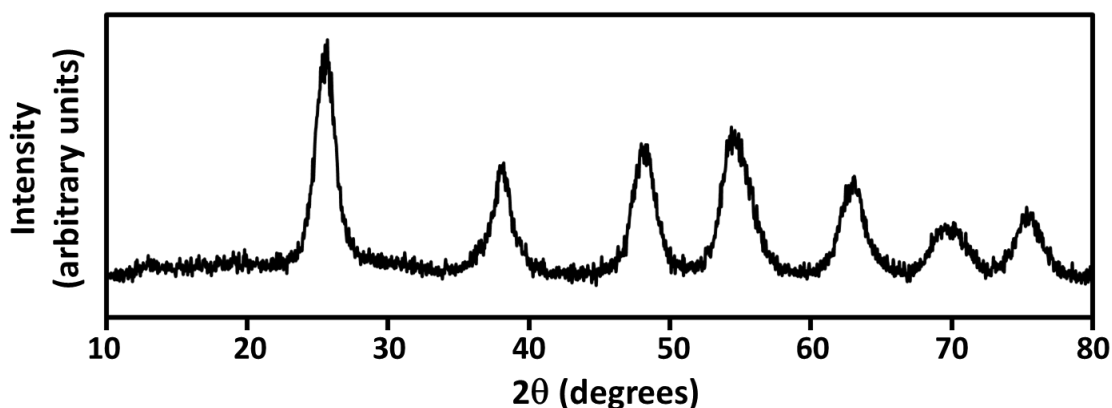


Figure A.1. XRD of TiO_2 powder.

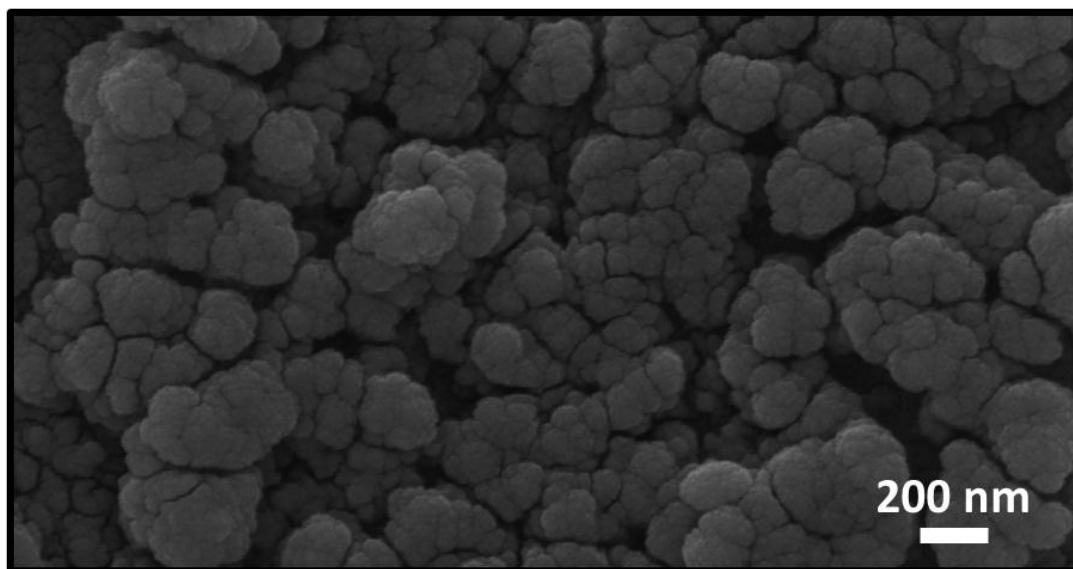


Figure A.2. SEM image of TiO_2 powder.

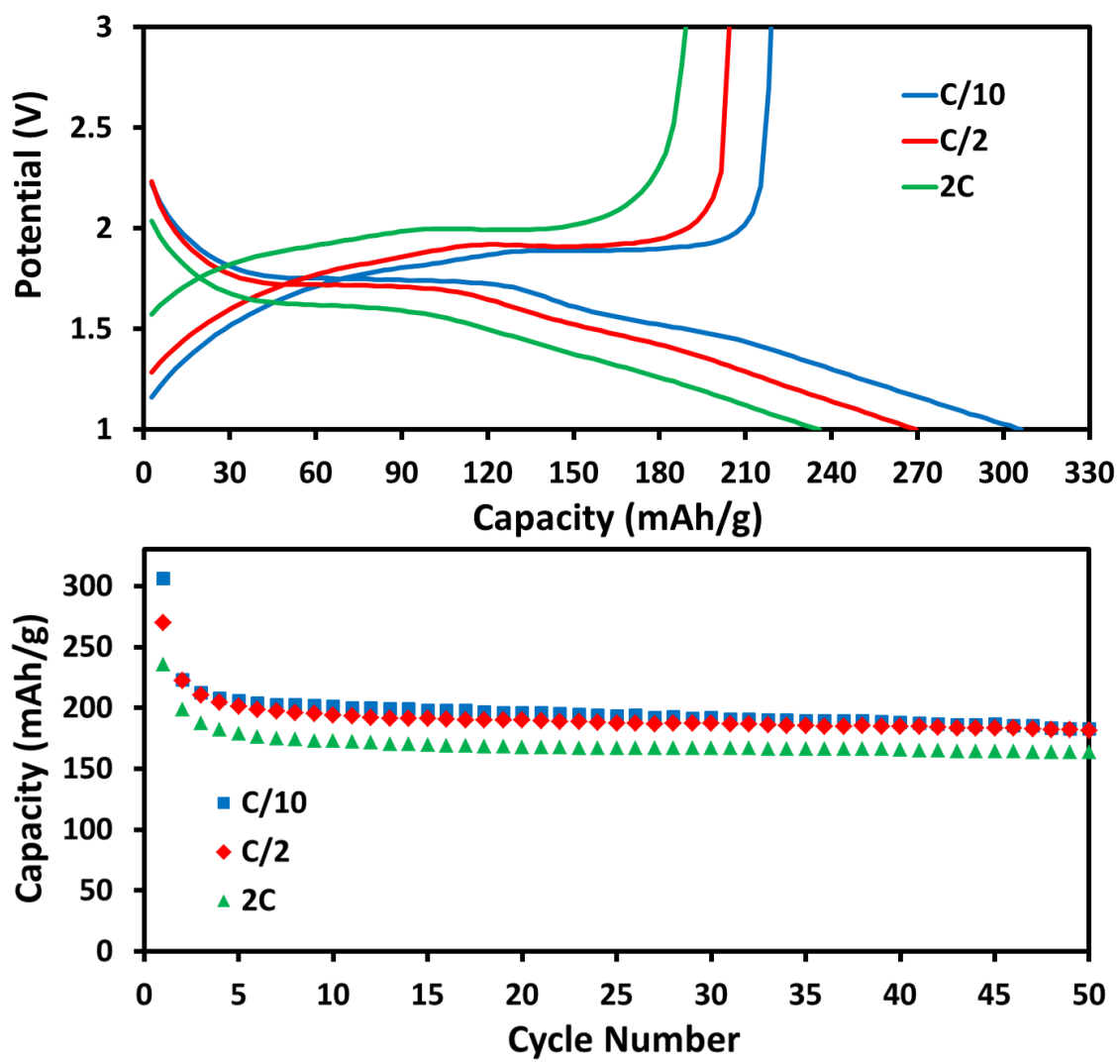


Figure A.3. First charge-discharge curves (top) and cycle performance (bottom) of TiO_2 .

B. SCALE UP OF MICROWAVE-ASSISTED SOLVOTHERMAL GRAPHENE SYNTHESIS

Many microwave-assisted solvothermal (MW-ST) synthesis methods have been described in this dissertation and in the literature. MW-ST methods are pursued because of the many advantages over conventional methods, including the energy, time, and cost savings associated with short reaction times and very efficient heating as well as the ability to tune material properties through particle morphology and purity control. To address the demand for microwaves with precise control and monitoring of reaction parameters, several companies have developed commercial microwave reactors designed specifically for material synthesis. Despite the advances in synthesis methods and available microwaves, the scalability of MW-ST reactions remains a major hurdle for commercialization of MW-ST synthesized materials. However, microwave manufacturers are beginning to address this shortcoming by developing large-scale reaction vessels which could make microwave-synthesized products more commercially viable. I had the opportunity to evaluate an Anton Paar Masterwave BTR microwave reactor to experiment with synthesis scale up. This microwave reactor is equipped with a 1 L vessel as opposed to the 80-100 mL vessels that can be used with the Anton Paar Synthos 3000.

Previously, the Manthiram group has demonstrated that graphene sheets can be synthesized by a MW-ST method in 15 min at 300 °C [143]. Graphene is of great interest in many applications due to its large thermal conductivity, high electrical conductivity, favorable mechanical properties, and interesting optical properties. Specifically for Li-ion batteries and electrochemical capacitors, graphene is pursued because it is chemically stable and has a large surface area to volume ratio, which is helpful for facilitating electrochemical reactions. Because graphene has many potential applications and is a

very active research area in the literature, scale up of graphene in the Masterwave was chosen as a test case.

The Masterwave vessel is made of polytetrafluoroethylene (PTFE), so the reaction temperature was limited to 250 °C unlike the Synthos, which can use quartz vessels that withstand 300 °C. Because of the Masterwave temperature limitation, the reaction could not be carried out under exactly the same conditions as has been done previously in the Synthos. Other than the temperature, the procedure was similar to that previously described [143]. Graphite oxide was prepared by Hummers method [144]. The resulting graphite oxide was ultrasonicated in tetraethylene glycol for 30 minutes and then transferred to the 1 L Masterwave vessel. The temperature was ramped to 250 °C and held for 15 min. Products were washed in acetone and ethanol several times and dried under vacuum at 80 °C. Electrodes were prepared by mixing 70 wt. % active material with 15 wt. % conductive carbon (super P) as a conductive agent and 15 wt. % polyvinylidene fluoride (PVDF) dissolved in N-methyl-2-pyrrolidone (NMP) as a binder to form a slurry. The slurry was coated onto a copper foil, and then pressed and dried under vacuum at 100 °C for at least 4 h. The coin cells were assembled in an argon-filled glove box with the graphene sheets as the working electrode, metallic lithium as the counter and reference electrode, 1 M LiPF₆ in 1:1 diethyl carbonate/ethylene carbonate as the electrolyte, and Celgard polypropylene separator. Charge-discharge measurements were carried out galvanostatically at a C/15 rate over a voltage range of 0.01-3 V vs. Li/Li⁺.

Despite lower reaction temperature and higher concentration for the products synthesized in the Masterwave vessel, graphene was still successfully synthesized, as was confirmed by XRD (Figure A.4). Published first charge-discharge results from graphene

prepared in the Synthos at 300 °C are shown in Figure A.5 and compared to the first charge-discharge results for graphene synthesized in the Masterwave at 250 °C. The capacities achieved were very similar, indicating that this synthesis method can be scaled up successfully.

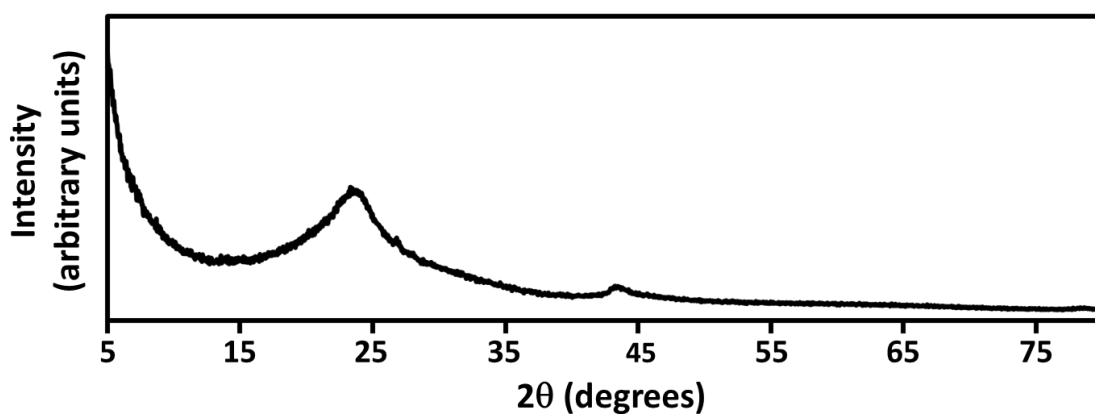


Figure A.4. XRD of graphene prepared in the Masterwave.

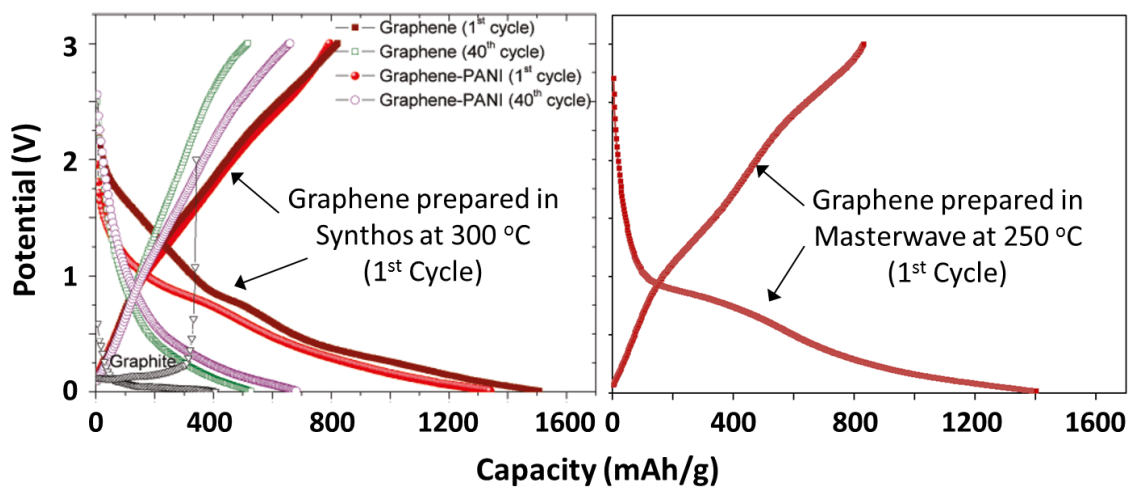


Figure A.5. First charge-discharge curves of graphene prepared in the Synthos (left) and Masterwave (right) microwaves.

Furthermore, synthesis in the 80 mL Synthos vessels yielded approximately 0.1 g graphene per vessel, whereas synthesis in the Masterwave was successfully scaled up to ~ 9 g graphene per vessel. The reaction took less than an hour including heating and cooling time. So, with a single microwave, it would be possible to synthesize ~ 200 g of graphene per day if continuously operated. If one owned several of these microwaves, correspondingly larger quantities could be prepared. Since the Masterwave was borrowed from Anton Paar for only a short period of time, attempts could not be made to further scale up the reaction, but that may also be possible. 9 g of TiO_2 powder was also synthesized in one batch in the Masterwave, indicating these reaction yields of this magnitude are possible for a variety of materials. Attempts to synthesize LiFePO_4 in the Masterwave yielded a poorly crystalline product due to the temperature limitation, so further advances allowing for higher temperature vessels in the Masterwave would be needed in order to evaluate whether MW-ST LiFePO_4 synthesis could be scaled up.

C. REDUCTION OF METAL OXIDES BY MICROWAVE-ASSISTED SOLVOTHERMAL PROCESS

The bulk of this dissertation is focused on developing synthesis methods to prepare materials from a mixture of precursors. The graphene synthesis described in Appendix B differs slightly because instead of dissolving precursors in a solution and then reacting to form a final product, it involves reducing a suspension of solid graphite oxide in a solvent to form graphene. Reduction of as-synthesized oxide materials by microwave irradiation represents a new and exciting area of opportunity that may be useful for obtaining a variety of lower-valent oxides from higher-valent oxides.

There are many oxide materials that are stable with widely varying oxygen contents in the structure. For example, $\text{YBa}_2\text{Cu}_3\text{O}_{7-\delta}$ can be stabilized with δ between approximately 0 and 1 [145]. The exact oxygen content has a tremendous influence on the material properties, as $\text{YBa}_2\text{Cu}_3\text{O}_{6.94}$ is a superconductor, but $\text{YBa}_2\text{Cu}_3\text{O}_6$ is a semiconductor. The oxygen content in several perovskite-related oxides that are often relevant for solid oxide fuel cells ($\text{GdBaCo}_2\text{O}_{5+\delta}$, $\text{NdBaCo}_2\text{O}_{5+\delta}$, $\text{La}_4\text{Ni}_3\text{O}_{10}$, and $\text{LaSr}_3\text{Fe}_{1.5}\text{Co}_{1.5}\text{O}_{10}$ are specifically studied here) can also be varied significantly and the oxygen stoichiometry can greatly influence their electronic and ionic transport and magnetic properties [146- 150].

Conventionally, reduction of oxides can be achieved by heating in an inert or reducing environment at high temperatures for long times. To determine if reduction and corresponding oxygen loss could be achieved by a fast microwave-assisted reaction in TEG, several lanthanide based oxides were synthesized. $\text{YBa}_2\text{Cu}_3\text{O}_{7-\delta}$ was synthesized similarly to previous methods [145] by first drying Y_2O_3 at 900 °C for 2 h, and then grinding stoichiometric amounts of Y_2O_3 , BaCO_3 , and CuO with a mortar and pestle for 1 h. The material was then heated to 900 °C for 20 h and cooled at a rate of 0.5 °C/min. It was ground for an additional hour and annealed at 450 °C for 24 h followed by a second

step at 350 °C for 48 h and was finally cooled slowly again at 0.5 °C/min to maximize oxygen content. The $\text{GdBaCo}_2\text{O}_{5+\delta}$, $\text{NdBaCo}_2\text{O}_{5+\delta}$, $\text{La}_4\text{Ni}_3\text{O}_{10}$, and $\text{LaSr}_3\text{Fe}_{1.5}\text{Co}_{1.5}\text{O}_{10}$ materials were synthesized by Young Nam Kim, as described elsewhere [151]. The oxides were mixed in TEG, sealed in quartz vessels as described in previous Chapters, and exposed to microwave irradiation at 300 °C for 30 min. Then the materials were cooled and washed with acetone.

Figure A.6 and Figure A.7 show XRD patterns for several oxides before and after the MW-ST reaction. The materials presented in Figure A.6 all decomposed during the reaction. It should be noted though that only one solvent, one reaction temperature, and one reaction time are presented here for these materials. It is likely that varying the solvent and reaction conditions may make it possible to control the oxygen stoichiometry in some of these samples, but more optimization would be required. Successful attempts at oxide reduction are shown in Figure A.7. The Ni^{3+} in $\text{La}_4\text{Ni}_3\text{O}_{10}$ was reduced to Ni^{2+} with corresponding oxygen loss, demonstrating the proof-of-concept. Furthermore, $\text{NdBaFe}_2\text{O}_{5+\delta}$ was stable under these conditions in TEG and did not decompose. However, there was a very obvious shifting in the peaks to lower angles. Lower angles imply higher unit cell volume, which is consistent with the longer bonds that would be associated with reduction of iron. Overall, microwave-assisted solvothermal reactions are promising as a rapid and low energy reduction method that warrants more detailed exploration.

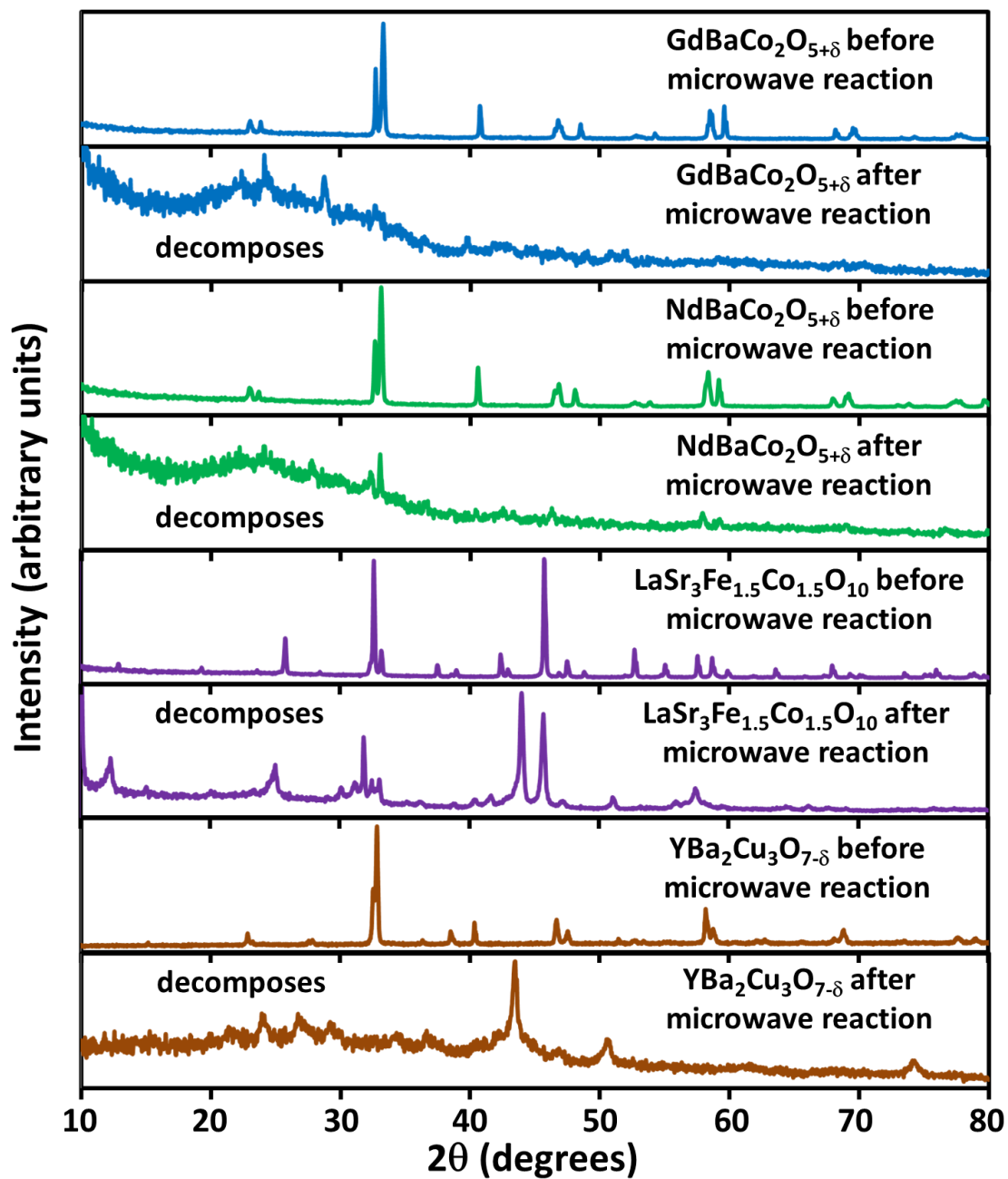


Figure A.6. XRD patterns of various oxides before and after microwave reaction.

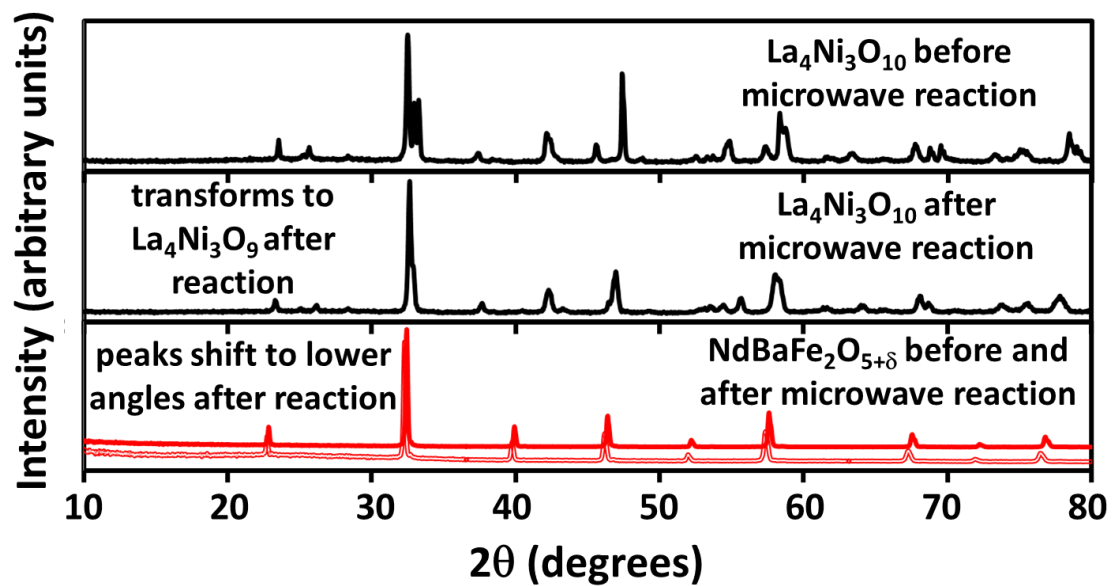


Figure A.7. XRD patterns for various oxides before and after microwave reaction.

References

- [1] A. Manthiram, "Materials Aspects: An Overview," in *Lithium Batteries: Science and Technology*, Springer (2004) 3-41.
- [2] A. Manthiram, "Battery Applications," in *Encyclopedia of Smart Materials*, John Wiley & Sons (2002) 68-82.
- [3] M. S. Whittingham, *Science*, **192**, 1126 (1976).
- [4] K. Mizushima, P. Jones, P. Wiseman and J. Goodenough, *Materials Research Bulletin*, **15**, 783 (1980).
- [5] R. V. Chebiam, F. Prado and A. Manthiram, *Chemistry of Materials*, **13**, 2951 (2001).
- [6] J. Choi and A. Manthiram, *Electrochemical and Solid State Letters*, **8**, C102 (2005).
- [7] M. M. Thackeray, P. J. Johnson, L. A. De Picciotto, P. G. Bruce and J. B. Goodenough, *Materials Research Bulletin*, **19**, 179 (1984).
- [8] T. Ohzuku, M. Kitagawa and T. Hirai, *Journal of the Electrochemical Society*, **137**, 40 (1990).
- [9] D. H. Jang, Y. J. Shin and S. M. Oh, *Journal of the Electrochemical Society*, **143**, 2204 (1996).
- [10] Y. Gao and J. R. Dahn, *Journal of the Electrochemical Society*, **143**, 100 (1996).
- [11] A. M. Kannan and A. Manthiram, *Electrochemical and Solid-State Letters*, **5**, A167 (2002).
- [12] K. Amine, H. Tukamoto, H. Yasuda and Y. Fuiita, *Journal of the Electrochemical Society*, **143**, 1607 (1996).
- [13] T. A. Arunkumar and A. Manthiram, *Electrochemical and Solid-State Letters*, **8**, A403 (2005).
- [14] J. Liu and A. Manthiram, *Chemistry of Materials*, **21**, 1695 (2009).
- [15] A. Manthiam and J. B. Goodenough, *Journal of Solid State Chemistry*, **71**, 349 (1987).
- [16] A. Manthiram and J. B. Goodenough, *Journal of Power Sources*, **26**, 403 (1989).
- [17] A. K. Padhi, K. S. Nanjundasawamy and J. B. Goodenough, *Journal of the Electrochemical Society*, **144**, 1188 (1997).
- [18] A. Yamada, M. Hosoyo, S.-C. Chung, Y. Kudo, K. Hinokuma, K.-Y. Liu and Y. Nishi, *Journal of Power Sources*, **119**, 232 (2003).
- [19] Z. Li, D. Zhang and F. J. Yang, *Journal of Materials Science*, **44**, 2435 (2009).
- [20] D. Jugovic and D. Uskokovic, *Journal of Power Sources*, **190**, 538 (2009).
- [21] B. Ellis, L. K. Perry, D. H. Ryan and L. F. Nazar, *Journal of the American*

- Chemical Society*, **128**, 11416 (2006).
- [22] B. Ellis, P. S. Herle, Y.-H. Rho, L. F. Nazar, R. Dunlap, L. K. Perry and D. H. Ryan, *Faraday Discussions*, **134**, 119 (2007).
 - [23] K. Zaghib, A. Mauger, J. B. Goodenough, F. Gendron and C. M. Julien, *Chemistry of Materials*, **19**, 2740 (2007).
 - [24] M. Gaberscek, R. Dominko and J. Jamnik, *Electrochemistry Communications*, **17**, 2778 (2007).
 - [25] A. Yamada, S. C. Chung and K. Hinokuma, *Journal of the Electrochemical Society*, **148**, A224 (2001).
 - [26] B. Ellis, W. H. Kan, W. R. M. Makahnouk and L. .. F. Nazar, *Journal of Materials Chemistry*, **17**, 3248 (2007).
 - [27] Y. Wang, J. Wang, J. Yang and Y. Nuli, *Advanced Functional Materials*, **16**, 2135 (2006).
 - [28] K.-S. Park, S. B. Schougaard and J. B. Goodenough, *Advanced Materials*, **19**, 848 (2007).
 - [29] A. V. Murugan, T. Muraliganth and A. Manthiram, *Journal of the Electrochemical Society*, **152**, A79 (2009).
 - [30] T. Muraliganth, A. V. Murugan and A. J. Manthiram, *Journal of Materials Chemistry*, **18**, 5661 (2008).
 - [31] A. V. Murugan, T. Muraliganth and A. Manthiram, *Journal of Physical Chemistry C*, **112**, 14665 (2008).
 - [32] A. V. Murugan, T. Muraliganth and A. Manthiram, *Electrochemistry Communications*, **10**, 903 (2008).
 - [33] A. Murugan, T. Muraliganth, P. J. Ferreira and A. Manthiram, *Inorganic Chemistry*, **48**, 946 (2009).
 - [34] P. Gibot, M. Casas-Cabanas, L. Laffont, S. Levasseur, P. Carlack, S. Hamelet, J.-M. Tarascon and C. Masquelier, *Nature Materials*, **7**, 741 (2008).
 - [35] N. Meethong, Y.-H. Kao, M. Tang, H.-Y. Huang, W. C. Carter and Y.-M. Chiang, *Chemistry of Materials*, **20**, 6189 (2008).
 - [36] G. Kobayashi, S.-i. Nishimura, M.-S. Park, R. Kanno, M. Yashima, T. Ida and A. Yamada, *Advanced Functional Materials*, **18**, 1 (2008).
 - [37] S.-Y. Chung, J. T. Bloking and Y.-M. Chiang, *Nature Materials*, **1**, 123 (2002).
 - [38] P. S. Herle, B. Ellis, N. Coombs and L. F. Nazar, *Nature Materials*, **3**, 147 (2004).
 - [39] N. Ravet, A. Abouimrane and M. Armand, *Nature Materials*, **2**, 702 (2003).
 - [40] M. S. Islam, D. J. Driscoll, C. A. J. Fisher and P. R. Slater, *Chemistry of Materials*, **17**, 5085 (2005).
 - [41] M. Wagemaker, B. L. Ellis, D. Lutzenkirchen-Hecht, F. M. Mulder and L. F. Nazar, *Chemistry of Materials*, **20**, 6313 (2008).

- [42] N. Meethong, Y.-H. Kao, S. A. Speakman and Y.-M. Chiang, *Advanced Functional Materials*, **19**, 1060 (2009).
- [43] C. Sun, Z. Zhou, Z. Xu, D.G.Wang, J.P.Wei, X. Bian and J. Yan, *Journal of Power Sources*, **193**, 841 (2009).
- [44] J. Hong, C. S. Wang, X. Chen, S. Upreti and M. S. Whittingham, *Electrochemical and Solid State Letters*, **12**, A33 (2009).
- [45] F. Omenya, N. A. Chernova, S. Upreti, P. Y. Zavalij, K.-W. Nam, X.-Q. Yang and M. S. Whittingham, *Chemistry of Materials*, **23**, 4733 (2011).
- [46] X. J. Chen, G. S. Cao, X. B. Zhao, J. P. Tu and T. J. Zhu, *Journal of Alloys and Compounds*, **463**, 385 (2008).
- [47] L.-L. Zhang, G. Liang, A. Ignatov, M. C. Croft, X.-Q. Xiong, I.-M. H. Hung, Y.-H. Huang, X.-L. Hu, W.-X. Zhang and Y.-L. Peng, *Journal of Physical Chemistry C*, **115**, 13520 (2011).
- [48] Y. Wen, L. Zenga, Z. Tong, L. Nong and W. Wei, *Journal of Alloys and Compounds*, **416**, 206 (2006).
- [49] N. Hua, C. Wanga, X. Kang, T. Wumair and Y. Han, *Journal of Alloys and Compounds*, **503**, 204 (2010).
- [50] J. Ma, B. Li, H. Du, C. Xu and F. Kanga, *Journal of The Electrochemical Society*, **158**, A26 (2011).
- [51] G. Yang, C. Jiang, X. He, J. Ying and F. Cai, *Ionics*, vol. 18, pp. 59-64, 2012.
- [52] B. M. Azmi, T. Ishihara, H. Nishiguchi and Y. Takita, *Journal of Power Sources*, **119**, 273 (2003).
- [53] B. M. Azmi, T. Ishihara, H. Nishiguchi and Y. Takita, *Electrochimica Acta*, vol. 48, pp. 165-170, 2002.
- [54] N. Dupre, J. Gaubicher, T. Le Mercier, G. Wallez, J. Angenault and M. Quarton, *Solid State Ionics*, **140**, 209 (2001).
- [55] N. Dupre, J. Gaubicher, J. Angenault, G. Wallez and M. Quarton, *Journal of Power Sources*, **97**, 532 (2001).
- [56] F. Girgsdies, M. Schneider and A. Bruckner, *Solid State Sciences*, **11**, 1258 (2009).
- [57] S. C. Lim, J. T. Vaughey, W. T. A. Harrison, L. L. Dussack, A. J. Jacobson and J. W. Johnson, *Solid State Ionics*, **84**, 219 (1996).
- [58] N. Dupre, G. Wallez, J. Gaubicher and M. Quarton, *Journal of Solid State Chemistry*, **177**, 2896 (2004).
- [59] N. Dupre, J. Gaubicher, J. Angenault and M. Quarton, *Journal of Solid State Electrochemistry*, **8**, 322 (2004).
- [60] C. J. Allen, Q. Jia, C. N. Chinnasamy, S. Mukerjee and K. M. Abraham, *Journal of The Electrochemical Society*, **158**, A1250 (2011).
- [61] X. Li-Zhi and H. Ze-Qiang, *Acta Phys. Chim. March Sin.*, **26**, 573 (2010).

- [62] B. M. Azmi, T. Ishihara, H. Nishiguchi and Y. Takita, *Journal of Power Sources*, **146**, 525 (2005).
- [63] J. Barker, M. Y. Saidi and J. L. Swoyer, *Journal of The Electrochemical Society*, **151**, A796 (2004).
- [64] J. Gaubicher, T. Le Mercier, Y. Chabre, J. Angenault and M. Quartona, *Journal of The Electrochemical Society*, **146**, 4375 (1999).
- [65] A. S. Hameed, M. Nagarathinam, M. V. Reddy, B. V. R. Chowdari and J. J. Vittal, *Journal of Materials Chemistry*, **22**, 7206 (2012).
- [66] T. A. Kerr, J. Gaubicher and L. F. Nazar, *Electrochemical and Solid-State Letters*, **3**, 460 (2000).
- [67] H. T. Kuo, N. C. Bagkar, R. S. Liu, C. H. Shen, D. S. Shy, X. K. Xing, J.-F. Lee and J. M. Chen, *Journal of Physical Chemistry B*, **112**, 11250 (2008).
- [68] K. H. Lii and C. H. Li, *Journal of Solid State Chemistry*, **95**, 352 (1991).
- [69] K. Nagamine, T. Honma and T. Komatsu, *Journal of the American Ceramic Society*, **91**, 3920 (2008).
- [70] M. M. Ren, Z. Zhou, X. P. Gao, L. Liu and W. X. Peng, *Journal of Physical Chemistry C*, **112**, 13043 (2008).
- [71] M. M. Ren, Z. Zhou, L. W. Su and X. P. Gao, *Journal of Power Sources*, **189**, 786 (2009).
- [72] K. Saravanan, W. S. L. Lee, M. Kuezman, J. J. Vittal and P. Balaya, *Journal of Materials Chemistry*, **21**, 10042 (2011).
- [73] L. Wang, L. Yang, L. Gong, X. Jiang, K. Yuan and Z. Hu, *Electrochimica Acta*, **56**, 6906 (2011).
- [74] Y. Yang, H. Fang, J. Zheng, L. Li, G. Li and G. Yan, *Solid State Sciences*, **10**, 1292 (2008).
- [75] A. V. Lavrov, V. P. Nikolaev, G. G. Sadikov and M. A. Porai-Koshits, *Soviet Physics Doklady*, **27**, 680 (1982).
- [76] N. J. Dudney and B. J. Neudecker, *Current Opinion in Solid State and Materials Science*, **4**, 479 (1999).
- [77] J. L. Souquet and M. Duclot, *Solid State Ionics*, **148**, 375 (2002).
- [78] J. F. M. Oudenhoven, L. Baggetto and P. H. L. Notten, *Advanced Energy Materials*, **1**, 10 (2011).
- [79] C. Natarajan, N. Fukunaga and G. Nogami, *Thin Solid Films*, **322**, 6 (1998).
- [80] W.-Y. Liu, Z.-W. Fu and Q.-Z. Qin, *Journal of the Electrochemical Society*, **155**, A8, (2008).
- [81] B. J. Neudecker, N. J. Dudney and J. B. Bates, *Journal of the Electrochemical Society*, **147**, 517 (2000).
- [82] M. Baghbanzadeh, L. Carbone, P. D. Cozzoli and C. O. Kappe, *Angewandte*

- Chemie International Edition*, **50**, 11312 (2011).
- [83] A. Fini and A. Breccia, *Pure Applied Chemistry*, **71**, 573 (1999).
 - [84] A. De la Hoz, A. Diaz-Ortiz and A. Moreno, *Chemical Society Reviews*, **34**, 164 (2005).
 - [85] H. M. Rietveld, *Journal of Applied Crystallography*, **2**, 65 (1969).
 - [86] J. Rodriguez-Carvaja, *Physica*, **192B**, 55 (1993).
 - [87] T. Roisnel and J. Rodriguez-Carvajal, *Epdic 7: European Powder Diffraction*, **378-3**, 118 (2001).
 - [88] A. C. Larson and R. B. v. Dreele, "GSAS, General Structure Analysis System," L. A. Los Alamos National Laboratory (1994).
 - [89] B. H. Toby, "EXPGUI, a graphical user interface for GSAS," *Journal of Applied Crystallography*, **34**, 210 (2001).
 - [90] B. Ravel and M. Newville, *Journal of Synchrotron Radiation*, **12**, 537 (2005).
 - [91] M. Newville, *Journal of Synchrotron Radiation*, **8**, 322 (2001).
 - [92] O. L. Krivanek, G. J. Corbin, B. F. Elston, R. J. Keyse and M. F. Murfitt, *Ultramicroscopy*, **179**, 108 (2008).
 - [93] T. Zhao, W. Xu, Q. Ye, J. Cheng, H. Zhao, Z. Wu, D. Xiac and W. Chu, *Journal of Synchrotron Radiation*, **17**, 584 (2011).
 - [94] Y. Jin, C. Yanga, X. Ruia, T. Chengb and C. Chena, *Journal of Power Sources*, **196**, 5623 (2011).
 - [95] H. Lin, Y. Wen, C. Zhang, L. Zhang, Y. Huang, B. Shan and R. Chen, *Solid State Communications*, **152**, 999 (2012).
 - [96] M.-R. Yang, W.-h. Ke and S.-h. Wu, *Journal of Power Sources*, **165**, 646 (2007).
 - [97] O. Clemens, M. Bauer, R. Haberkorn and H. P. Beck, *Journal of Inorganic and General Chemistry*, **637**, 1036 (2011).
 - [98] G. Silcersmit, D. Depla, H. Poelman, G. B. Marin and R. De Gryse, *Journal of Electron Spectroscopy and Related Phenomena*, **135**, 167 (2004).
 - [99] X. W. Lin, Y. Y. Wang and V. P. Dravid, *Physical Review B*, **47**, 3477 (1993).
 - [100] M. Chi, T. Mizoguchi, L. Martin, J. Bradley, H. Ikeno, R. Ramesh, I. Tanaka and N. Browning, *Journal of Applied Physics*, **110**, 046104-1 (2011).
 - [101] E. J. Baran and M. B. Vassallo, *Journal of Raman Spectroscopy*, **25**, 203 (1994).
 - [102] A. A. Salah, P. Jozwiak, K. Zaghib, J. Garbarczyk, F. Gendron, A. Mauger and C. Julien, *Spectrochimica Acta Part A*, **65**, 1007 (2006).
 - [103] C. M. Burba and R. Frech, *Journal of The Electrochemical Society*, **151**, A1032 (2004).
 - [104] P. Fu, Y. Zhao, Y. Dong, X. An and G. Shen, *Electrochimica Acta*, **52**, 1003 (2006).
 - [105] M. S. Bhuvaneswari, S. Selvasekarapandian, O. Kamishima, J. Kawamura and T.

- Hattori, *Journal of Power Sources*, **139**, 279 (2005).
- [106] G. T.-K. Fey, Y.-D. Cho and P. Muralidharan, *Pure Applied Chemistry*, **80**, 2521 (2008).
- [107] X. Wang, L. Liu and A. J. Jacobson, *Journal of the American Chemical Society*, **124**, 7812 (2002).
- [108] F. Sauvage, E. Quarez, J.-M. Tarascon and E. Baudrin, *Solid State Sciences*, **8**, 1215 (2006).
- [109] S. De, A. Dey and S. K. De, *Journal of Physics and Chemistry of Solids*, **68**, 66 (2007).
- [110] V. S. R. Channu, R. Holze, B. Rambabu, R. R. Kalluru, Q. L. Williams and C. Wen, *Internation Journal of Electrochemical Science*, **5**, 605 (2010).
- [111] G. Yang, H. Liu, H. Ji, Z. Chen and X. Jiang, *Electrochimica Acta*, **55**, 2951 (2010).
- [112] N. A. Chernova, M. Roppolo, A. C. Dillonb and M. S. Whittingham, *Journal of Materials Chemistry*, **19**, 2526 (2009).
- [113] L. J. M. Davis, K. J. He, A. D. Bain and G. R. Goward, *Solid State Nuclear Magnetic Resonance*, **42**, 26 (2012).
- [114] M. M. Ren, Z. Zhou and X. P. Gao, *Journal of Applied Electrochemistry*, **40**, 209 (2010).
- [115] Y. Song, P. Y. Zavalij and M. S. Whittingham, *Journal of The Electrochemical Society*, **152**, A721 (2005).
- [116] M. S. Whittingham, *Chemical Reviews*, **104**, 4271 (2004).
- [117] M. S. Whittingham, *Materials Research Society Bulletin*, **33**, 411 (2008).
- [118] M. S. Whittingham, Y. Song, S. Lutta, P. Y. Zavalij and N. A. Chernova, *Journal of Materials Chemistry*, **15**, 3362 (2005).
- [119] R. Pozas, S. Maduefio, S. Bruque, L. Moreno-Real, M. Martinez-Lara, C. Criado and J. Ramos-Barrado, *Solid State Ionics*, **51**, 79 (1992).
- [120] X. Rui, N. Yesibolati and C. Chen, *Journal of Power Sources*, **196**, 2279 (2011).
- [121] V. Koleva, W. Zhecheva and R. Stoyanova, *Journal of Alloys and Compounds*, **950**, 476 (2009).
- [122] G. Arnold, J. Garche, R. Hemmer, S. Strobele, C. Vogler and M. Wohlfahrt-Mehrens, *Journal of Power Sources*, **119**, 247 (2003).
- [123] P. Zavalij, Institute for Materials Research, Department of Chemistry, SUNY at Binghamton, ICDD Grant-in-Aid Report, New York (2004).
- [124] K. Coakley and M. McGehee, *Applied Physics Letters*, **83**, 3380 (2003).
- [125] U. Diebold, *Surface Science Reports*, **48**, 53 (2003).
- [126] Y. J. Park, J. G. Kim, M. K. Kim, H. T. Chung, W. S. Um, M. H. Kim and H. G. Kim, *Journal of Power Sources*, **76**, 41 (1998).

- [127] Y. H. Rho and K. Kanamura, ", " *Journal of Electroanalytical Chemistry*, **559**, 69 (2003).
- [128] K.-S. Han, S.-W. Song and M. Yoshimura, *Chemistry of Materials*, **10**, 2183 (1998).
- [129] K.-S. Han, *Journal of the American Chemical Society*, **85**, 2444 (2002).
- [130] N. J. Dudney, *Electrochemical Society Interface*, vol. fall, 44 (2008).
- [131] M. Hayashi, M. Takahashi and Y. Sakurai, *Journal of Power Sources*, **174**, 990 (2007).
- [132] J. F. Whitacre, W. C. West, E. Brandon and B. V. Ratnakumar, *Journal of the Electrochemical Society*, **148**, A1078 (2001).
- [133] F. T. Quinlan, R. Vidu, L. Predoana, M. Zaharescu, M. Gartner, J. Groza and P. Stroeve, *Ind. Eng. Chem. Res.*, **43**, 2468 (2004).
- [134] T. Djenizian, I. Hanzu and P. Knauth, *Journal of Materials Chemistry*, **21**, 9925 (2011).
- [135] E. Vigil, L. Saadoun, J. A. Ayllon, X. Domenech, I. Zumeta and R. Rodriguez-Clemente, *Thin Solid Films*, **365**, 12 (2000).
- [136] J. A. Ayllon, A. M. Peiro, L. Saadoun, E. Vigil, X. Domenech and J. Peral, *Journal of Materials Chemistry*, **10**, 1911 (2000).
- [137] H. Xue, X. Kong, Z. Liu, C. Liu, J. Zhou, W. Chena, S. Ruan and Q. Xu, *Applied Physics Letters*, **90**, 201118 (2007).
- [138] B. R. Jayan, *Ph. D. Dissertation, University of Texas at Austin* (2006).
- [139] K. Yang, *Ph. D. Dissertation, University of Texas at Austin* (2012).
- [140] D. Obermayer, B. Gutmann and C. O. Kappe, *Angewandte Chemie International Edition*, **121**, 8471 (2009).
- [141] D. Deng, M. G. Kim, J. Y. Lee and J. Cho, *Energy & Environmental Science*, **2**, 818 (2009).
- [142] Y. Yoon, E.-S. Lee and A. Manthiram, *Inorganic Chemistry*, **51**, 3505 (2012).
- [143] A. V. Murugan, T. Muraliganth and A. Manthiram, *Chemistry of Materials*, **21**, 5004 (2009).
- [144] W. S. Hummers and R. E. Offeman, *Journal of the American Chemical Society*, **80**, 1339 (1958).
- [145] A. Manthiram, J. S. Swinnea, Z. T. Sui, H. Steinfink and J. B. Goodenough, *Journal of the American Chemical Society*, **109**, 6668 (1987).
- [146] A. Taranc, A. Morata, G. Dezanneau and S. J. Skinner, *Journal of Power Sources* , **174**, 255 (2007).
- [147] A. Maignan, C. Martin, D. Pelloquin, N. Nguyen and B. Raveau, *Journal of Solid State Chemistry*, **142**, 247 (1999).
- [148] A. Manthiram, J.-H. Kim, Y. N. Kim and K.-T. Lee, *Journal of Electroceramics*,

- 27**, 93 (2011).
- [149] J.-G. Cheng, J.-S. Zhou, J. B. Goodenough, H. D. Zhou, K. Matsubayashi and Y. Uwatoko, *Physical Review Letters*, **108**, 236403-1 (2012).
- [150] J.-H. Kim, K.-T. Lee, Y. N. Kim and A. Manthiram, *Journal of Materials Chemistry*, **21**, 2482 (2011).
- [151] Y. N. Kim, *Ph. D. Dissertation, University of Texas at Austin* (2011).

Vita

Katharine Lee Harrison was born in 1982 in California, where she grew up. After graduating from high school, Katharine attended the University of California at San Diego. She graduated with honors (*magna cum laude*) in 2005 with a B.S. degree in mechanical engineering. She received the undergraduate chancellor's research scholarship at UC-San Diego in 2003 to conduct research on a bioengineering project. Then Katharine worked in the mechanical engineering design studio during 2004 and she interned at Lockheed Martin Space Systems Company during the summers of 2004 and 2005 working on vibration testing of satellites. During the summer of 2005, Katharine married Richard Harrison. In August 2005, she began graduate studies at the University of Texas at Austin in the thermal fluids focus area of mechanical engineering where she worked as a research assistant on film cooling of gas turbine vanes and blades for jet engines. She greatly appreciated financial support through a College of Engineering Doctoral Scholarship. After graduating with her M.S. degree in mechanical engineering in 2006 (thermal fluid systems area), she continued with doctoral studies in mechanical engineering (materials science area). She was supported by a National Science Foundation graduate research fellowship and worked on electrode materials for lithium-ion batteries.

Permanent address: 8460 Dover Drive
Granite Bay, CA 95746

This dissertation was typed by the author.